Nonlinear pressure fields due to focused rectangular apertures in water

Sahin, Ali

Award date:
1992

Awarding institution:
University of Bath

NONLINEAR PRESSURE FIELDS DUE TO FOCUSED RECTANGULAR APERTURES IN WATER

submitted by Ali Sahin

for the degree of Ph.D.
of the University of Bath.

1992

ProQuest LLC
789 East Eisenhower Parkway
P.O. Box 1346
Ann Arbor, MI 48106-1346

ABSTRACT

This thesis examines the nonlinear propagation of finite amplitude ultrasound from focused rectangular apertures. A 2.25 MHz plane piston transducer with a rectangular aperture in front of it was used as a source of finite amplitude ultrasound and the resulting pressure fields were monitored with a 1 mm diameter membrane hydrophone mounted on a computer controlled translation stage. The acoustic beam was focused by the addition of plano-concave perspex lenses to the aperture face. Theoretical models are developed based on a numerical solution to the nonlinear wave equation and a first order perturbation model. Extensive comparisons are made between experimental results and theoretical predictions obtained from both models and the agreement with each model is discussed.

TABLE OF CONTENTS

CHAPTER 1

INTRODUCTION

1.1. GENERAL

A sound wave is a mechanical disturbance in a gas, liquid or solid that travels outward from the source with some definite velocity. It is usually assumed that the disturbances are of infinitesimal amplitude to simplify the theoretical treatments. Such simplified theories are linear and many acoustical phenomena can be treated this way. This means that forces acting on the medium produce motions in exact proportion and we are entitled to use the extremely powerful concept of superposition. However, in some circumstances, when the wave amplitude is large, an increase in the amplitude does not lead to a proportional increase in acoustic pressure. This is called the finite amplitude case, and causes harmonic generation within the field resulting in distortion of wave shapes. In that case some energy is transferred from the fundamental to the harmonics and from the harmonics to the propagation medium.

Although problems in finite amplitude acoustics have been pondered since the 18^{th} century [1], practical applications of the nonlinear process have grown over the past few decades as the existence of nonlinear effects has become more widely understood. Most recently, the interest in nonlinear effects in medical ultrasound has grown considerably as the existence of such effects are more widely realised. For example, ultrasonic waves are used for the treatment of cancer cells by ultrasonically induced hyperthermia and the destruction of kidney stones using shock wave

lithotripsy. However, all of these developments bring with them a need for the characterization and the better understanding of ultrasonic fields due to the sources used in medical equipment, most of which employ either circular or rectangular transducers and arrays.

1.2. AIMS OF THE PROJECT

Nonlinear effects are of importance in design of medical ultrasound systems, this provides the motivation for better understanding of pressure fields which are often used in medicine. Some published work is available on finite amplitude effects both theoretically and experimentally as a result of extensive use of circular piston radiators in early medical equipment. However, recently, an increasing number of diagnostic systems use arrays which are of a rectangular construction but such apertures are not so well understood, especially at finite amplitudes. So, it is of interest to examine the propagation from rectangular type sources. In calculating fields of rectangular apertures, diffraction and attenuation have to be accounted for simultaneously with nonlinearity. Nonlinearity means that all factors have to be solved together because the principle of superposition no longer applies. Such effects are of importance in the design of medical ultrasound systems and have to be well understood, so the main aims of the project were;

1. To develop a theoretical model capable of predicting the harmonic content a rectangular source.

2. To obtain a better understanding of unfocused and focused pressure fields due to rectangular sources.

3. To present experimental data for rectangular apertures of various sizes and for different drive levels; to the author's knowledge the only experimental results published are some very recent measurements made in air, at low amplitudes and frequencies [2].

1.3 THESIS CONTENT

The majority of the results in this thesis are presented in terms of amplitude plots up to the fifth harmonic. Phase information was also available but it has not been widely presented owing to lack of phase information for the hydrophone calibration. Time waveforms would also be sensitive to phase information and also the contribution of the higher harmonics for which the hydrophone calibration is uncertain. Despite the lack of phase plots and time waveforms, the amplitude plots are still useful as they show the extent of nonlinear propagation in addition thermal calculations are insensitive to phase.

Although the geometries used in this study are not taken directly from medical ultrasound, the aperture sizes, aperture shapes, focal lengths and drive levels are similar to those incountered in medical ultrasound. The longer focal lengths made the experimental measurements easier to carry out.

The reminder of this chapter describes the importance of nonlinear effects in design of medical ultrasound systems. Some of the key concepts of finite amplitude propagation are also considered. The relevant studies in areas related to this work are outlined in Chapter 2, in two parts: firstly the infinitesimal pressure fields due to the plane and focused circular and rectangular sources, secondly the finite amplitude pressure fields are considered. Chapter 3 contains details of the experimental configuration and Chapter 4 presents the theoretical approaches to the

problem. The main results and discussion are given in Chapter 5 and Chapter 6 contains the conclusions. There are two appendices attached containing some of the mathematical steps in the perturbation model.

1.4 INTRODUCTION TO NONLINEAR PROPAGATION

The propagation of ultrasound is inherently nonlinear and in order to provide an accurate mathematical description of the process the equations describing wave propagation are required to be nonlinear. It has however been common to make the assumptions of linearity and this has allowed a comparatively simple mathematical description of the propagation process to be obtained which is adequate in many situations. Thus for the case of low amplitude waves, it can easily be shown [3] that the wave propagation in a fluid is completely determined through the following equations and exact equations of acoustics in a fluid can be reduced to the linearised equations, resulting in a simple wave equation. That is,

Equation of continuity expressing the conservation of mass,

$$\frac{\partial \rho}{\partial t} = -\rho_0 \nabla . u \qquad 1.1$$

equation of momentum expressing the conservation of momentum,

$$\rho_0 \frac{\partial u}{\partial t} = -\nabla . p \qquad 1.2$$

and equation of state describing the fluid's response to thermal or mechanical stress,

$$p = \left(\frac{\partial P}{\partial \rho_T}\right)\rho_0 \qquad 1.3$$

Where p is the acoustic pressure, being difference of the total pressure P and hydrostatic pressure P_0. ρ_T is the total density, ρ_0 being its value in undisturbed state. (Note that $(\rho_T - \rho_0)/\rho_0$ is a very small fraction). u is the velocity of particles, being zero in the absence of acoustic disturbance and t is time.

The differential coefficient in Equation 1.3 is related to the elastic properties of the medium, such that;

$$p=\left(\frac{B}{\rho_0}\right)(\rho-\rho_0) \qquad 1.4$$

Where B is the Bulk modulus [4] for the medium at the ambient conditions being considered. Ignoring ρ_0 in the second term in Equation 1.4 and eliminating ρ between Equation 1.1 and 1.4,

$$\frac{\partial p}{\partial t}=-B\nabla.u \qquad 1.5$$

Thus, the two differential equations 1.2 and 1.5 relate u and p. Eliminating u, we obtain

$$\frac{\partial^2 p}{\partial t^2}=\left(\frac{B}{\rho_0}\right)\nabla^2.p \qquad 1.6$$

Where B/ρ_0 is related to the velocity of propagation c,

$$c=\sqrt{\frac{B}{\rho_0}} \qquad 1.7$$

If we define the velocity potential Φ in the following differential form,

$$u = -\nabla.\Phi \qquad 1.8$$

substituting Equation 1.8 into Equation 1.5 and writing p in terms of Φ (i.e $p=\rho_0\frac{\partial\Phi}{\partial t}$),

we obtain the wave equation for the velocity potential Φ,

$$\frac{\partial^2\Phi}{\partial t^2}=c^2\nabla^2\Phi \qquad 1.9$$

As the wave equation 1.9 is linear, it is easy to find a general solution, which is often written as;

$$\Phi(\omega,z)=\Phi(\omega)e^{-jkz} \qquad 1.10$$

Here k is the wave number ($=\omega/c$) in the propagation direction z.

However, once the waves are considered to be of finite amplitude Equation 1.9 and its solution no longer hold as linear assumptions become less valid for the waves of finite amplitude, and it can be shown that an initially sinusoidal finite amplitude plane wave will distort progressively as it propagates and in the case of maximum distortion will resemble a sawtooth waveform. There are two reasons for this; one is due to the nonlinear nature of the medium and the other is due to the finite particle velocity of the wave. Both sources of the nonlinearity cause the same type of effects on the waveform and these are described below.

1.4.1 Nonlinearity due to the medium

The passage of a sound wave through a medium causes pressure, density and temperature variations in the medium. As a fluid is compressed its stiffness increases

and there is a corresponding increase in the speed of sound. This results in the compressional phase of a wave experiencing a higher speed than the decompressional phase. The relationship between pressure and density, may be expressed as

$$P=P(\rho) \tag{1.11}$$

where P is the sum of static pressure and the acoustic pressure. The precise form of this equation of state is unknown but it is common to approximate it as a Taylor series expansion of Equation 1.11 to give

$$P=P_0+\left(\frac{\partial P}{\partial \rho}\right)_{\rho_0}(\rho-\rho_0)+\frac{1}{2!}\left(\frac{\partial^2 P}{\partial \rho^2}\right)_{\rho_0}(\rho-\rho_0)^2+\ldots \tag{1.12}$$

where P_0 and ρ_0 are the equilibrium pressure and density respectively. This can be written as

$$p=P-P_0=As+\frac{Bs^2}{2!}+\frac{Cs^3}{3!}+\ldots \tag{1.13}$$

Where $s=(\rho-\rho_0)/\rho$ and is known as the condensation and,

$$A=\rho_0\left(\frac{\partial P}{\partial \rho}\right)_{\rho_0}=\rho_0 c^2, \qquad B=\rho_0^2\left(\frac{\partial^2 P}{\partial \rho^2}\right)_{\rho_0}, \text{and so on} \tag{1.14}$$

Here c is the speed of sound for infinitesimal amplitude waves. For very low amplitude waves second and higher order terms can be neglected and in this case the acoustic pressure and density in the medium are linearly related by the following relationship

$$p=c^2(\rho-\rho_0) \qquad 1.15$$

where $p=P-P_0$. As the wave amplitude becomes larger it is necessary to include higher order terms. Inclusion of the second order term results in the following relationship

$$p \approx \Delta\rho c^2+\frac{B}{2A}\Delta\rho^2\frac{c^2}{\rho_0} \qquad 1.16$$

where $\Delta\rho = (\rho-\rho_0)$ and B/A represents the first order parameter of nonlinearity and it is common to express B/A in terms of nonlinearity parameter β which is

$$\beta = 1+\frac{B}{2A} \qquad 1.17$$

Equation 1.17 describes the nonlinear relationship between changes in pressure and changes in density within the fluid due to finite wave propagation. The higher order term C/A may also be defined, but its contribution is extremely small and it is usual to consider only the first order parameter β.

The propagation speed of infinitesimal waves is defined by

$$c^2=\left(\frac{\partial P}{\partial\rho}\right)_{\rho_0}. \qquad 1.18$$

For waves of finite amplitude the relationship is modified by second order terms in the expansion of the equation of state. Thus nonlinearity inherent in this equation results in a change in propagation velocity in the medium.

1.4.2 Nonlinearity due to finite particle velocity

The second source of nonlinearity can be seen by considering the wave motion in terms of the particle velocity u, in the linear case, the particle velocity is very much smaller than the propagation velocity and the entire waveform propagates at the same speed. In the finite amplitude case, since the sound waves are longitudinal, a high particle velocity will add to the propagation velocity in a compressional half cycle and subtract from it during the rarefraction. The result is that the wave peaks travel faster than the troughs, eventually the peaks catch up with the troughs and a shock front is formed since the wave can not become multi-valued (see Figure 1.1). The limiting case is a sawtooth waveform, the distance at which occurs is called the shock formation distance [5,6].

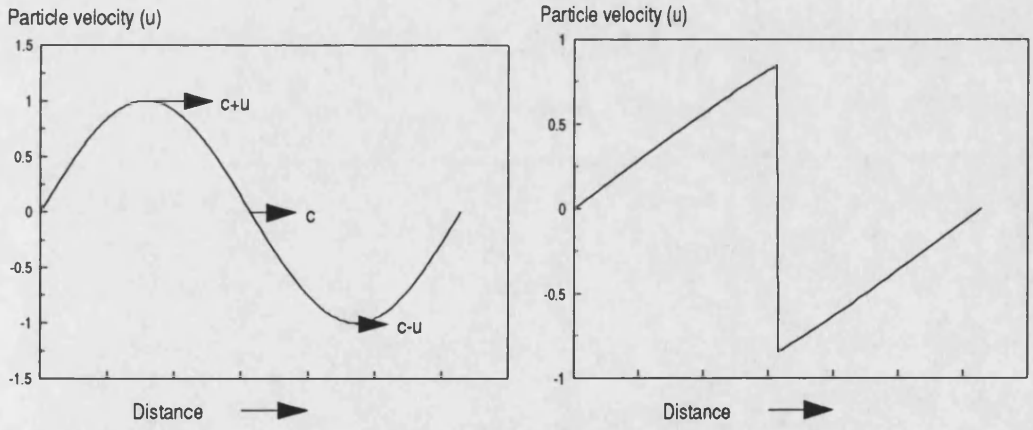

Figure 1.1 Effect of finite particle velocity on a initially sinusoidal waveform

1.4.3 Burger's Equation

Blackstock [5] combined the effect of two sources of nonlinearity mentioned above in a one dimensional nonlinear wave equation known as Burger's equation [6] for a lossless medium, which is of the form,

$$\frac{du}{dt}+\left(1+\frac{\beta u}{c}\right)\frac{du}{dz}=0 \qquad 1.19$$

Where z is the spatial coordinate in the propagation direction. The term $\beta u/c$ quantifies the nonlinearity of the medium and when it tends to zero, we get a simple linear wave equation having solutions of the form.

$$u=f(\omega t-kz) \qquad 1.20$$

Where f is an arbitrary function and the velocity of the propagation does not include the extra term βu. The inclusion of nonlinear effects then gives rise to a waveform that travels with velocity $c(1+\beta u/c)$, i.e., the propagation velocity is a function of particle velocity and the nonlinearity parameter. The quantity $\beta u/c$ can be regarded as the shift in the peak positive pressure per cycle and it is common to define a shock parameter

$$\sigma=\beta\varepsilon kz \qquad 1.21$$

Here $\varepsilon=u/c$ and $\beta\varepsilon kz$ is the total shift in peak positive pressure in a propagating wave with wave number k over a distance z. The term $\beta\varepsilon k$ in σ appears as a product in the solutions of many nonlinear problems. When σ is small then relatively little distortion has occurred (see Fig. 1.2). When it is equal to unity a shock front is just forming and a value of $\sigma=\pi/2$ indicates that a full shock front has formed. For higher values of σ, there is a significant reduction in the amplitude of the wave.

In the description of nonlinear propagation given above it was assumed that the wave was propagating through a lossless medium. If instead, propagation is through an attenuating medium, the degree of distortion which occurs depends on two competing processes. One is nonlinearity and the other is attenuation. In an attenuating medium

such as soft tissue a mature shock will not form if attenuation dominates over nonlinear effects. Gold'berg [6] introduced the coefficient, Γ, to describe the ratio between the opposing effects of nonlinear distortion and absorption as given in the following definition.

$$\Gamma=\frac{\beta\varepsilon k}{\alpha}=\frac{1}{\alpha l_d} \qquad 1.22$$

Where α is linear absorption coefficient and l_d is the shock formation distance. Finite amplitude waves cause various degrees of distortion to occur depending on the values of Γ. Thus the Γ value is a measure of the relative nonlinearity and absorption. For higher values of Γ shock formation occurs closer to the source.

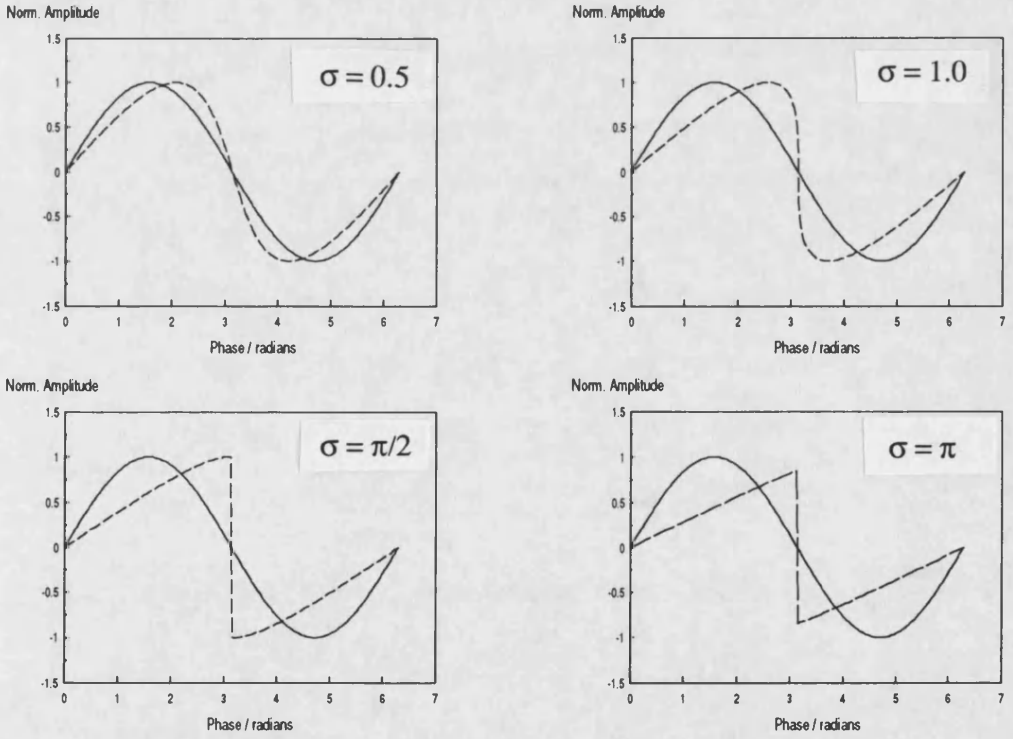

Figure 1.2 Effect of shock parameter (σ) on a sinusoidal waveform. — Initial waveform, --- Distorted waveform.

CHAPTER 2

REVIEW OF LITERATURE

This chapter covers some of the relevant studies in areas related to this work. The first part includes the linear fields of plane circular, rectangular and focused transducers. The second part reviews plane waves at finite amplitudes, the finite amplitude fields of unfocused and focused circular and rectangular transducers including; perturbation methods, one dimensional and numerical solutions to the wave equation.

2.1 INFINITESIMAL ACOUSTICS

In order to calculate the low amplitude pressure field of transducer, it is required to find a solution to the surface integral (which sometimes called the diffraction integral or Rayleigh integral) of the form

$$p=\frac{j\rho c u_0}{\lambda}\int_s \frac{e^{-jkR}}{R}ds \qquad 2.1$$

where R is the distance of the field point from an elemental source ds. The above equation is based on the hypothesis that every point on the transducer's surface vibrates with the same amplitude and phase. Thus the pressure at a point in the field is obtained by summing pressure contributions from different elements on the surface. One of the difficulties of this method is expressing the distance from the

source to the field point in a form that makes the integration straightforward. One way of doing that is limiting the calculations to points near or on the acoustic axis. With this assumption the integration becomes possible and remaining integrals can be evaluated using straightforward numerical techniques.

2.1.1 Circular plane piston source

Calculation of the pressure distribution in the field of a circular piston has been the subject of many papers. The article published by Zemanek [7] in 1971, generated considerable interest. Although Zemanek was not the first to calculate the pressure field of a circular radiator, his calculations showed clearly the near field oscillations mostly in the form of three dimensional and contour plots. Zemanek's calculation was based on a numerical integration of the two dimensional Rayleigh integral and results are presented for transducers with a/λ's ranging from 1 to 20. His calculations are of importance since he discussed implications for ultrasound imaging. However, for large ka values, the grid points need to be much finer in order to map the rapid variations accurately closer to the source.

If a solution for the impulse response of a piston is known, then the pressure field may be computed by evaluating the driving frequency component of the Fourier transform of the impulse response. Such a method is called an impulse response method and was first proposed by Oberhettinger [8] and later used more efficiently by Lockwood and Willette [9]. They showed that the plots they obtained for the circular piston are essentially the same as corresponding plots published by Zemanek and also revealed that Zemanek's double integration requires more steps than the impulse response method by a factor of more than a/λ, the ratio of piston radius to wavelength.

Experimental measurements were compared with theoretical predictions by Hutchins *et al* [10]. Their predictions showed good agreement for plane circular sources at low amplitudes.

2.1.2 Rectangular plane piston source

Some of the first calculations on the acoustic field of a rectangular source were presented by Freedman [11,12] who theoretically examined the amplitude and phase of the pressure field due to a rectangular piston, vibrating in an infinite, rigid baffle for ranges down to the order of the piston length. Freedman also compared the near field of a circular piston with the near field of a rectangular transducer and revealed certain interesting differences between their pressure fields, such as different pressure amplitude fluctuations in the near field of both sources. In the Fresnel region, his calculations showed that for the circular piston the axial pressure amplitude fluctuates between zero and twice the unit level (unit level denotes the pressure amplitude corresponding to a plane wave in which the velocity amplitude of the particles is equal to that of piston surface). However, for the rectangular case, these extreme fluctuations do not occur due to the lack of circular symmetry of the piston boundary with respect to the acoustic axis.

The more efficient impulse response method was also used for rectangular source geometry by Lockwood and Willette [9]. They showed that a time domain Green's function approach could be used to reduce the problem to a single integral rather than a double integral in the case of rectangular piston, since the impulse response of the piston could be expressed in closed form in a similar way to that of circular source. They went on to produce Zemanek's result and showed that the method is equivalent to, but computationally more efficient than, the exact double integral method.

Comparisons between the fields of circular, square, and rectangular transducers were made by Marini and Rivenez [13]. They discussed the possibility of dividing the pressure field of a rectangular piston into three zones rather than two; the very near field, the near field and the far field. Their results for pressure and intensity in the ultrasonic fields produced by rectangular transducers showed the general characteristics of the pressure fields of various size rectangular transducers, however, they did not show much of the complex structure of the field of rectangular transducers, especially close to the sources.

A more general formalism was presented by Szabo [14] for calculating the diffraction field of arbitrary source functions radiating into an isotropic and anisotropic medium. Under the Fresnel approximation, the pressure amplitude at any point in the field of a given source function was simply expressed as the Fourier transform of the aperture source function for both the near field and the far field. For the two dimensional case, he obtained a closed form field expressions for a rectangular, Gaussian, truncated cosine and a truncated Gaussian source geometries. This method is suitable for rapid numerical calculations for pressure field calculations from source functions of arbitrary shape. Using this approach, complicated source functions can be analysed from simpler shapes by piecewise continuous functions and linear transform properties [15] of the Fourier transform. This formulation has been programmed for the general case using efficient fast Fourier transform algorithms and has been used as a reference in this study to generate different sets of data for the linear case.

Weyns [16] examined the effect of short pulses on the near field of planar circular, square and annular transducers. In order to calculate the ultrasonic field of various radiators, the real pulse was replaced by a sine modulated Gaussian pulse. Using the theoretical pulse, the pressure function was evaluated numerically in a way similar to that of Zemanek. He also discussed the effect of transducer shapes on the beam

patterns comparing with the radiation field of circular, annular and square radiators and noted the two points of interest.

1. The square shape reduces the beam narrowing effect. In a vertical plane, the near field is not complicated but side lobes are more pronounced.

2. The annular shape increases the constructive effect without an augmentation of the angle of aperture, but at the cost of an amplification of side lobes.

Another acoustic field calculation method was developed by Ocheltree and Frizzell [17] to determine the field from continuous wave rectangular sources. They evaluated the surface integral using Huygen's principle and summing the contributions from incremental areas representing the radiating surface. The source was divided into a number of rectangular elements that were too large to be represented as point sources but small enough that the field point was in the far field of each. Several fields were illustrated for a number of square sources ranging in size 0.5 to 100λ wide and compared with those for circular sources published by Zemanek. Presented results showed that the field of a square source lacks the on axis nulls and deep variations that occur in the field of a circular source as noted by Lockwood and Willette [9]. Whereas Lockwood and Willette showed the field calculation results for only one rectangular source, the comparisons that Ocheltree and Frizzell made covered several sizes of circular and square sources. In addition, without going into very much detail they presented some plots showing the effects of attenuation on the sound field of a rectangular source in an attenuating medium. They successfully pictured the modification of the on axis acoustic pressure profile due to the attenuation for rectangular sources.

2.1.3 Focused sources

One of the earliest papers on the radiated field of focused circular piston was that of O'Neil [18]. The result was an exact solution along the axis. It was assumed that the curvature of the piston was so small that each source point on it's surface could be considered to be radiating freely into half space without any secondary diffraction effects. The surface integral was evaluated numerically at a single frequency for high and low gains. O'Neil's measure of gain was different to that which is now generally used but he made a number of observations, including;

1. The point of maximum pressure does not occur at the geometric focus but occurs on the source side of the focal plane and moves toward the centre of the curvature with increasing gain.

2. The relative pressure in the focal plane has the same form as the far field directivity pattern of a piston radiator.

Other authors have also considered the wave fields from focusing transducers. Lucas and Muir [19] found a single integral solution for any point in the field of focused source using the Parabolic approximation of Naze Tjøtta and Tjøtta [20] and by applying a Hankel transform to the surface integral. Their model is applicable to focusing sources that are large in comparison to the wavelength and that subtend fairly small aperture angles. The advantage of this kind of general solution is that it requires only one numerical integration to describe the field at any given point while a double integration is needed in O'Neil's solution. They also obtained good agreement with experimental measurements for a focused circular array.

An almost equivalent but more general expression was derived by Thompson *et al* [21] for the pressure fields of elliptical and bicylindrically focused piston radiators within the parabolic approximation. Their general expression reduces to that of Lucas and Muir in the case of a circular aperture with the lens adjacent to the radiator.

An exact expression that eliminates the need for integration and does not use any approximations was presented by Hasegawa *et al* [22,23]. However, their solution includes infinite series involving Legendre polynomials, Bessel, Hankel and spherical Neumann functions.

With the growth of interest in acoustical imaging, the fields from pulsed radiators became of increasing interest and several authors used the impulse response method for the calculation of pulsed fields from focused circular sources by performing a convolution between the impulse response of the radiator at a point and the waveform with which the transducer is driven. An analytical solution for the impulse response of a focused radiator was first derived by Pentinen and Luukkala [24]. Cobb [25] used a frequency domain impulse response for an attenuating media to overcome sampling problems in discrete Fourier transforms that occur when high frequency components are present in the time domain impulse response. This time domain Green's function approach has also been used by Stephanishen [26], Beaver [27], Naze Tjøtta and Tjøtta [28] and Hutchins *et al* [29].

Pulsed fields of concave transducers were also examined by Weyns [16] who examined the field variation with the pulse length.

It would appear that to date there has been not been enough study either theoretical or experimental, examining the fields from focused rectangular transducer either in the near field or in the far field.

2.2 FINITE AMPLITUDE ACOUSTICS

2.2.1 Plane waves at finite amplitudes

The developments of finite amplitude acoustics has been reviewed by Bjørnø [30], Beyer [31] and Hamilton [32]. The theory of finite sound propagation can be traced back to Euler's equation of motion and continuity for a fluid from which in 1765 he derived the nonlinear wave equation for propagation of finite amplitude waves in a lossless gas. Although Euler did not solve this equation he concluded that the wave propagation velocity would be greater than the isothermal speed of sound. A similar equation led Lagrange [33] to the conclusion that the propagation velocity of a finite amplitude wave should depend on the original amplitude of the wave. This so shocked his confidence in his own calculations that he concluded that the only possible means of wave propagation was the linear one (see ref 30). Poisson in 1808 obtained an exact solution to a one dimensional wave equation for finite amplitude waves in a gas which was later used by Stokes to describe how waveform distortion might occur during propagation. The connection between thermodynamics and kinematics was established by Earnshaw [34] in 1860 enabling the local wave velocity to be expressed in terms of pressure and density variations in a fluid. Rankine and Huganiot went on to formulate the relationship between thermodynamics and kinematic quantities on either side of shock front which became known as the Rankine-Huganiot equations.

Two Fourier series solutions were published for a plane progressive periodic wave of finite amplitude by Fay [35] and Fubini [36]. The Fubini solution assumed a sinusoidal wave propagating into a lossless fluid and described how waveform distortion would occur by the generation of higher harmonics during propagation. This solution is only valid in the region close to the transducer and before a shock

front becomes established. The Fay solution on the other hand is valid for a viscous fluid in the region where shock waves are already fully developed and have begun to decay. In the transitition region, around the shock front, neither solution is valid but the relationship between them has been established by Blackstock [37].

While in principle an exact numerical solution of the partial differential equations governing wave propagation is possible, considerable computational time is involved. As an alternative, reasonable assumptions have been made which simplify the governing equations making exact or approximate analytical solutions easier to obtain. This was the approach adopted by Burger [38] who formulated a simple approximate partial differential equation which contained nonlinear and dissipative terms and had the advantage that for plane waves an exact analytical solution was possible. A number of theoretical solutions have been based on Burger's equation, for example Blackstock [37]. Another approach to the solution of the finite amplitude wave propagation has been so-called weak shock theory which has been shown to be a limiting case of the solution on Burger's equation. This theory permits a solution for small amplitude shocks only. Blackstock [37] made use of this approach to obtain a mathematical model of wave propagation in the region in which shocks are generated within an acoustic field.

An early numerical solution of Burger's equation by Fox and Wallace [39] applied distortion in the time domain and attenuation in the frequency domain necessitating repeated application of Fourier transforms. The later numerical solution of Trivett and Van Buren [40] had the advantage that all the calculations were carried out in the frequency domain, thus reducing the computational requirements.

2.2.2 Circular piston source at finite amplitudes

As the literature on finite amplitude, diffractive fields is extensive, only the most relevant studies are outlined below, including numerical methods and the perturbation approach to the problem of finite amplitude propagation.

a. Perturbation methods

The second harmonic can be calculated as a perturbation of the fundamental pressure field. In the most basic form the second harmonic at a point in the space is proportional to the integral of the fundamental pressure squared along the path from the source to the field point. The chief advantage of such a method is that the reduced complexity of the problem leads to a simple numerical solution but there are a number of drawbacks. Firstly, the method is only applicable to relatively low levels of nonlinearity and does not account for loss from the fundamental. Secondly, diffraction effects in the second harmonic beam are not included. Ingenito and Williams [41] were the first to use a perturbation solution to derive the second harmonic for a circular source. They neglected absorption and possible backscattering and assumed that ka was large (a is the transducer radius). They obtained solutions for the second harmonic both for the axial value and that averaged over the receiver. Their results predicted significant structure for axial value of the second harmonic, and were found to agree with experiment however they were only valid for propagation distances greater than 2.5 transducer diameters but could be evaluated using tabulated functions or by quite straightforward numerical integration.

After Ingenito and Williams, Cobb [42] extended the analysis for the average value of the second harmonic to account for absorption. He obtained good agreement with

experiment and used the solution to calculate values of β for several different media. Kunitsyn and Rudenko [43] used the parabolic wave equation to calculate the second harmonic amplitude. Their approach assumes that the pressure amplitude does not vary significantly over a distance equal to the wavelength and is generally valid for $z > a(ka)^{1/3}$ where z is the propagation distance. They also obtained an analytical expression which was valid for $z < a^2/\lambda$ and which had a similar form to the result of Ingenito and Williams.

In a later paper, Lapidus and Rudenko [44] introduced a coordinate transformation to the parabolic wave equation before obtaining a perturbation solution. The transformation describes the nonlinear distortion of a plane wave and so overcomes some of the limitations of the perturbation approach, permitting the prediction of asymmetric waveforms close to the point of shock formation. The limitation of the method lies in its separation of the description of distortion and diffraction, but nevertheless reasonable agreement was obtained with numerical calculations.

An alternative perturbation approach was used by Ginsberg [45] to obtain an integral expression for the second harmonic component in terms of Hankel transforms. This theoretical approach has similar limitations to that of Ingenito and Williams in that it can not describe accurately rapid radial fluctuations in the beam profile and is limited to the case where the nonlinear distortion is small. These limitations were addressed in a second paper [46] where the integral was corrected in an ad hoc fashion to account for rapid fluctuations of the beam and a coordinate straining transformation was used to derive a solution for significant amounts of distortion. The method can predict the waveform anywhere in the field, provided that a shock front is not formed, and thus represents a significant advantage on the previous work; however to evaluate the result implicit equations must be solved for the coordinate transformations and an oscillatory integral must be evaluated, all of which depend on a number of special

functions and so the method is costly in terms both of effort and computing time.

All of the works reviewed above demonstrate that progress can be made in the analytical description of diffractive fields, using a perturbation method. However, it is necessary to make a number of approximations, and the final result is usually quite complicated and must be evaluated numerically.

b. Other methods

Some authors assumed that waves propagate independently in each direction and can therefore be treated using a one dimensional solution to the wave equation. For example, Lockwood *et al* [47] presented an experimental and theoretical investigation of such an approach on the far field distortion of a finite amplitude wave generated by a circular piston. They neglected near field distortion and presented some data obtained for a fundamental frequency of 450 kHz.

Lancaster's approach [48] to the solution of the near field problem was to take the one dimensional solutions of Burger's equation by Trivett and Buren [40] and force the fundamental component to follow the small signal pressure field of the plane circular piston. This gave reasonably good agreement with experimental results on the acoustic axis but because of the lack of the interactions of harmonics with the fundamental and each other, effects such as saturation of the fundamental could not be modelled.

Another approach to finding a solution to the nonlinear, three dimensional wave equation is to solve it for all harmonics generated. The chief advantage of such a method is that the entire pressure field is calculated and interactions between harmonics and fundamental can be seen. However, this method has the disadvantage that is more complex and requires heavy computational efforts.

Khokhlov and Zabolotskaya [49] derived a nonlinear parabolic wave equation by assuming that wave profile varied slowly both along and transversely to the acoustic beam axis. That equation was generalized by Kuznetsov [50] to include thermoviscous dissipative effects and after that has been known as the KZK equation which is a nonlinear partial differential equation and accounts for coupling between nonlinearity, dissipation and diffraction.

Since the exact solutions of the KZK equation are not known, extensive treatments have been coupled with numerical methods for the solution of that equation. Collobarative efforts between groups in Norway (Univ. Of Bergen) and the U.S (Univ. Of Texas, Austin) have used the parabolic approximation and Fourier series expansion (i.e frequency domain solution) to calculate the sound fields from continuous, axially symmetric sources [51,52]. The parabolic approximation is useful for narrow beam profiles which vary slowly in the axial direction, and at some distance from the source.

Recently an increase in the computational power available has led to a renewed interest in numerical solutions of the nonlinear wave equation. Baker *et al* [53] obtained a solution for circular sources based on the KZK equation and demonstrated good agreement with experimental results.

The most recent model of Christopher and Parker [54] accounts for the effects of refraction and reflection in the case of propagation through multiple, parallel layers of fluid medium and the physics of diffraction, attenuation and nonlinearity. Their model also makes possible the calculation of spatial heating rate associated with a diffractive nonlinear source and provides significant reductions in computational complexity.

2.2.3 Rectangular piston source at finite amplitudes

It is noticeable that most of the papers reviewed above consider the linear or nonlinear propagation in the field of an axially symmetric circular source. It would appear that to date there has been little study of the nonlinear structure of the field of rectangular sources and to the authors knowledge, the only experimental work related to the finite amplitude field of a rectangular transducer was recently published by Kamakura *et al* [2] using a planar source of size 24 x 44 cm. They also compared experimental measurements with theoretical results based on the KZK equation for the first three harmonics but results were only presented at low frequencies (25 and 30 kHz) in air. No experimental data has appeared in the literature for focused rectangular case.

The first numerical approach for the pressure field of a square source at finite amplitudes was published by Lahalle *et al* [55]. They took a plane parallel to the source, calculated the plane wave spectrum in that plane, allowed the wave to propagate and put the attenuation and nonlinear effects in their calculation for each step; combining a Fourier series decomposition of the velocity potential, a Fourier transform in the antenna plane and a finite difference scheme in normal direction. Their method was validated for Gaussian distribution as well as a uniform circular piston. However, they only presented a simple calculation for the case of a square aperture (10 cm in size) at quite low frequency (150 kHz.) and high pressure levels (around 3 MPa).

Most recently, the amplitude and phase of the fundamental and the second harmonic due to various rectangular apertures and a circular one having the same area examined by Berg [56]. It was assumed that the sound pressure level at the source is low enough that the effects of nonlinear attenuation and distortion are small, thus a quasilinear approximation to the KZK equation was used and produced a set of coupled

differential equations which had to be evaluated using numerical computational methods. Numerical results were presented for primary and the second harmonic fields generated by rectangular apertures and compared with those obtained for circular sources. However, the numerical results obtained for rectangular sources were only tested comparing with theoretical results obtained for circular sources having the same source area with rectangular sources but not with the experimental data for rectangular apertures.

2.2.4 Focused sources at finite amplitudes

The problem of finite amplitude propagation for nonplanar sources has been addressed by a number of authors. In general the experimental measurements and the solutions were presented for focused circular sources, but not for the rectangular source owing to the complicated nature of the rectangular source geometry. The solutions produced for circular sources often do not apply to conditions in which hard shocks form and commonly they fail to predict the behaviour in the focal zone.

In 1963, Naugol'nykh, Soluyan and Khokhlov [57] developed a model for nonlinear acoustical focusing systems based upon spherical wave theory, and their results were later compared to experimental data by Smith and Beyer [58]. The experiment was performed with a spherical cap radiator operated at finite amplitudes. The measurements exhibit a highly oscillatory axial field due to diffraction caused by the edges of the spherical cap. Because the spherical wave theory [59] does not account for diffraction, it provides only crude agreement with the experimental data in the pre-focal region, and it is of no use within the focal region.

Ostrovskii and Sutin [59] performed an analysis that employed spherical wave theory in the pre-focal region up to just before the focal region. Within the focal region they

utilise a wave model that accounts for diffraction, but not nonlinearity. Their model therefore does not account for the nonlinear losses in the focal region, where this phenomenon is most pronounced.

An analytical model which predicted levels of second harmonic for a spherically concave source of limited aperture was developed by Lucas and Muir [60]. They based their analysis on the KZK equation and integral solutions were developed for the fundamental and second harmonic fields. Their solution is limited to moderately nonlinear systems because of the complicated integral representation of the field. For example, the solution for the second harmonic contains a triple integral, and the retention of higher harmonics would have been analytically intractable. Saito *et al* [61] compared a modified form of Lucas and Muir's result with experimental measurements made on a focused radiator with amplitude shading across the aperture. They concluded that the ratio of the second harmonic to fundamental was a maximum at the focus and that the second harmonic component focused more tightly that the fundamental.

The numerical solution of Hart [62] was based on a finite difference solution developed by Aanonsen [63] to model the near field behaviour of an unfocused, nonlinear sound beam. Aanonsen's solution was modified by introducing a coordinate transformation that follows the convergent geometry of a focused beam. The computational efficiency of the algorithm was thus improved for focused sound fields.

Recent experiments performed by Baker [64] showed good agreement with the theory for different drive levels and focal gains in the field of a focused circular transducer.

CHAPTER 3

EXPERIMENTAL CONFIGURATION

3.1 GENERAL

The general configuration used for the experimental measurements is shown in Figure 3.1. All the measurements were made in tank filled with fresh top water. The water was left for a few days after filling to allow the entrained gas to diffuse out. The water temperature was not regulated but it was fairly constant at room temperature (about 20 $^{\circ}C$). The maximum variation in water temperature was about one or two degrees during the course of the day. Measurements were made using a plane circular transducer with a rectangular aperture in front of it. The transducer was mounted at one end of the water tank which was 1.3 m long by 0.3 m wide and 0.3 m deep.

The acoustic beam was focused by the addition of a spherical perspex lens to the aperture face. The pressure field generated by the rectangular aperture was sampled using a broadband hydrophone mounted an a two dimensional translation stage. The output from the hydrophone was recorded on a digital storage oscilloscope (DSO) and the waveform from the DSO was the transferred to a micro-computer for analysis.

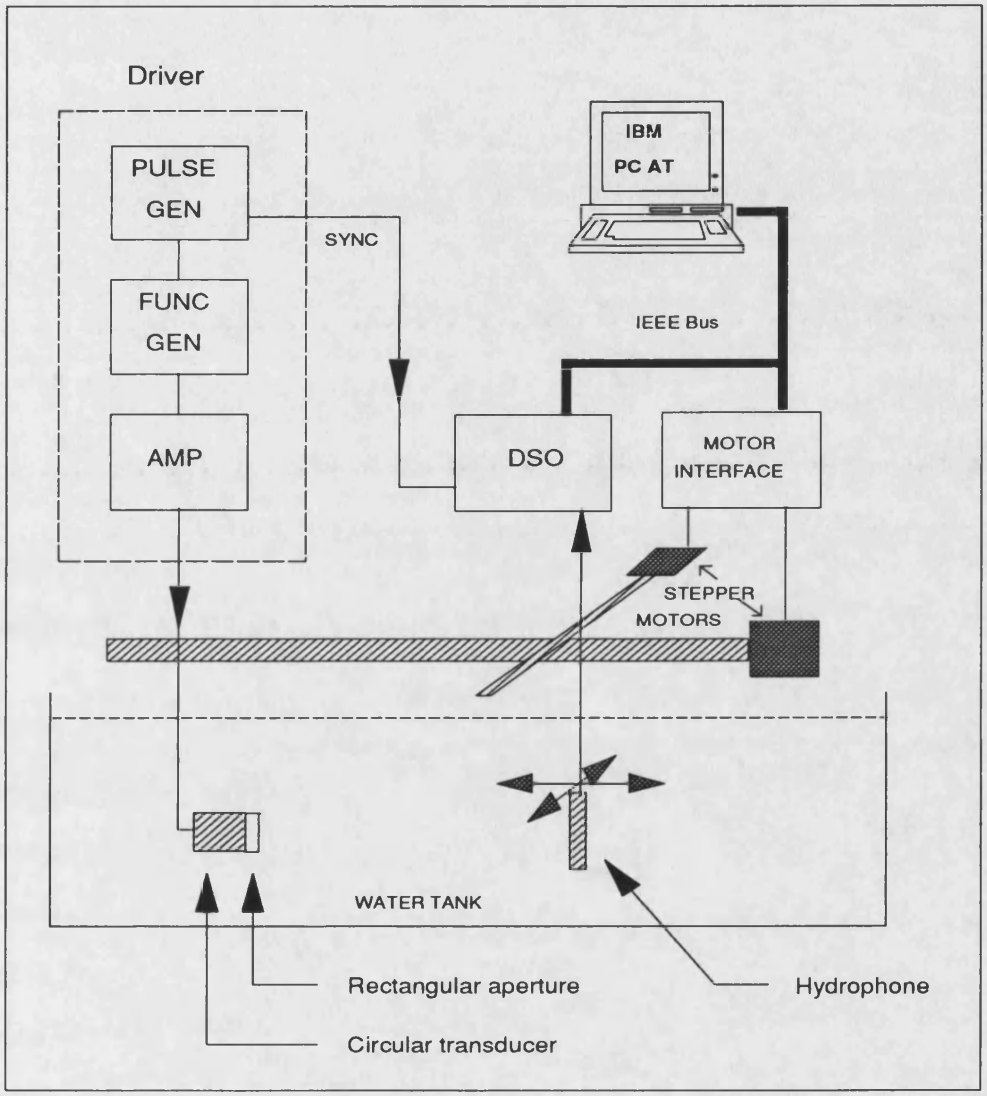

Figure 3.1 A schematic diagram of the experimental arrangement.

3.2 TRANSDUCER

Measurements were made on a Panametrics 2.25 MHz, 38 mm diameter, plane circular transducer with various rectangular apertures in front of it. Focusing was achieved by the addition of perspex lenses to the aperture face as discussed later in this chapter.

3.3 RECTANGULAR APERTURE

Since well characterised ready-made rectangular transducers were not available, rectangular apertures were used to generate the necessary acoustic fields. The aperture material used and the placement of the aperture in front of the transducer played an important role in the behaviour of the pressure field measured, depending on the thickness, the softness and the ease of cutting of aperture material.

Initially, different materials were used to make rectangular apertures and the usefulness of each aperture material was tested by making some experimental measurements with it and comparing the results with theoretical predictions. Initially brass was used to make a rectangular aperture as shown in Figure 3.2. A brass plate of 2.5 mm thickness and 240 mm long by 150 mm wide with a square aperture (25 mm by 25 mm) at its centre was placed approximately 2.5 cm away from the circular transducer and the generated acoustic pressure field was measured. The disadvantages of using this method and the material were the reflections between the transducer and plate. Since these effects caused some modification of the shape of the driving pulse, this method was not used and instead adjacent apertures were used.

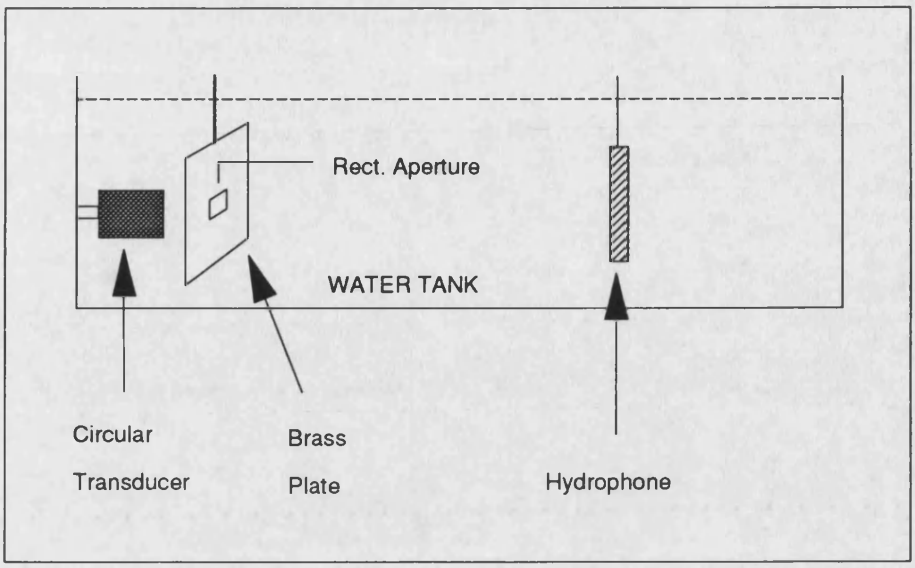

Figure 3.2 Initial aperture configuration.

Taking account of the diameter of the circular transducer, rectangular apertures were designed and cut using a sharp blade, and placed in front of the transducer using a simple mounting system (see Figure 3.3.). Open cell polyurethane foam (OCPF) of 4.0 mm thickness gave good results but was very difficult to cut accurately and deformed easily when wet. An alternative was the use of 3 mm thick Neoprene rubber (NR). Although NR was harder than OCPF, the difficulty was in cutting the edges of the apertures at the right angle. A better solution was found to be the use of the same thickness NR glued on the back of a sheet of brass shim-stock of 0.105 mm thickness. This gave a rigid aperture that was relatively easy to make in different sizes and shapes. As a result of the ease of manufacture of apertures in different sizes and the agreement obtained with the theoretical predictions, the NR and sheet brass method was chosen.

3.4 LENSES

Focused fields were obtained using spherical acoustic lenses coupled to the front face of the aperture. Since it was very difficult to obtain different radii of curvature on a single lens, two separate lenses with different curvatures were used for focusing the ultrasound beam in two planes. The curvature on each lens was achieved by clamping a 50 mm diameter perspex rod to a fabricated fixture which was in turn attached to a rotary table of the lathe. The correct lens curvature was then machined on a milling machine using a 1 inch diameter end mill. The correct arc was then set and machined by indexing the radius length using the digital readouts of the milling machine and rotating the round table. After machining, a reasonable surface finish was achieved by using copious quantities of cutting fluid. Final polishing was obtained with 600 grit Wet and Dry Emery Cloth and a suitable fine abrasive wax. This method produced some very satisfactory lenses.

Three pairs of lenses were made with a geometric focal lengths of 160 mm, 250 mm, and 350 mm respectively. The gain of a lens focused in a plane is given by the formula [65]

$$G_x = \frac{a}{\sqrt{\lambda F_x}} \qquad 3.1$$

Where G_x is the focal gain in xz plane, λ is the wavelength, F_x is the geometric focal length in xz plane and a is the aperture size in x direction. Similarly, focal gain in both directions may be written as,

$$G = \frac{ab}{\lambda\sqrt{F_x F_y}} \qquad 3.2$$

Where G is the combined focal gain, b is the aperture size in y direction and F_y is the geometric focal length for yz plane.

Lenses were held in place by a simple mounting system placed around the transducer (see Figure 3.3) and were acoustically coupled to the aperture face using a commercial ultrasonic coupling gel.

3.5 HOLDER

The arrangements used to hold the aperture and the perspex lenses is shown in Figure 3.3. An aluminium tube, 40 mm long, was machined on a lathe to give 38.5 mm inside diameter which was enough to leave some space between the transducer and the holder, so it was easy to move the holder along the transducer and to turn it around for necessary alignments. The screw at the top of the holder was used to fix the mountings after replacement of aperture and lenses if necessary.

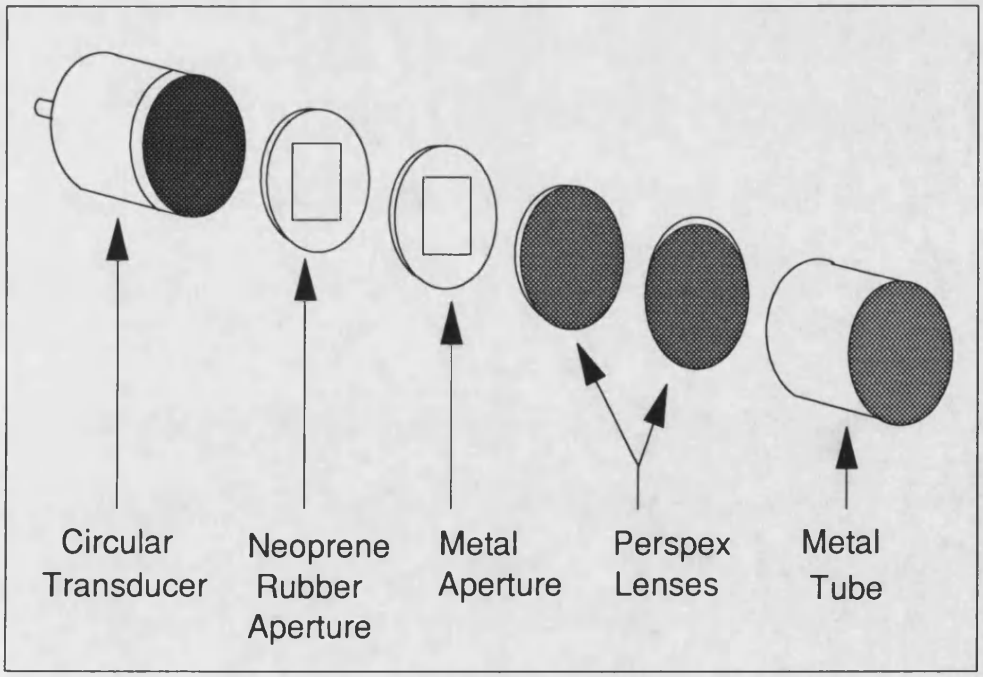

Figure 3.3 Mounting system used for holding apertures and lenses.

3.6 HYDROPHONE

The pressure field generated by the rectangular apertures were sampled using a GEC polyvinylidene difluoride (PVdF) bilaminar membrane hydrophone (Type Y-33-7611, Number MRQ IP018) with a standard 65 cm, 75 Ω cable. The sensitive area of the hydrophone used in these measurements was 1 mm in diameter and the PVdF membrane had a total thickness of 50 microns. The hydrophone had an open circuit sensitivity of 0.175 V/MPa at 1 MHz.

In the construction of these hydrophones, the membrane is stretched over an annular frame 100 mm in diameter, which is large enough not to perturb the acoustic field. Gold film electrodes are evaporated onto each surface of the PVdF membrane so that they are overlap only in a small central area. This area becomes piezo-electrically active when the device is poled at a raised temperature. Electrical radio-frequency pick-up is reduced by gold electrodes surrounding the active element which are connected to the screen of the coaxial cable and an earthing pin on the supporting frame.

One of the advantages of this type of hydrophone is its broadband frequency response which allows high amplitude distorted waveforms to be measured accurately. Another advantage is that PVdF has an acoustic impedance of $4x10^6$ Rayls, which is close to the water; this combined with the fact that the hydrophone is constructed using a thin film makes the transmission coefficient very high. The hyrophone therefore causes minimal disturbance of the acoustic field and the acoustic beam passes through the membrane. At 10 MHz, 95% of the beam impinging on the membrane is transmitted [66]. However, with wider beams the frame reflects the signal but this effect can be eliminated by time gating.

It was also necessary to ensure that the hydrophone was submerged to a constant depth in water since the sensitivity changes if the water does not cover the membrane. This effect occurred due to a change in the capacitive loading associated with the electrode leads which was dependent on the height of the water.

The hydrophone was mounted on a two dimensional translation stage with movement in the horizontal plane driven by stepper motors controlled by the computer which allowed the hydrophone to be positioned anywhere in a horizontal plane parallel to the acoustic axis. Manual adjustment was also available to vary the angle of the hydrophone relative to the vertical, its vertical position and the hydrophone azimuth. The output from the hydrophone was connected directly to the input of a digital storage oscilloscope.

The same hydrophone used in this study has already been used successfully by another member of the Acoustic Group at the Bath University and excellent agreement was obtained with the theory for circular case [67].

3.6.1 Sensitivity and Calibration of the Hydrophone

The sensitivity of a hydrophone is defined as the ratio of the open circuit voltage at its output terminals to the sound pressure in the undisturbed field of a plane wave.

When a hydrophone is connected to an electrical load such as an oscilloscope, the sensitivity of the hydrophone changes. The sensitivity of a hydrophone connected to any electrical load, S_L, can be calculated from the unloaded sensitivity, S, by combining the impedance of the hydrophone and the load; assuming that the impedance of both is wholly capacitative, according to the equation

$$S_L = S\frac{C_h}{C_h + C_L} \qquad 3.3$$

For example, for the DSO the input capacitance was 25 pF and that of the hydrophone was 92 pF thus the connection of the DSO led to a reduction of the output voltage by 22%. So the hydrophone sensitivity was corrected to account for the loading caused by the DSO input impedance.

The calibration of the hydrophone was made by Baker [68] comparing it with two other nominally identical devices that had been calibrated at the National Physics Laboratory (NPL). The NPL calibrations covered the amplitude response from 1 MHz to 15 MHz in steps of 1 MHz.

3.6.2 Frequency Response

Although the PVdF devices offer a significant improvement in performance characteristics, great care should be taken in measuring the harmonic components of a nonlinear acoustic beam since the frequency response of the PVdF hydrophones depends on the variation the mean pressure amplitude $\overline{p}$ averaged over the thickness of the active element of the hyrophone [69].

The frequency response of such hydrophones was modelled by Bacon [69] by considering the mean pressure through the membrane. The sensitivity was then expressed as:

$$S = T_1\frac{\sin(\Theta)}{\Theta(e^{-j\Theta} - R_2 e^{j\Theta})} \qquad 3.4$$

Where;

$$\Theta = \frac{kx}{2}$$

$$T_1 = \frac{2}{1+Z}$$

$$R_2 = \frac{Z-1}{Z+1}$$

k is the wave number in the film, x is the film thickness and Z is the ratio of the acoustic impedance of water (Z_{water}), over the acoustic impedance of the film (Z_{film}). The expression ignores the acoustic losses and the effect of gold electrode as Θ, T_1, and R_2 become more complicated. Equation 3.4 gives the frequency response of the PVdF hyrophones in terms of amplitude as shown in Figure 3.4 Assuming the following parameters which are representative of the hydrophone used:

x = 50 microns

$Z_{film} = \rho_{film} c_{film}$ =1780 x 2400 Rayls

$Z_{water} = \rho_{water} c_{water}$ =1000 x 1486 Rayls

$$k = 2\pi \frac{f}{c_{film}}$$

Theoretical predictions by Bacon [69] and NPL measurements indicated that variation of the amplitude of the frequency response of the PVdf hydrophones was small within the frequency range of interest used in this study.

The variation of the phase of the hydrophone response can be considered in a similar manner to that of the amplitude and is shown in Figure 3.5

3.6.3 Directional Response and Effect of the Finite Hydrophone Size

Hydrophones inevitably show a directional response to incident ultrasound since the element size is finite. Directional response can be defined in terms of the beamwidth, θ_{3dB}, such that the hydrophone response at θ_{3dB} is reduced to $1/\sqrt{2}$ of that at normal incidence. The magnitude of the directional response depends on the size of the element and the frequency of the ultrasound incident on the element. The model developed by Bacon [69] showed that above about 2 MHz a hydrophone with an active area 1 mm in diameter behaves like a piston receiver with the output voltage (V) obeying the following equation:

$$V \approx \frac{2J_1(ka \sin\theta)}{ka \sin\theta} \qquad 3.5$$

Where k is the acoustic wave number, a is the radius of the receiver, J_1 is the first order Bessel function and θ is the angle of incidence. For a frequency of 100 MHz, this equation predicts a drop in received signal of 50% for an angle of incidence 0.5°. If the angle is 0.1 degrees, then the signal is reduced by 3%, so it is necessary to align the hydrophone with this precision to provide accurate measurements up to 100 MHz. However, a detailed knowledge of the directivity is not required at low frequencies such as the fundamental and first few harmonics at a 2.25 MHz. The main consequence of these considerations is that reliable measurements can be made at distances greater than twice the maximum aperture dimension from the source.

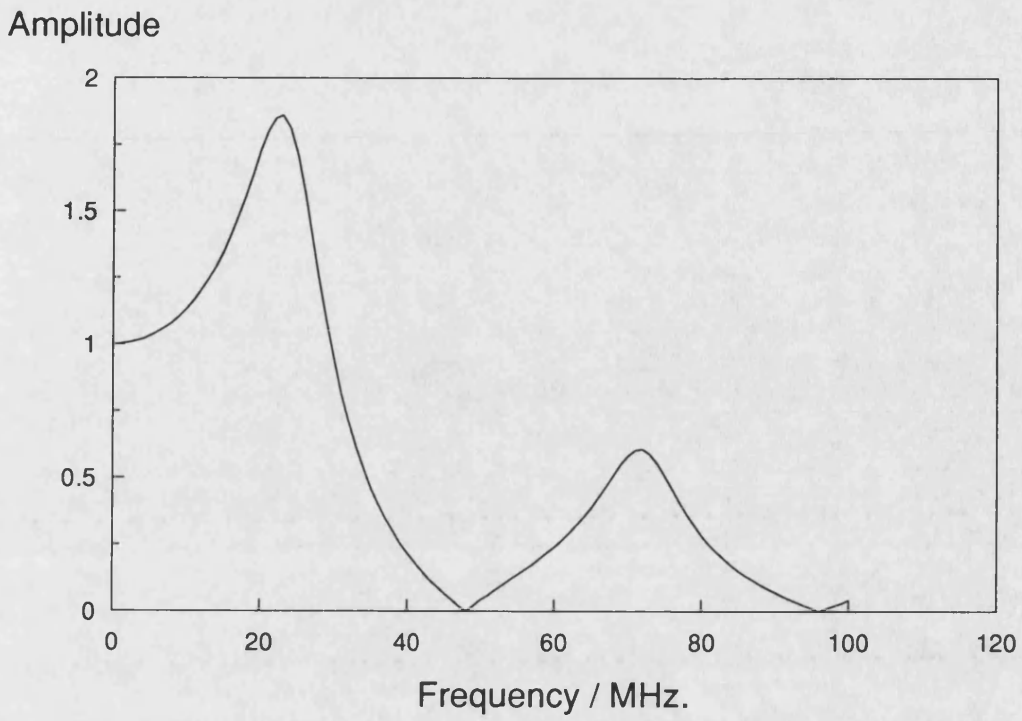

Figure 3.4 Normalised amplitude variation of the hydrophone sensitivity

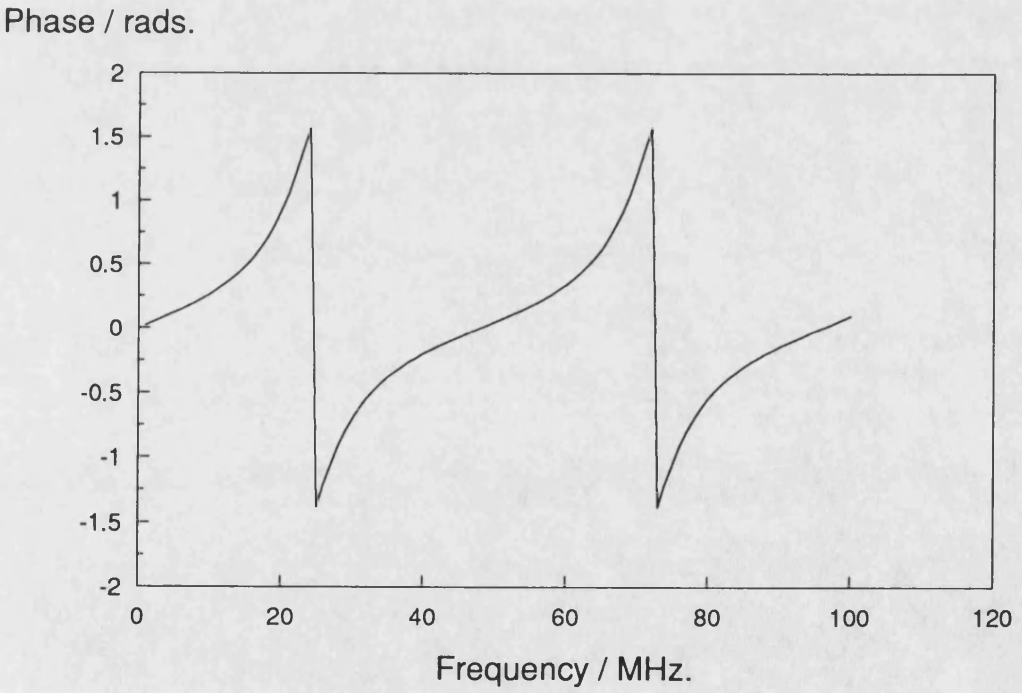

Figure 3.5 Phase variation of the hydrophone sensitivity

The finite size of the hydrophone has some important consequences. Ideally, a hydrophone would produce a measurable voltage (V) proportional to the acoustic pressure (P) at a point in space (i.e V=S.P, where S is the hydrophone sensitivity). However, the finite size of the active area and the thickness of the hydrophone only allows measurement of an output voltage which is proportional to the integrated pressure over the volume of the hydrophone.

The main problem with a small diameter hydrophone is that because it integrates the pressure field over a small area, the voltage produced at its output will be proportionally smaller. A further effect of the finite hydrophone size is that in finite amplitude fields, the harmonics have narrower beams so that the effect of spatial averaging becomes more important at higher harmonics although the harmonics tend to show less variation across the beam. This averaging effect can also be considered in terms of a loss due to the characteristic diffraction pattern of the hydrophone or its directivity pattern. The hydrophone is more sensitive to signals on its acoustic axis so that the edge wave from the aperture has less effect on the hydrophone output as the angle from the axis to the edge of the transducer increases. If the hydrophone size is increased, it becomes more directional and less of the edge wave is seen and the diffraction loss becomes more dominant on the pressure field measurements and requires correction to get very precise results.

Accurate diffraction theories are available for predicting diffraction loss due to a circular transducer and a circular receiver [70,71] but there is almost no theoretical model available for calculating the diffraction loss due to a rectangular transmitter and a circular receiver. Perhaps the only work which is close to this subject is the diffraction loss calculation of Szabo [72] due to a rectangular source and a rectangular receiver of different size.

It was assumed in this study, as is often done in diffraction loss calculations, that the hydrophone response is proportional to the integral of the undisturbed sound pressure over its sensitive area. Furthermore, it was assumed that the hydrophone face is centred on and aligned properly perpendicular to the acoustic axis of the rectangular source. The geometrical arrangement used to predict the diffraction loss is shown in Figure 3.6. The rectangular piston was assumed to be set in an infinite rigid baffle to oscillate harmonically with angular frequency ω and velocity amplitude u_0 radiating into the medium with a sound velocity c. With these assumptions the diffraction loss predictions were made following definition of diffraction loss by Woldron [73] which gives

$$D.L = -10\log_{10}\left\{\frac{\int_0^{2\pi}\int_0^{r_a}|P(r,\theta)r\,dr\,d\theta|^2}{P^2(0,0,z)\int_{-a}^{a}\int_{-b}^{b}dx\,dy}\right\} \qquad 3.6$$

Where $P(r,\theta)$ is the pressure at a point on the circular receiver having radial coordinate (r,θ); r_a is the radius of the active area of receiver and the denominator is the on axis pressure due to the rectangular transmitter of the size a and b. Thus, the behaviour of the acoustic beam launched from the rectangular transducer and intercepted by the circular hydrophone depends on the size of the transmitter and both the size and the position of the receiver.

In order to calculate the average pressure over the active surface of the receiving hydrophone and the on axis pressure due to rectangular aperture; the double integrals in Equation 3.6 had to be evaluated numerically using NAG routine facilities on the University mainframe computer (gdr). The expected magnitude and phase of the diffraction loss for a square aperture (20 by 20 mm) can be gauged from Figure 3.7 where the solid line shows the acoustic pressure without averaging and the dotted

line shows the averaged acoustic pressure over the sensitive area of the hydrophone. Figure 3.8 characterises the same effect for a rectangular source of size 10 mm by 30 mm. Figure 3.9 confirms that the diffraction loss effect can be reduced by using a smaller hydrophone (* shows calculated results with 0.05 mm hydrophone diameter) but this would lead a reduction in hydrophone output voltage due to the reduced sensitivity. It should also be noted that the effect of diffraction loss is reduced in comparison with the circular case, because the pressure field variations are less extreme in the rectangular case. It is only in the case of a uniform circular radiator that perfect cancellation and addition is achieved giving rise to pressure field that varies at the aperture face. This means that the finite hydrophone size does not pose such severe problems when measuring pressure fields of rectangular apertures.

3.7 ALIGNMENT

Great care was taken to ensure that the transducer, aperture, acoustic lenses and the hydrophone were accurately aligned with the acoustic axis of the beam since the alignment was an important factor in achieving reasonable results.

Firstly, the hydrophone and transducer were approximately aligned by eye and the hydrophone position adjusted perpendicular to the beam in order to maximise the received signal. The knowledge of the expected pressure field waveforms was frequently used to aid alignment, in particular location of the acoustic axis by driving the transducer at higher drive levels and adjusting the alignment for maximum distortion due to nonlinear propagation. Normally, two measurements were made to check the alignment; one in the near field, the other one further away from the transducer.

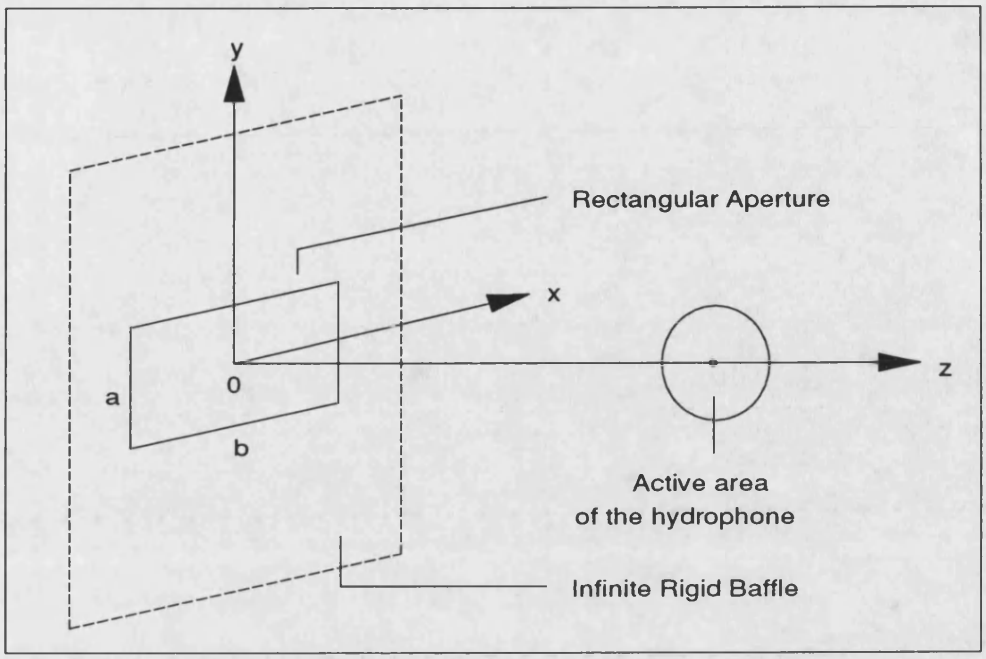

Figure 3.6 Geometrical arrangement of transmitter and receiver.

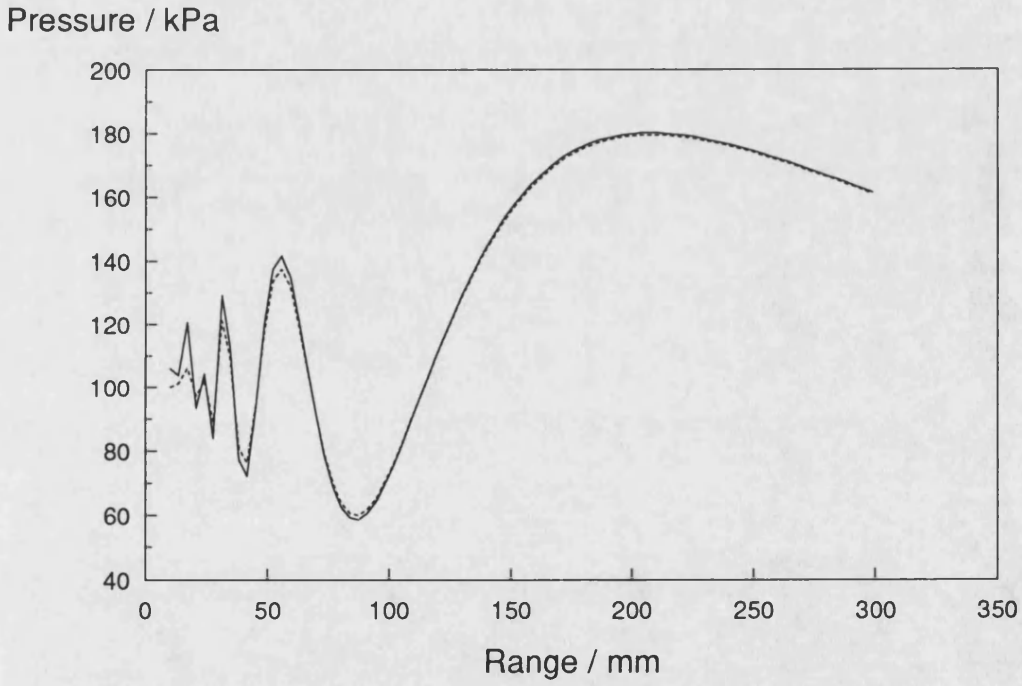

Figure 3.7 Diffraction loss prediction for a square aperture 20 mm by 20 mm. Solid line: Infinitesimal hydrophone, dashed line: 1 mm diameter hydrophone.

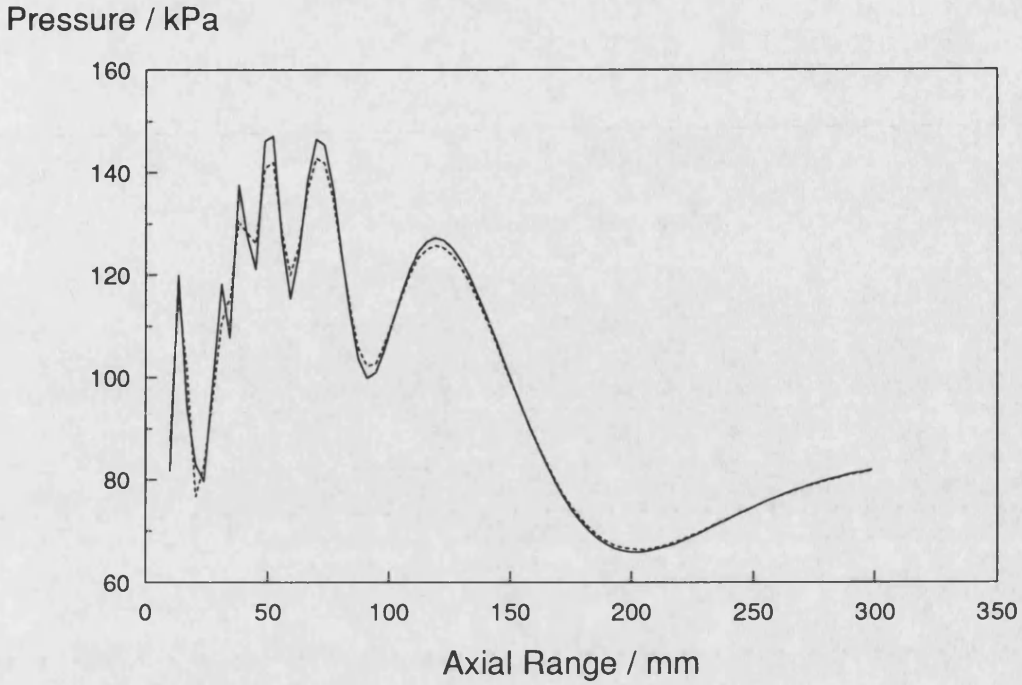

Figure 3.8 Diffraction loss prediction for a rectangular aperture 10 mm by 30 mm. Solid line: Infinitesimal hydrophone, dashed line: 1 mm diameter hydrophone.

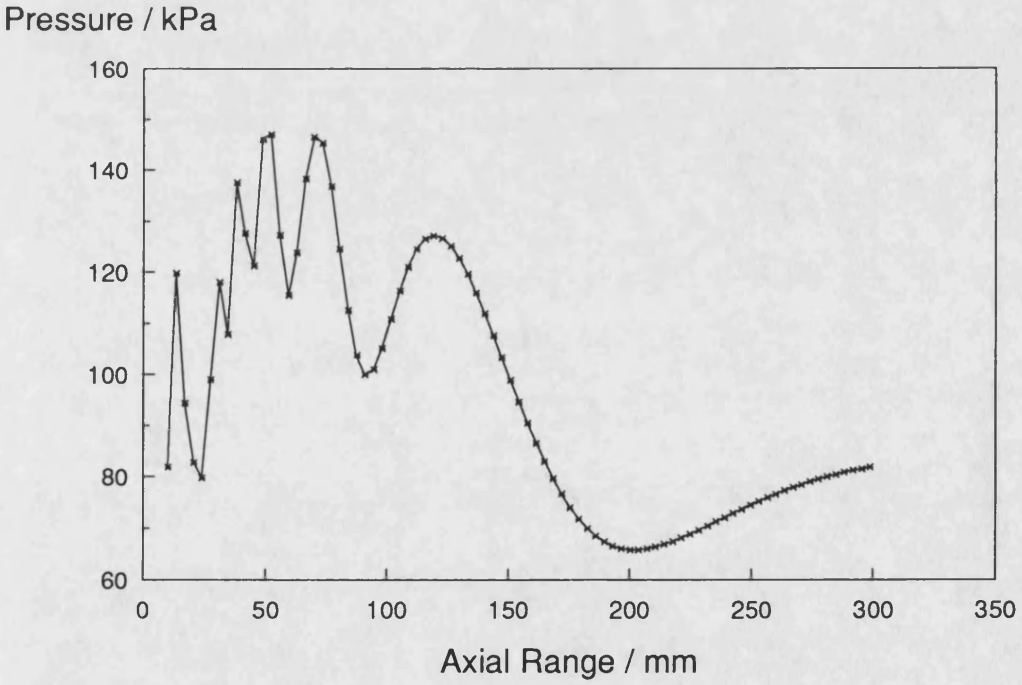

Figure 3.9 Reduction in the diffraction loss due to a smaller hydrophone size. Solid line: Infinitesimal hydrophone, (*): Calculated pressure values with 0.05 mm hydrophone.

Measured pressure waveforms were compared with the expected theoretical results and the hydrophone was then located on the acoustic axis of the beam. It was also possible to check the alignment through the acoustic axis by noting the location and the amplitude of the axial minimas and maximas.

The same procedure was repeated after the placement of apertures and lenses, which was quite time consuming but necessary to achieve accurate alignment. The vertical alignment had to be performed by hand as the translation stage had only two motion axis (in the horizontal plane) and none in the vertical plane.

3.8 DRIVING SIGNAL

Measurements on the pressure field of rectangular apertures were made under quasi-continious wave conditions with a tone burst of about 35 cycles duration, at a pulse repetition frequency (prf) of about 100 Hz.

The signal was produced by a function generator (Krohn-Hite KH 1400) which was triggered by a Farnell PG102 pulse generator and amplified with a radio frequency (RF) power amplifier (E.N.I 2100L) which gave 50 dB gain over the frequency range 10 kHz to 12 MHz. The transducer was then driven with the amplified signal via a matching transformer.

The harmonic content of the acoustic signal initially launched into the medium was important as it affected the harmonic generation in the medium. That is why, great care was taken to ensure that the driving pulse was as close to a sinusoidal waveform as possible and had no second or third harmonic component, so that the nonlinear effects in the medium could be observed in isolation. This problem was eliminated using an attenuater (Hatfield, Type 2002, 0 to 121 dB) which allowed the necessary attenuation in the driving pulse in 1 dB steps. However, it was not possible to

completely eliminate the second harmonic component in the driving pulse at the highest drive levels. The maximum amplitude of the second and third harmonic was -45 dB and -47 dB below the fundamental respectively. It was also necessary to keep the pulse repetition frequency as low as possible in order to minimise the total power dissipated by the transducer at the highest drive levels. This produced a quasi-continuous wave field without standing waves. It also allowed higher drive levels to be achieved since the time average power dissipated in the power amplifier and the transducer was reduced.

Measurements were made over a range of drive levels; the maximum electric drive at the transducer was 350 volts (peak to peak). The majority of nonlinear results were obtained with drive levels of 84 V, 165 V, 325 V, or 350 V. The time waveforms and the FFT magnitudes of the initial driving pulse are shown in Figure 3.10-3.17 respectively. It is noticeable that the FFT magnitude of the fundamental shows some broading at each drive level. This is due to the number of points used in the windowing of the time waveforms.

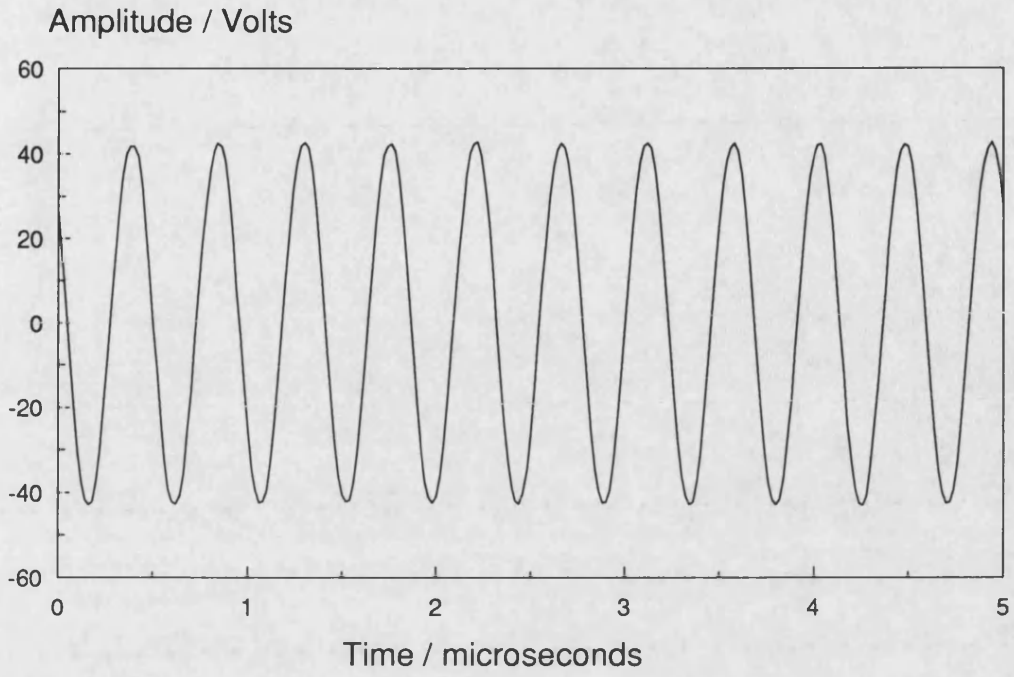

Figure 3.10 Time waveform of the initial signal at a drive level of 84 V_{p-p}.

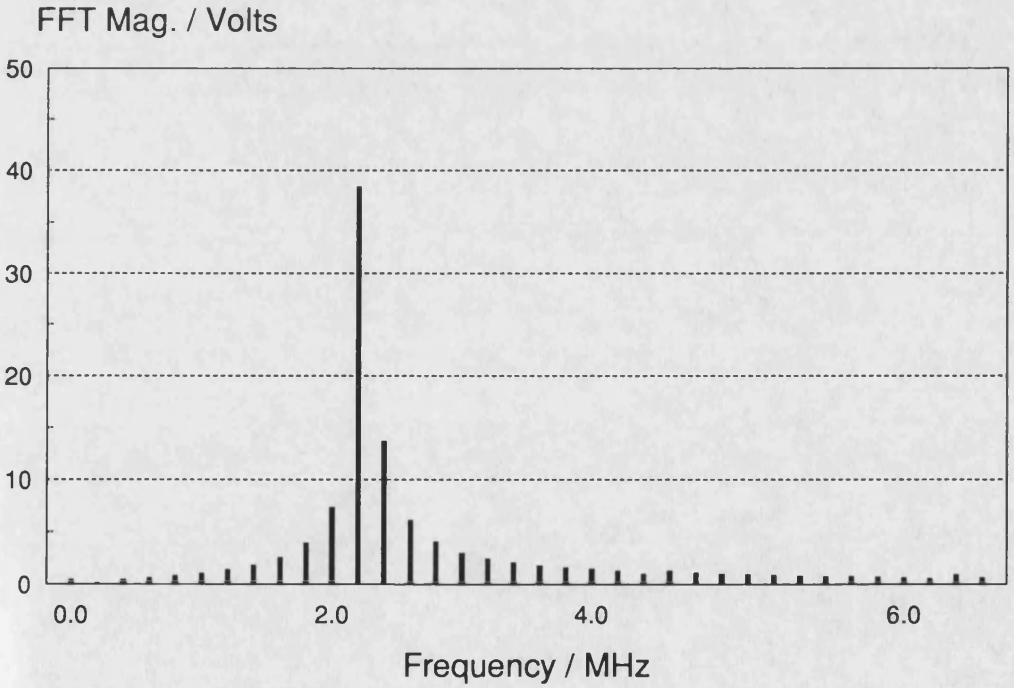

Figure 3.11 FFT magnitudes of the initial signal at a drive level of 84 V_{p-p}.

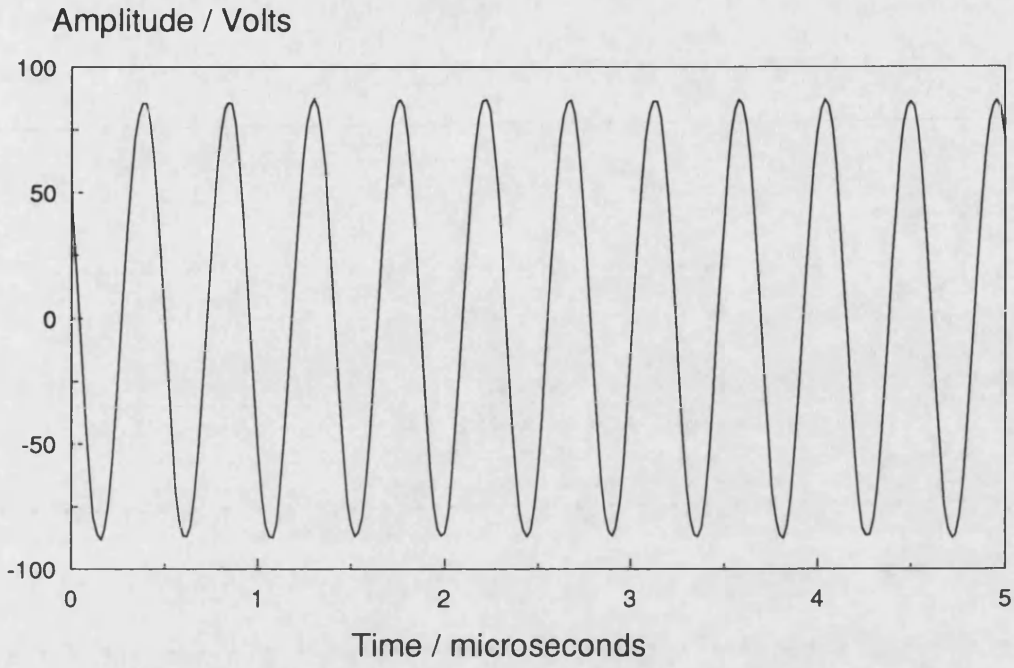

Figure 3.12 Time waveform of the initial signal at a drive level of 165 $V_{p\text{-}p}$.

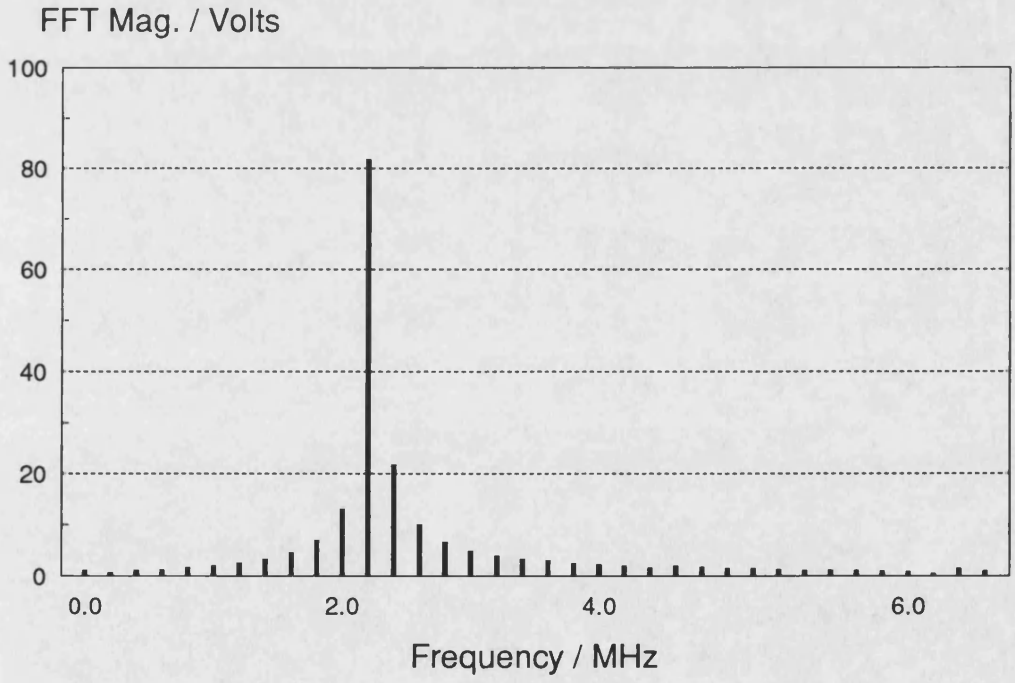

Figure 3.13 FFT magnitudes of the initial signal at a drive level of 165 $V_{p\text{-}p}$.

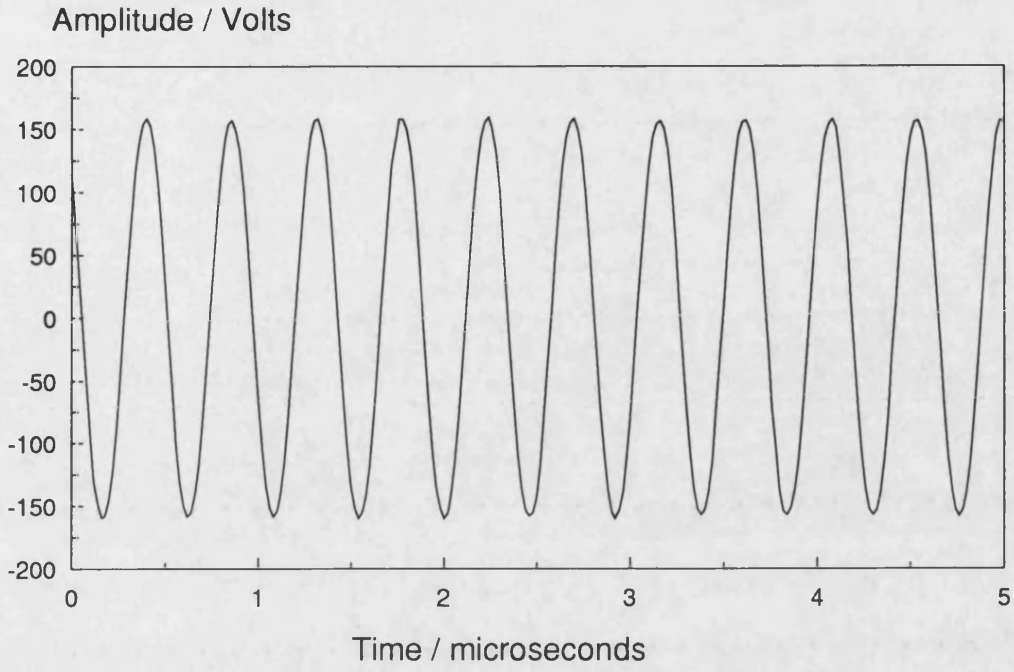

Figure 3.14 Time waveform of the initial signal at a drive level of 325 V_{p-p}.

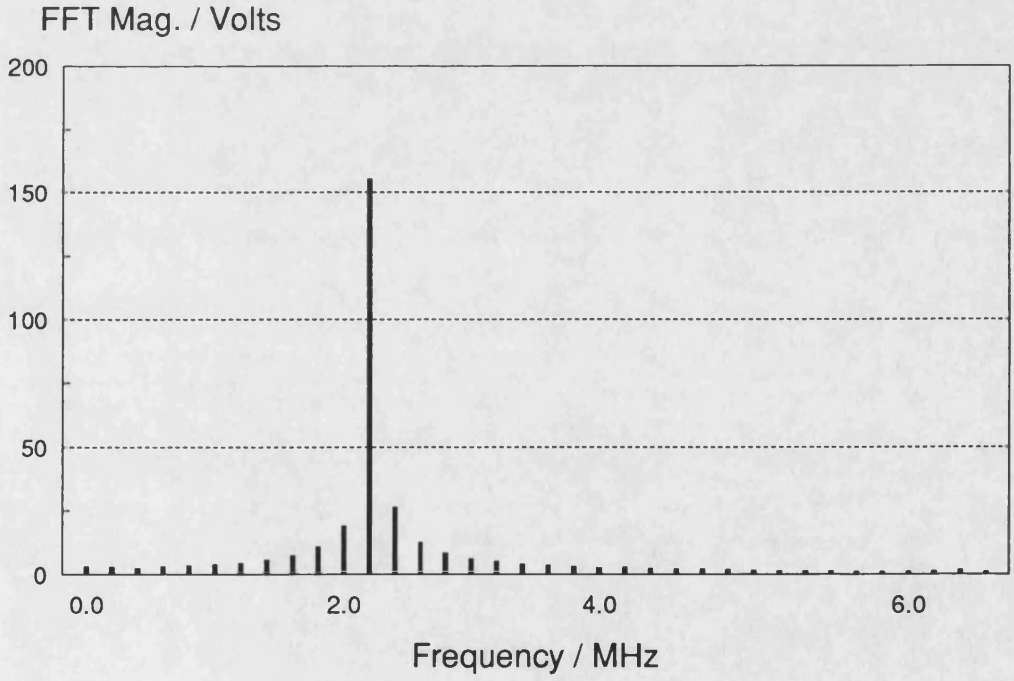

Figure 3.15 FFT magnitudes of the initial signal at a drive level of 325 V_{p-p}.

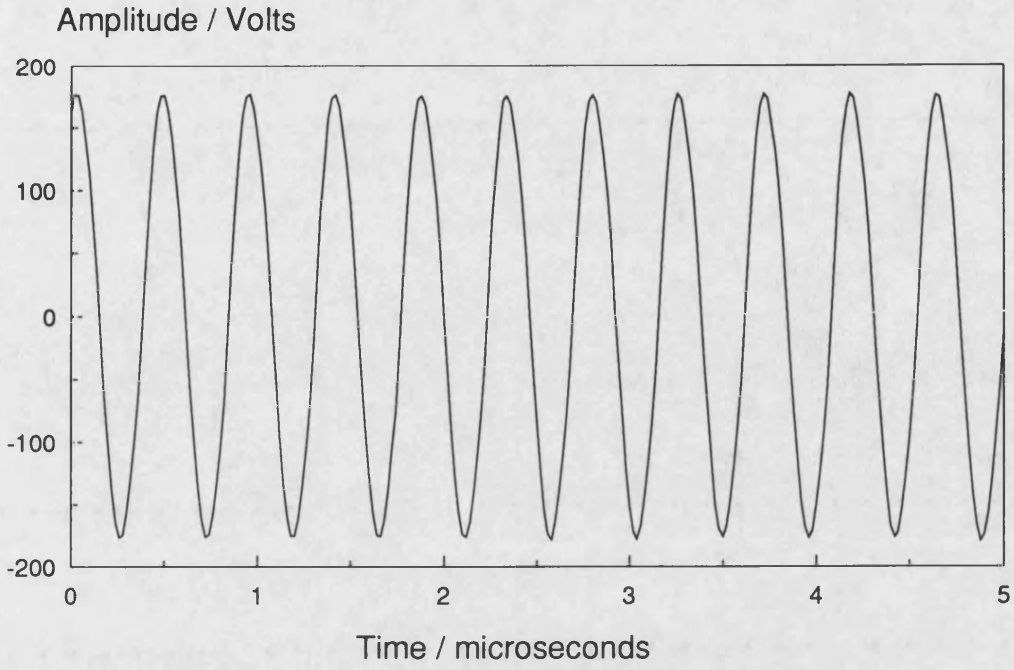

Figure 3.16 Time waveform of the initial signal at a drive level of 350 $V_{p\text{-}p}$.

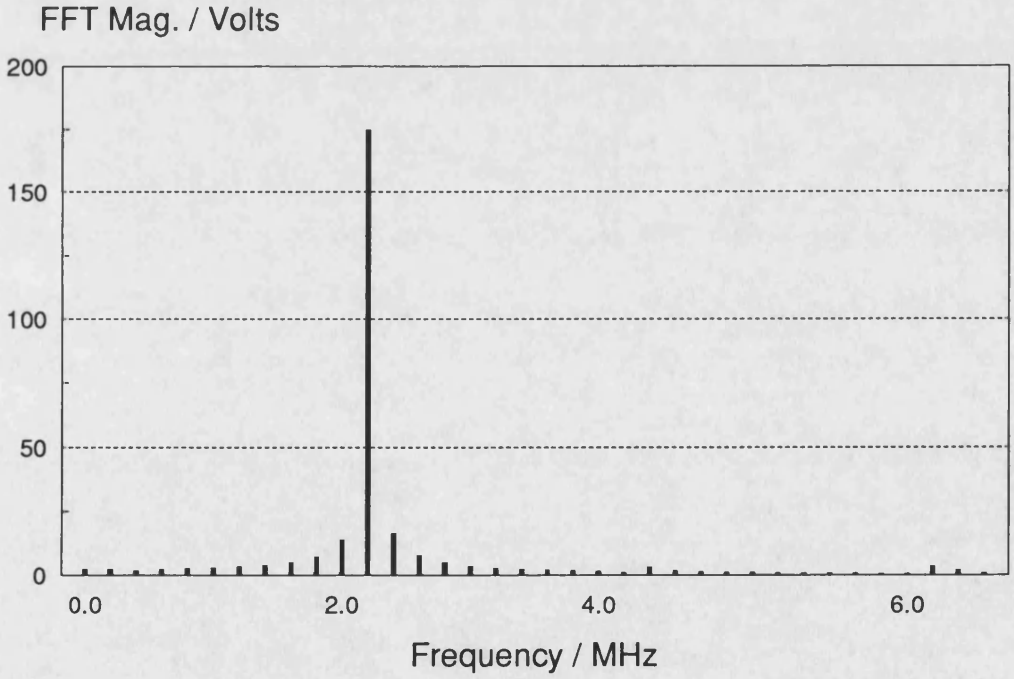

Figure 3.17 FFT magnitudes of the initial signal at a drive level of 350 $V_{p\text{-}p}$.

3.9 DIGITAL STORAGE OSCILLOSCOPE

The digital oscilloscope used to monitor and capture the time waveform was a Philips PM3315. The DSO had an eight bit analogue to digital convertor with a sampling rate of 125 MHz (8 ns between samples) which made it ideal for the range of frequencies used. It should be noted that although the fundamental frequency used was fairly low (2.25 MHz) in comparison with the sampling rate of the DSO, there was a need for such a sampling rate when the harmonics and the bandwidth of the hydrophone considered. The input amplifiers of the PM3315 had a -3 dB bandwidth of 60 MHz and input impedance of 1MΩ in parallel with 25 pF. The input capacitance was significant since it was comparable with the hydrophone capacitance of 92 pF. Thus, it was necessary to correct the open circuit hydrophone sensitivity to account for the loading effect of the DSO. The record length of the DSO was 256 bytes with 8 bits per byte, thus at the maximum direct sampling rate (125 MHz) the maximum time slice that could be captured was 2 μs. The relatively short record length of the DSO was compensated for by a trigger delay that could be varied from -10 to 9999 divisions of time base; allowing the user to select a particular portion of a signal for digitasation [74]. Almost all of the functions that could be set from the front panel could also be set via the IEEE-488 interface thus the DSO could be used under full software control. Computer control also allowed auto ranging to be carried out for the attenuators and the trigger delay could be determined by the computer and set automatically each time the hydrophone was moved allowing a highly automated data capture sequence. The captured wavefroms were transferred via the IEEE bus to the computer for analysis.

3.10 TRANSLATION STAGE

The translation stage comprised two Time and Precision Uni-slides mounted in the horizontal plane at 90 degrees to each other. The hydrophone support was mounted on the cross slide and incorporated manual adjustment vertically and in azimuth. The Uni-slides had a resolution of about 6 microns and were driven by the computer via the IEEE bus and a Digiplan stepper motor drive (Type CD20). The translation stage was mounted over a water filled tank 1.2 m long, 0.3 m wide and 0.3 m deep. Measurements were typically made at intervals of 1 to 10 mm along the acoustic axis and 0.5 mm to 1.0 mm intervals across the axis.

3.11 PERSONAL COMPUTER

An IBM personal computer, PC AT, was extensively used to control the translation stage and the DSO via an IEEE interface. This helped to move the hydrophone between measurements and to set up the system for a series of measurements to be made. Experimental measurements could be made in a fraction of the time that it would take if the operation were carried out manually and at much closer spatial intervals than would normally be practical. Such experimental measurements were stored and processed by the computer.

A certain amount of software was available such as IBM's own Professional Fortran which was used for the majority of programming in conjunction with the IBM General Purpose Interface Bus (GPIB) routines. In particular, the IBM Plotting system and the Numerical Algorithm Group's (NAG) PC-50 Mathematical Subroutine Library were extensively used for theoretical predictions. However, the speed of the execution and the limited memory (512 K Bytes) and the hard disk size (21 M Bytes) did pose some problems. A terminal emulator was also available on

the computer which was used to gain acsess to the Gould NP1 Mainframe system that was used to reduce the theoretical run times considerably. Thus, direct comparisons could be made between experimental results held on the IBM and the theoretical results held on the Mainframe.

3.12 PRESSURE FIELD MEASUREMENTS

Pressure field measurements were made under quasi-continious wave conditions. Before each measurement was taken, the frequency of the driving pulse and the drive level were set. The transducer, aperture and hydrophone were aligned with great care and the DSO was set to trigger externally from the 'SYNC' pulse and the trigger delay adjusted until the required part of the pulse in the view on the DSO, usually the central portion of the pulse.

For the axial measurements the FORTRAN program AXM.FOR and for the radial measurements ALN.FOR was set running and then the related program took control of the hydrophone position and the DSO. The time series data from the DSO was received in the form of 256 integers in the range 0 to 255, where 0 was the minimum display reading and 255 was the maximum. If any of the integer values were 0 or 255, then the attenuator setting was increased to ensure that signal was not being clipped. The peak to peak voltage was calculated from the difference between the highest voltage in the series and the lowest, if it was less than half of the full scale value, the attenuator setting was decreased. The voltages were converted to a pressure using the nominal sensitivity of the hydrophone. The data at this stage was an array of 256 pressure values. The array was normalised to give zero mean and the zero crossings were used to extract a portion of the time series data exactly one cycle long. This cycle was then resampled over 256 points to ease the FFT calculations. The single resampled cycle was then operated on by an FFT routine which returned

an array containing the real and the imaginary parts of the FFT components. The magnitude and phase of the FFT components were calculated and the range (axial or radial), the magnitude and phase of the first five harmonics were stored in a file on the PC. Measuring the pressure field in this way provided a quick measurement scheme. The results also could be displayed in graphical form with the FFT magnitudes and FFT phases after each measurement.

3.13 EXPERIMENTAL UNCERTAINTIES

The properties of the medium could potentially effect the accuracy of experimental measurements. For example, the attenuation coefficient of the water, the nonlinearity parameter β and the velocity of sound in water changes depending upon the water quality and the temperature fluctuations.

The attenuation coefficient of water is known with an error less than 2%. A noticeable point that was encountered in any published results for the attenuation coefficient of the water was the fact that the attenuation coefficient increases if the water is not completely clean and the likely size of this effect is not known. However, it is reasonable that the uncleanliness of the water does not significantly effect the attenuation coefficient under the present experimental conditions.

There are several ways of determining the nonlinearity parameter β for water but the highest accuracy is obtained with the thermodynamic method. This involves the measurement of the velocity of sound as a function of temperature and pressure. Wilson's calculation of β value [75], which was based on the thermodynamic method, gives 3.52 and Beyer [76] estimates it to have an uncertainty of 2%.

The variation in water temperature during the day and the experiments did have a significant effect on the pressure field measurements. The water temperature recorded was typically steady to within $\pm 1°C$ which caused a variation in the sound speed about $\pm 3m/s$ according to the empirical expression given by Kinsler *et al* [77]. The accuracy was guaranteed to 0.05% for temperatures between $0°C$ and $100°C$ pressures in the range 0 to 200 bar (1 bar= 10^5 Pa). The calculated experimental value for the speed of sound was 1486±60 m/s which compares favourably with the expected value of 1482 m/s at 20 $°C$.

Additional uncertainties also arise from the equipment used in the experimental arrangements. The digital storage oscilloscope used for the capture of time waveforms in this study was quoted by the manufacture as having a vertical accuracy of better than 3%. The input amplifiers of the DSO had a -3 dB bandwidth of 60 MHz, thus the phase shift at frequencies below 30 MHz and should be negligible. The uncertainty in the time base of the DSO was guaranteed to less than 2% [74], thus the frequency measurements inferred from the zero crossing frequency of the time waveform could be expected to have similar uncertainty. The frequency meter (RACAL-DANA 9900) used to set the frequency of the initial continuous wave signal was left switched on about half an hour before the measurements to get accurate frequency setting and had a uncertainty of 5%.

The reference hydrophone, used to calibrate the 1 mm diameter bilaminar hydrophone used in these measurements, had been calibrated in amplitude only, at the National Physical Laboratory and had uncertainty, at 95% confidence level, certificated as 6% over the frequency range 1 to 15 MHz [66].

It was assumed that the circular transducer behaved as a perfect plane piston on the basis of the good agreement of the small signal measurements with theory and early measurements by Baker [78].

Errors in making rectangular apertures had direct effect on the experimental measurements since the positions of the axial maxima and minima are proportional to the aperture size squared over wavelength for each direction. A couple of apertures were made to the same nominal size and the one closest to the correct size was chosen. The effective aperture size and the accuracy of the size was also tested comparing experimental results with predicted values. It was assumed that the each pair of lenses had the same focusing properties and could be made with an accuracy 5%.

CHAPTER 4

THEORY

4.1 INTRODUCTION

The linear fields generated at ultrasonic frequencies by various sizes of rectangular apertures, both focused and unfocused, were predicted using generalised Fourier transform diffraction theory [14]. The nonlinear predictions were made using two different approaches, the plane wave propagation model and a perturbation approach. Each model is reviewed in this chapter. Predicted results from each model are presented in section 4.8 as an example calculation and more details will be discussed in the chapter 5, Results and Discussion.

4.2 THE GENERALISED FOURIER TRANSFORM THEORY

The Rayleigh-Sommerfeld diffraction integral allows the calculation of electromagnetic field at a point away from an aperture in terms of the field distribution on the aperture face and is an exact formulation of Huygen's principle for isotropic media. When applied to the ultrasonic case, this diffraction integral becomes [79],

$$f(x,y,z) = \frac{jk}{2\pi}\int\int f_0(x_0,y_0,0)\frac{e^{-jkR}}{R}dx_0dy_0 \qquad 4.1$$

relating the complex amplitude $f(x,y,z)$ at the observation point (x,y,z) to the complex amplitude $f_0(x_0,y_0,0)$ in the aperture plane, where the distance between the source and observation point is (see Figure 4.1),

$$R = [(x - x_0)^2 + (y - y_0)^2 + z^2]^{1/2} \tag{4.2}$$

If we define an acoustic amplitude as

$$A(x, y, z, t) = A_0(x, y, z)e^{j(\omega t - kz)} \tag{4.3}$$

where ω is the angular frequency, t is time and k is the acoustic wave number. For the anisotropic case, under the usual Fresnel approximations (which is valid for field points that are greater than one aperture width away from the transducer) Equation 4.1 becomes [14]

$$A(x, y, z) = \frac{jk}{2\pi} \int_{-\infty}^{\infty} \int_{-\infty}^{\infty} A_0(x_0, y_0, 0) e^{-\frac{jk}{2z}[(x - x_0)^2 + (y - y_0)^2]} dx_0 dy_0 \tag{4.4}$$

where $A_0(x_0, y_0, 0)$ describes the acoustic amplitude over the aperture region and is identically zero outside the limits of the aperture.

Using Fourier transform operations [80] and with some manipulation, Equation 4.4 can be rewritten in the following form

$$A(x, y, z) = \frac{j}{\beta_0} e^{-j\pi\beta_0(x^2 + y^2)} \int_{-\infty}^{\infty} \int_{-\infty}^{\infty} \left\{ a\left(\frac{s}{\beta_0}, \frac{p}{\beta_0}\right) e^{-j\frac{\pi}{\beta_0}(s^2 + p^2)} \right\} e^{j2\pi(sx + py)} ds\, dp \tag{4.5}$$

in which $a(s/\beta_0, p/\beta_0) = A_0(x_0, y_0, 0)$. Equation 4.5 states that the complete nearfield and the amplitude at a farfield point can be written as the inverse Fourier transform of the source distribution. In a similar manner to that of Papoulis [81] we can also show that the farfield can also be written as

$$A(x, y, z) \approx \frac{j}{\beta_0} \int_{-\infty}^{\infty} \int_{-\infty}^{\infty} \left\{ a\left(\frac{s}{\beta_0}, \frac{p}{\beta_0}\right) \right\} e^{j2\pi(sx + py)} ds\, dp \tag{4.6}$$

As we discussed earlier in the second chapter, this approach provides analytical expressions for several important source distributions.

4.3 THE LINEAR FIELD OF A RECTANGULAR SOURCE

We can now apply the Fourier transform theory to the rectangular source function, [80] $A_0(x_0,0)=\Pi(x_0/a)$ with ,

$$\Pi(x_0/a)=\begin{cases}1, & |x_0|<a/2,\\ \frac{1}{2}, & |x_0|=a/2,\\ 0, & |x_0|>a/2.\end{cases} \qquad 4.7$$

where a is the aperture size and $\Pi(x_0/a)$ is the amplitude at the source. With this rectangular source function Equation 4.5 gives

$$A(x,z)=\frac{1}{\beta_0}e^{j\frac{\pi}{4}}e^{-j\pi\beta_0 x^2}F^{-1}\left[\Pi\left(\frac{s}{\beta_0 a}\right)e^{-j\pi\frac{s^2}{\beta_0}}\right] \qquad 4.8$$

or in terms of Fresnel integrals [80],

$$FR(\omega)=\int_0^{\omega}e^{-j\pi\frac{v^2}{2}}dv \qquad 4.9$$

Equation 4.8 becomes:

$$A(x,z)=\frac{e^{j\frac{\pi}{4}}}{\sqrt{2}}\{FR[\sqrt{2\beta_0}(x+a/2)]-FR[\sqrt{2\beta_0}(x-a/2)]\} \qquad 4.10$$

Similarly, the farfield can be expressed as:

$$A(x,z) \approx \frac{e^{j\frac{\pi}{4}}}{\sqrt{\beta_0}} F^{-1}[\prod(s/\beta_0 a)] \qquad 4.11$$

$$\approx \frac{e^{j\frac{\pi}{4}}}{\sqrt{\beta_0}} [\beta_0 a\, sinc(\beta_0 a x)]$$

where $sinc(\theta) = (\sin(\theta)/\theta)$. Equation 4.6 can also be extended to focused case considering the source function [80] $A_0(x_0, 0)$,

$$A_0(x_0, 0) = \prod(x_0/a) e^{j\frac{kx_0^2}{2R}} \qquad 4.12$$

where R is the curvature of the transducer. Substituting Equation 4.12 into Equation 4.5 reveals that focusing occurs at $z = R$.

The Fourier transform approach outlined above sheds light on the properties of the linear field of rectangular sources thus provided a head start when turning to the nonlinear case.

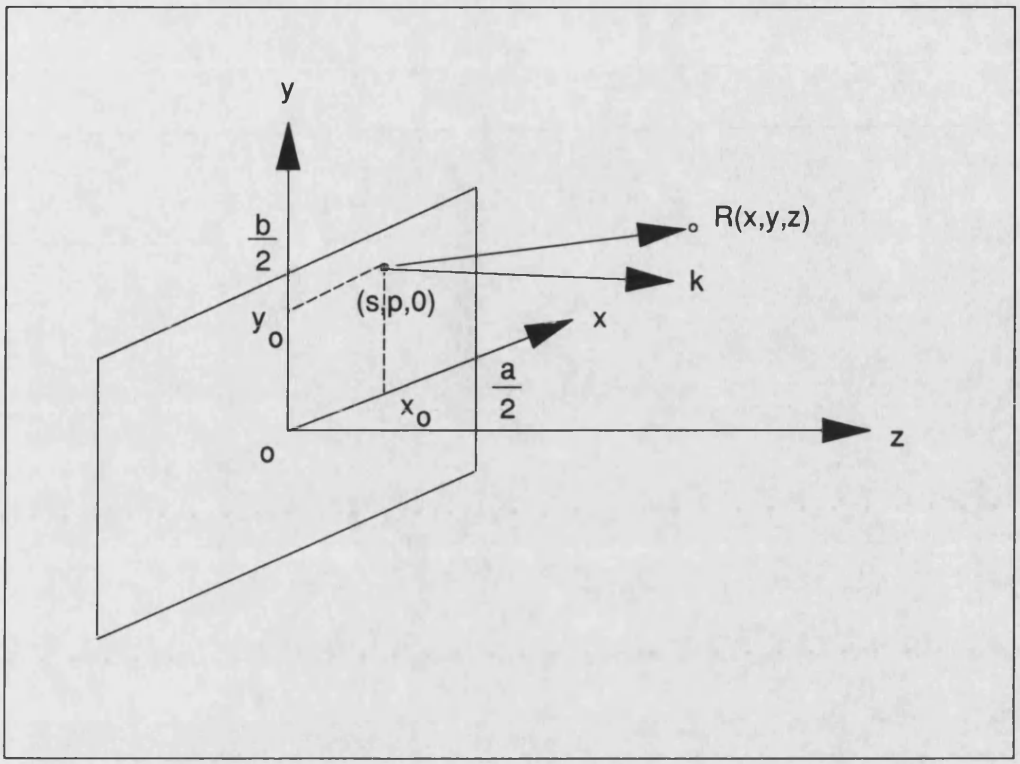

Figure 4.1 Coordinate geometry for a rectangular source in the plane z=0, radiating along a direction k into the positive z half space. The source coordinate is (s,p,0) or is equal to $(x_0, y_0, 0)$ and R is the vector between the source point and the field point (x,y,z).

4.4 NONLINEAR WAVE EQUATION

Although a linear theory is sufficient in many applications, there are some areas (such as parametric arrays, medical applications of ultrasound and the acoustic microscope) where nonlinear effects play an important role. For example if an imaging system uses information from waves that are nonlinear, it is important to take into account the diffraction effects, nonlinearity and absorption due to the propagation medium.

Khokhlov and Zabolotskaya [49] developed an equation for circular geometry to describe the propagation of finite amplitude sound beams in a nonlinear medium without absorption. Kuznetsov [50] incorporated the effect of absorption and after that it has been widely known as the KZK equation which describes the simplest possible way of coupling between nonlinearity, absorption and diffraction.

$$\frac{\partial^2 W}{\partial\sigma\partial\tau} = \alpha r_0 \frac{\partial^3 W}{\partial\tau^3} + \frac{r_0}{2l_d}\frac{\partial^2 (W^2)}{\partial\tau^2} + \frac{1}{4}\nabla^2 W \qquad 4.13$$

Where:

$W = \frac{u}{u_0}$ is the normalised particle velocity,

$\sigma = \frac{z}{r_0}$ is the normalised axial distance,

α is absorption coefficient,

$\tau = \omega t - kz$ is the retarted time,

$l_d = \frac{1}{\beta\varepsilon k}$ is the shock parameter,

$r_0 = \frac{ka^2}{2}$ is the Rayleigh distance,

$\nabla^2 = \frac{\partial^2}{\partial x^2} + \frac{\partial^2}{\partial y^2} = \frac{1}{r}\frac{\partial}{\partial r}\left(r\frac{\partial}{\partial r}\right)$ is the transverse Laplacian operator.

Equation 4.13 is based on the parabolic approximation [20] which assumes that the aperture is several wave-lengths across, i.e $ka \gg 1$. This also puts a limit on the maximum angle that a vector from the origin to the field point can subtend to the

acoustic axis, hence positions close to the aperture or far off axis must be avoided. The parabolic approximation is also known as the paraxial approximation and is equivalent to the Fresnel approximation [80].

No analytical solution exists for Equation 4.13 thus the main approach to solve it has been through numerical methods [51,53-56].

4.5 MODIFICATION OF THE KZK EQUATION FOR THE PLANE WAVE PROPAGATION

A common procedure for the numerical solution of the KZK equation is to stepwise calculate the harmonic content of a finite amplitude sound beam in the frequency domain. This has the advantage that the entire pressure field is calculated and interactions between harmonics and the fundamental can be seen. However, it involves heavy computational requirements.

A numerical scheme to solve the KZK equation has been implemented by Aanonson [63] and extended by Hart [62], changing the grid size at the focus, pre- and post-focal regions to give high resolution around the focal plane. Good agreement was obtained between experiment and Aanonson's solution by Baker *et al* [67] up to fifth harmonic.

The analysis of plane wave propagation presented in this section closely follows the treatment of Aanonsen [63] and Baker *et al* [67]. As they suggested, we assume a solution in the form of a Fourier series with amplitude and phase that are functions of the spatial coordinates x, y and σ;

$$W(x,y,\sigma,\tau) = \sum_{n=1}^{\infty} W_n(x,y,\sigma)\sin(n\tau + \psi_n(x,y,\sigma))$$

$$= \sum_{n=1}^{\infty} [g_n(x,y,\sigma)\sin(n\tau) + h_n(x,y,\sigma)\cos(n\tau)] \qquad 4.14$$

where n is the harmonic number, g_n and h_n are the Fourier solution coefficients for n^{th} harmonics and ψ_n is the phase. By substituting Equation 4.17 into 4.16 and identifying the terms in $\cos(n\tau)$ and $\sin(n\tau)$, we obtain an infinite set of coupled partial differential equations for the components g_n and h_n:

$$\frac{\partial g_n}{\partial \sigma} = -n^2 \alpha r_0 g_n + \frac{1}{4n}\nabla^2 h_n + \frac{n r_0}{2 l_d}\left[\frac{1}{2}\sum_{k=1}^{n-1}(g_k g_{n-k} - h_k h_{n-k}) - \sum_{p=n+1}^{\infty}(g_{p-n}g_p + h_{p-n}h_p)\right] \qquad 4.15$$

and

$$\frac{\partial h_n}{\partial \sigma} = -n^2 \alpha r_0 h_n - \frac{1}{4n}\nabla^2 g_n + \frac{n r_0}{2 l_d}\left[\frac{1}{2}\sum_{k=1}^{n-1}(h_k g_{n-k} + g_k h_{n-k}) + \sum_{p=n+1}^{\infty}(h_{p-n}g_p - g_{p-n}h_p)\right] \qquad 4.16$$

In order to solve Equations 4.15 and 4.16 numerically, the infinite series in those equations must be truncated limiting the number of harmonics in the solution. Implementing these changes in Equation 4.15 and 4.16 produces

$$\frac{\partial g_n}{\partial \sigma} = -n^2 \alpha r_0 g_n + \frac{1}{4n}\nabla^2 h_n + \frac{n r_0}{2 l_d}\left[\frac{1}{2}\sum_{k=1}^{n-1}(g_k g_{n-k} - h_k h_{n-k}) - \sum_{p=n+1}^{M}(g_{p-n}g_p + h_{p-n}h_p)\right] \qquad 4.17$$

$$\frac{\partial h_n}{\partial \sigma} = -n^2 \alpha r_0 h_n - \frac{1}{4n}\nabla^2 g_n + \frac{n r_0}{2 l_d}\left[\frac{1}{2}\sum_{k=1}^{n-1}(h_k g_{n-k} + g_k h_{n-k}) + \sum_{p=n+1}^{M}(h_{p-n}g_p - g_{p-n}h_p)\right] \qquad 4.18$$

where M is the number of harmonics retained in the solution. The change in g_n and h_n with propagation distance z can be seen more clearly if we rewrite one of the equations in terms of z:

$$\frac{\partial g_n}{\partial z} = -n^2 \alpha g_n + \frac{1}{4nr_0}\nabla^2 h_n$$
$$+\frac{n}{2l_d}\left[\frac{1}{2}\sum_{k=1}^{n-1}(g_k g_{n-k} - h_k h_{n-k}) - \sum_{p=n+1}^{M}(g_{p-n}g_p + h_{p-n}h_p)\right] \qquad 4.19$$

This equation shows that the change in g_n with distance along the acoustic axis is due to the three main effects; attenuation, diffraction and nonlinearity due to the medium.

The first term on the right hand side of Equation 4.19 represents the effect of attenuation and has n^2 dependence. As the attenuation coefficient α is proportional to frequency squared, we have the classic frequency squared dependence.

The second term on the right hand side of Equation 4.19 is responsible for the diffraction and the effect of the diffraction may be explained by means of the Rayleigh distance (r_0). This term also depends on the harmonic number n, thus the diffraction terms becomes less important as the frequency, harmonic number and the aperture size increases. In other words, the more wave-lengths across the aperture the more beam looks like a plane wave travelling in the propagation direction. Diffraction also depends on the transverse gradient ∇, with rapid changes in the field in the radial direction giving rise to large diffraction effects such as occurs at the piston edge.

The term with summations in Equation 4.19 represents the nonlinearity and interactions between harmonics. The first sum is responsible for the contributions to the n^{th} harmonic due to the interaction of lower harmonics producing a sum

frequency component at n[th] harmonic. The second sum evaluates the interactions of higher harmonics producing a difference frequency component at the n[th] harmonic. The nonlinear term also depends on the harmonic number n and the shock distance l_d which is defined for a plane wave as:

$$l_d = \frac{1}{\beta \varepsilon k} \tag{4.20}$$

where β is the nonlinearity parameter, ε is the acoustic Mach number ($= u_0/c_0$ where u_0 is the particle velocity amplitude at the source and c_0 is the infinitesimal sound speed) and k is the wavenumber. According to Equation 4.20, this dependence shows that nonlinear term becomes more dominant with increasing frequency and harmonic number and a plane wave goes into shock more quickly with increasing value of the parameter of nonlinearity, acoustic Mach number and fundamental frequency.

Although the attenuation, diffraction and nonlinearity have some important consequences as discussed above, it is not necessarily a simple problem to combine all effects in a single model and those effects may be examined separately. Under this assumption, we take the diffraction term out in Equation 4.19 getting a simplified equation:

$$\frac{\partial g_n}{\partial z} = -n^2 \alpha g_n + \frac{n}{2l_d}\left[\frac{1}{2}\sum_{k=1}^{n-1}(g_k g_{n-k} - h_k h_{n-k}) - \sum_{p=n+1}^{M}(g_{p-n} g_p + h_{p-n} h_p)\right] \tag{4.21}$$

Similar changes can be made to Equation 4.18, i.e, for h_n and these simplified equations can be stepwise integrated by an implicit backward difference formula (IBDF) to ensure a high degree of stability. Thus the individual terms for g_n (and for h_n as well) can be approximated according to the following scheme:

$$g_n \rightarrow g_{(n,i)}$$

$$\frac{\partial g_n}{\partial z} \rightarrow \frac{1}{\Delta z}[g_{(n,i+1)} - g_{(n,i)}] \qquad 4.22$$

where i is the grid point in IBDF and Δz is the axial step size. These approximations are standard and may be found in any textbook on numerical integration of partial differential equations (e.g., [83] or [84]).

Approximated equations for g_n and h_n were programmed in FORTRAN in order to calculate the plane wave propagation stepwise in the frequency domain. The initial condition for a plane wave was unit amplitude and zero phase for the fundamental and zero for all the other harmonic components retained in the calculation. The program then calculated the change in each harmonic component at every grid point in the axial direction and absorption and nonlinearity were accounted for at each step. The step size was kept as small as possible and varied if necessary, depending on the pressure levels generated. However in order to reduce the run-time, the number of harmonics decreased and the step size were increased for rough predictions on a PC.

Figure 4.2 illustrates the frequency domain representation of a predicted plane wave propagation at finite amplitudes with a loss from the fundamental to the harmonics which in turn corresponds to distortion of the waveform in the time domain. The loss of energy from the fundamental can be seen as the harmonics increase in amplitude during the propagation of the wave.

4.5.1 Inclusion of diffraction for rectangular apertures

As we discussed earlier in this chapter, the effect of diffraction can be taken into account separately. This could be managed by calculating this effect from the linear on-axis pressure variations calculated by the Fourier transform theory. By adding or subtracting the diffraction effect for the fundamental component at each step in the calculation of plane wave propagation, the second and higher harmonics could be predicted as a direct result of the small signal field variation for the fundamental. However this puts a restriction on the step size which had to be equalized both in the calculation of linear field by Fourier transform method and the plane wave propagation. Predicted results obtained in this manner provided the understanding of the general structure of the harmonic components in the field of a rectangular aperture but this does not mean that the diffraction effects were fully accounted for as we ignored the diffraction effects due to the second and higher harmonics. More details of this effect are discussed in the next chapter.

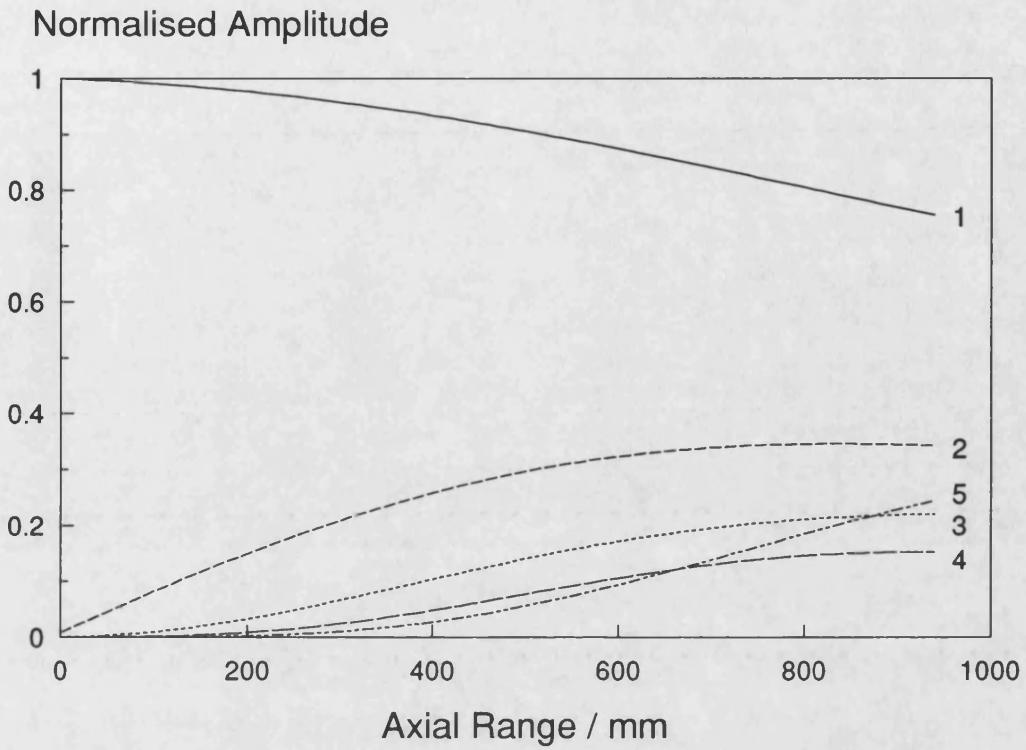

Figure 4.2 Predicted harmonic amplitudes (up to 5th harmonic was shown) of a plane wave in water with a fundamental frequency 2.25 MHz, p_0=175 kPa.

4.6 MAIN FACTORS AFFECTING THE CALCULATIONS

4.6.1 Number of Harmonics

The choice of the number of harmonics retained in the calculation should be a careful one as it affects the amplitude of the higher harmonics generated. Ideally, an infinite number of harmonics should be included in the solution to ensure a negligibly small error in the highest harmonics of interest. However, at relatively low drive levels only a small amount of energy is transferred to higher harmonics so the maximum number of harmonics retained in the calculation could be reduced. In order to obtain

some measure of the retained number of harmonics, the program was run for different harmonic numbers. It can be seen in Figure 4.2 that the calculated values for the fifth harmonic decrease too slowly with distance and become abnormally large relative to the lower harmonics at ranges beyond about 500 mm. Table 4.1 lists the calculated amplitude of harmonic components of a plane wave depending on the maximum harmonic number retained in the calculation. The wave was propagated almost one metre. It is noticeable that when 3 and 5 harmonics are retained, the amplitude of the highest harmonic exceeds the lower harmonics but this almost disappears after 10 harmonics are retained in the calculation.

There is another factor related to the choice of the maximum number of harmonics and has to be taken into consideration; the execution time of the computer program.

4.6.2 Step Size

Ideally, in the calculation, a finer step size should be used in the near field, where the diffraction effects are most important, and larger step size in the farfield, where the diffraction effects are not so important. In practice it was simpler to use a constant step size (typically 0.25 mm) so that the diffraction and nonlinearity could both be calculated over equal intervals.

Max. Harmonic Number	Amplitude of Each Harmonic Component				
	1st	2nd	3rd	4th	5th
3	0.746	0.341	0.396	0.000	0.000
5	0.742	0.339	0.221	0.151	0.259
10	0.740	0.335	0.212	0.150	0.118
30	0.740	0.335	0.211	0.151	0.116

Table 4.1 Effect of the number of harmonics retained in the calculation on the amplitude of the first five harmonics at the max. propagation distance z_{max}=980 mm at 2.25 MHz. Initial amplitude for the first harmonic was set to unity, p_0=175 kPa.

4.6.3 Initial Conditions

The initial conditions are specified by the amplitude and phase of each harmonic at each point on the plane of aperture at $z = 0$. It was assumed that fundamental has unit amplitude and phase but the higher harmonic amplitudes and phases were set to zero. It was also necessary to initialise the aperture size (***a*** and ***b***) in each direction, attenuation coefficient (α), step size (Δz), the plane wave shock distance (l_d), maximum harmonic number (M) and the pressure amplitude at the transducer face (P_0). As it was difficult to measure the value of P_0 experimentally, data points much closer to the aperture face were taken as reference points to give a good fit between predicted and measured values of fundamental.

4.7 PERTURBATION METHOD

Another approach that was used to find a solution to the nonlinear wave equation was the perturbation solution. This approach assumes a solution to the nonlinear wave equation of the form [41]

$$\Phi = \Phi_1 e^{j\omega t} + \Phi_2 e^{j2\omega t} + \ldots + \Phi_n e^{jn\omega t} \qquad 4.23$$

where Φ_i are the velocity potentials applicable to the each harmonic, ω is the angular frequency and t is time. It is also assumed that the acoustic amplitude of the first harmonic is large enough to produce a second harmonic component of frequency 2ω, but not so large as to cause significant generation of higher harmonics. We also assume that the fundamental frequency ω is high enough to make $ka \gg 1$, where k is the wavenumber of the first harmonic and a is the aperture dimension. For each Φ_i we also define a particle velocity

$$u_i(x,y,z,t) = -\nabla\Phi_i \qquad 4.24$$

If Equation 4.23 is substituted into the following nonlinear wave equation, which

$$c^2\nabla^2\Phi - \frac{\partial^2\Phi}{\partial t^2} = \frac{\beta}{c^2}\frac{\partial}{\partial t}\left(\frac{d\Phi}{dt}\right)^2 - \frac{2\varepsilon c\beta}{\Gamma k}\nabla^2\left(\frac{\partial\Phi}{\partial t}\right) \qquad 4.25$$

emcompasses both nonlinear and dissipative effects, differential equations of the first and second order can be derived by grouping the terms of the same order of magnitude, such as:

$$\nabla^2\Phi_1 + k^2\Phi_1 = 0$$

$$\nabla^2\Phi_2 + (2k)^2\Phi_2 = \frac{jk^3\beta}{c}\Phi_1^2 \qquad 4.26$$

where Φ_2 is the second harmonic velocity potential within the Fourier series in Equation 4.23. The condition that Φ_2 is small compared with Φ_1 holds for weakly nonlinear waves and is appropriate for conditions near to the source. Equation 4.26 was derived by Heaps [85] from the exact equations and the term on the right hand side can be regarded as a source term, giving rise to the second harmonic in the fundamental field. Thus, the second harmonic generated from any fundamental field could be expressed in terms velocity potential of the fundamental. Ingenito and Williams [41] and Lancaster [48] have used this expression to calculate the second harmonic variation in the near field of a circular source and arrived at an approximate expression for Φ_2 at a field point (r,z),

$$\Phi_2(r,z) \approx -\beta\frac{k^2}{4c}\int_{\sigma=0}^{z} e^{jk\sigma}\Phi_1^2\left(r, z-\frac{\sigma}{2}\right)d\sigma \qquad 4.27$$

This expression is interesting as it states that the important regions of sources which give rise to the second harmonic are only on an axis toward to the piston. Regions outside the acoustic axis are of less importance as are sources between the piston and halfway to the field point.

A similar procedure has been used to predict the second harmonic generation in the field of a rectangular transducer finding a suitable substitution Φ_1, for to source term in Equation 4.27. In principle, Equation 4.8 could be used in the perturbation solution but in practice it is simpler to derive a more specific form for the plane rectangular source without focusing. Thus we review the linear field of a rectangular source in terms of the geometry we used as shown in Figure 4.3 (Note that the source geometry is different from the previous geometry used in section 4.3). A rectangular piston source of dimensions $2a$ by $2b$ lies in the plane $z=0$ and is centred at $x=y=0$. The rest of the source plane is assumed to be a rigid baffle and the piston is driven at angular frequency ω radiating a beam which is symmetric about the z axis into

the half space $z > 0$. The boundary condition at $z = 0$ is that the z component of the particle velocity has constant amplitude u_0 over the piston face and vanishes everywhere on the baffle. Under these assumptions, the primary field of a rectangular source at $R'(x, y, z)$ could be written as [11,12,82]

$$\Phi_1(R') = \frac{u_0}{2\pi} \int_{-a}^{a} \int_{-b}^{b} \frac{e^{-jkr}}{r} dx_0 dy_0 \qquad 4.28$$

where r is the distance from the centre of the source to the field point $R'(x, y, z)$ and is equal to:

$$r = \sqrt{z^2 + (x - x_0)^2 + (y - y_0)^2} \qquad 4.29$$

With the Fresnel approximation [80] we get

$$r \approx z + \frac{(x - x_0)^2}{2z} + \frac{(y - y_0)^2}{2z} \qquad 4.30$$

and

$$\frac{1}{r} \approx \frac{1}{z} \qquad 4.31$$

Substitution of Equation 4.30 and 4.31 into Equation 4.28 gives

$$\Phi_1(R') = \frac{u_0}{2\pi z} e^{-jkz} \int_{-a}^{a} e^{-j\frac{k}{2z}(x - x_0)^2} dx_0 \int_{-b}^{b} e^{-j\frac{k}{2z}(y - y_0)^2} dy_0 \qquad 4.32$$

In order to evaluate the integrals in Equation 4.32, we need to change variables. If we assume that

$$u = x - x_0$$

$$h = y - y_0$$

$$\frac{k}{2z}u^2 = \frac{\pi}{2}t^2 \qquad 4.33$$

$$\frac{k}{2z}h^2 = \frac{\pi}{2}q^2$$

then the integrals in Equation 4.32 reduce to the form

$$\int_{-a}^{a} e^{-j\frac{k}{2z}(x-x_0)^2} dx_0 = \int_{x-a}^{x+a} e^{-j\frac{k}{2z}u^2} du = \sqrt{\frac{\pi z}{k}} \int_{t_1}^{t_2} e^{-j\frac{\pi}{2}t^2} dt \qquad 4.34$$

and

$$\int_{-b}^{b} e^{-j\frac{k}{2z}(y-y_0)^2} dy_0 = \int_{y-b}^{y+b} e^{-j\frac{k}{2z}h^2} dh = \sqrt{\frac{\pi z}{k}} \int_{q_1}^{q_2} e^{-j\frac{\pi}{2}q^2} dq \qquad 4.35$$

with

$$t_1 = \sqrt{\frac{k}{\pi z}}(x-a) \qquad t_2 = \sqrt{\frac{k}{\pi z}}(x+a)$$

$$q_1 = \sqrt{\frac{k}{\pi z}}(y-b) \qquad q_2 = \sqrt{\frac{k}{\pi z}}(y+d) \qquad 4.36$$

thus we obtain the velocity potential of the primary field as

$$\Phi_1(R') = \frac{u_0}{2k} e^{-jkz} \int_{t_1}^{t_2} e^{-j\frac{\pi}{2}t^2} dt \int_{q_1}^{q_2} e^{-j\frac{\pi}{2}q^2} dq \qquad 4.37$$

(Notice that Equation 4.37 has a similar form to Equation 4.10 except a phase factor). The first integral in Equation 4.37 represents the total contribution of individual points at the aperture face in the x direction to the pressure field and the second

integral is due to the contribution of the points in y direction. Hence, the total pressure waveform is the combination of pressure waveforms in each direction multiplied by a phase factor.

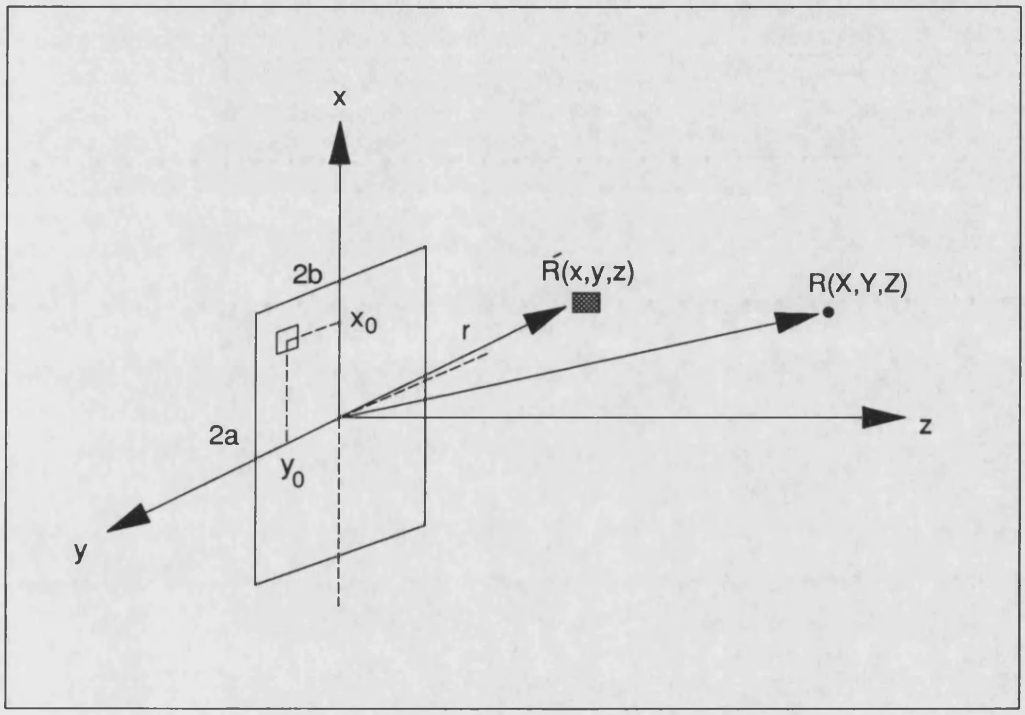

Figure 4.3 Geometry of the rectangular source and the coordinate system used for the perturbation method.

We can now work on the second harmonic generation in the field of a rectangular source. It is obvious that the on the right hand side of the equation 4.26 can be regarded as a source term giving rise to spherical sources of second harmonic in the fundamental field and this can be written in terms of the velocity potential in integral form as [86],

$$\Phi_2(\underline{R}) = \frac{1}{4\pi}\int\int\int q_s(\underline{R}')\frac{e^{-j\underline{K}\underline{R}}}{|\underline{R}|}dv \qquad 4.38$$

where dv is the volume element, K is the wave vector for the second harmonic field with $|\underline{K}| = 2k$ and

$$q_s(\underline{R}') = -j\frac{k^3\beta}{c_0}\Phi_1^2(\underline{R}') \qquad 4.39$$

where $\underline{R}'$ is the vector to the second harmonic source point and $\underline{R}$ is the vector to the field point. As the second term in the integrand of Equation 4.38 has spherical symmetry, it is therefore natural to solve the problem by expanding the spherical wave in plane waves [86]. In its most basic form, the plane wave spectrum of a spherical wave is the double Fourier transform of the spherical wave and for $z \geq 0$ we get [86]

$$\frac{e^{-j\underline{K}\underline{R}}}{|\underline{R}|} = -\frac{j}{2\pi}\int_{-\infty}^{\infty}\int_{-\infty}^{\infty}[e^{-j\underline{K}\underline{R}}]\frac{dK_x dK_y}{dK_z} \qquad 4.40$$

where K_x, K_y, K_z are the components of the second harmonic wave vector in directions x, y, z respectively. With this plane wave expansion and substituting Equation 4.39 into Equation 4.38 we get

$$\Phi_2(\underline{R}) \cong -\frac{j}{8\pi^2}\int_{-\infty}^{\infty}\int_{-\infty}^{\infty} e^{-j\underline{K}\underline{R}}\frac{dK_x dK_y}{K_z}\int_{z=0}^{Z}\int_{-\infty}^{\infty}\int_{-\infty}^{\infty} q_s(\underline{R}')e^{j\underline{K}\underline{R}'}dx\,dy\,dz \qquad 4.41$$

Substitution for $q_s(\underline{R}')$, this expression becomes

$$\Phi_2(\underline{R}) \cong -\frac{k\beta u_0^2}{32\pi^2 c_0}\int_0^Z e^{-j2kz}dz\int_{-\infty}^{\infty}\int_{-\infty}^{\infty} e^{-j\underline{K}\underline{R}}\frac{dK_x dK_y}{K_z}$$

$$\int_{-\infty}^{\infty}\int_{-\infty}^{\infty} e^{j\underline{K}\underline{R}'}f(x)g(x)dx\,dy \qquad 4.42$$

with

$$f(x) \equiv \left\{\int_{t_1}^{t_2} e^{-j\frac{\pi}{2}t^2}dt\right\}^2 \qquad 4.43$$

and

$$g(y) \equiv \left\{\int_{q_1}^{q_2} e^{-j\frac{\pi}{2}q^2}dq\right\}^2 \qquad 4.43$$

Also noting that $\underline{K}.\underline{R} = K_z Z + K_x X + K_y Y$ and $\underline{K}.\underline{R}' = K_x x + K_y y + K_z z$ we may rewrite Equation 4.42 in the form

$$\Phi_2(\underline{R}) \cong -\frac{k\beta u_0^2}{32\pi^2 c_0}\int_0^Z e^{-j2kz}dz\int_{-\infty}^{\infty}\int_{-\infty}^{\infty} e^{-jK_z(Z-z)}e^{-jK_x X}e^{-jK_y Y}dK_x\frac{dK_y}{K_z}$$

$$\int_{x=-\infty}^{\infty} e^{jK_x x}f(x)dx\int_{y=-\infty}^{\infty} e^{jK_y y}f(y)dy \qquad 4.45$$

If we define integrals for x and y as $F(K_x)$ and $G(K_y)$, then we have

$$F(K_x) = \int_{-\infty}^{\infty} e^{jK_x x} f(x)dx \qquad 4.46$$

and

$$G(K_y) = \int_{-\infty}^{\infty} e^{jK_y y} g(y)dy \qquad 4.47$$

As we recognize that the Equations 4.46 and 4.47 are of the Fourier transform integral forms which could be evaluated using F.F.T techniques. In order to simplify the Equation 4.45, we use the parabolic approximation [20] for K_z, i.e,

$$K_z \approx 2k - \frac{K_x^2 + K_y^2}{4k} \qquad 4.48$$

and

$$\frac{1}{K_z} \approx \frac{1}{2k} \qquad 4.49$$

Then we have,

$$\Phi_2(\underline{R}) \approx -\frac{\beta u_0^2}{64\pi^2 c_0} e^{-j2kZ} \int_0^Z dz$$

$$\int_{-\infty}^{\infty}\int_{-\infty}^{\infty} e^{j\frac{K_x^2+K_y^2}{4k}(Z-z)} e^{-jK_x X} e^{-jK_y Y} F(K_x)G(K_y)dK_x dK_y \qquad 4.50$$

Grouping the terms in x and y we get

$$\Phi_2(\underline{R}) \approx -\frac{\beta u_0^2}{64\pi^2 c_0} e^{-j2kZ} \int_0^Z dz \left\{ \int_{-\infty}^{\infty} e^{j\frac{K_x^2}{4k}(Z-z)} e^{-jK_x X} F(K_x) dK_x \right\}$$

$$\left\{ \int_{-\infty}^{\infty} e^{j\frac{K_y^2}{4k}(Z-z)} e^{-jK_y Y} G(K_y) dK_y \right\} \qquad 4.51$$

The integrals in K_x and K_y in Equation 4.51 are the inverse Fourier transform integrals and could be evaluated using NAG library and F.F.T algorithms. In order to facilitate the computations further, it would be useful to obtain analytical expressions for $F(K_x)$ and $G(K_y)$. This is considered in Appendix 1 and the result is given in the form

$$F(K_x) = \frac{2\sqrt{2}}{K_x} e^{j\frac{\pi}{4}} e^{j\frac{z}{2k}K_x^2} F_0(K_x) \qquad 4.52$$

and

$$G(K_y) = \frac{2\sqrt{2}}{K_y} e^{j\frac{\pi}{4}} e^{j\frac{z}{2k}K_y^2} G_0(K_y) \qquad 4.53$$

where

$$F_0(K_x) = e^{jK_x a} sgn(A+B) \int_0^{A+B} e^{-j\frac{\pi}{2}t^2} dt +$$

$$e^{-jK_x a} sgn(A-B) \int_0^{A+B} e^{-j\frac{\pi}{2}t^2} dt - 2\cos(K_x a) sgn(A) \int_0^{A} e^{-j\frac{\pi}{2}t^2} dt \qquad 4.53$$

and

$$G_0(K_y) = e^{jK_y b} sgn(A+B) \int_0^{A+B} e^{-j\frac{\pi}{2}q^2} dq +$$

$$e^{-jK_y b} sgn(A-B) \int_0^{A+B} e^{-j\frac{\pi}{2}q^2} dq - 2\cos(K_y b) sgn(A) \int_0^{A} e^{-j\frac{\pi}{2}q^2} dq \qquad 4.54$$

with

$$A = \sqrt{\frac{z}{2\pi k}} K_x \qquad B = \sqrt{\frac{2ka^2}{\pi z}} \tag{4.55}$$

For a square transducer, normalisation of the result is straightforward and we use:

$$K_x a = \omega \qquad \frac{z}{a} = \eta$$

$$X' = \frac{X}{a} \qquad Y' = \frac{Y}{b} \tag{4.66}$$

$$Z' = \frac{Z}{a} \qquad ka = M$$

Then, in terms of normalised coordinates, A, B and $F_0(K_x)$ become

$$A = \sqrt{\frac{\eta}{2\pi M}}\omega, \qquad B = \sqrt{2\frac{M}{\pi\eta}} \tag{4.67}$$

and

$$F_0(\omega) = e^{j\omega} sgn(A+B) \int_0^{A+B} e^{-j\frac{\pi}{2}t^2} dt$$

$$+e^{-j\omega} sgn(A-B) \int_0^{A-B} e^{-j\frac{\pi}{2}t^2} dt - 2\cos(\omega) sgn(A) \int_0^{A} e^{-j\frac{\pi}{2}t^2} dt \tag{4.68}$$

Therefore, the result for a square transducer becomes

$$\Phi_2(\underline{R'}) = -j\frac{\beta u_0^2 a}{8\pi^2 c_0} e^{-j2kZ} \int_0^{Z'} d\eta \left\{ \int_{-\infty}^{\infty} e^{j\frac{\omega^2}{4M}(Z'+\eta)} e^{-j\omega X'} \frac{F_0(\omega)}{\omega} d\omega \right\}$$

$$\left\{ \int_{-\infty}^{\infty} e^{j\frac{\omega^2}{4M}(Z'+\eta)} e^{-j\omega Y'} \frac{F_0(\omega)}{\omega} d\omega \right\} \tag{4.69}$$

However, in order to avoid any singularity, we need to consider the behaviour of $F_0(\omega)/\omega$ term in the infinite integrals in Equation 4.69 and this is given in Appendix 2. The infinite integral can then be written;

$$\int_{-\infty}^{\infty} e^{j\frac{\omega^2}{4M}(Z'+\eta)} e^{-j\omega X'} \frac{F_0(\omega)}{\omega} d\omega = 2\int_0^{\infty} e^{j\frac{\omega^2}{4M}(Z'+\eta)} \frac{F_0(\omega)}{\omega} \cos(\omega X') d\omega \qquad 4.70$$

As a result, we only need to compute

$$\Phi_2(\underline{R}) = -j\frac{\beta u_0^2 a}{2\pi c_0} e^{-j2kZ} \int_0^{Z'} d\eta \left\{ \int_0^{\infty} e^{j\frac{\omega^2}{4M}(Z'+\eta)} F_0(\omega)\cos(\omega X')\frac{d\omega}{\omega} \right\}$$
$$\left\{ \int_0^{\infty} e^{j\frac{\omega^2}{4M}(Z'+\eta)} F_0(\omega)\cos(\omega Y')\frac{d\omega}{\omega} \right\} \qquad 4.71$$

,which still requires heavy computational effort, however, it allows for understanding of the general characteristics of the second harmonic component due to a rectangular source at moderate amplitudes. The solutions break down when the second harmonic amplitude becomes comparable with fundamental amplitude.

4.8 EXAMPLE CALCULATIONS

The axial fields of rectangular apertures are used here as an example to illustrate general behaviour of the linear and nonlinear pressure field of plane and focused rectangular apertures. For the clarity, axial pressures are presented, in terms of magnitudes and a few across axis plots are presented for the linear case.

4.8.1 Linear field of plane rectangular apertures

Figure 4.4 shows the calculated pressure field distribution on the acoustic axis of a plane square transducer of size 30 x 30 mm. The linear theory predicts usual near field oscillations close to the aperture, a last minima at about 190 mm and a last maxima at about 500 mm from the aperture. Notice that the oscillations close to the aperture are similar to those of a circular source but the amplitude of the last axial maxima is not equal to twice the level of the on-souce amplitude and the minima are not zero as in the circular case.

Figure 4.5 presents the predicted axial pressure field of a 15 x 25 mm rectangular source and shows that the last axial maxima is smaller than the penultimate one. This depends on the ratio of the aperture size in each direction and is a result of the different contributions from each axis of the aperture.

Typical across axis pressure variations for a 30 x 30 mm square aperture are presented in Figure 4.6 (at z=50 mm) and in Figure 4.7 (at z=200 mm). Figure 4.8 (at z=50 mm) and Figure 4.9 (at z=200 mm) show that the nearfield region is narrower in the case of rectangular aperture than 30 x 30 mm square aperture. This is an expected result of the rectangular aperture as the aperture size in x direction is reduced to 15 mm.

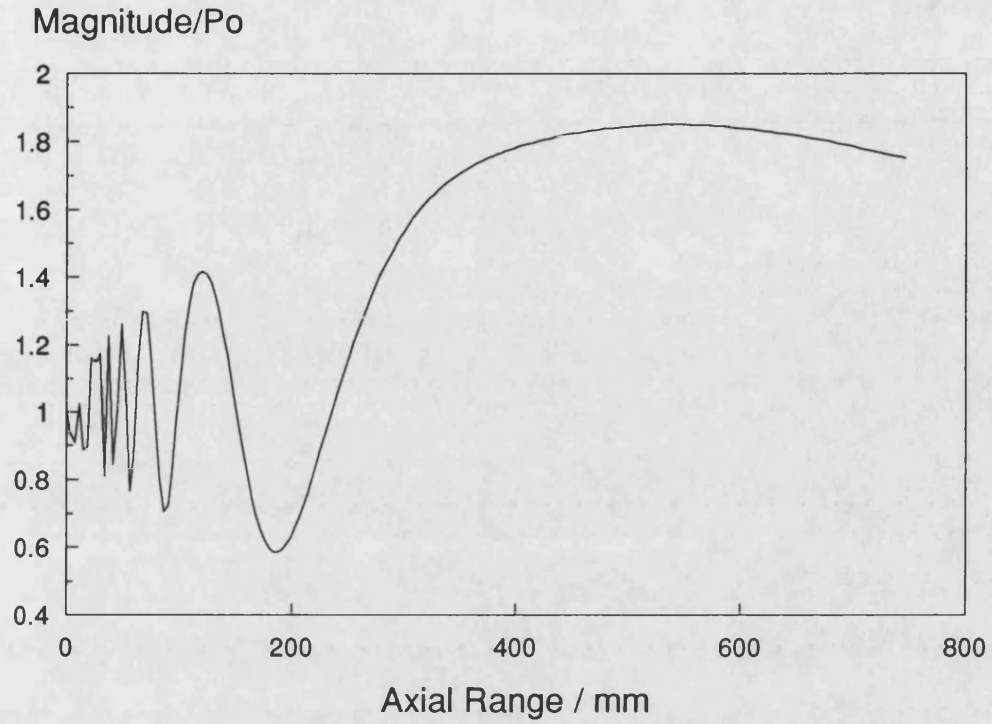

Figure 4.4 Axial pressure field of a plane square (a=30 mm, b=30 mm) transducer, f_0=2.25 MHz, p_0=10 kPa, Number of points (N)=500.

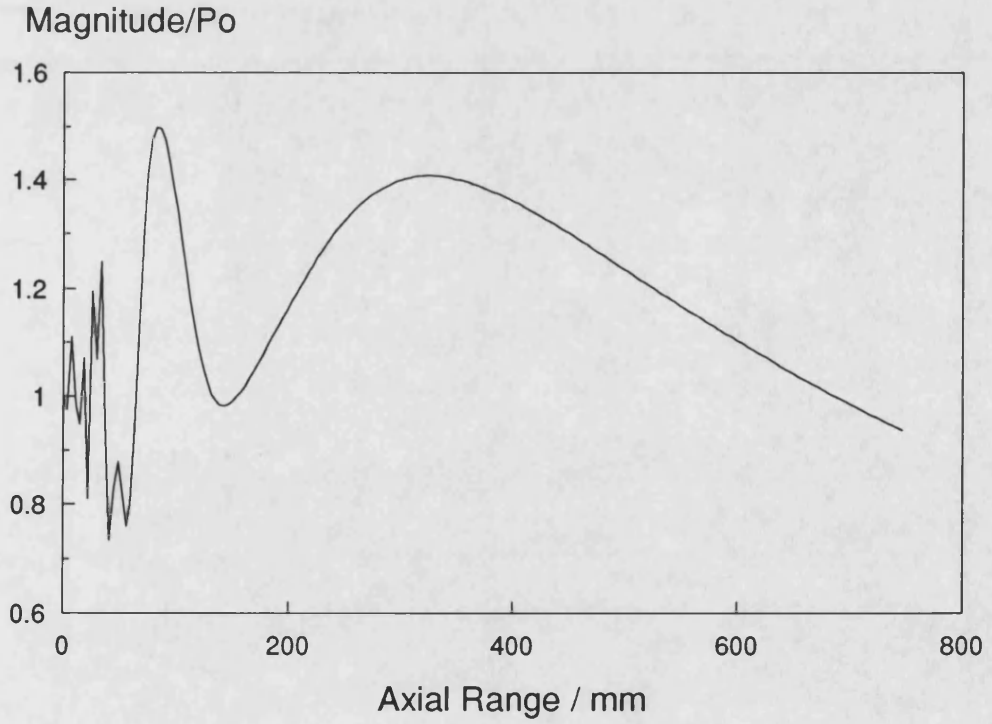

Figure 4.5 Axial pressure field of a plane rectangular (a=15 mm, b=25 mm) transducer, f_0=2.25 MHz, p_0=10 kPa, N=500.

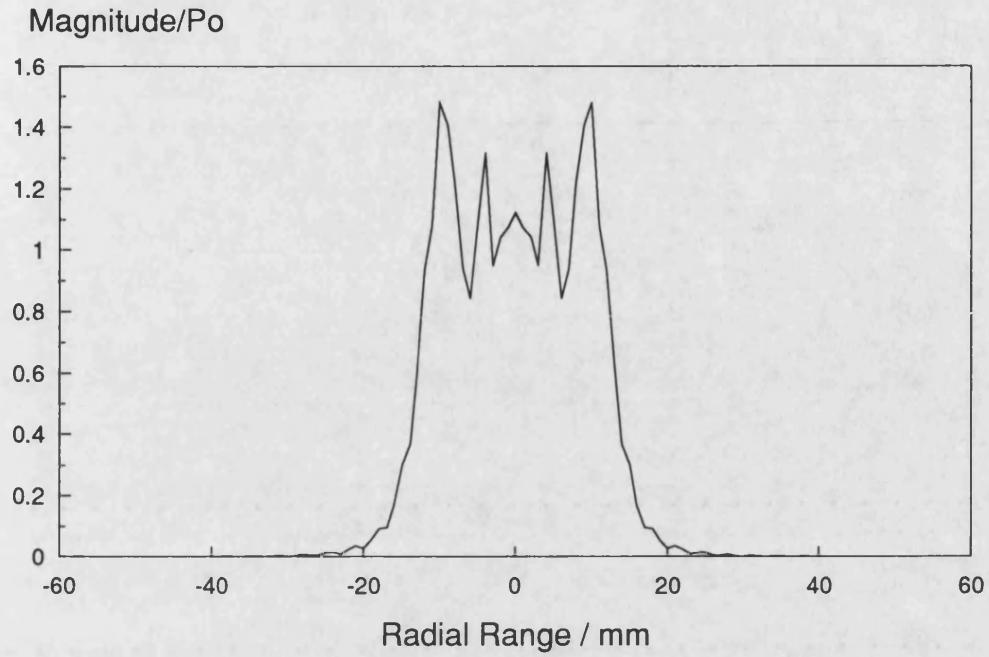

Figure 4.6 Across axis pressure field of a plane square (a=30 mm, b=30 mm) aperture 50 mm away from the source, f_0=2.25 MHz, p_0=10 kPa, N=99.

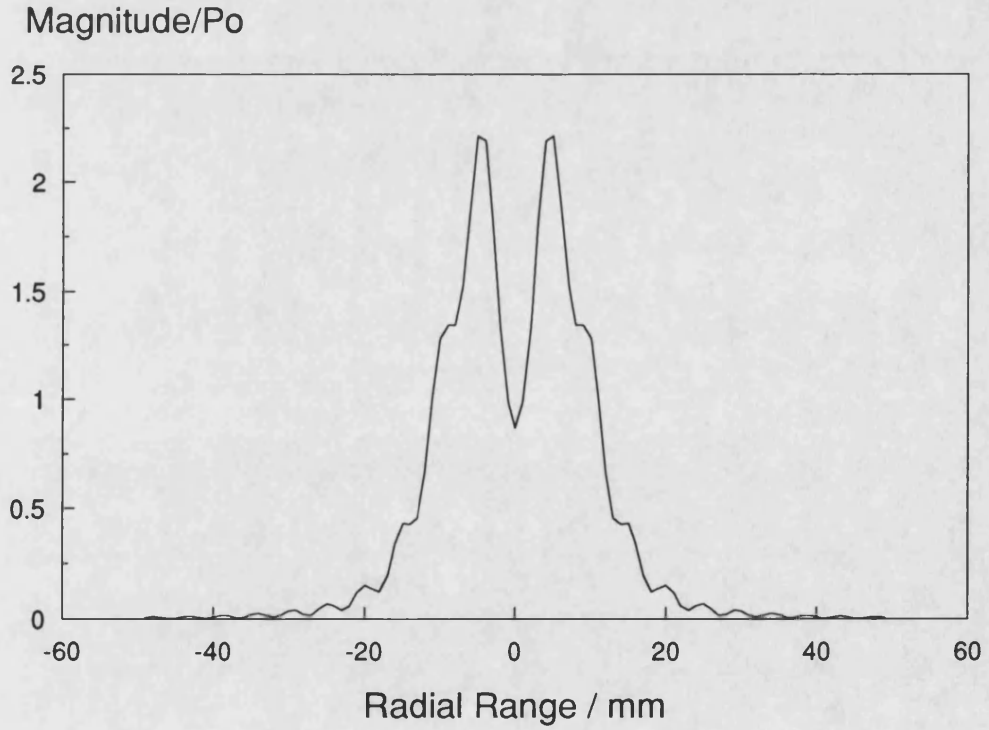

Figure 4.7 Across axis pressure field of a plane square (a=30 mm, b=30 mm) aperture 200 mm away from the source, f_0=2.25 MHz, p_0=10 kPa, N=99.

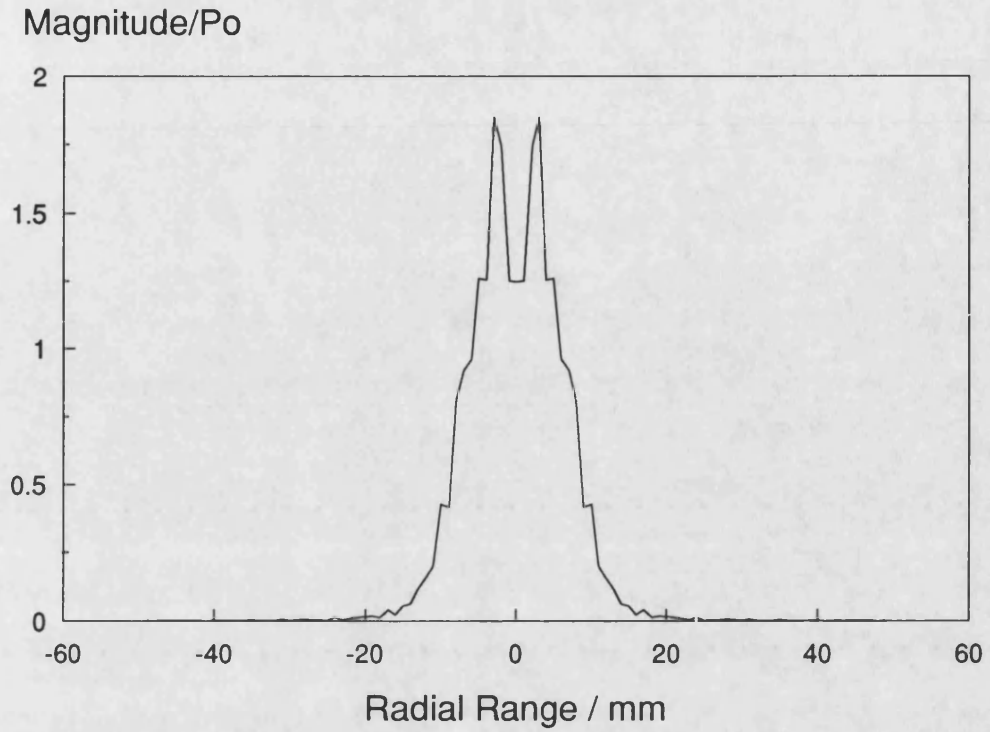

Figure 4.8 Across axis pressure field of a plane rectangular (a=15 mm, b=25 mm) aperture 50 mm away from the source, f_0=2.25 MHz, p_0=10 kPa, N=99.

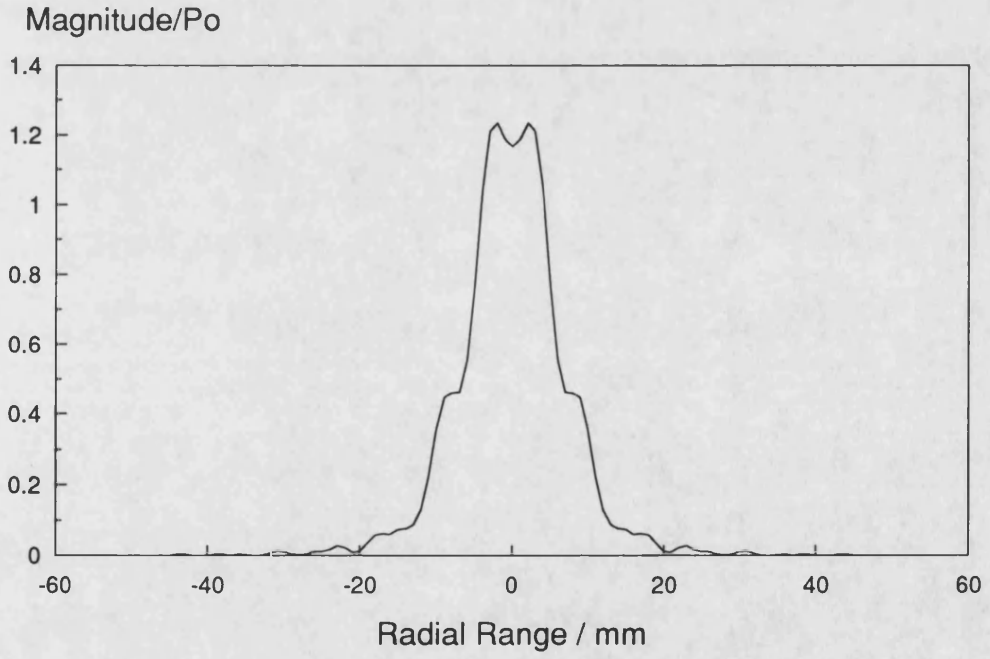

Figure 4.9 Across axis pressure field of a plane rectangular (a=15 mm, b=25 mm) aperture 200 mm away from the source, f_0=2.25 MHz, p_0=10 kPa, N=99.

4.8.2 Linear field of focused rectangular apertures

Figure 4.10 illustrates two dimensional focusing (F_x=F_y=160 mm) for a square aperture of 30 mm size. The plot shows that theory predicts a last maxima at about the focal plane and oscillations close to the aperture are smaller in amplitude and shifted toward the aperture in comparison with the plane piston case of the same aperture (Figure 4.4). Figure 4.11 confirms that the beam is quite narrow around the focal plane for the same square aperture and the side lobes are smaller in amplitude comparison with the unfocused case.

One dimensional focusing (F_x=50 mm) for a 15 x 25 mm rectangular aperture is shown in Figure 4.12 for axial pressure field and in Figure 4.13 for the across axis pressure field (z=50 mm). It is obvious from Figure 4.13 that the main lobe and the side lobes at each side of the axis are not well pronounced. This is a result of small number of points used in the calculations.

4.8.3 Nonlinear pressure field of rectangular apertures

Nonlinear pressure field results are only presented in terms of axial pressure fields since the theory is not able to predict the transverse nonlinear pressure fields of rectangular apertures. The fundamental frequency (f_0), attenuation coefficient (α) for the water, and the speed of sound (c) for the water were the same for all the nonlinear calculations and had the values, 2.25 MHz, 0.0562 Npm^{-1}, and 1480 m/s respectively. Additional parameters are presented below each plot.

Figure 4.14 is the predicted axial pressure field of a plane square transducer of 25 x 25 mm at 150 kPa. The plot shows the first three harmonics but the axial variations in the second and third harmonic are not clear due to the lack of diffraction effects for the second and higher harmonic components. This effect is discussed in more

detail in chapter 5. Figure 4.15 shows the growth of the first three harmonics for 15 x 25 mm rectangular transducer focused only in y direction with a focal length of 160 mm. The first and the second harmonic axial variation calculated by the first order perturbation theory is presented in Figure 4.16 for a 30 x 30 mm plane square aperture. The first harmonic shows a steady fall off after its last axial maxima, however, the second harmonic does not fall off in comparison with the fundamental. The reason is that the transfer of energy from the fundamental stops after the second harmonic component and interactions between higher harmonics are ignored by the perturbation model. Especially, at the higher drive levels this becomes more obvious as the third and higher harmonics start growing up with increasing drive level.

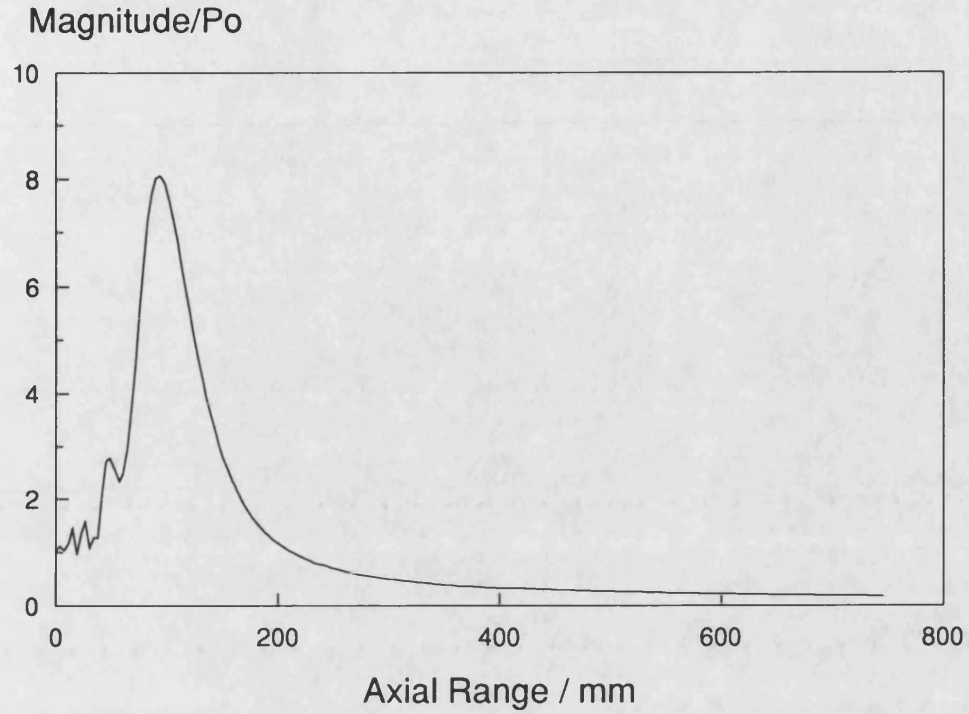

Figure 4.10 Axial pressure field of a focused square (a=30 mm, b=30 mm) aperture, f_0=2.25 MHz, p_0=10 kPa, F_x=100 mm, F_y=100 mm, N=500.

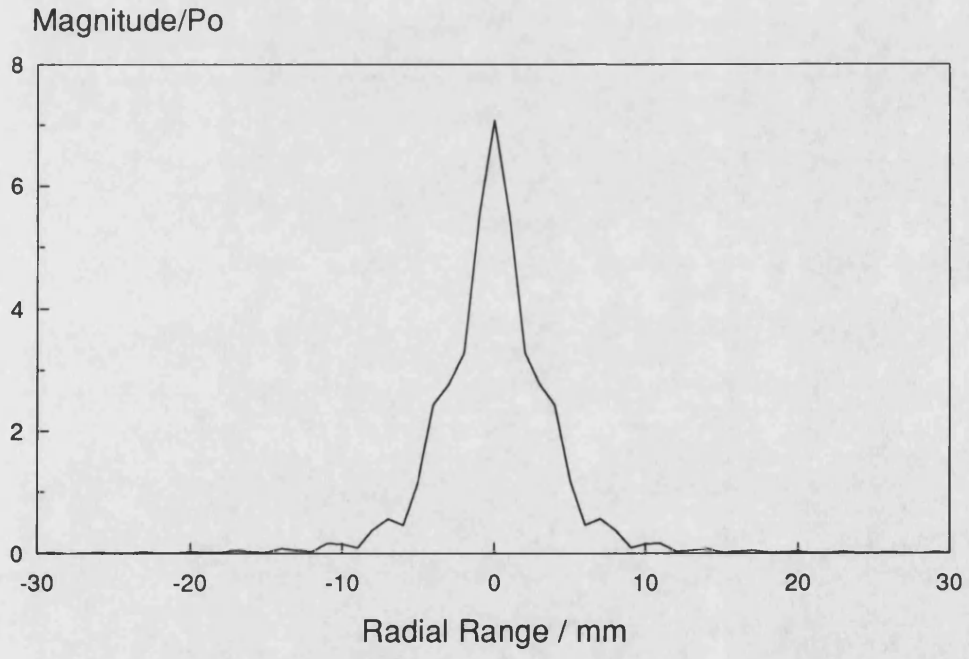

Figure 4.11 Across axis pressure field of a focused square (a=30 mm, b=30 mm) aperture 100 mm away from the source, f_0=2.25 MHz, p_0=10 kPa, F_x=100 mm, F_y=100 mm, N=99.

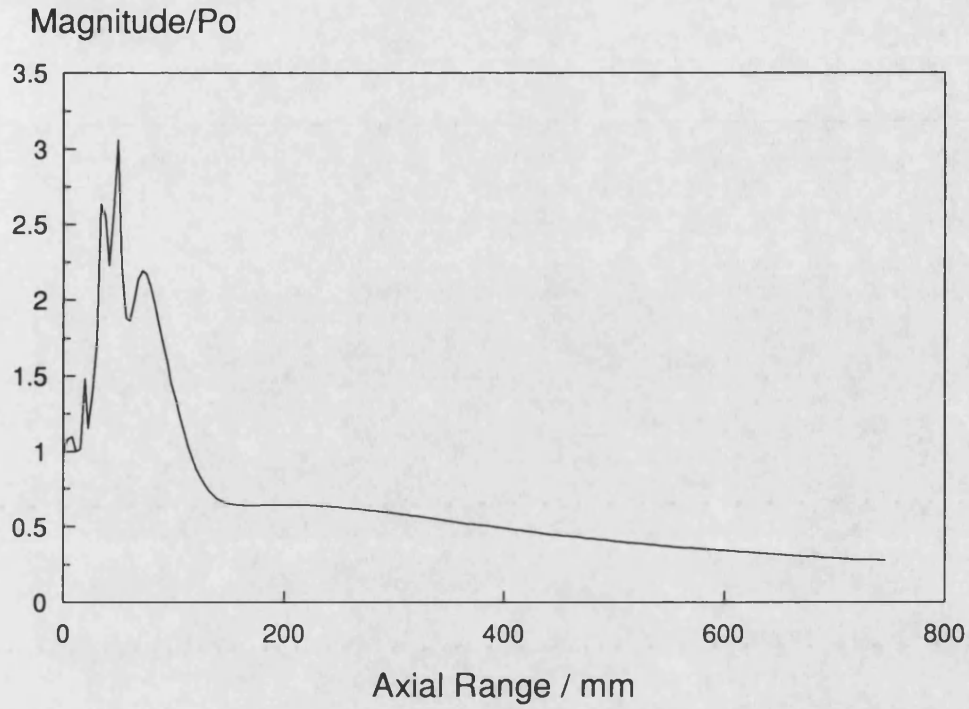

Figure 4.12 Axial pressure field of a focused rectangular (a=15 mm, b=25 mm) aperture, f_0=2.25 MHz, p_0=10 kPa, F_x=50 mm, F_y=unfocused, N=500.

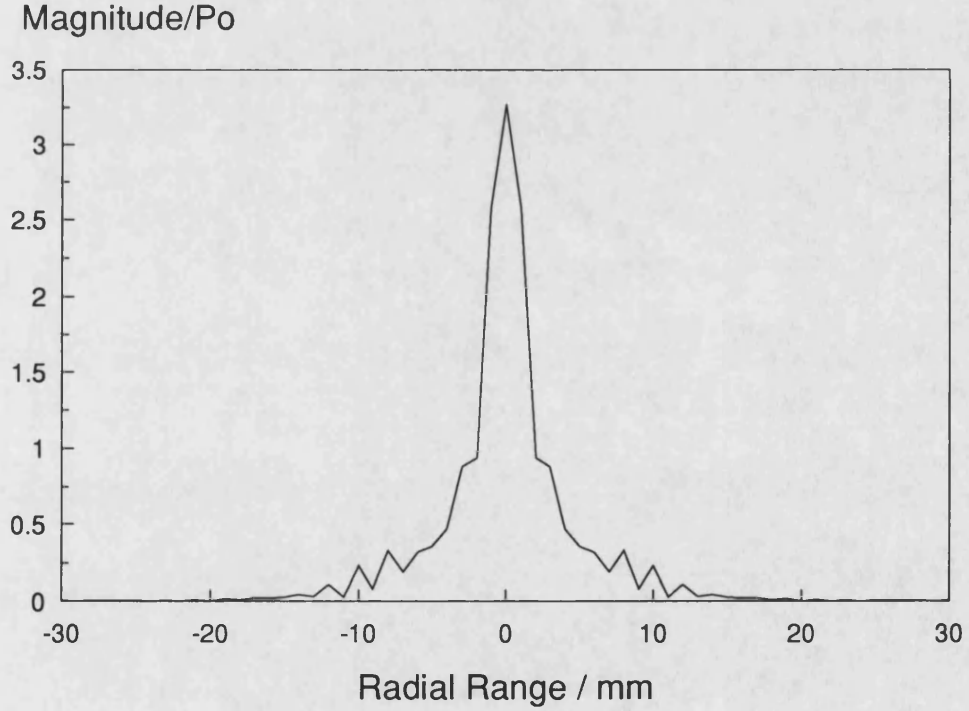

Figure 4.13 Across axis pressure field of a focused rectangular (a=15 mm, b=25 mm) aperture 40 mm away from the source. f_0=2.25 MHz, p_0=10 kPa, F_x=50 mm, F_y=unfocused, N=99.

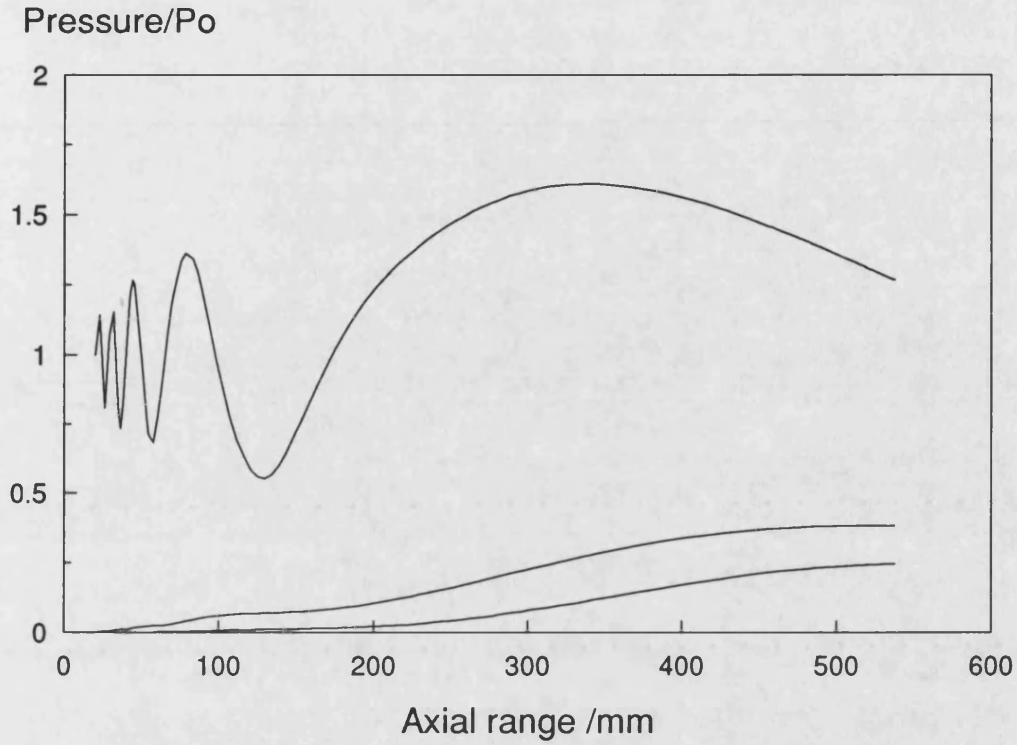

Figure 4.14 Axial nonlinear pressure field of a plane square (a=25 mm, b=25 mm) transducer as predicted by plane wave model.

The following parameters were used in the calculation:

Aperture size, a=25 mm, b=25 mm,

Pressure amplitude at the piston face, p_0=150 kPa,

Axial step size ,Δz=1.12 mm,

Number of harmonics retained, M=10,

Number of points, N=500

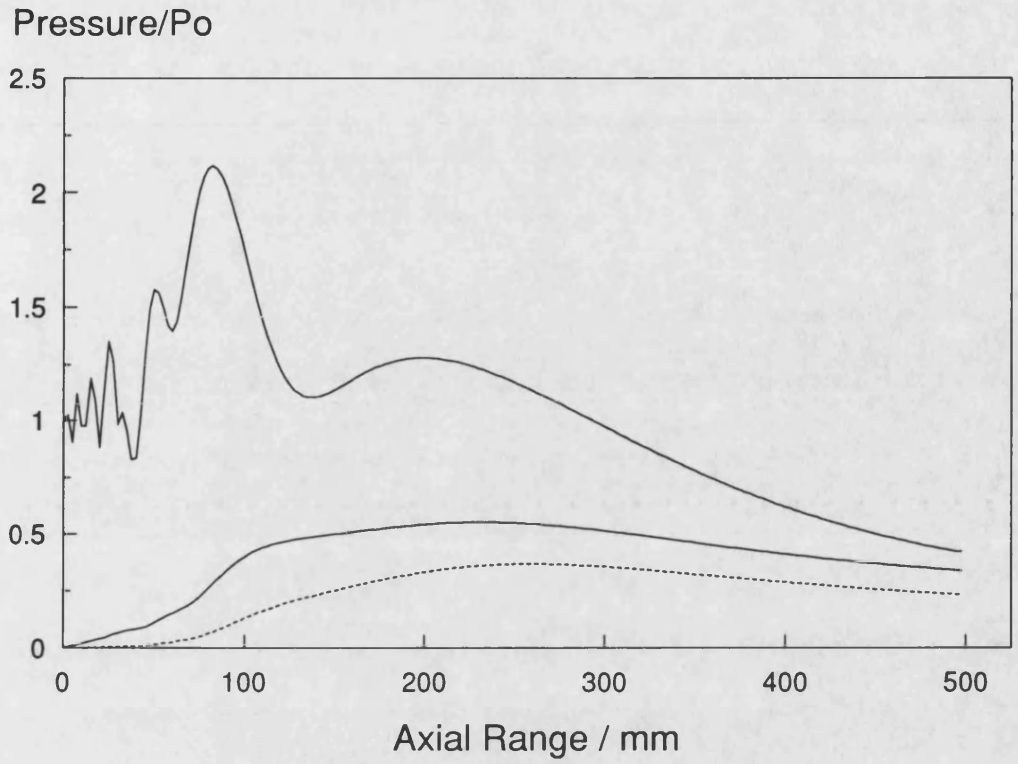

Figure 4.15 Axial nonlinear pressure field of a focused rectangular (a=15 mm, b=25 mm) transducer, as predicted by plane wave model.

The following parameters were used in the calculation:

Aperture size, a=15 mm, b=25 mm,

Pressure amplitude at the piston face, p_0=150 kPa,

Focal lengths: in x direction F_x=160 mm, in y direction F_y=unfocused,

Axial step size ,Δz=1 mm,

Maximum number of harmonics retained, M=10,

Number of points, N=500

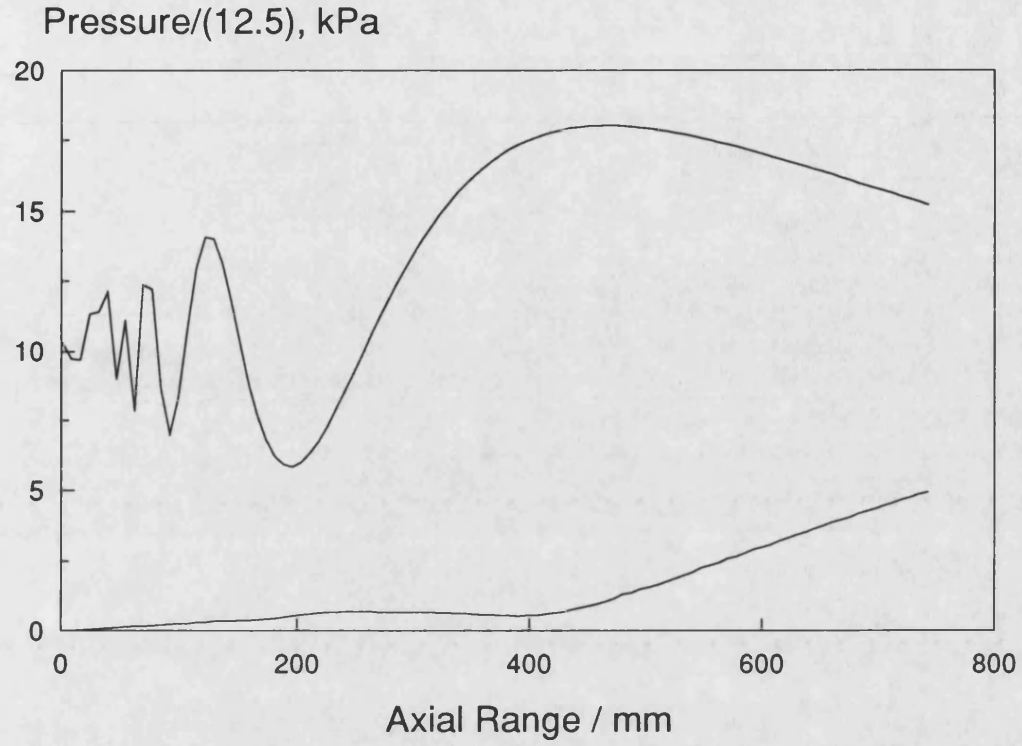

Figure 4.16 Axial nonlinear pressure field of a plane square (a=30 mm, b=30 mm) transducer calculated by the perturbation method.

The following parameters were used in the calculation:

Aperture size, a=30 mm, b=30 mm,

Pressure amplitude at the piston face, p_0=125 kPa,

Axial step size ,Δz=1.5 mm

Number of points, N=500

CHAPTER 5

RESULTS AND DISCUSSION

5.1 INTRODUCTION

This chapter presents a number of results, mostly in the form of comparisons between experimental measurements and theoretical predictions. A large quantity of experimental and theoretical data was available for inclusion both for the linear and nonlinear case, however, in an attempt to make the thesis more readable only a limited number of results are included.

The first part of this chapter examines the small signal pressure fields of rectangular transducers along the acoustic axis, showing the agreement between the linear theory and experimental results. Next, the finite amplitude axial and transverse pressure fields of various size rectangular apertures are considered. The effect of focusing on the pressure field was studied with lenses of geometric focal lengths 160 mm and 250 mm, including focusing in one and two directions and both directions focused with different focal lengths. Finally, agreement with the perturbation results is discussed and some time domain waveforms are presented to highlight the distortion of the initial time waveform during its propagation in the pressure field of a plane rectangular transducer.

In general, experimental results are shown with square markers and theoretical curves are plotted as dotted lines since they vary more slowly in many cases. No error bars are shown but, in general, experimental results were subject to an error of about 10%.

5.2 SMALL SIGNAL FIELDS

Since the general structure of the pressure fields of rectangular transducers are not well known, it was sometimes necessary to go back to the circular case and compare its pressure field with those obtained from rectangular transducers. This assisted with interpretation of the results.

Figure 5.1 shows the typical pressure field distribution on the acoustic axis of a plane rectangular transducer of size a=20 mm and b= 25 mm, at 2.25 MHz and 10 kPa. Figure 5.2 presents the small signal, on axis pressure field variation of a 19 mm plane circular transducer at the same frequency and drive level. It is noticeable that the pressure amplitude of the circular source fluctuates between zero and twice the on-source pressure level P_0. This behaviour can be understood as a superposition of the edge wave and the centre wave of the circular transducer. If the waves are in phase, the resultant wave has an amplitude twice on-source level, and if there is a phase difference causing destructive interference, the resultant wave has the minimum amplitude which is zero. There is also a contribution to the acoustic axis pressure from the edges of the rectangular source but, there is never a full reinforcement or destruction of the on-source amplitude along the acoustic axis for the case of a rectangular aperture. That is why the pressure amplitude along the acoustic axis of a rectangular plane source fluctuates between a maximum smaller than twice the level on source and a minimum greater than zero.

It was also important to establish experimentally the small signal behaviour of the circular transducer used in conjunction with rectangular aperture before making nonlinear pressure field measurements. Earlier results with the same circular transducer by Baker [64] and

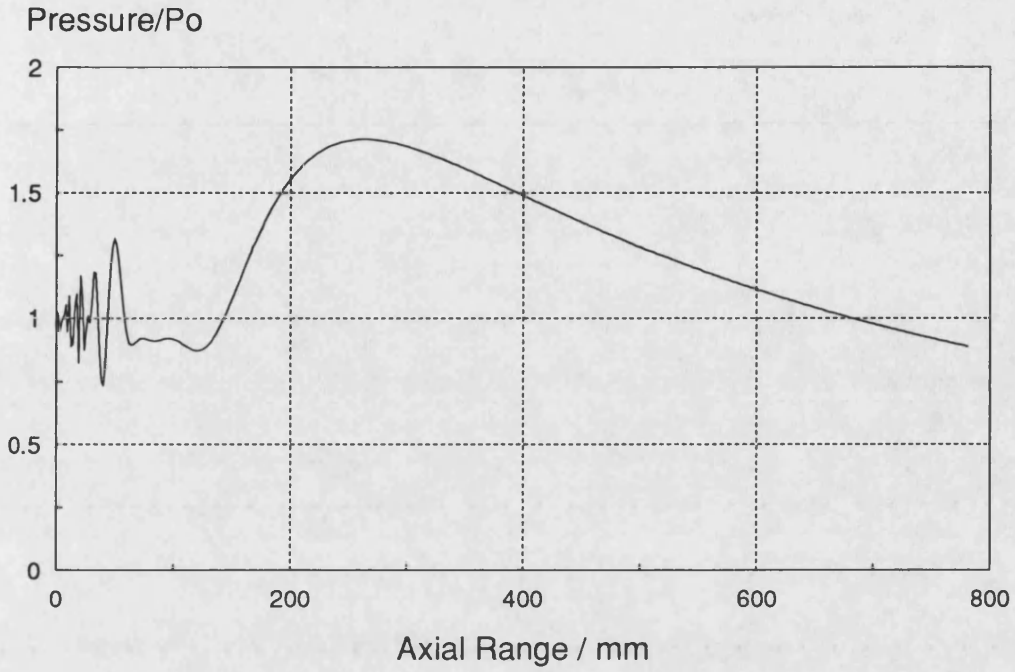

Figure 5.1 Axial pressure field of a plane rectangular aperture, a=20 mm, b=25 mm, f=2.25 MHz, P_0=10 kPa.

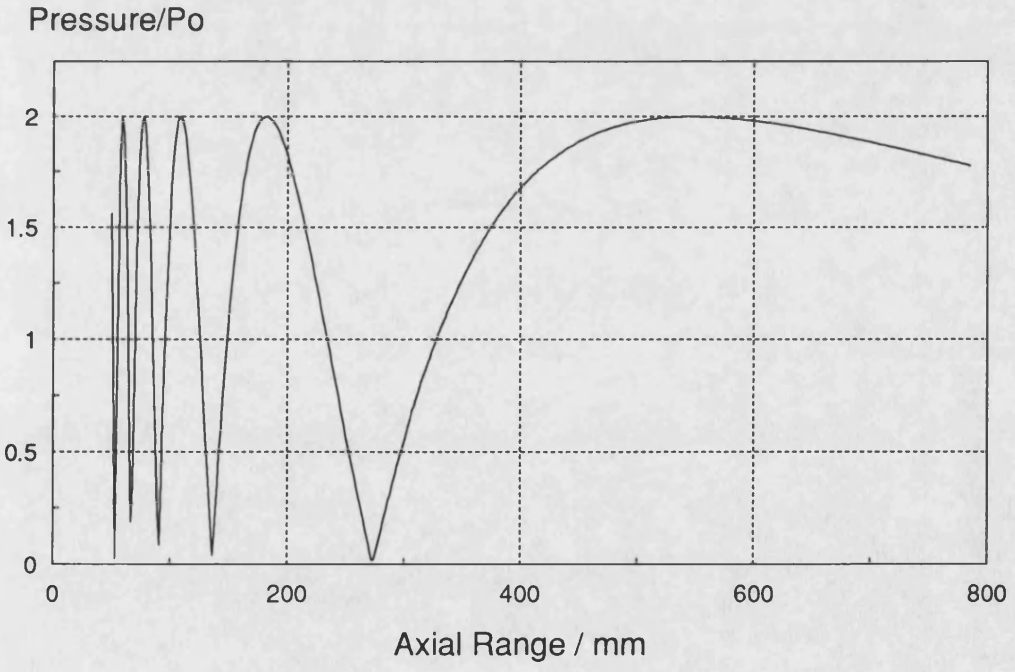

Figure 5.2 Axial pressure field of a plane circular transducer of 38 mm diameter, f=2.25 MHz, P_0=10 kPa.

measurements made for the rectangular case show that the plane circular transducer behaves as a perfect piston and that rectangular apertures generate the expected pressure field at low drive levels.

Figure 5.3 compares the theoretical axial pressure field with experimental measurements for a square aperture (25 x 25 mm) at a drive level of 75 kPa. The small signal theory (dotted lines) predicts usual near field oscillations close to the aperture, a final minima around 140 mm from the aperture face, a last maxima at about 300 mm and a steady decline into the far field. Experimental results (square markers) closely follow the theoretical predictions in the far field, nearer the aperture there are some discrepancies. This is attributed in part to inaccuracies in the experimental geometry and partly to diffraction losses.

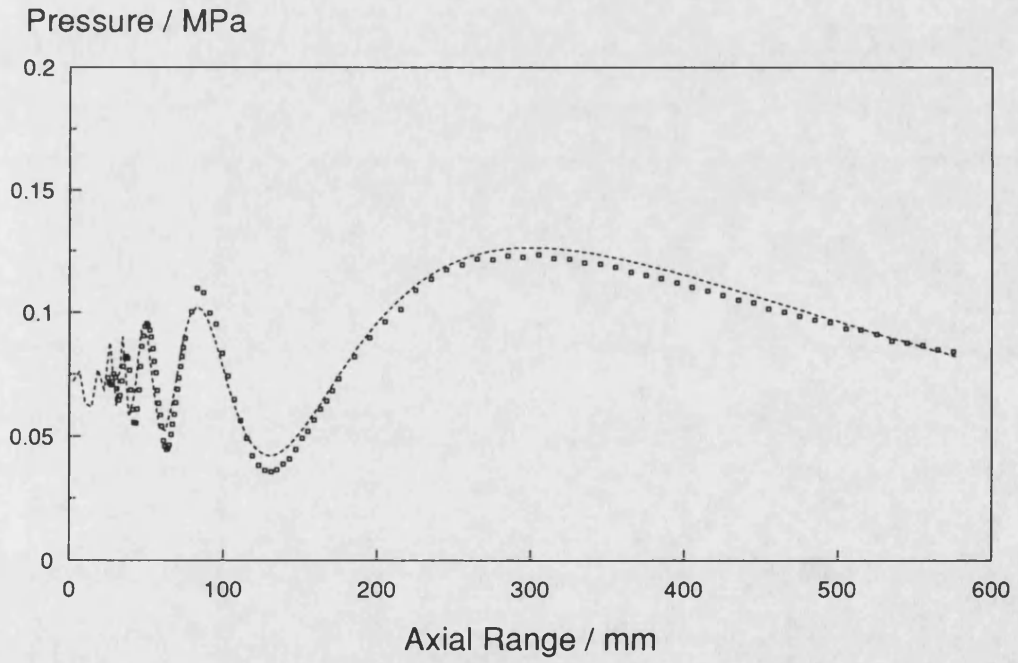

Figure 5.3 Comparison of theoretical fundamental with experimental measurement for a square aperture at 75 kPa, a=b=25 mm, f=2.25 MHz, Theory (dotted line), Experiment (markers).

As it has been discussed in Chapter 3, the magnitude of diffraction losses could be reduced by using a smaller hydrophone but this would lead to a reduction in hydrophone output due to a reduced sensitivity. It is worth noting that the diffraction losses were reduced in comparison with the circular case because the pressure field variations due to a rectangular source are less extreme. Thus the finite hydrophone size does not pose such severe problems when measuring pressure fields due to rectangular apertures.

In Figure 5.4, the measured pressure field distribution across the axis of the same square aperture is compared with theoretical predictions with the agreement better than 10%.

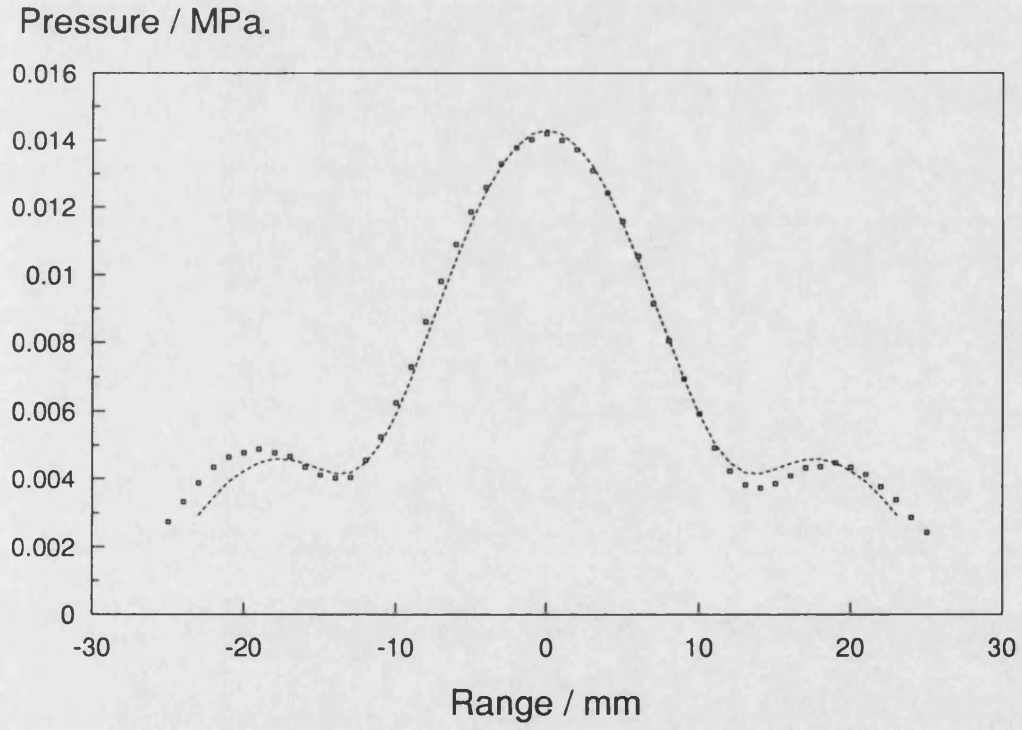

Figure 5.4 Comparison of across axis pressure field with measured experimental values, f=2.25 MHz, z=300 mm, Theory (dotted line), Experiment (markers).

Figure 5.5 - 5.10 show comparisons between measurements of the axial pressure field and corresponding theoretical predictions for different size of rectangular apertures. Figure 5.5 compares the results for 10 x 15 mm rectangular aperture at a drive level of 100 kPa. Although the theoretical predictions start close to the aperture, the experimental curve only starts at 25 mm away from the aperture face, due to limitations of the water tank and mountings used to hold the aperture and hydrophone. In general agreement between experiment and theory is good, the maximum discrepancy occurs at about 50 mm range and is about 15% , at longer ranges, the agreement is much better.

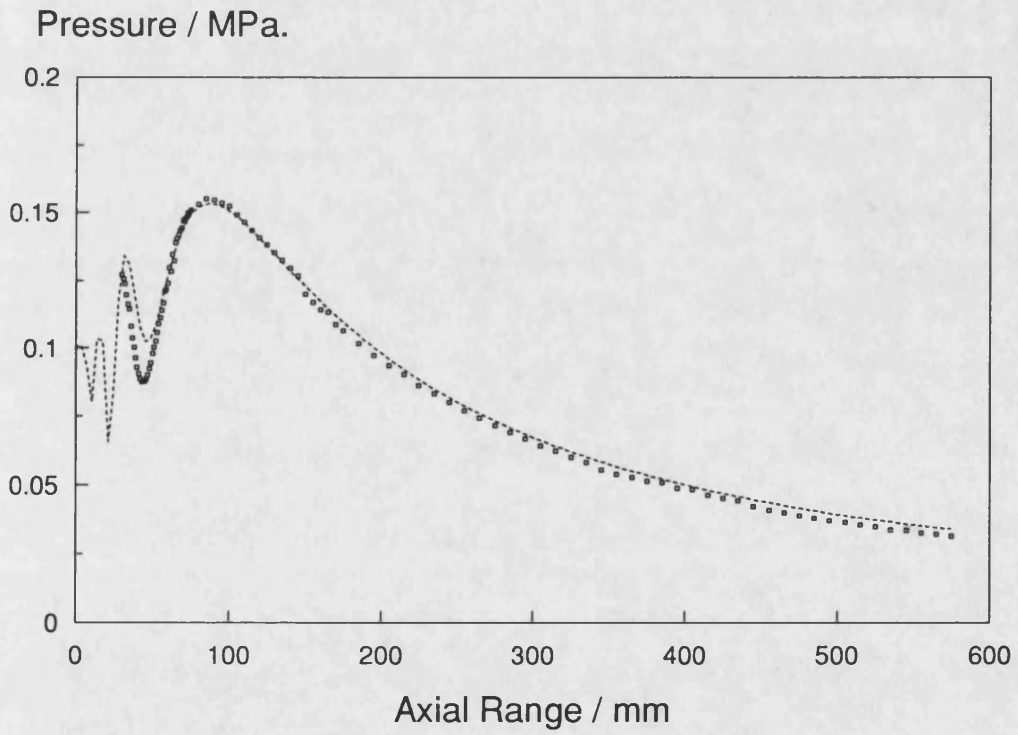

Figure 5.5 Comparison of theoretical axial pressure field with measured experimental values at 100 kPa, f=2.25 MHz, a=10 mm, b=15 mm. Theory (dotted line), Experiment (markers).

Comparison of results with focusing in one direction for the same aperture (10 x 15 mm) is given in Figure 5.6 for a geometric focus F_x=160 mm for the x plane of the aperture. Figure 5.7 shows results for an aperture of the same size using two perspex lenses focusing in the x and y planes both at the same distance, F_x=F_y=160 mm. It can be seen clearly that the difference in amplitudes of the final maxima is larger for two dimensional focusing case and in general the agreement is not as good as the single lens case. The difference in the amplitudes of the two maxima probably arises from errors in lens manufacture. It also appears that the peak pressures reduce for the one and two dimensional focusing in comparison with unfocused case, but this is partly due to a change in drive level.

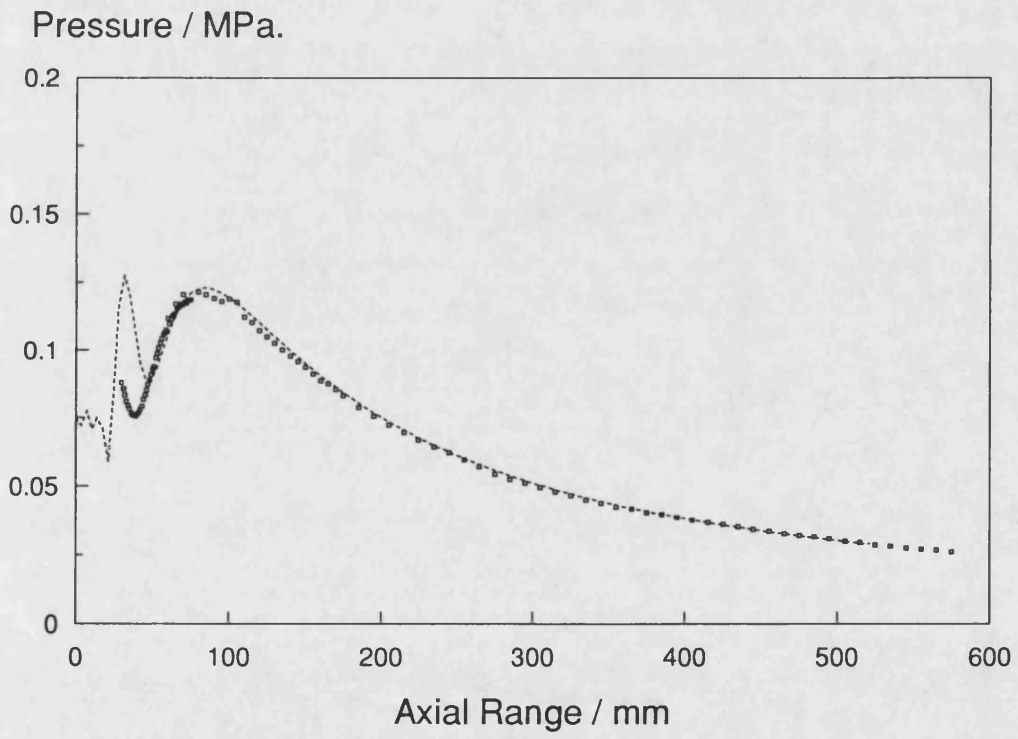

Figure 5.6 One dimensional focusing for a rectangular aperture, a=10 mm, b=15 mm, F_x=160 mm, f=2.25 MHz, P_0=75 kPa.

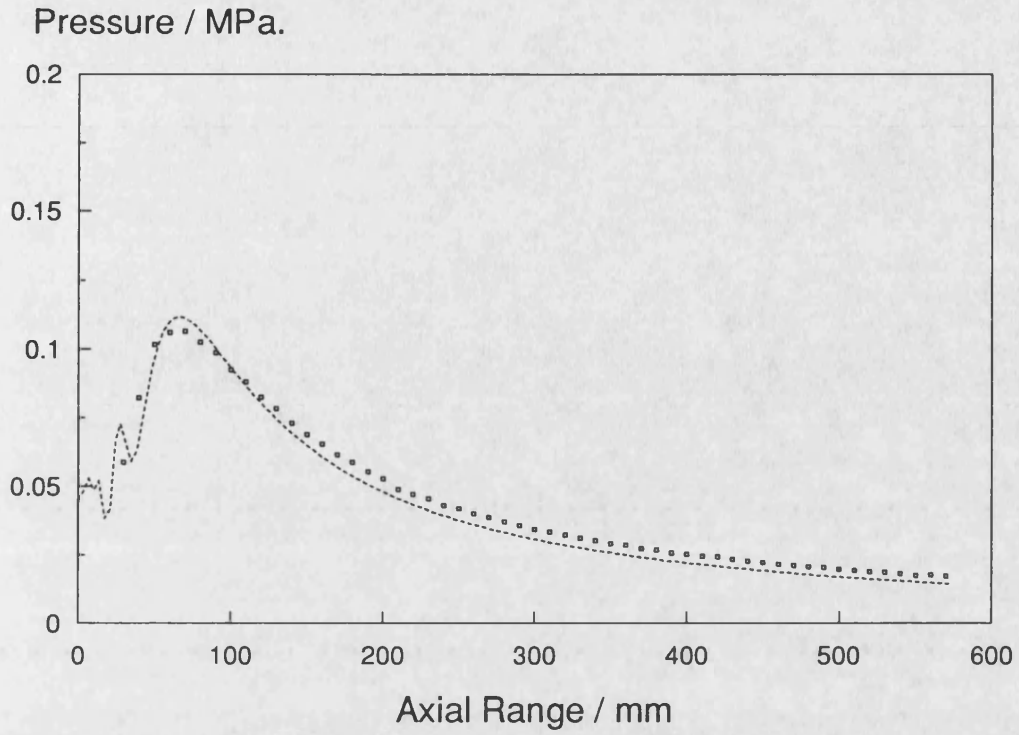

Figure 5.7 Two dimensional focusing for a rectangular aperture, a=10 mm, b=15 mm, F_x=160 mm, F_y=160 mm, f=2.25 MHz, P_0=40 kPa.

Figures 5.8, 5.9 and 5.10 relate to the axial field of an aperture 10 mm by 18 mm, unfocused and focused in one and two directions respectively. In all three cases the agreement is better than 10%. The unfocused case (Figure 5.8) shows the last axial maximum to be considerable smaller than the penultimate axial maximum in contrast the corresponding case for the 10 x 15 mm aperture (Figure 5.5), this highlights one of the advantages of the rectangular aperture, and in particular this method of generating such apertures; namely the ability to vary the pressure field distribution by relatively small changes in geometry. Figure 5.9 is the 10 x 18 mm aperture with a single lens added with a focal length of 160 mm, and Figure 5.10 has two such lenses added with the radii of curvature perpendicular to each other.

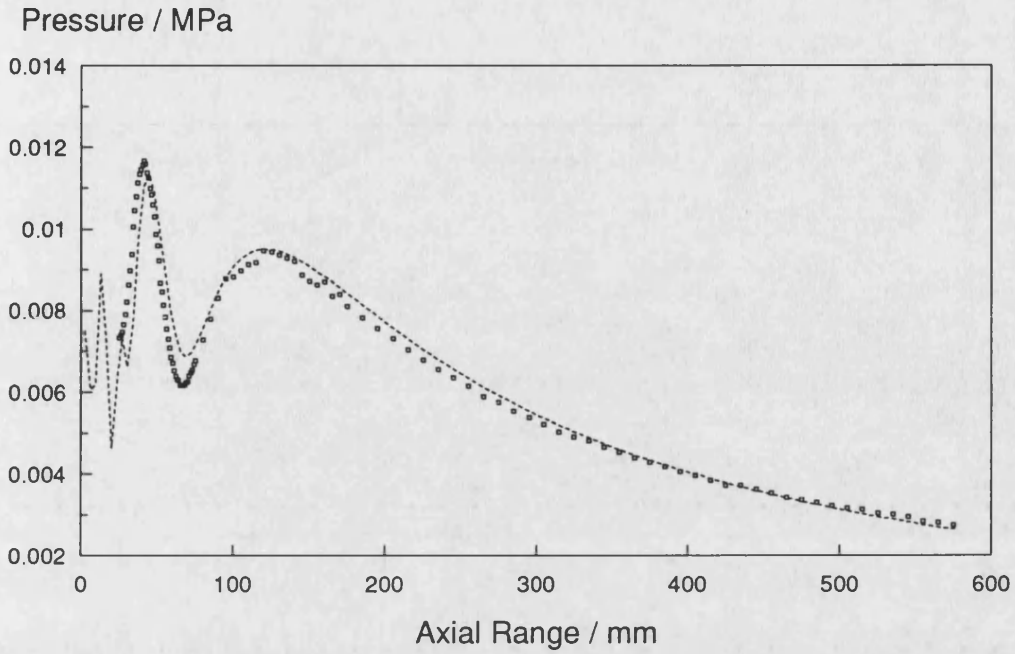

Figure 5.8 Comparison of theoretical axial pressure field with experimental measurements for a rectangular aperture, a=10 mm, b=18 mm, f=2.25 MHz. Theory (dotted lines), Experiment (markers), P_0=7.25 kPa.

It is evident that experimental results are reasonably consistent with theoretical predictions at this frequency and drive levels, much of the fine detail is accurately revealed by the experimental method implemented, even though the experimental measurements were made using adjacent apertures and lenses instead of "real" rectangular transducers.

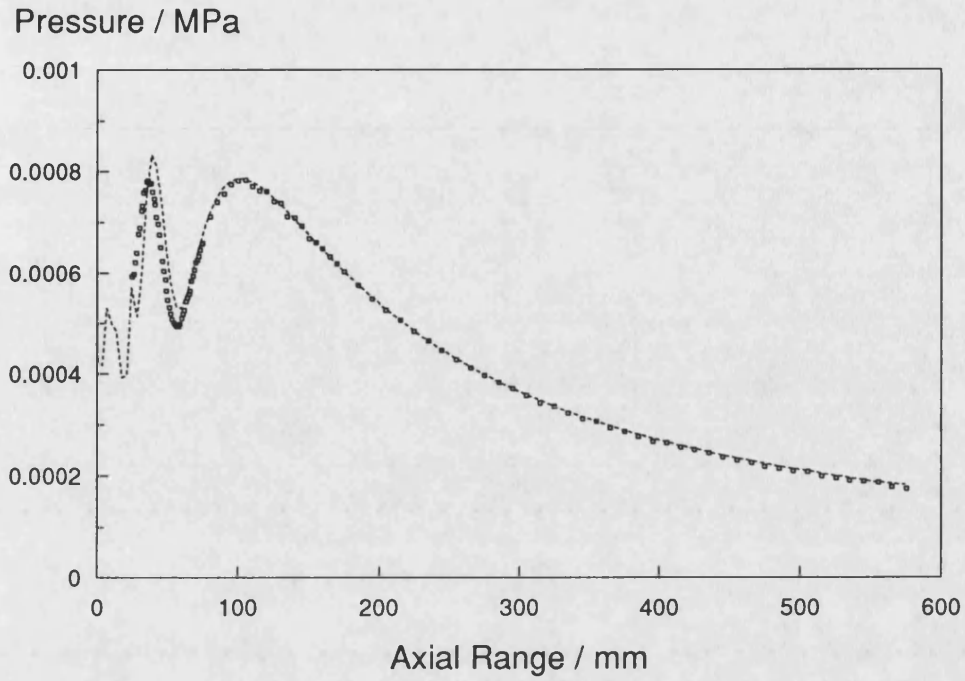

Figure 5.9 One dimensional focusing for a rectangular aperture, a=10 mm, b=18 mm, F_x=160 mm, f=2.25 MHz.

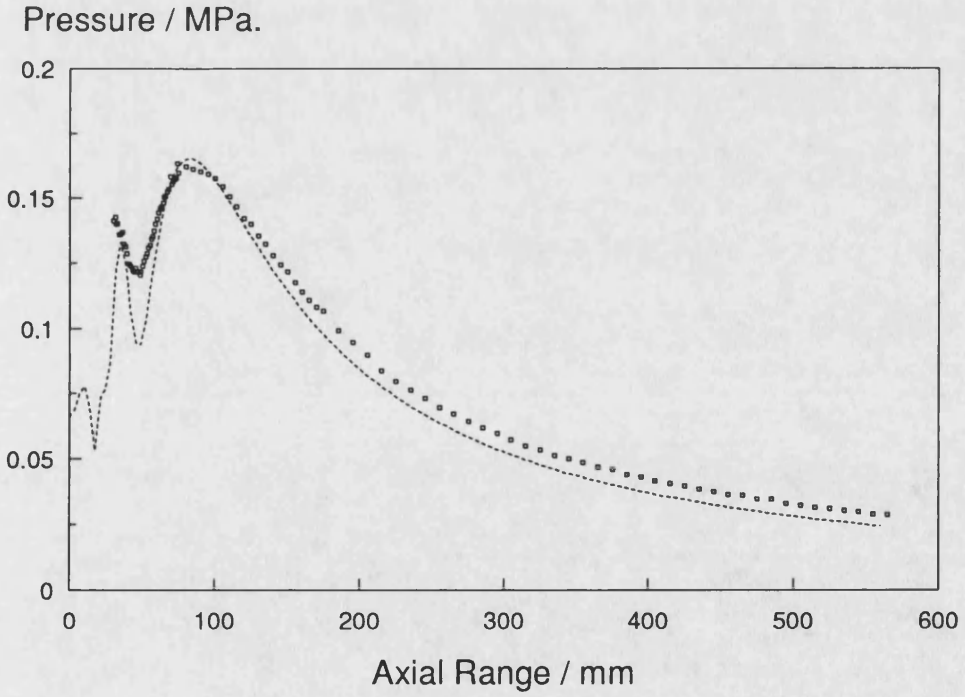

Figure 5.10 Two dimensional focusing for a rectangular aperture, a=10 mm, b=18 mm, F_x=F_y=160 mm, f=2.25 MHz.

5.3 FINITE AMPLITUDE FIELDS

5.3.1 Plane rectangular aperture

The finite amplitude pressure fields of plane rectangular transducers were studied with various apertures. A range of drive levels were used which allowed the harmonic generation to be understood more clearly as the growth of the harmonics strongly depends on the drive level at the source. Since it was difficult to measure the drive level in terms of the acoustic pressure at the source, drive levels were measured in terms of peak to peak voltage at the transducer corresponding 84 V at low drive level (DL1), next at 165 V (DL2) and the highest drive level at 350 V (DL3). At the lowest drive level, the measured amplitudes of higher harmonics become noisy due to low signal level.

Figures 5.11 - 5.14 show the experimental measurements made at each drive level for a plane square aperture of 25 mm size. At the low drive level (Figure 5.11), the harmonic generation observed at short ranges is negligibly small that means the harmonic generation observed is occurring as the wave propagates in the medium, not at the source. At this drive level, the last minimum of the fundamental frequency occurred at about 120 mm from the aperture face without immediate effect on the second harmonic which has its own last minimum at about 175 mm. It is noticeable that each minimum observed in the fundamental gives rise to a double minimum, one before and the other after a greater range creating more phase jump in the related harmonic phase. A steady fall off out into the far field started for all the harmonics after the last maximum of the fundamental at about 275 mm and at the maximum axial range (675 mm) the second, third, fourth and fifth harmonics reached their pressure level -7.62 dB, -12.51 dB, -16.57 dB, and -20.31 dB below the fundamental respectively. It is also noticable form Figure 5.11 that the fundamental phase shows

a marked maxima around 150 mm from the aperture face where the axial pressure starts increasing after the last axial minima and starts fall of into the far field. This is also true for the other harmonics and for each drive level.

At DL2, (Figure 5.12) the last maximum of the fundamental was about at the same pressure level with the penultimate maximum as more energy was transferred from the fundamental frequency to the higher harmonics with increasing drive level. The last minimums of each harmonic become more pronounced and each harmonic reached its own maximum more or less at the same axial range at about 340 mm where the fundamental has started decreasing. At this drive level the second harmonic was observed -5.94 dB, the third harmonic -9.51 dB, the fourth harmonic - 12.37 dB and the fifth harmonic was -14.43 dB below the fundamental at the maximum axial range 675 mm.

It was noticed that the last axial maximum of the fundamental has moved closer to the aperture at DL3 (Figure 5.13 and 5.14) in comparison with DL2, DL1 and with the small signal case. Instead of at 275 mm at DL1, at 250 mm at DL2 it has occurred at about 225 mm away from the source. This shift toward the aperture is due to the loss of energy at longer ranges caused by the built up of harmonics with increasing drive level.

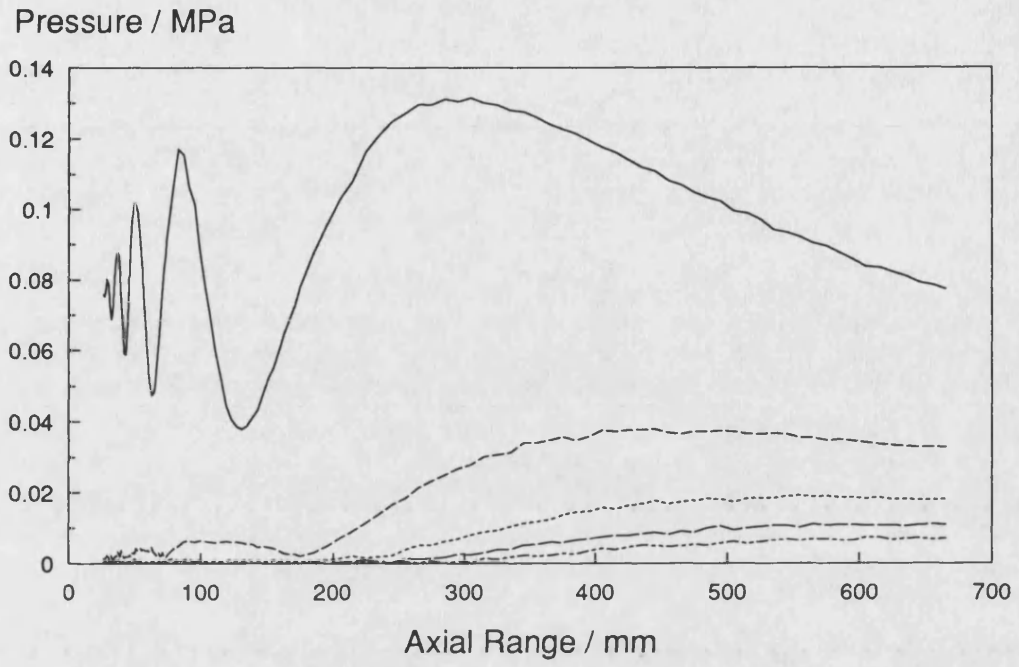

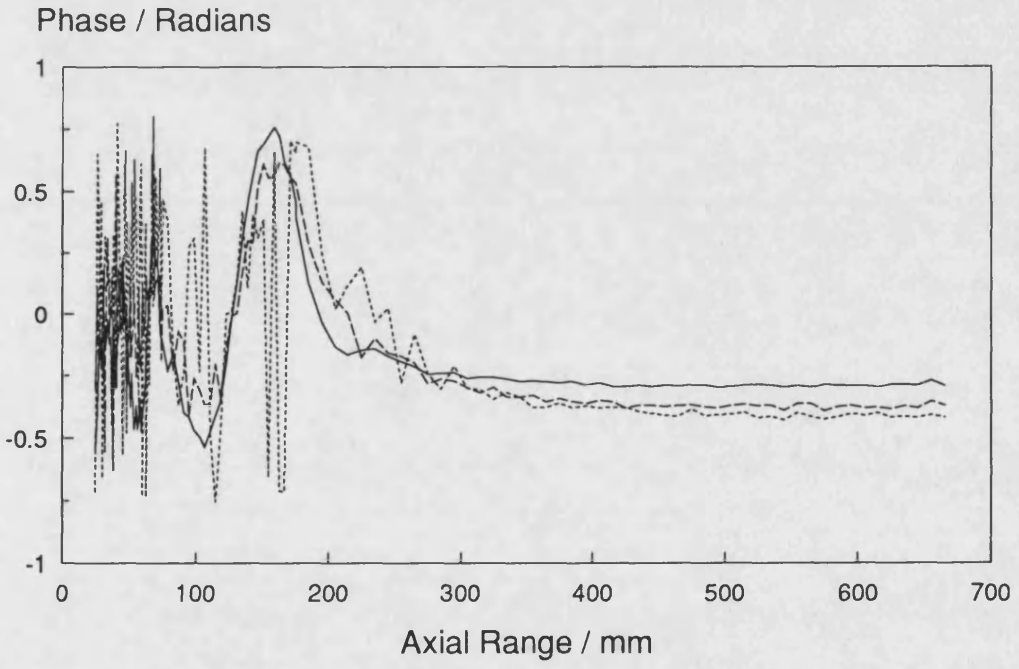

Figure 5.11 Top: The measured axial pressure field of a plane square aperture at DL1, a=b=25 mm, f=2.25 MHz, P_0=77.5 kPa. Bottom: Phase of the first three harmonics.

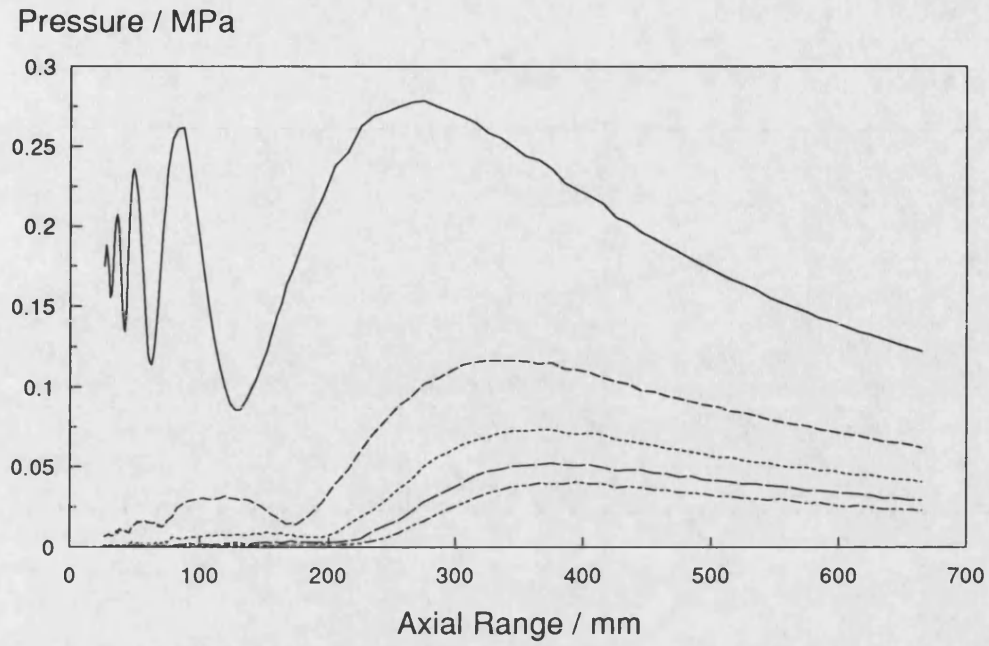

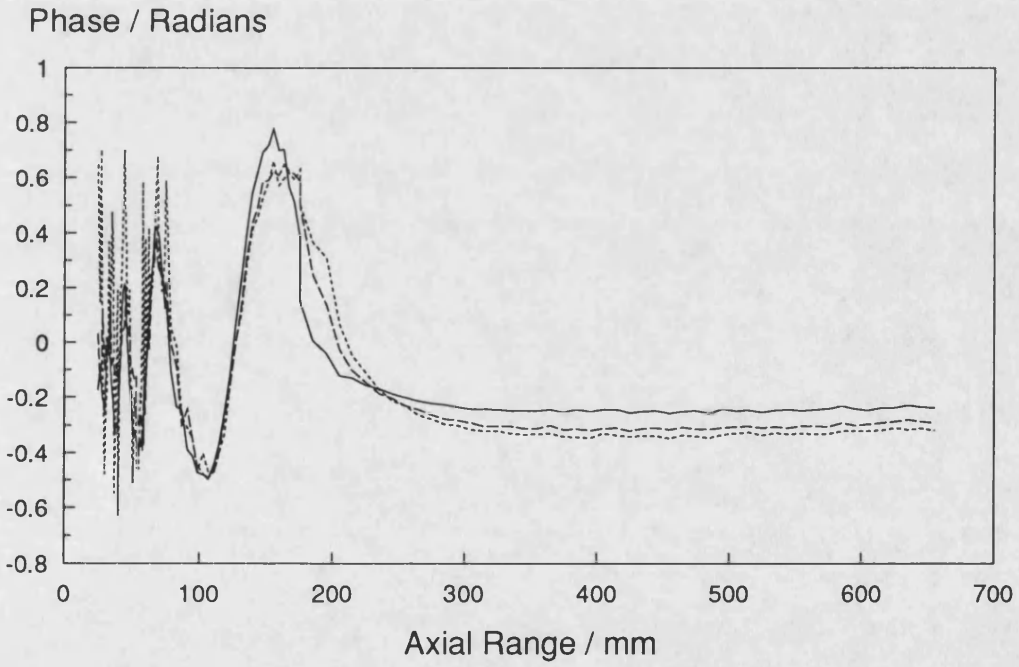

Figure 5.12 Top: The measured axial pressure field of a plane square aperture at DL2, a=b=25 mm, f=2.25 MHz, P_0=180 kPa. Bottom: Phase of the first three harmonics.

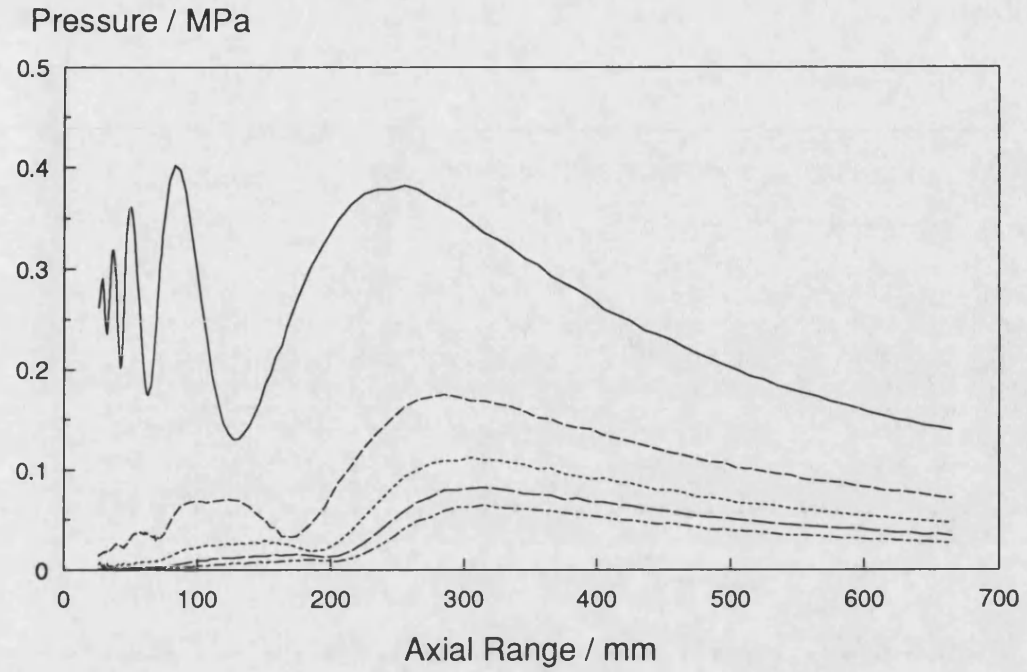

Figure 5.13 Measured axial pressure field of a plane square aperture at DL3, a=b=25 mm, f=2.25 MHz, P_0=260 kPa.

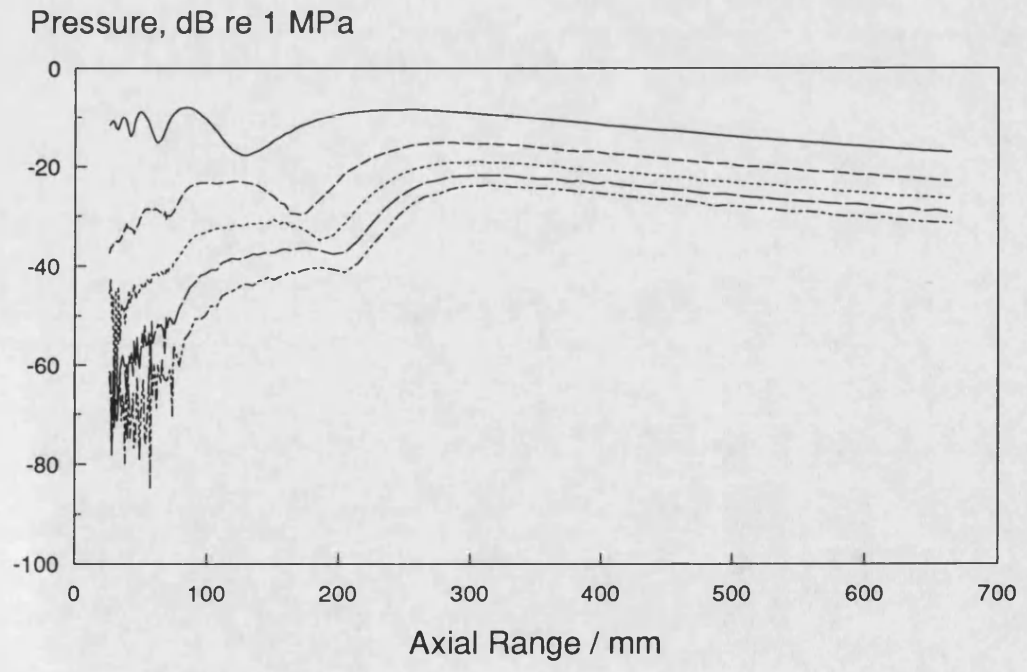

Figure 5.14 Measured axial pressure field of a plane square aperture at DL3, (plotted relative to 1 MPa), a=b=25 mm, f=2.25 MHz, P_0=260 kPa.

Figures 5.15 - 5.23 compare the theoretical results from the plane wave model with experimental measurements up to third harmonic for 25 mm square aperture at each drive level. The fundamental shows good agreement at DL1 (Figure 5.15) between the theory and experimental measurements although there are some small discrepancies. Figure 5.16 shows the corresponding plot for the second harmonic, here there are some marked discrepancies, particularly near the measured minimum at 180 mm and the largest maxima, this is discussed in detail later.

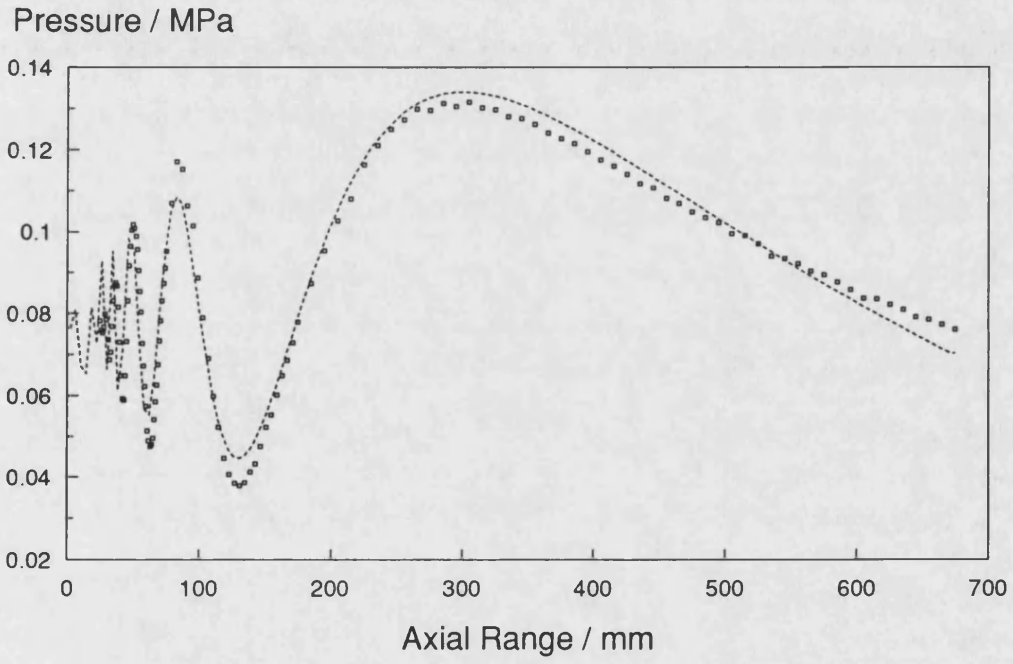

Figure 5.15 Comparison of the predicted first harmonic with measured values at DL1, a=b=25 mm, f=2.25 MHz, P_0=77.5 kPa. Theory (dotted line), Experiment (markers).

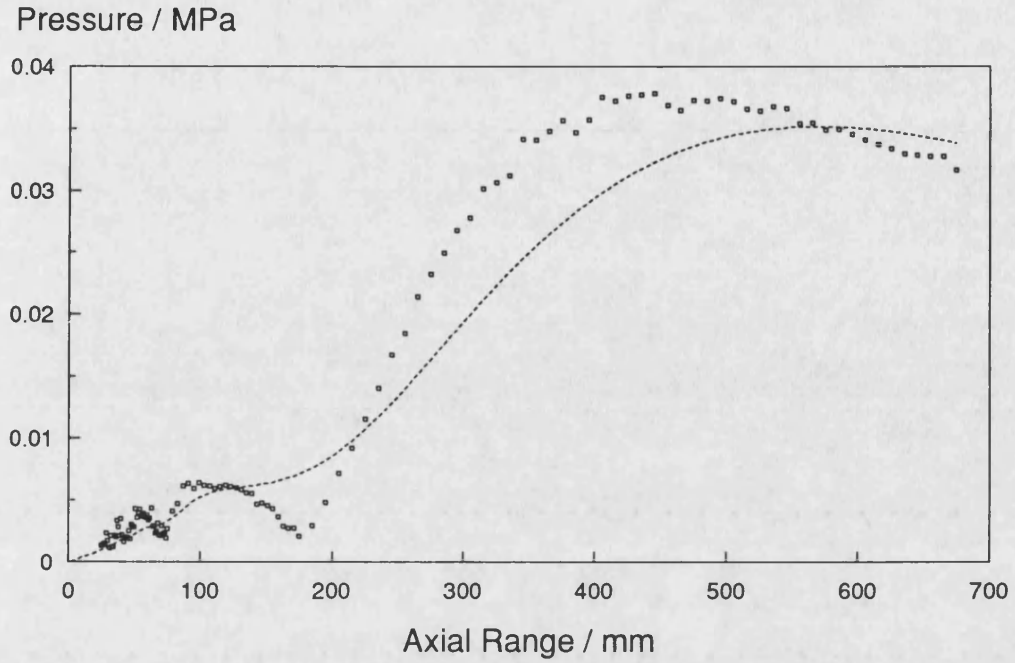

Figure 5.16 Comparison of the predicted second harmonic with measured values at DL1, a=b=25 mm, f=2.25 MHz, P_0=77.5 kPa. Theory (dotted line), Experiment (markers).

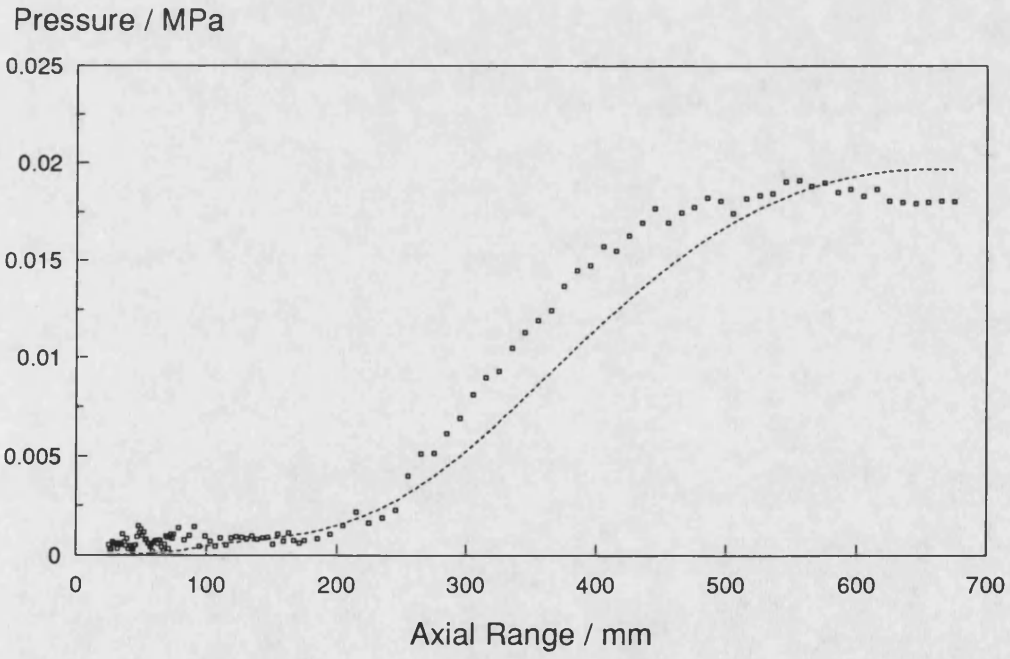

Figure 5.17 Comparison of predicted third harmonic with measured values at DL1, a=b=25 mm, f=2.25 MHz, P_0=77.5 kPa. Theory (dotted line), Experiment (markers).

Although Figure 5.17 shows good agreement between the calculated and measured pressure amplitudes for the third harmonic, some disagreement between the predicted last minimum and measured one was observed. But because the measured pressure level of the last minimum is small at this drive level, the theoretical and experimental results are in quite good agreement until 250 mm axial range from the aperture.

It was observed that the increase in the drivel level to DL2 did not affect the agreement for the fundamental (Figure 5.18), but the second and third harmonics are much more affected. The measured minima in the second harmonic (Figure 5.19) become deeper and the disagreement between two curves increases. This departure was more severe for the third harmonic as shown in Figure 5.20 for DL2. At the highest drive level (DL3), the fundamental (Figure 5.21) is showing some marked deviations between experiment and theory and the second and third harmonic agreement has deteriorated further (Figures 5.22 and 5.23).

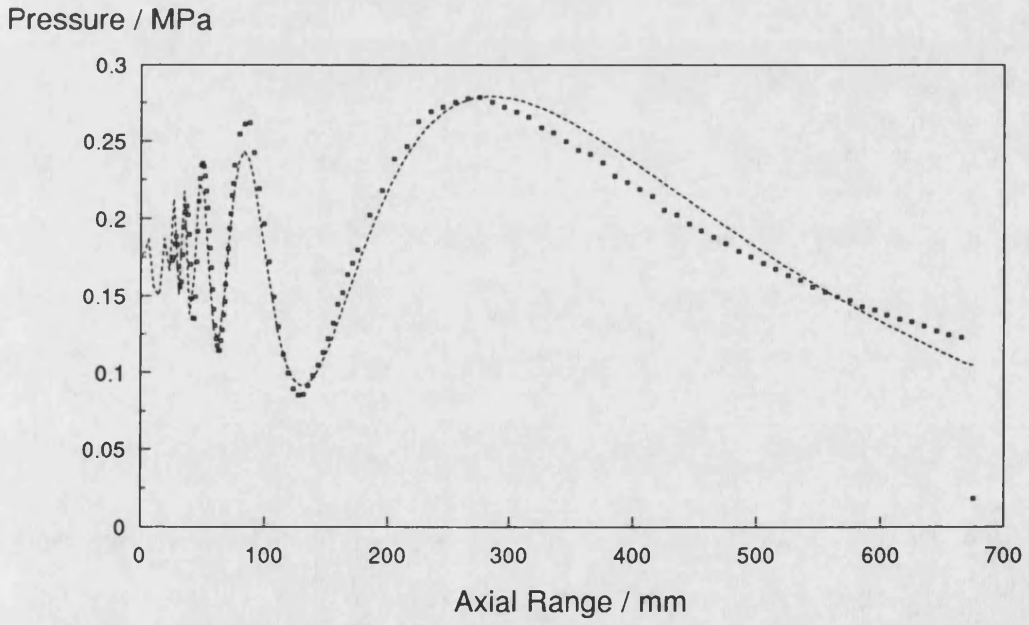

Figure 5.18 Comparison of predicted fundamental with measured values at DL2, a=b=25 mm, f=2.25 MHz, P_0=180 kPa. Theory (dotted line), Experiment (markers).

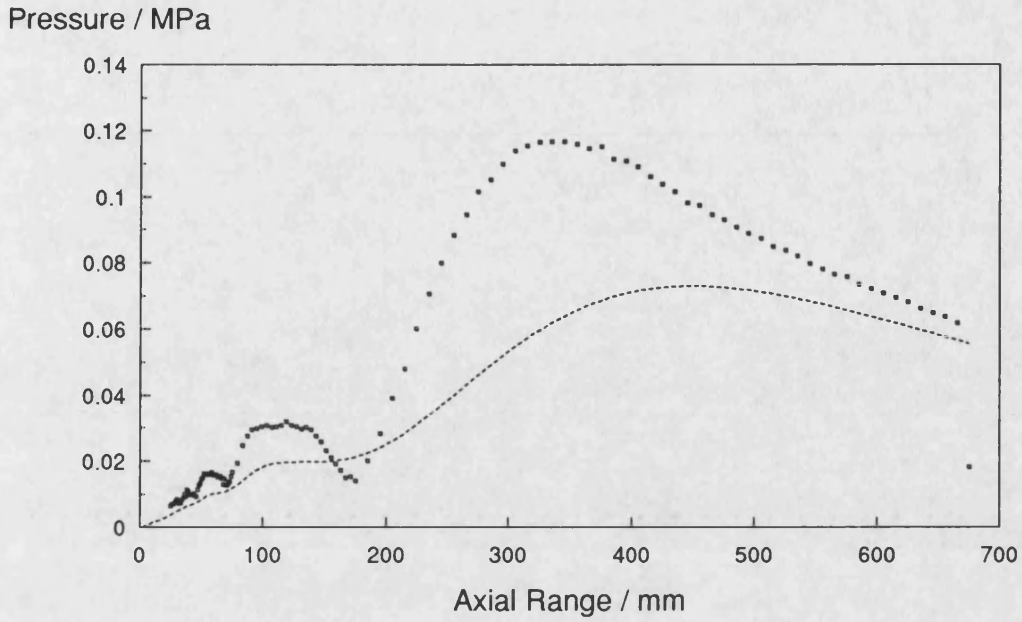

Figure 5.19 Comparison of predicted second harmonic with measured values at DL2, a=b=25 mm, f=2.25 MHz, P_0=180 kPa. Theory (dotted line), Experiment (markers).

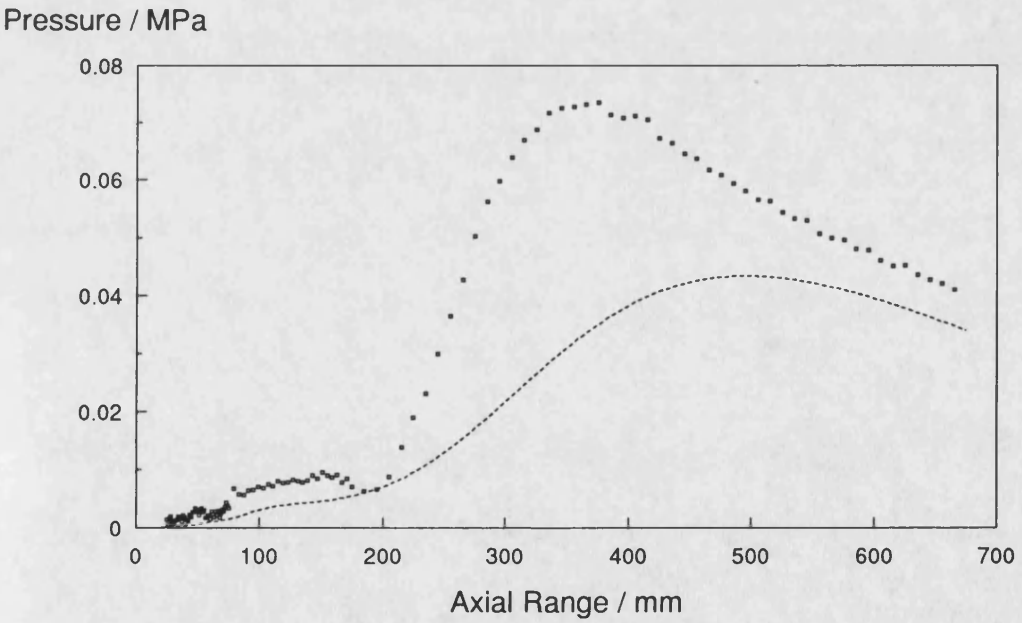

Figure 5.20 Comparison of predicted third harmonic with measured values at DL2, a=b=25 mm, f=2.25 MHz, P_0=180 kPa. Theory (dotted line), Experiment (markers).

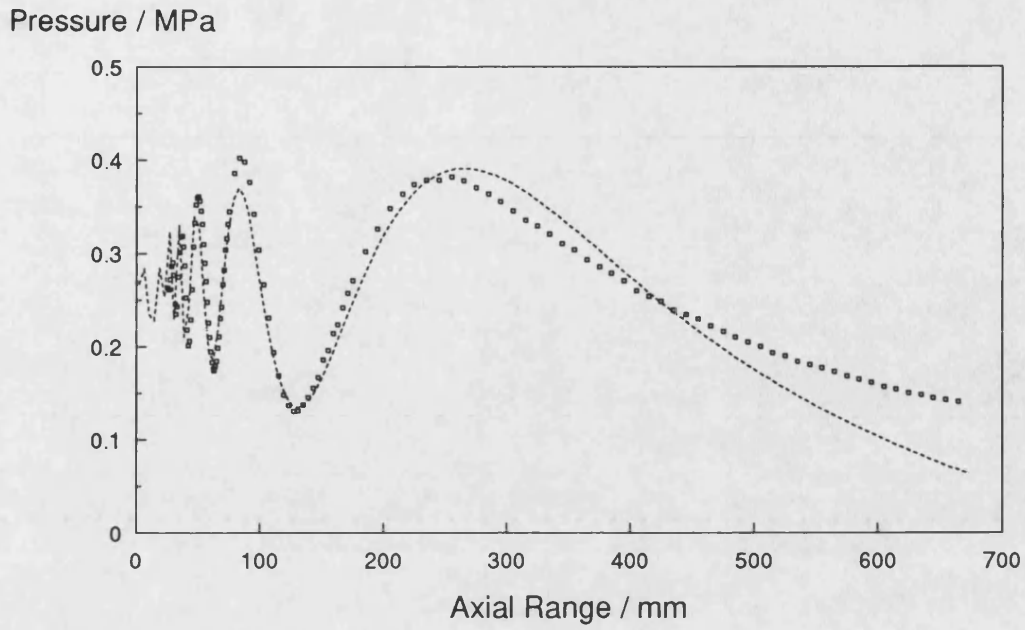

Figure 5.21 Comparison of predicted fundamental with measured values at DL3, a=b=25 mm, f=2.25 MHz, P_0=260 kPa. Theory (dotted line), Experiment (markers).

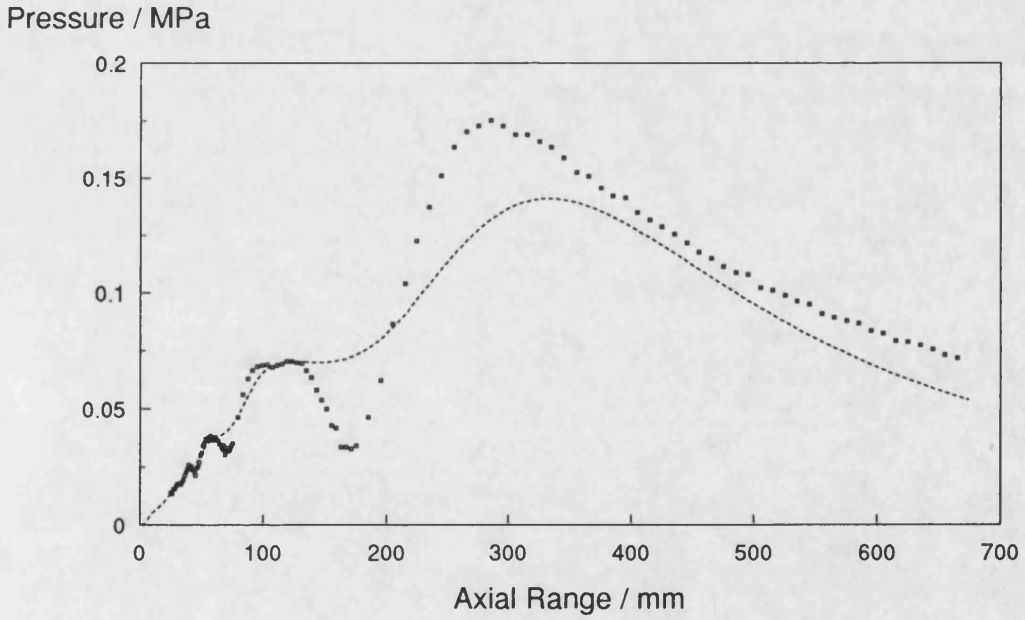

Figure 5.22 Comparison of predicted second harmonic with measured values at DL3, a=b=25 mm, f=2.25 MHz, P_0=260 kPa. Theory (dotted line), Experiment (markers).

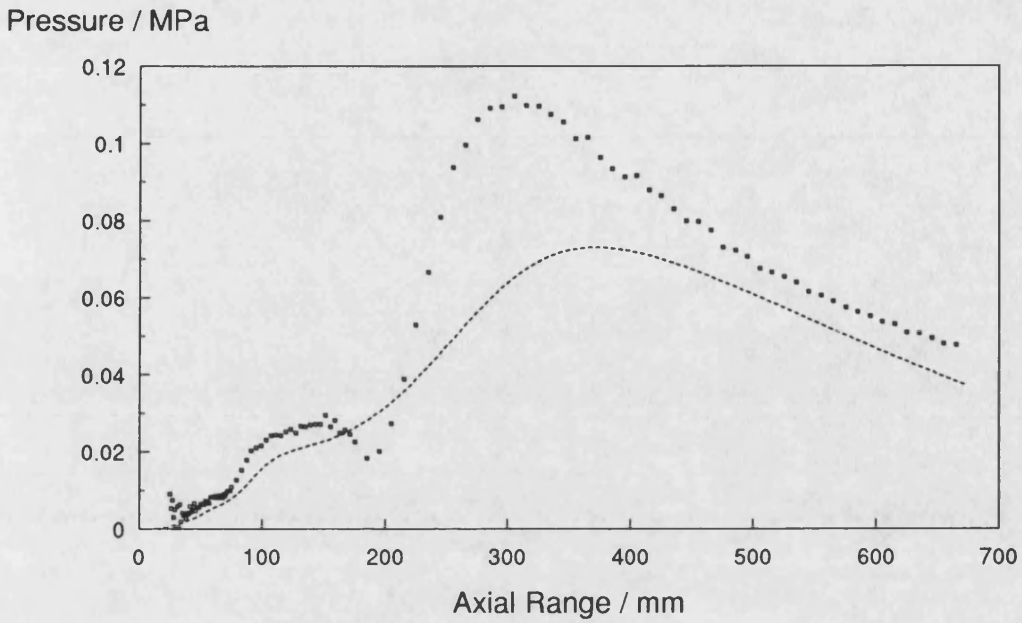

Figure 5.23 Comparison of predicted third harmonic with measured values at DL3, a=b=25 mm, f=2.25 MHz, P_0=260 kPa. Theory (dotted line), Experiment (markers).

It is thought that disagreement in the maximum and minimum pressure levels of the second and higher harmonics is due to diffraction affecting the harmonics generated in the medium during nonlinear propagation. The theory, as implemented here, does not take account of diffraction for the higher harmonics. This hypothesis was tested on the circular case as a full numerical solution (FOCAB) that takes into account diffraction for all the harmonics was available [63].

The first step was to run the program FOCAB [63] in the usual way with diffraction for all the harmonics, for a circular transducer of 38 mm diameter. Figure 5.24 presents the axial pressure variation for such a circular transducer up to fifth harmonic, including diffraction for all the harmonics retained in the calculation. Notice that the fundamental shows the effect of reflections from the radial boundary at normalised ranges greater than about 0.4 where a few ripple can be seen in the amplitude on axis.

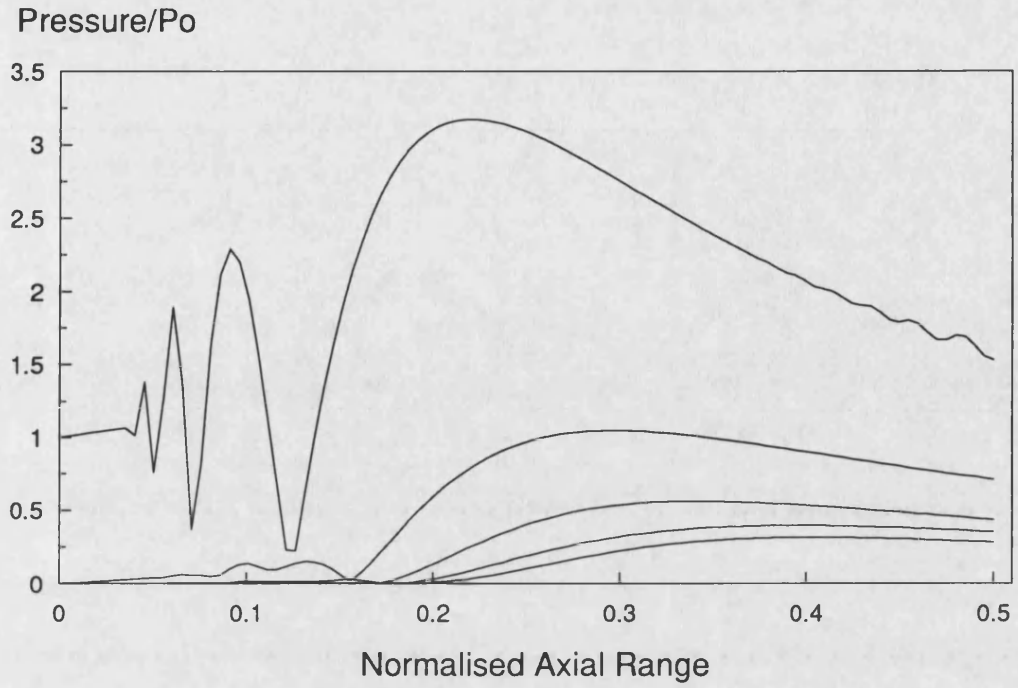

Figure 5.24 Axial pressure field of a focused circular transducer (38 mm diam.) including full diffraction, f=2.25 MHz, Gain=2.0

The expected variation was observed for the fundamental giving rise to the more pronounced oscillations in the second and third harmonic in comparison with the rectangular case. Re-running the program with the diffraction term for the harmonics disabled showed that the behaviour of the harmonics was not the same as that observed with full diffraction (Figure 5.25). Figure 5.26 - 5.30 compare the results calculated including full diffraction (solid lines) with those obtained including diffraction only for the fundamental (dotted lines). The second and third harmonics calculated including full diffraction show more fluctuation than those obtained without diffraction.

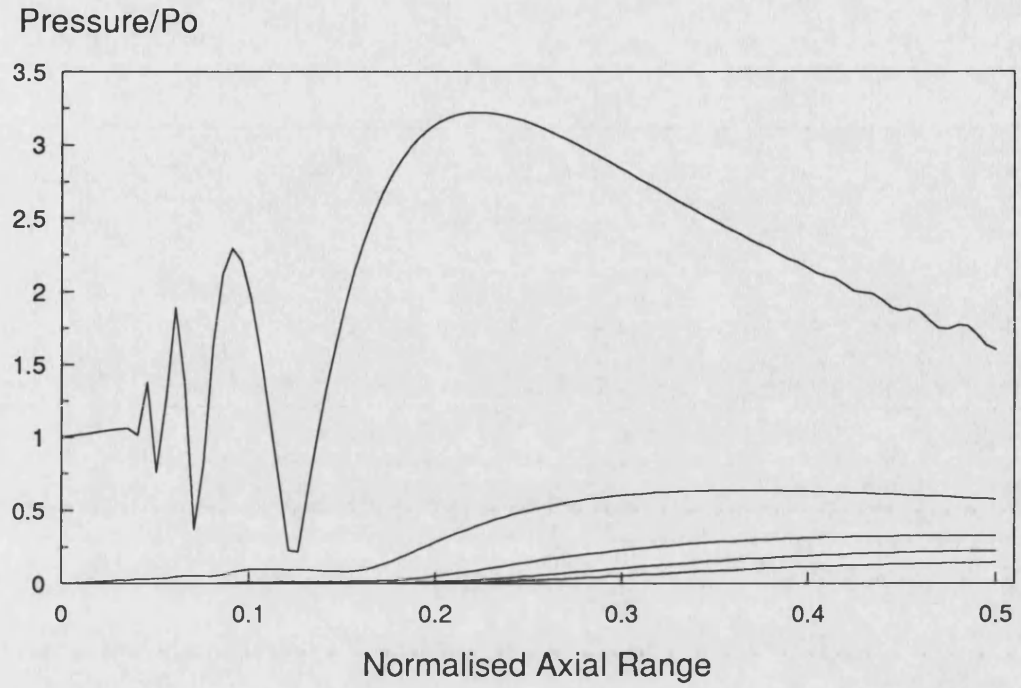

Figure 5.25 The first five harmonics for a circular transducer (38 mm in diam.) with no diffraction after the fundamental, f=2.25 MHz, Gain=2.0

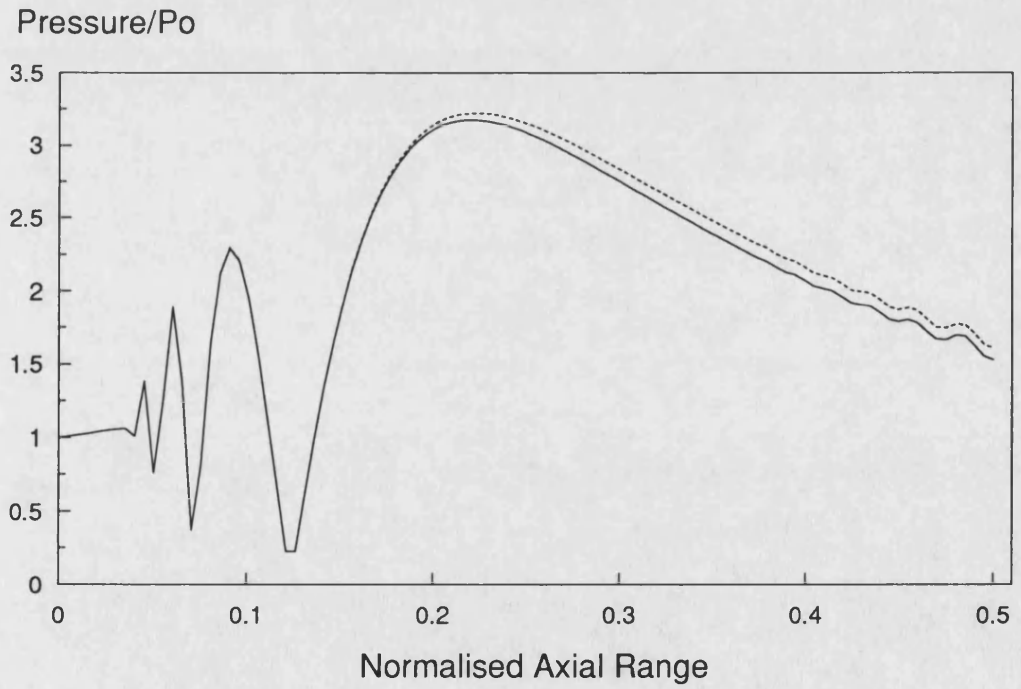

Figure 5.26 Comparison of the first harmonic calculated with full diffraction (solid line) and no diffraction (dotted line) after the first harmonic.

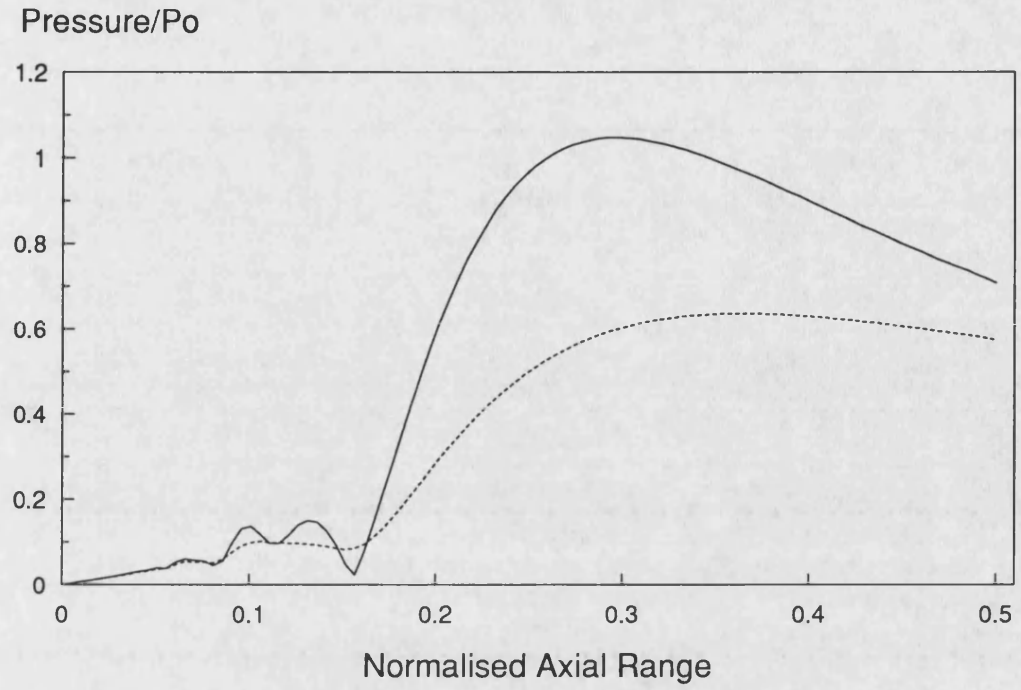

Figure 5.27 Comparison of the second harmonic calculated with full diffraction (solid line) and no diffraction (dotted line) after the first harmonic.

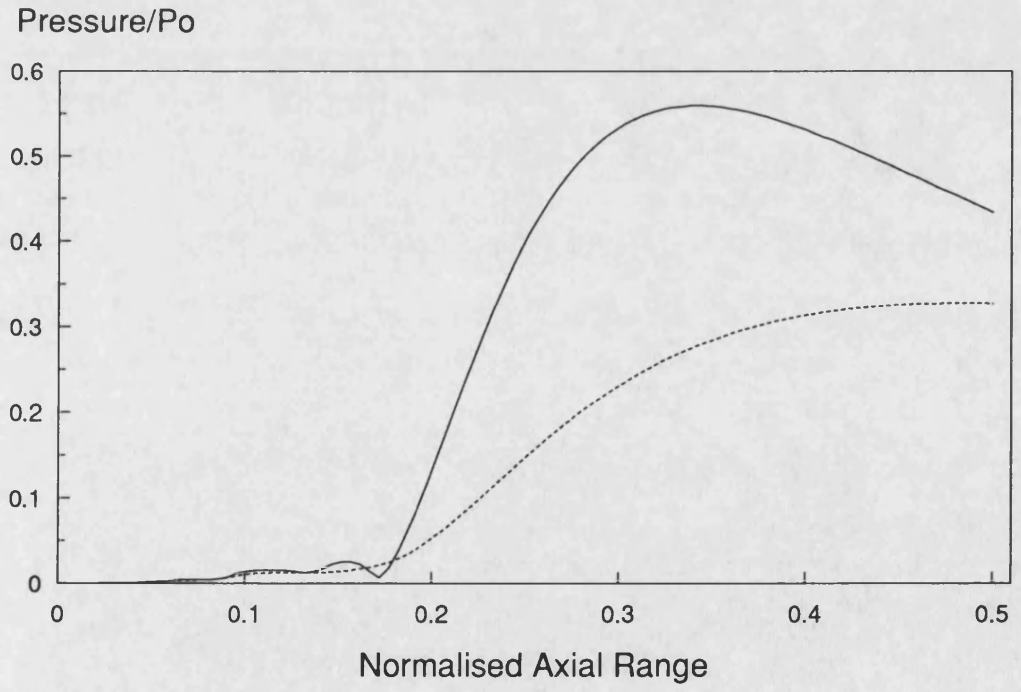

Figure 5.28 Comparison of the third harmonic calculated with full diffraction (solid line) and no diffraction (dotted line) after the first harmonic.

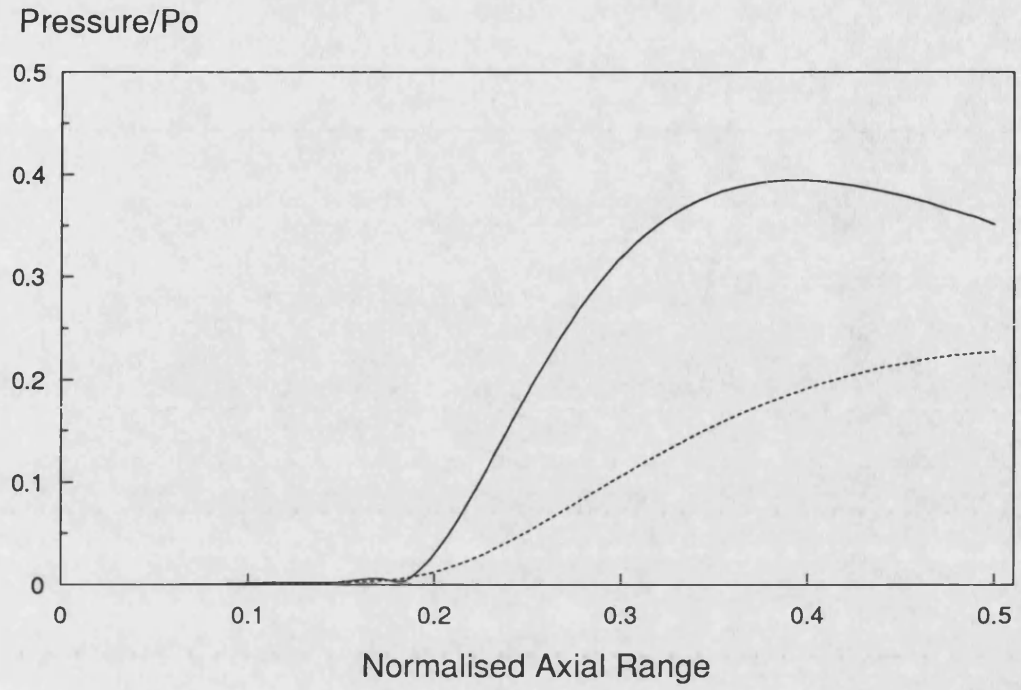

Figure 5.29 Comparison of the fourth harmonic calculated with full diffraction (solid line) and no diffraction (dotted line) after the first harmonic.

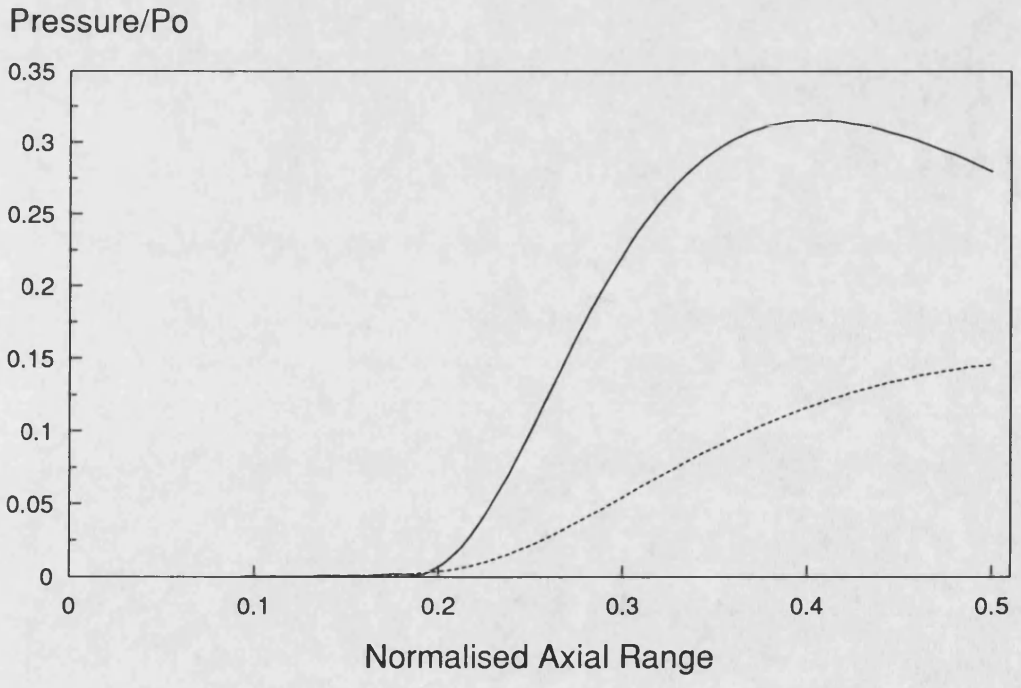

Figure 5.30 Comparison of the fifth harmonic calculated with full diffraction (solid line) and no diffraction (dotted line) after the first harmonic.

The modified program FOCAB was also run for various drive levels and it was seen that increasing the drive level caused more disagreement between results with diffraction and without diffraction except fundamental, but for the clarity, these results are not presented here. These investigations confirmed that the disagreement observed for the rectangular piston results arise due to the diffraction effect of the second and higher harmonic components of the finite amplitude acoustic beam.

A similar investigation was also carried out for the radial pressure fields of the same circular source and a similar reduction was observed in the peak pressure amplitudes on the acoustic axis as well as off axis, but the maximum discrepancy was on the acoustic axis. These results up to fifth harmonic are given in Figure 5.31 - 5.35.

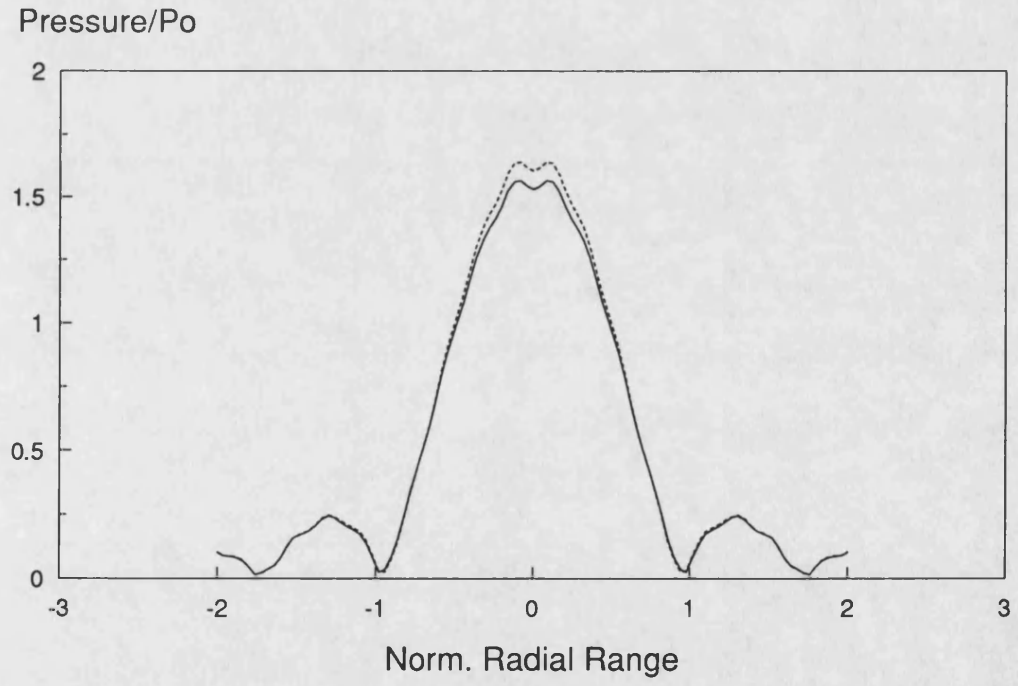

Figure 5.31 Across axis fundamental with full diffraction (solid line) and without diffraction except fundamental (dotted line), at normalised range 0.25

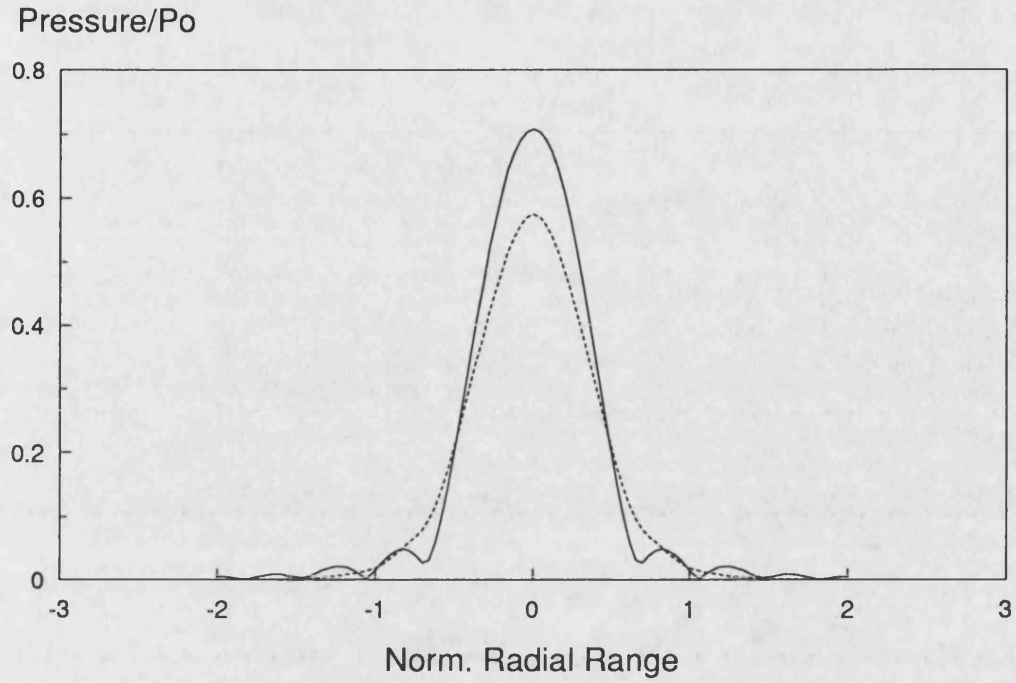

Figure 5.32 Across axis second harmonic with full diffraction (solid line) and without diffraction except fundamental (dotted line), at normalised range 0.25

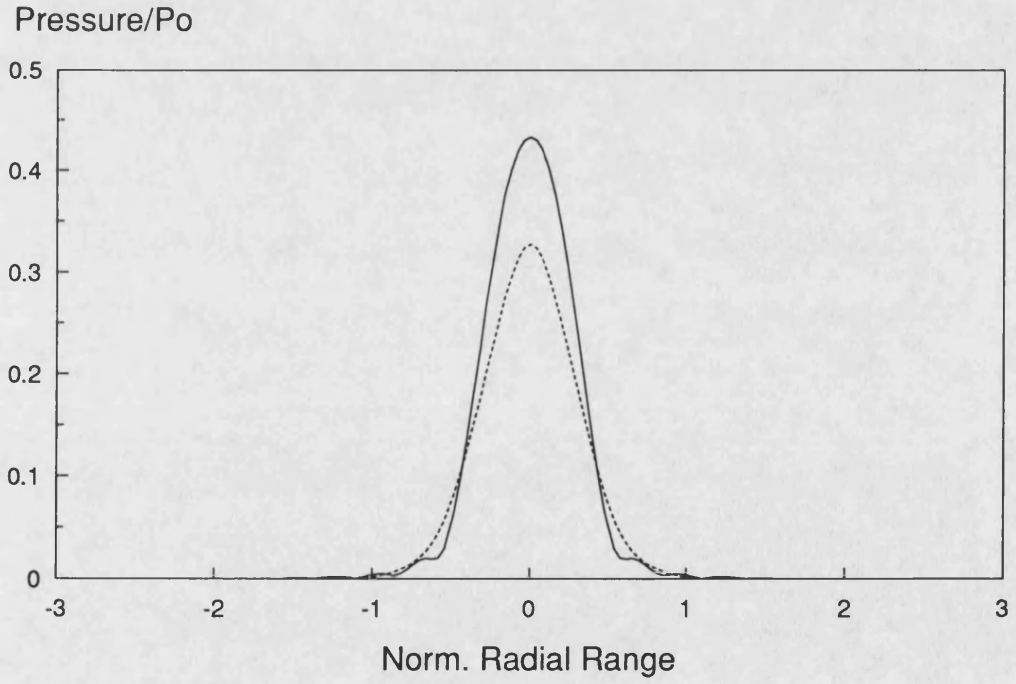

Figure 5.33 Across axis third harmonic with full diffraction (solid line) and without diffraction except fundamental (dotted line), at normalised range 0.25

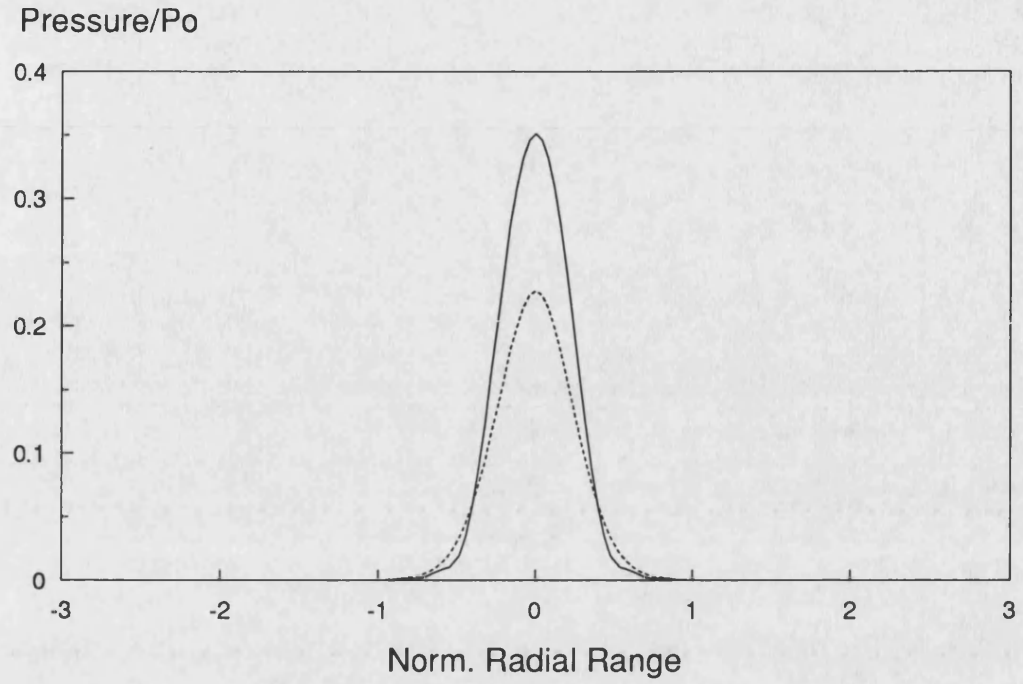

Figure 5.34 Across axis fourth harmonic with full diffraction (solid line) and without diffraction except fundamental (dotted line), at normalised range 0.25

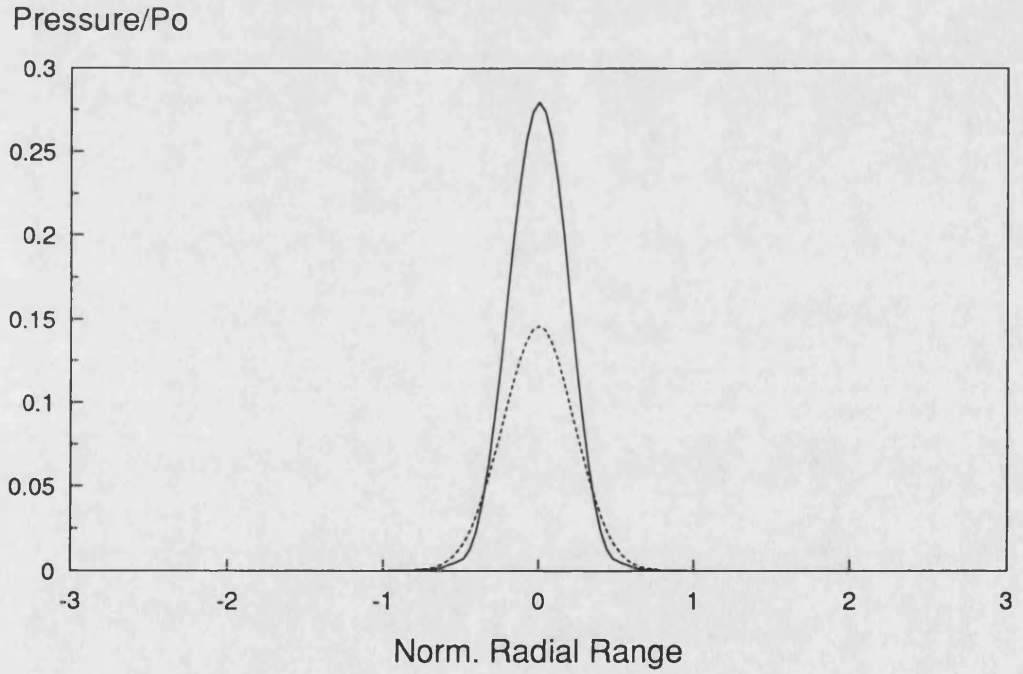

Figure 5.35 Across axis fifth harmonic with full diffraction (solid line) and without diffraction except fundamental (dotted line), at normalised range 0.25

Figure 5.36 and 5.37 are related to the axial pressure field of 10 x 15 mm rectangular aperture at DL1 and show that there is less variation of the pressure field on the acoustic axis for rectangular case, in comparison with square and circular cases. This is true for the fundamental and for the higher harmonics. The last minimum in the fundamental and the higher harmonics are less deep in the case of rectangular aperture than in the case of square and circular case. The circular source causes the deepest minima and the least pronounced was seen in the rectangular case. The depth of the minimum played an important role in comparing the agreement between the theory and experimental measurements. Figures 5.38 - 5.40 show the agreement at this drive level for the first, second and third harmonics respectively. The best agreement was obtained for the first harmonic but with a discrepancy in the maximum and minimum pressure levels. The experimental results at DL3 for the same aperture are presented in Figure 5.41 and in Figure 5.42 in terms of logarithmic scale relative to 1 MPa. The agreement for this drive level is comparable to the low drive level (DL1) for the fundamental (Figure 5.43), second (Figure 5.44) and for the third harmonics (Figure 5.45).

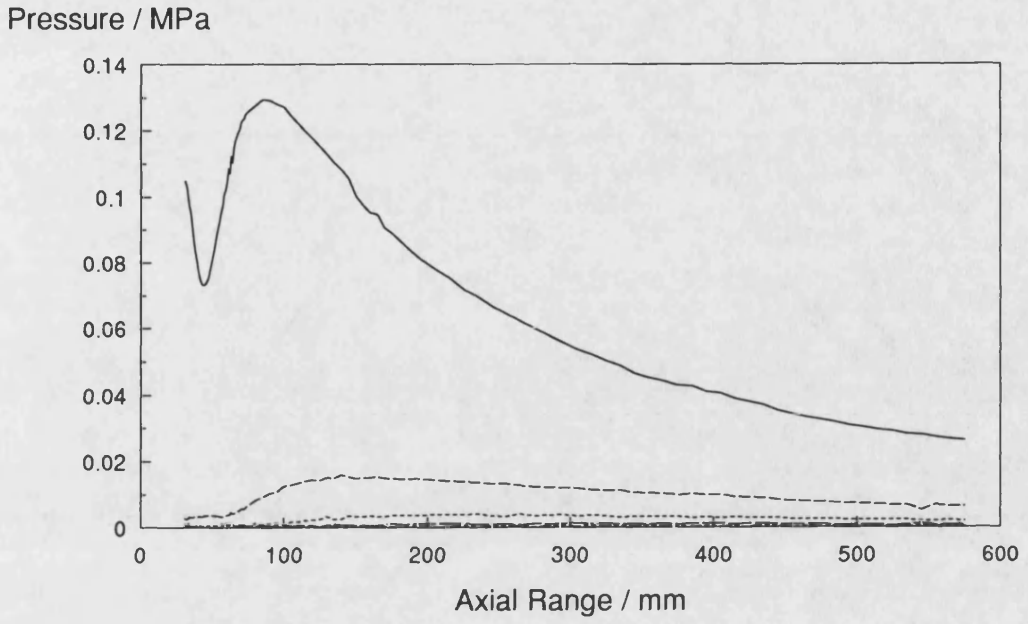

Figure 5.36 Measured axial pressure field of 10 x 15 mm rectangular aperture at DL1, f=2.25, P_0=90 kPa.

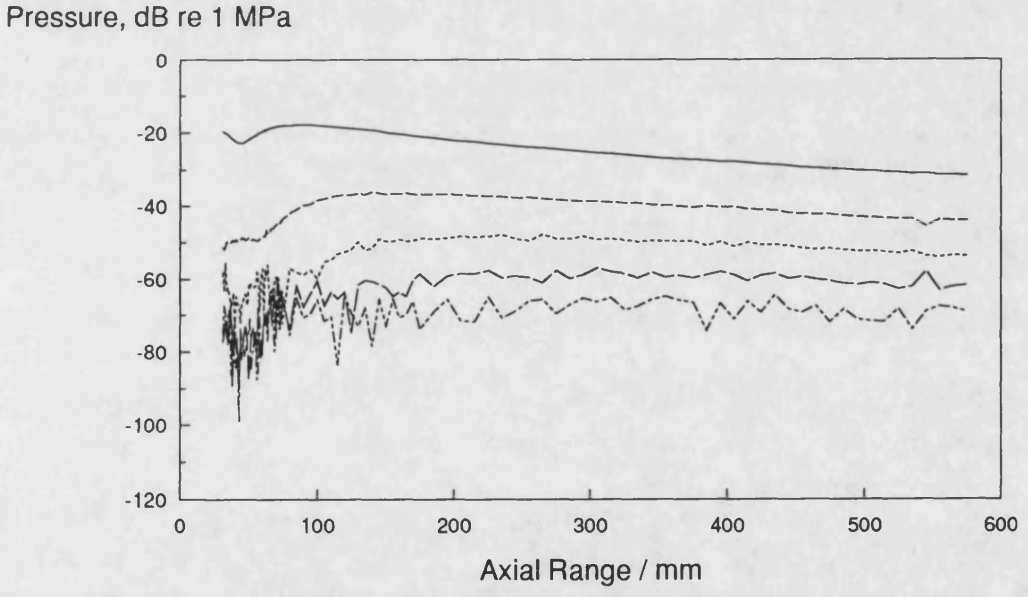

Figure 5.37 Measured axial pressure field of 10 x 15 mm rectangular aperture at DL1 (plotted relative to 1 MPa), f=2.25 MHz, P_0=90 kPa.

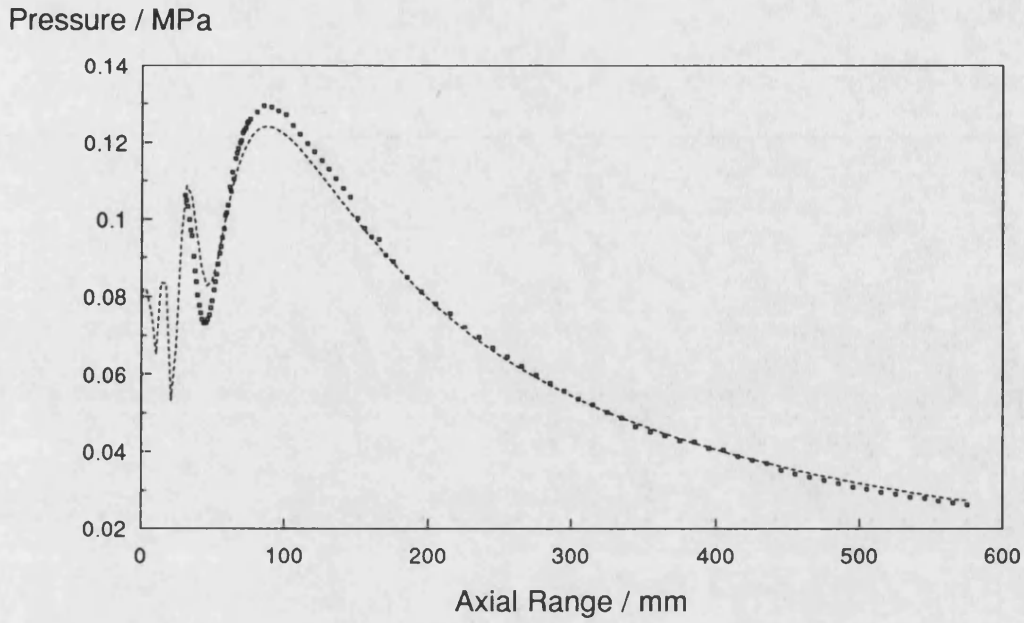

Figure 5.38 Comparison of the predicted fundamental (dotted line) with measured values (markers) at DL1, f=2.25 MHz, P_0=90 kPa, a=10 mm, b=15 mm.

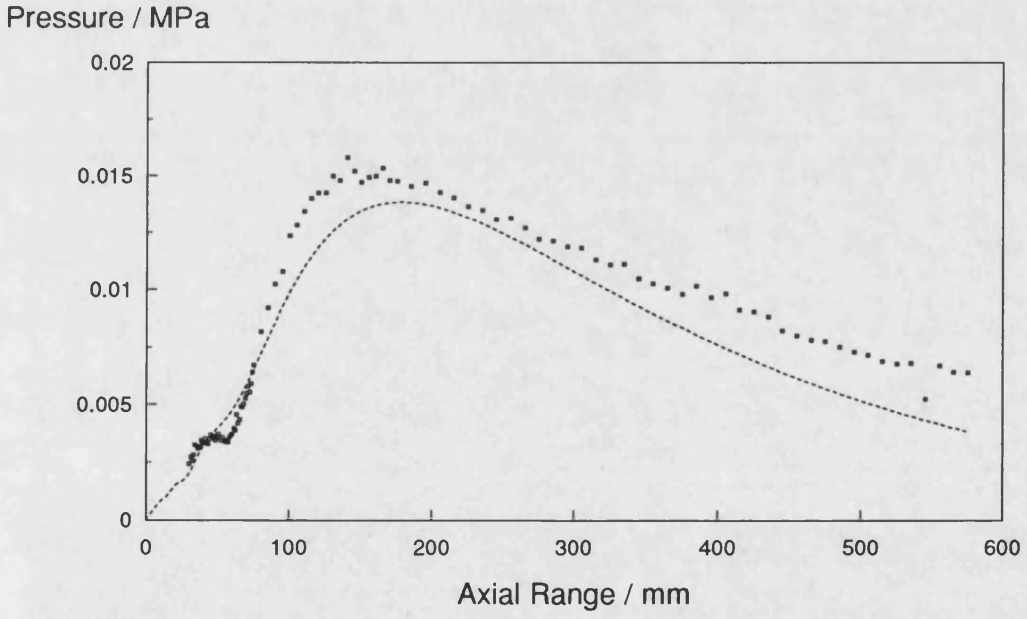

Figure 5.39 Comparison of the predicted second harmonic (dotted line) with measured values (markers) at DL1, f=2.25 MHz, P_0=90 kPa, a=10 mm, b=15 mm.

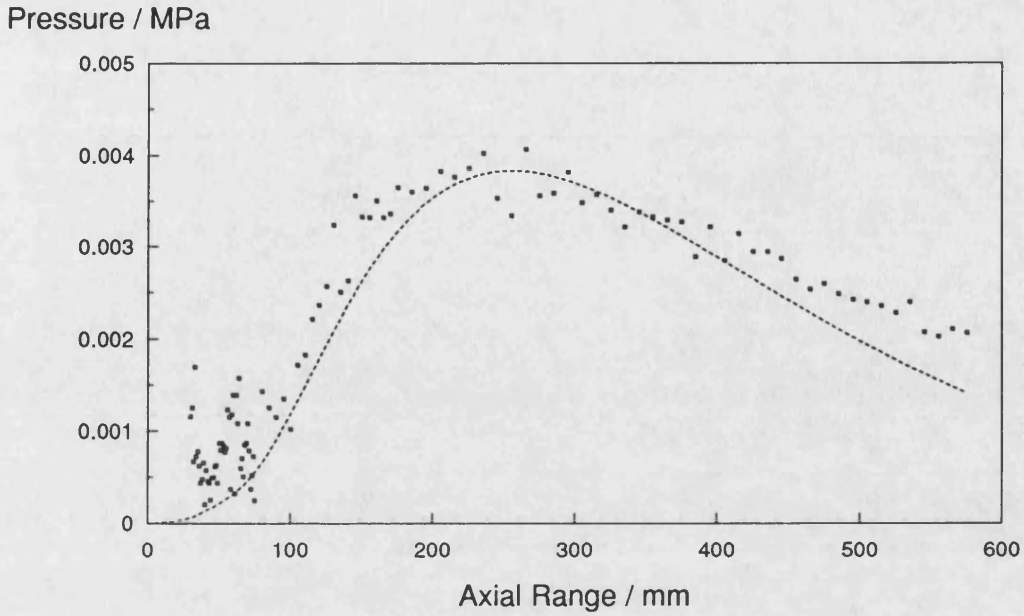

Figure 5.40 Comparison of the predicted third harmonic (dotted line) with measured values (markers) at DL1, f=2.25 MHz, P_0=90 kPa, a=10 mm, b=15 mm.

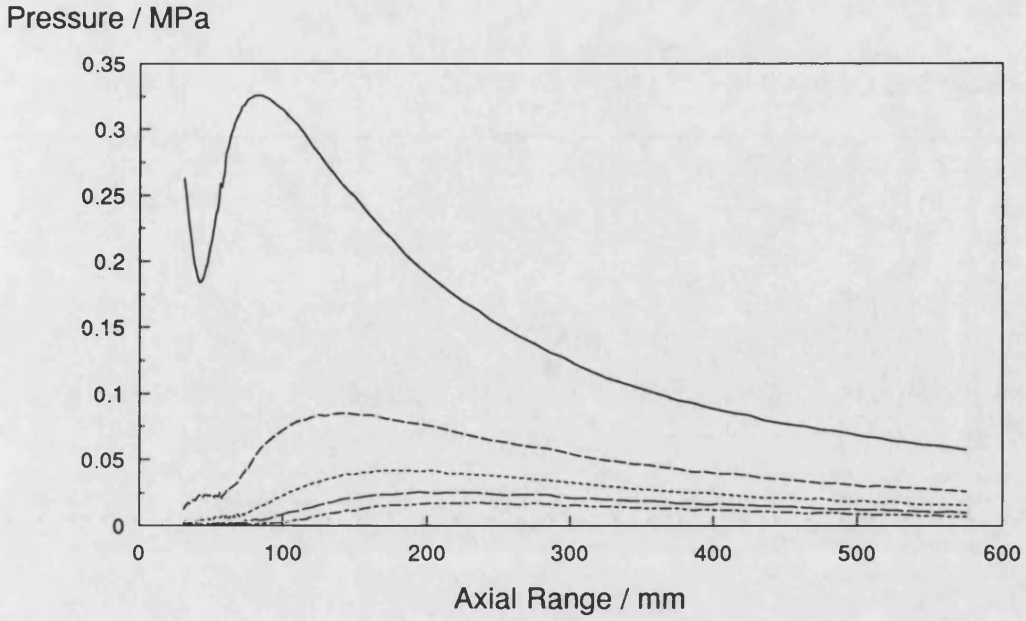

Figure 5.41 Measured axial pressure field of 10 x 15 mm rectangular aperture at DL3, f=2.25, P_0=230 kPa.

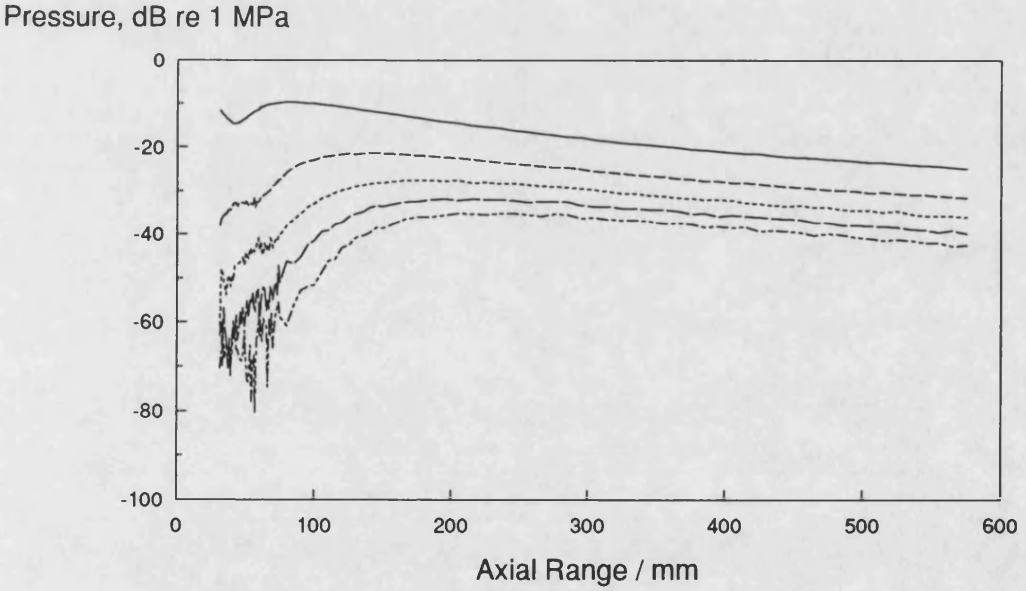

Figure 5.42 Measured axial pressure field of 10 x 15 mm rectangular aperture at DL3 (plotted relative to 1 MPa), f=2.25 MHz, P_0=230 kPa.

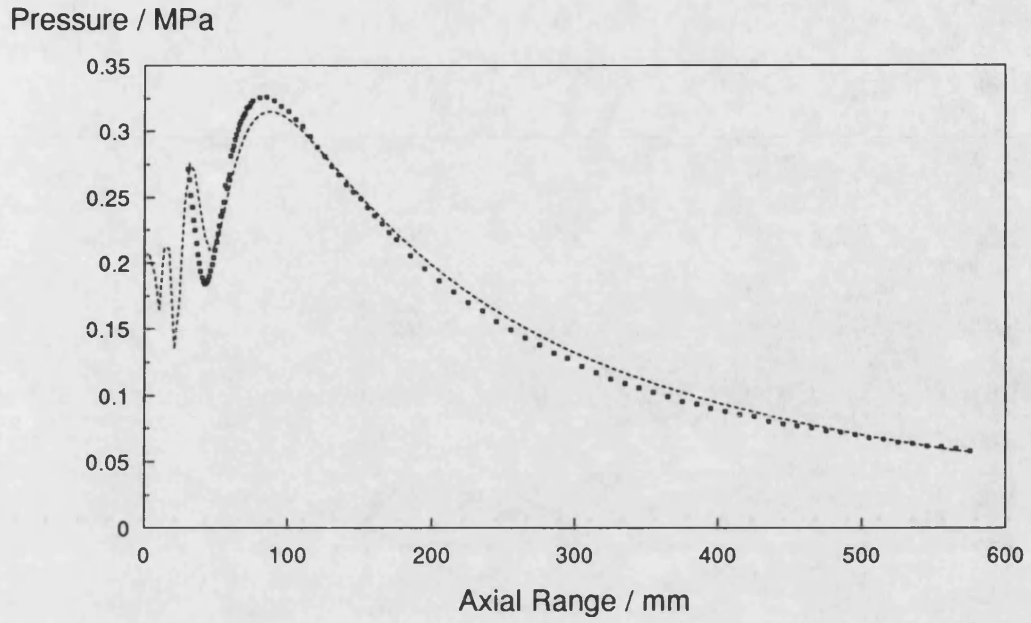

Figure 5.43 Comparison of the predicted fundamental (dotted line) with measured values (markers) at DL3, P_0=230 kPa, f=2.25 MHz, a=10 mm, b=15 mm.

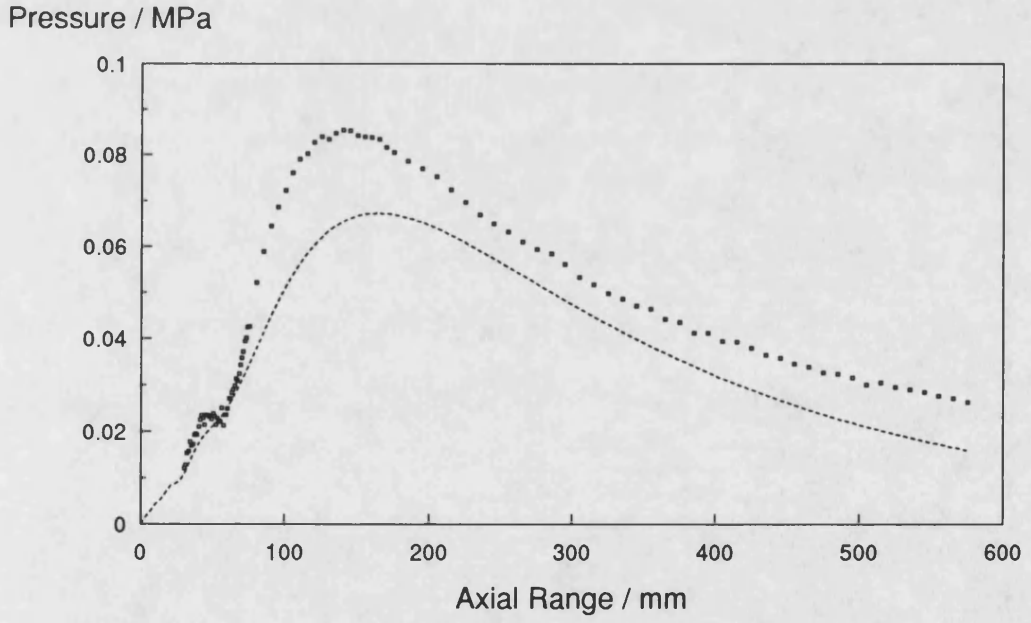

Figure 5.44 Comparison of the predicted second harmonic (dotted line) with measured values (markers) at DL3, f=2.25 MHz, P_0=230 kPa, a=10 mm, b=15 mm.

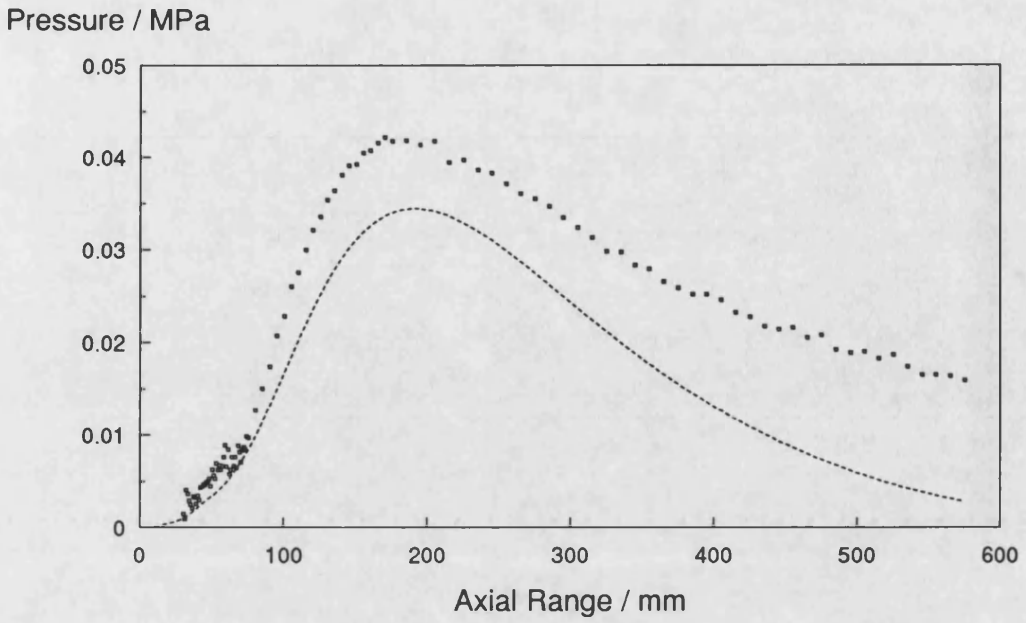

Figure 5.45 Comparison of the predicted third harmonic (dotted line) with measured values (markers) at DL3, f=2.25 MHz, P_0=230 kPa, a=10 mm, b=15 mm.

The characteristics of the 10 x 18 mm rectangular aperture (Figure 5.46 - 5.55) at DL1 and DL2 were small variations in the pressure amplitude closer to the aperture and a maximum at between 40 mm and 55 mm (depending on the drive level). The last axial maxima were always smaller in amplitude than the penultimate axial maxima. The agreement for the fundamental at all drive levels was very good after the last maximum of the fundamental but it was not as good as before the last maximum due to errors in aperture manufacturing. These errors do not show their effects very much far away from the source as the side lobes have disappeared and a more uniform pressure field is obtained with increasing range.

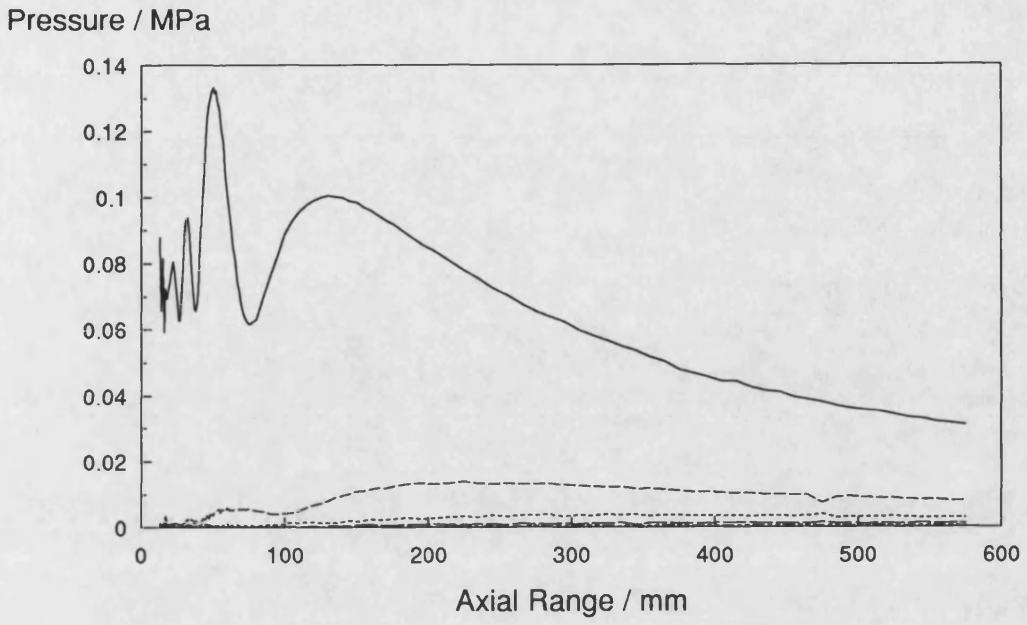

Figure 5.46 Measured axial pressure field of 10 x 18 mm rectangular aperture at DL1, f=2.25 MHz, P_0=80 kPa.

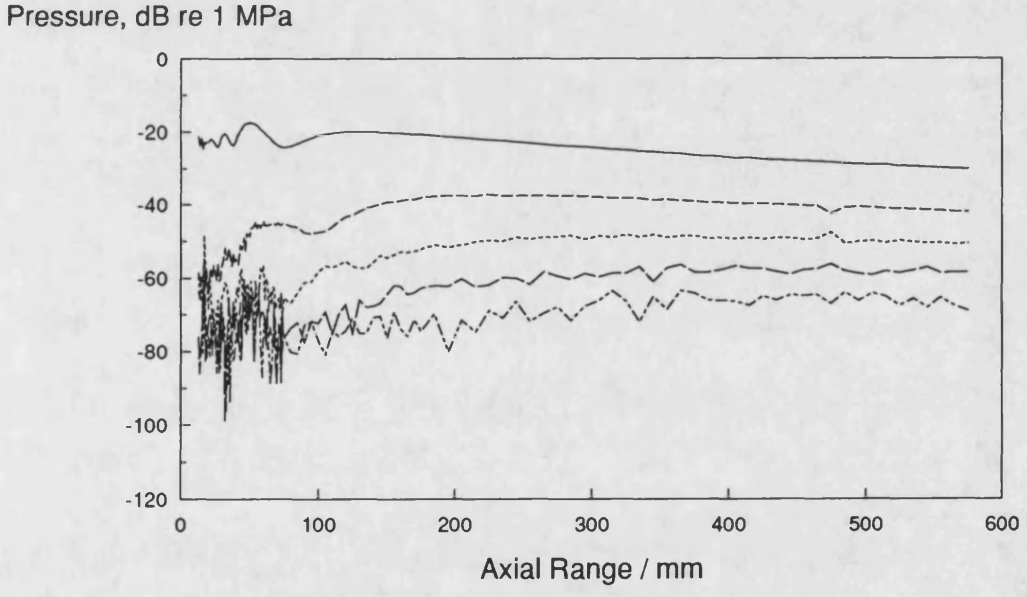

Figure 5.47 Measured axial pressure field of 10 x 18 mm rectangular aperture at DL1 (plotted relative to 1 MPa), f=2.25 MHz, P_0=80 kPa.

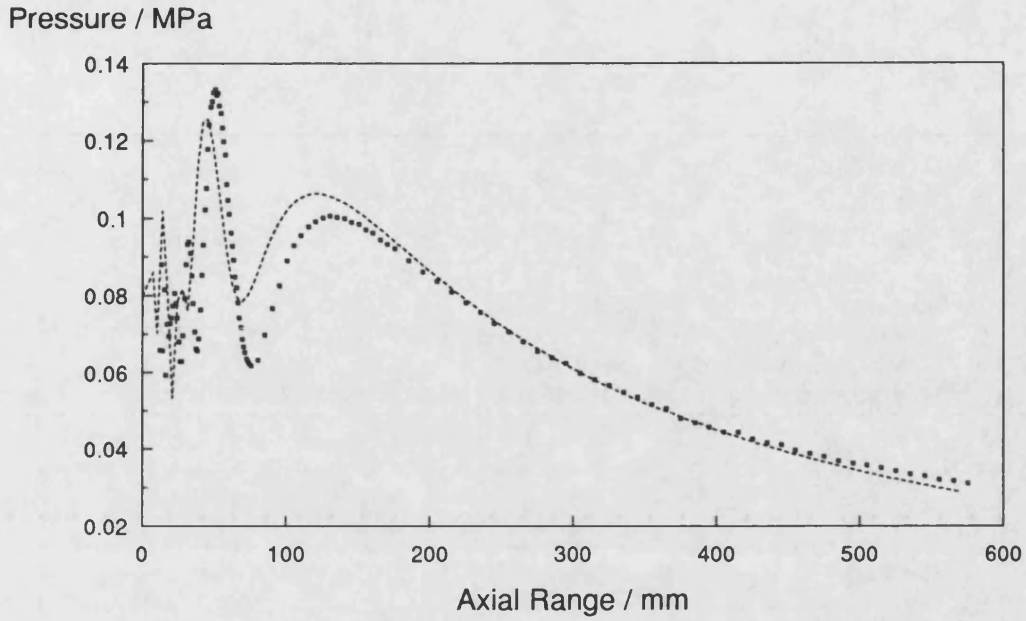

Figure 5.48 Comparison of the predicted fundamental (dotted line) with measured values (markers) at DL1, f=2.25 MHz, a=10 mm, b=18 mm, P_0=80 kPa.

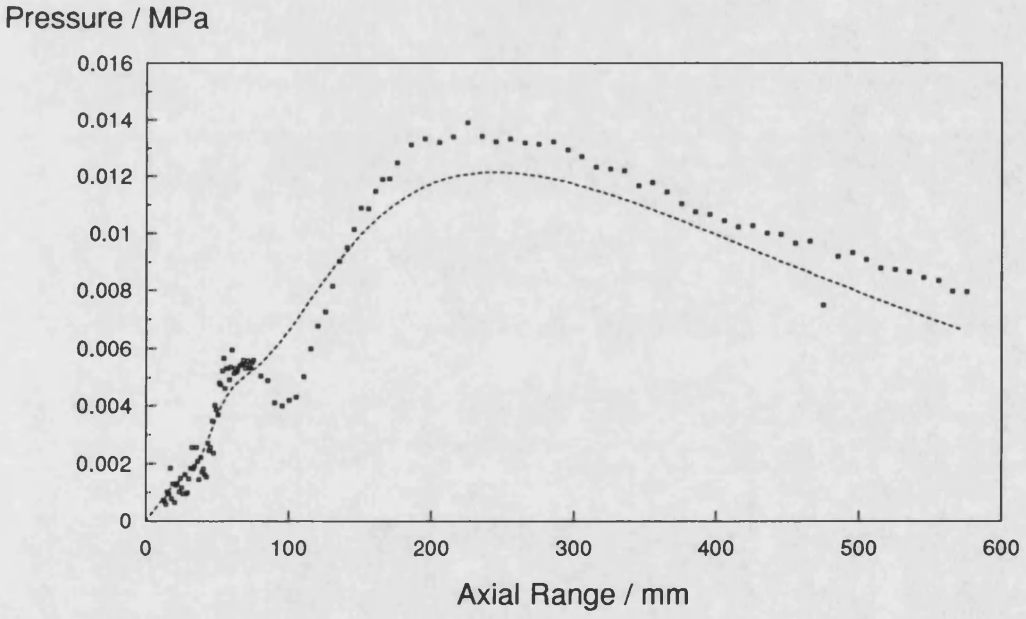

Figure 5.49 Comparison of the predicted second harmonic (dotted line) with measured values (markers) at DL1, f=2.25 MHz, a=10 mm, b=18 mm, P_0=80 kPa.

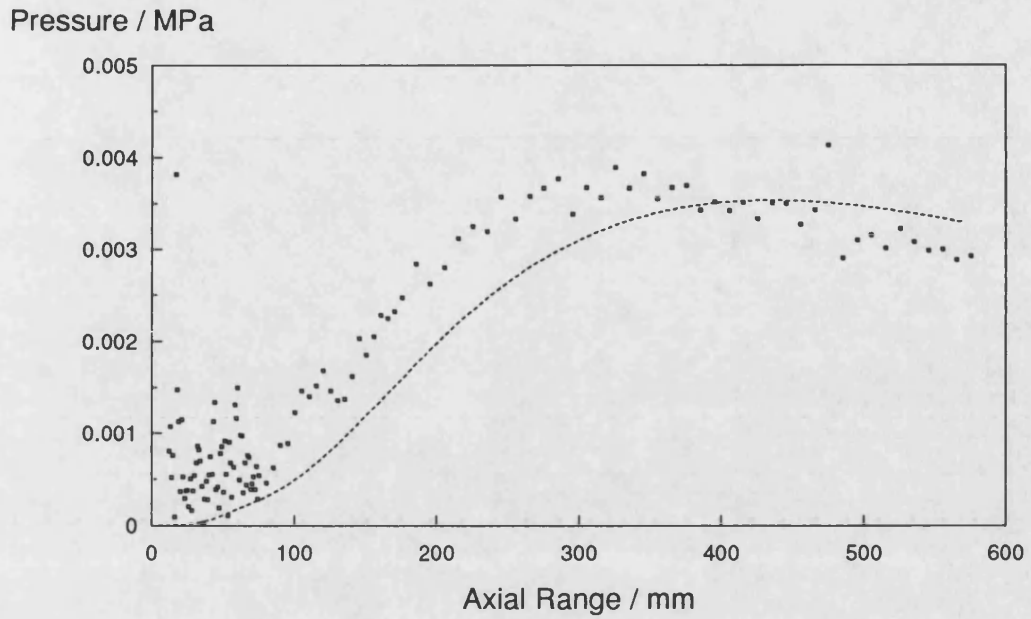

Figure 5.50 Comparison of the predicted third harmonic (dotted line) with measured values (markers) at DL1, f=2.25 MHz, a=10 mm, b=18 mm, P_0=80 kPa.

In order to reveal the effect of drive level on the near field structure of the axial pressure field, measurements were made closer to the aperture at DL1 (Figure 5.46) and DL3 (Figure 5.51). It was observed that the difference between the measured last axial peak and the penultimate was relatively small at DL3 in comparison with DL1 due to the early harmonic generation with increasing drive level.

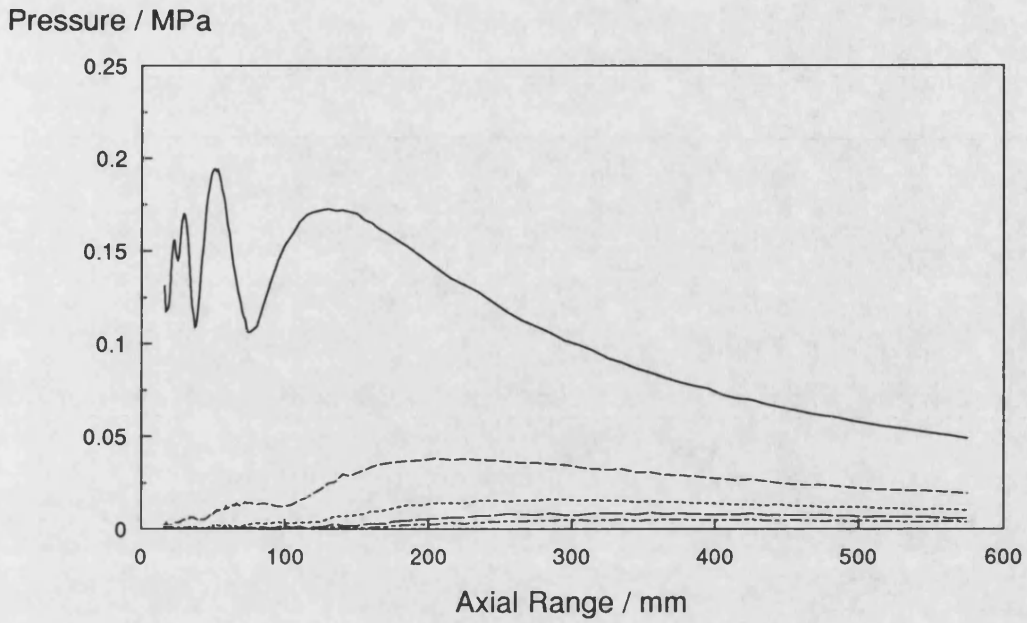

Figure 5.51 Measured axial pressure field of 10 x 18 mm rectangular aperture at DL3, f=2.25 MHz, P_0=125 kPa.

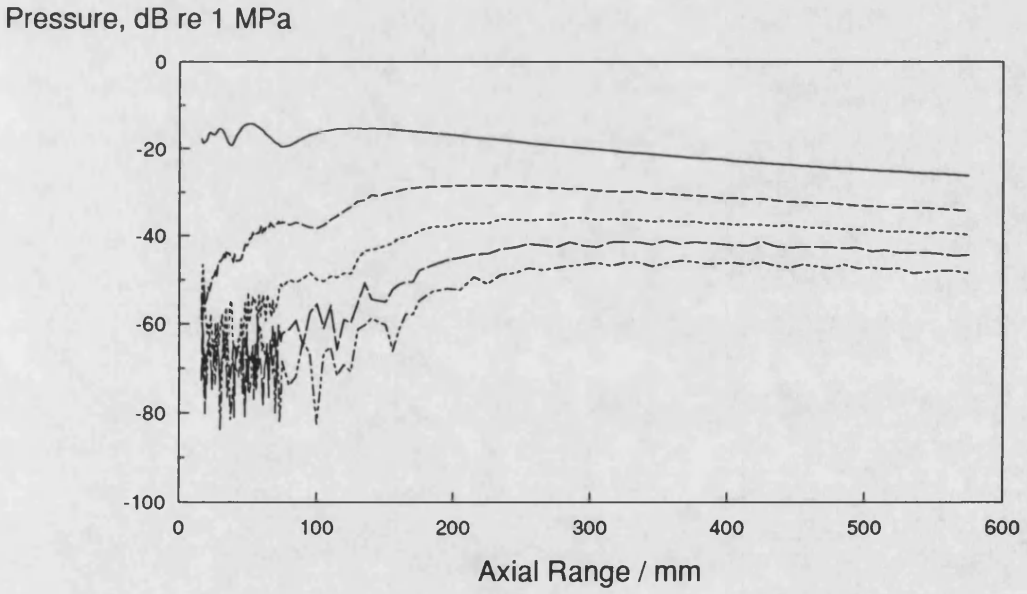

Figure 5.52 Measured axial pressure field of 10 x 18 mm rectangular aperture at DL3 (plotted relative to 1 MPa), f=2.25 MHz, P_0=125 kPa.

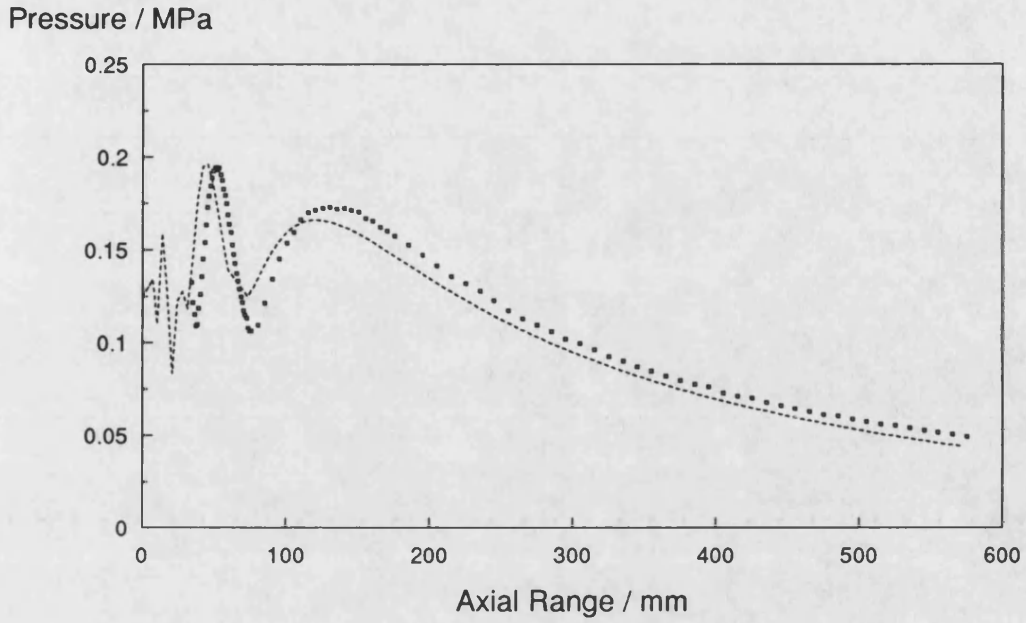

Figure 5.53 Comparison of the predicted fundamental (dotted line) with measured values (markers) at DL3, f=2.25 MHz, a=10 mm, b=18 mm, P_0=125 kPa.

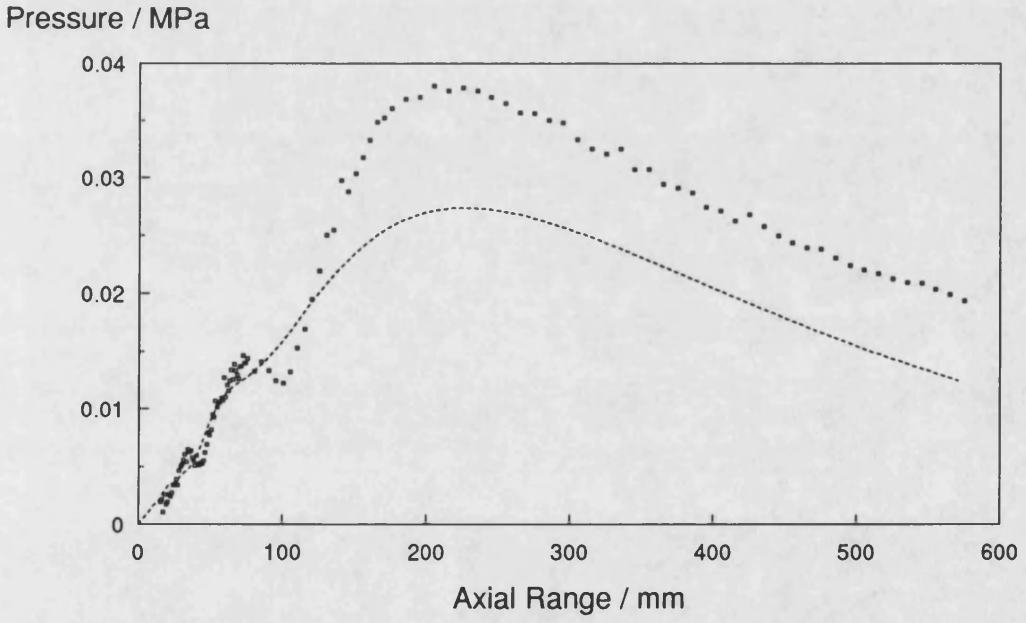

Figure 5.54 Comparison of the predicted second harmonic (dotted line) with measured values (markers) at DL3, f=2.25 MHz, a=10 mm, b=18 mm, P_0=125 kPa.

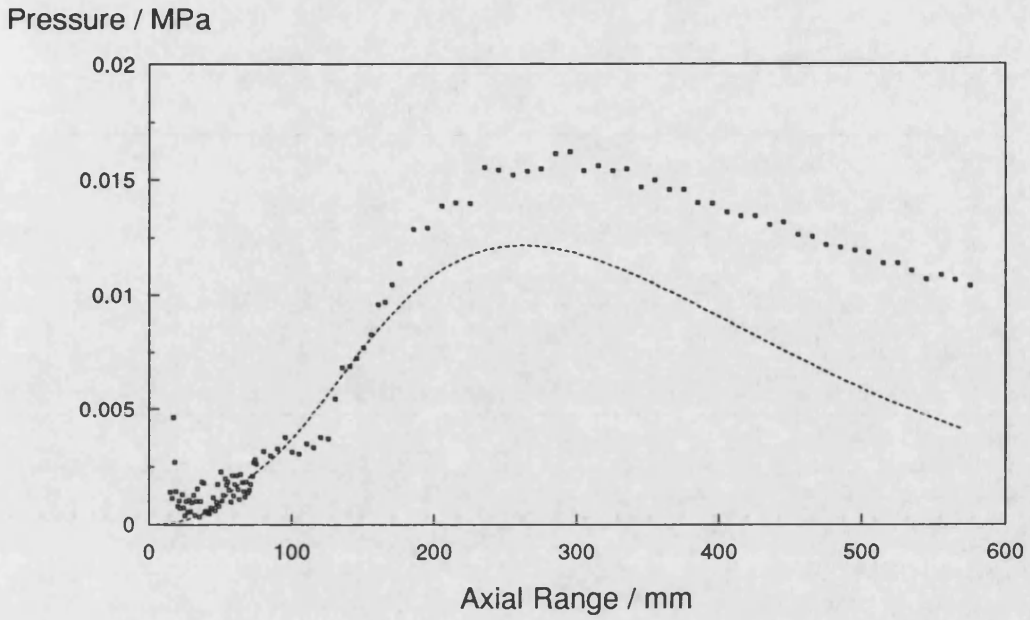

Figure 5.55 Comparison of the predicted third harmonic (dotted line) with measured values (markers) at DL3, f=2.25 MHz, a=10 mm, b=18 mm, P_0=125 kPa.

It is noticeable from Figure 5.56 and 5.57 that there is a difference in the near field structure of the fundamental for 15 x 30 mm rectangular aperture and as a result of the change in the fundamental pressure field, the second and higher harmonic pressure field changed, compared to 10 x 15 mm and 10 x 18 mm rectangular transducer's near field pressure variations. The results for this aperture are presented in Figures 5.56 - 5.60 at lowest drive level, and in Figures 5.61 - 5.65 at the highest drive level. The noticeable change in the near field structure is due to the increased aperture size and could be explained by examining the superposition of the edge wave and the central wave of the such a large rectangular aperture.

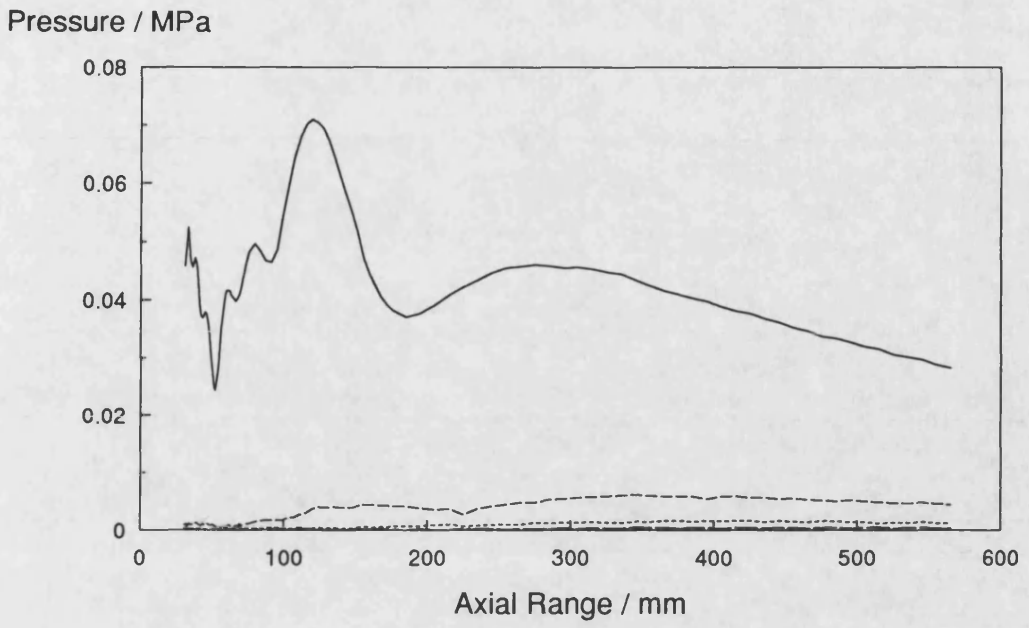

Figure 5.56 Measured axial pressure field of 15 x 30 mm rectangular aperture at DL1, f=2.25 MHz, P_0=47.5 kPa.

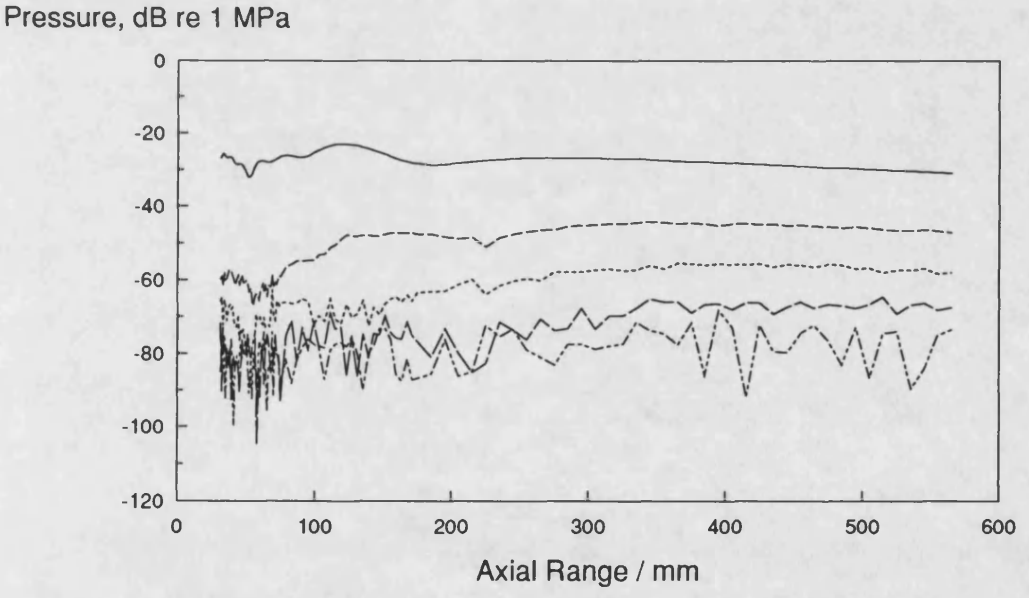

Figure 5.57 Measured axial pressure field of 15 x 30 mm rectangular aperture at DL1 (plotted relative to 1 MPa), f=2.25 MHz, P_0=47.5 kPa.

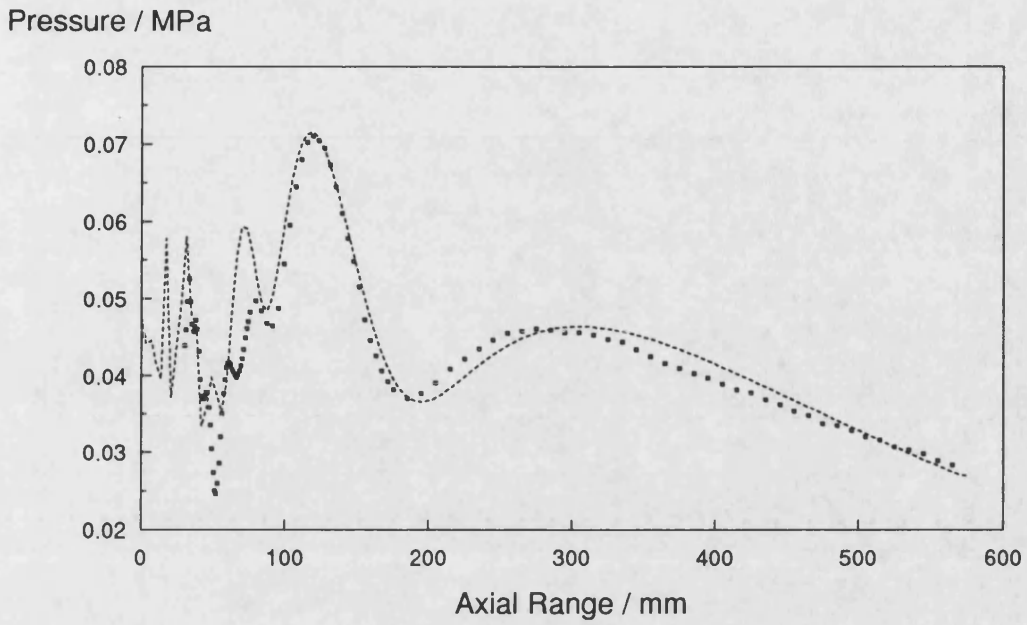

Figure 5.58 Comparison of the predicted fundamental (dotted line) with measured values (markers) at DL1, f=2.25 MHz, a=15 mm, b=30 mm, P_0=47.5 kPa.

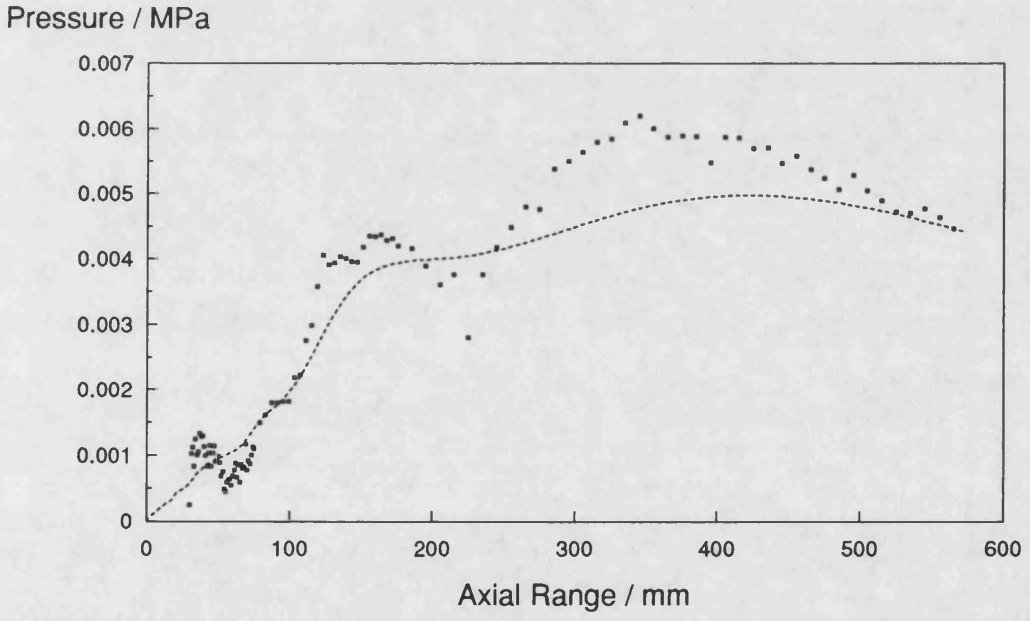

Figure 5.59 Comparison of the predicted second harmonic (dotted line) with measured values (markers) at DL1, f=2.25 MHz, a=15 mm, b=30 mm, P_0=47.5 kPa.

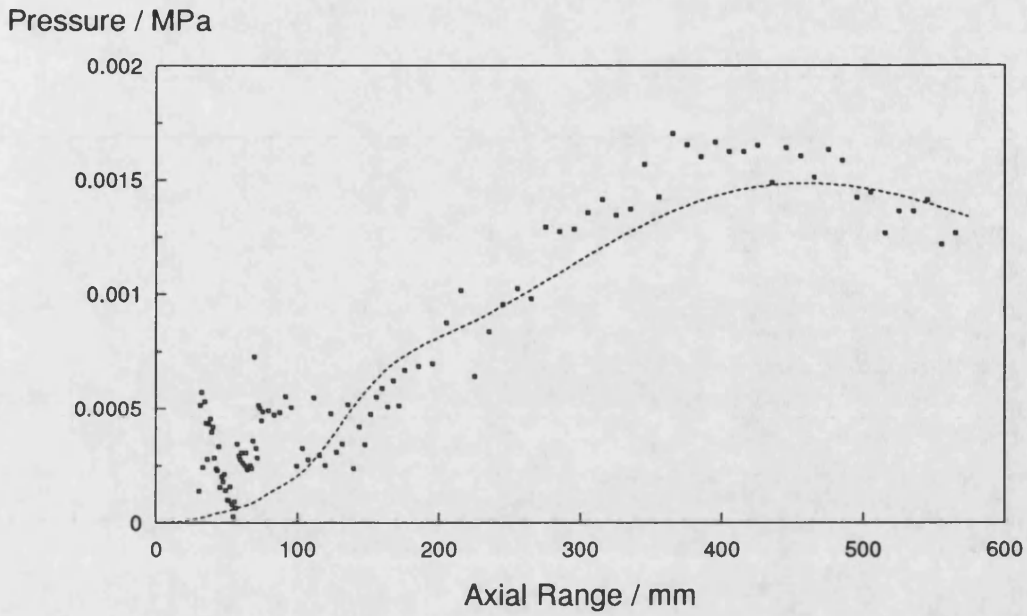

Figure 5.60 Comparison of the predicted third harmonic (dotted line) with measured values (markers) at DL1, f=2.25 MHz, a=15 mm, b=30 mm, P_0=47.5 kPa.

Normally, there should be constructive or destructive interference depending on whether the two waves (the central and the edge wave) are in phase or not. In the case of square aperture, there will never be full construction or full cancellation of the waves and this is due to the contribution from the corners of the square source. However, in the case of rectangular aperture of larger size, the contribution from the edge wave increases changing the near field structure, but this never causes full cancellation of the waves. However, the constructive or destructive interface is much greater for rectangular apertures of larger size than for a square or circular source.

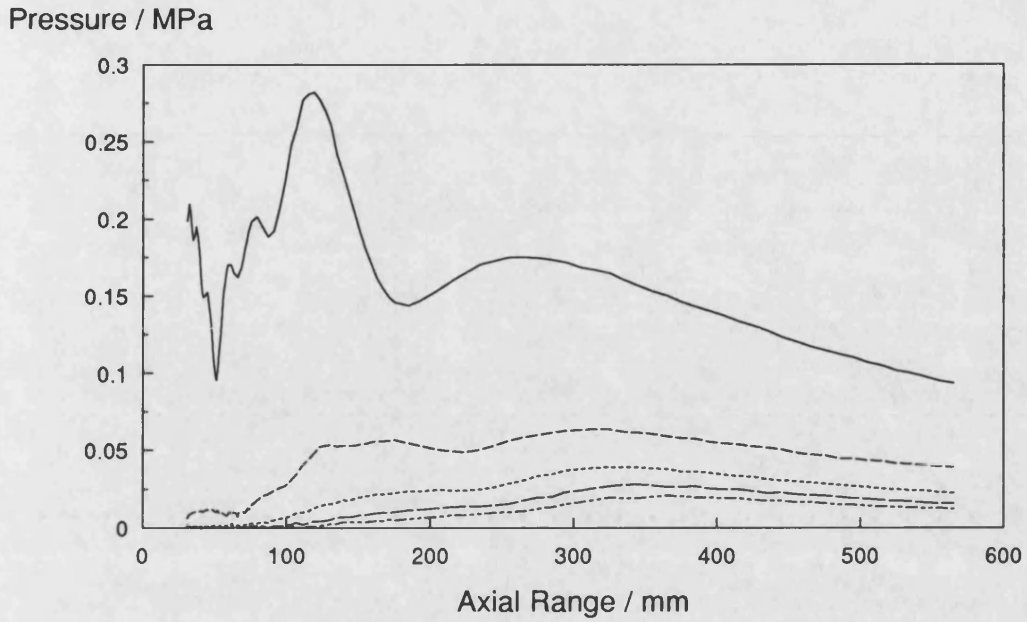

Figure 5.61 Measured axial pressure field of 15 x 30 mm rectangular aperture at DL3, f=2.25 MHz, P_0=180 kPa.

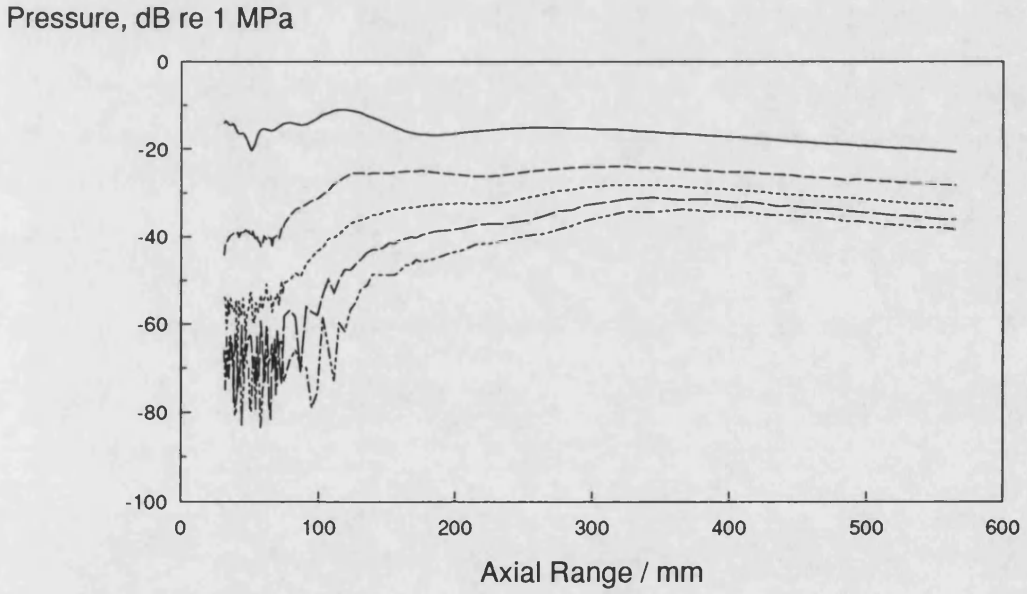

Figure 5.62 Measured axial pressure field of 15 x 30 mm rectangular aperture at DL3 (plotted relative to 1 MPa), f=2.25 MHz, P_0=180 kPa.

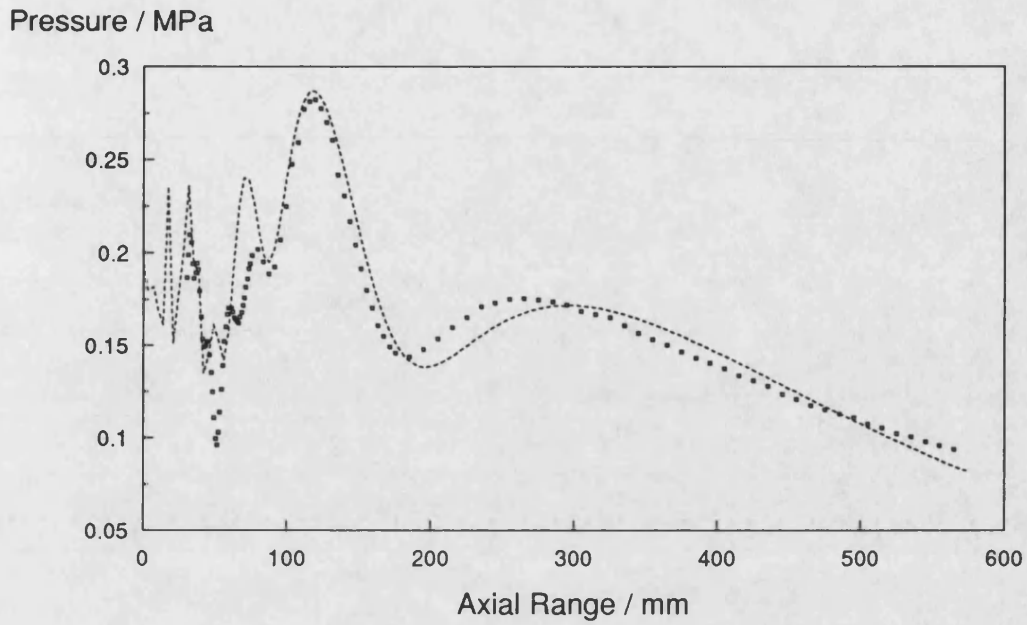

Figure 5.63 Comparison of the predicted first fundamental (dotted line) with measured values (markers) at DL3, f=2.25 MHz, a=15 mm, b=30 mm, P_0=180 kPa.

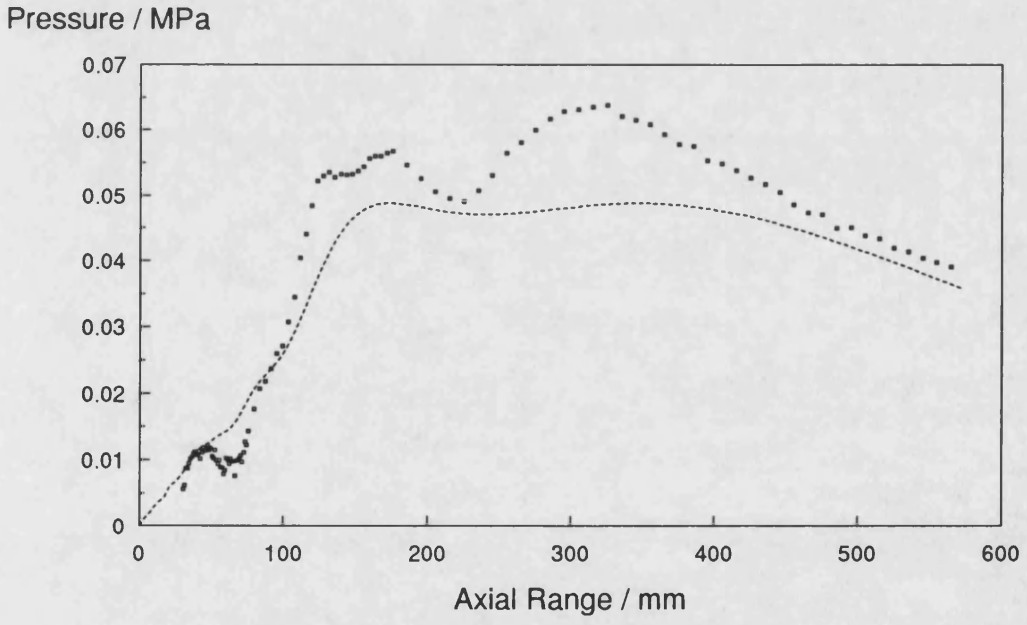

Figure 5.64 Comparison of the predicted second harmonic (dotted line) with measured values (markers) at DL3, f=2.25 MHz, a=15 mm, b=30 mm, P_0=180 kPa.

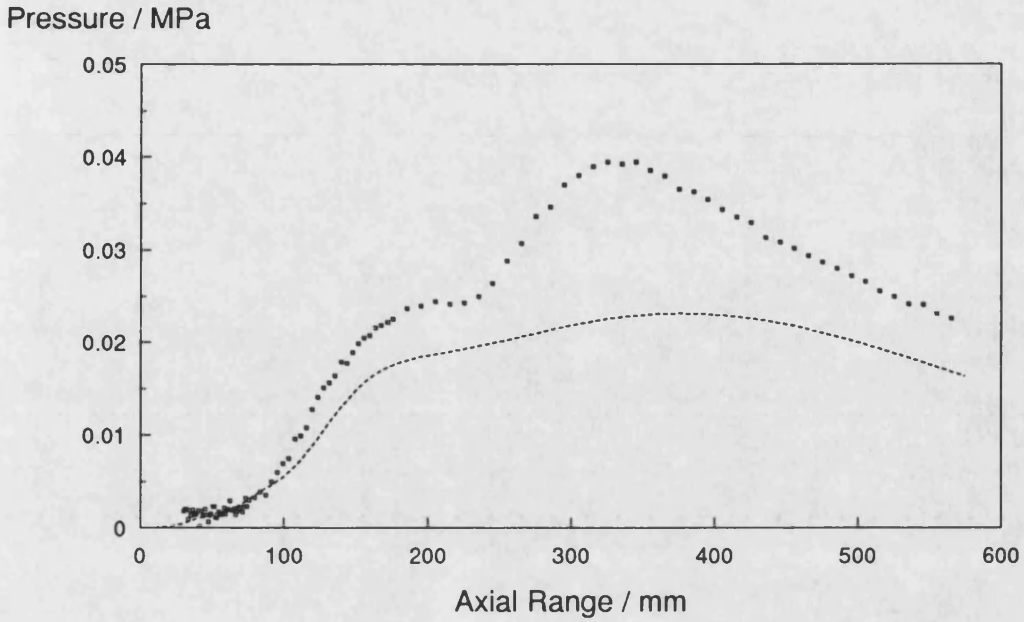

Figure 5.65 Comparison of the predicted third harmonic (dotted line) with measured values (markers) at DL3, f=2.25 MHz, a=15 mm, b=30 mm, P_0=180 kPa.

5.3.2 Focused rectangular aperture

Because of its geometry, rectangular apertures allow various kinds of focusing such as: focusing in one direction only (x or y), in both directions with equal focal gains and various focal gains in each direction. However, this complex geometry makes the theoretical and experimental work more difficult.

One dimensional focusing was studied with a rectangular aperture of 10 x 15 mm with a lens in front of it with a geometric focal length of 160 mm and measured results at the lowest drive level are presented in Figure 5.66. The agreement with the theory for this case is presented in Figure 5.67 for the fundamental and in Figure 5.68 for the second harmonic. In general, the agreement between theory and experiment is good, the maximum discrepancy occurs between the last and penultimate axial maximum of the first harmonic and is about 15%, at longer ranges, the agreement is much better.

Figure 5.69 shows the measured axial pressure field at DL3 and agreement for the fundamental, second and third harmonics are presented in Figure 5.70, 5.71 and 5.72 respectively. It is noticeable that the fundamental shows the similar agreement to that of obtained at DL1 but more discrepancy was observed for the second and third harmonic components, because of the reasons discussed earlier in this chapter.

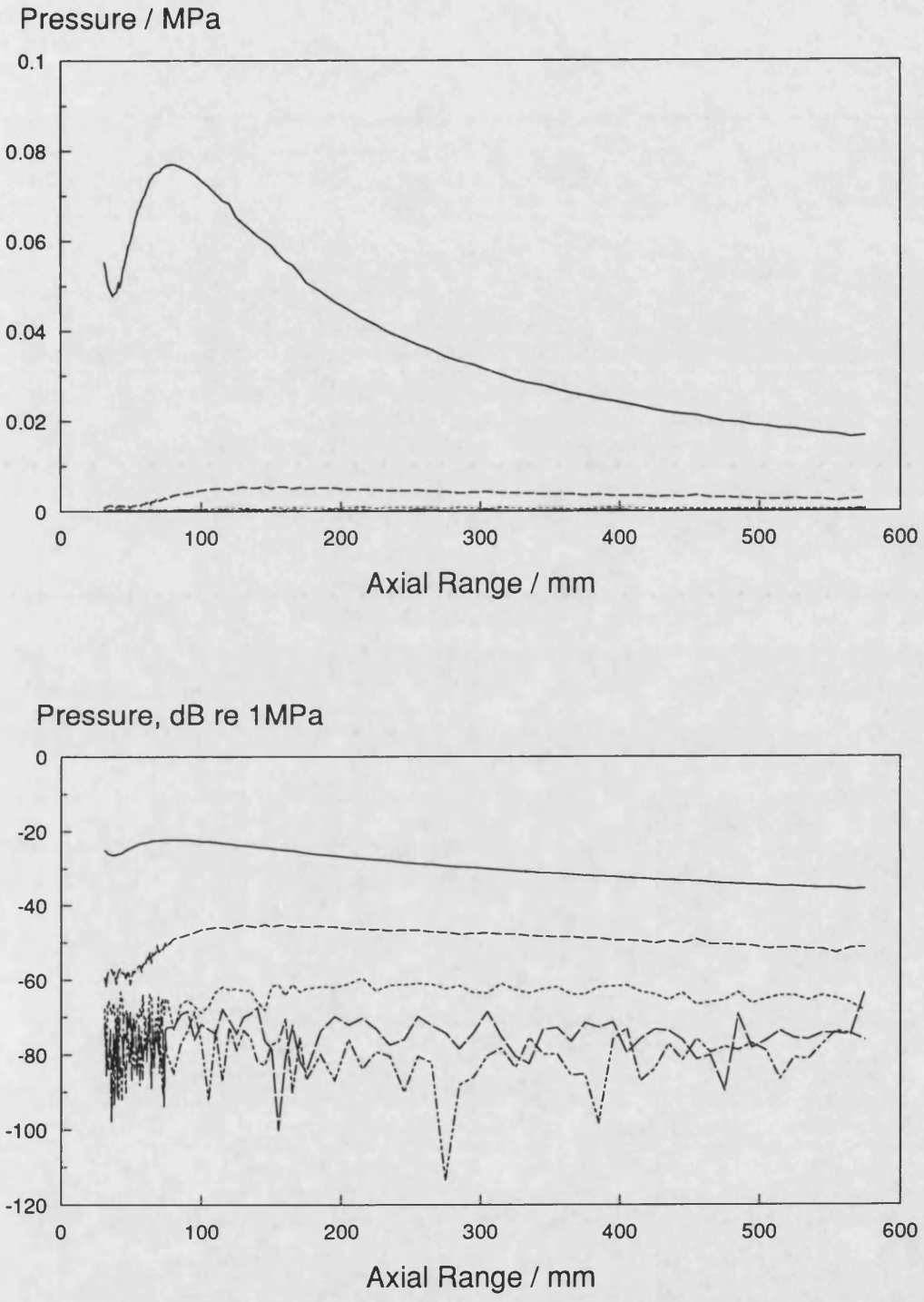

Figure 5.66 Measured axial pressure field of 10 x 15 mm focused rectangular aperture at DL1, f=2.25 MHz, F_y=160 mm, P_0=50 kPa.

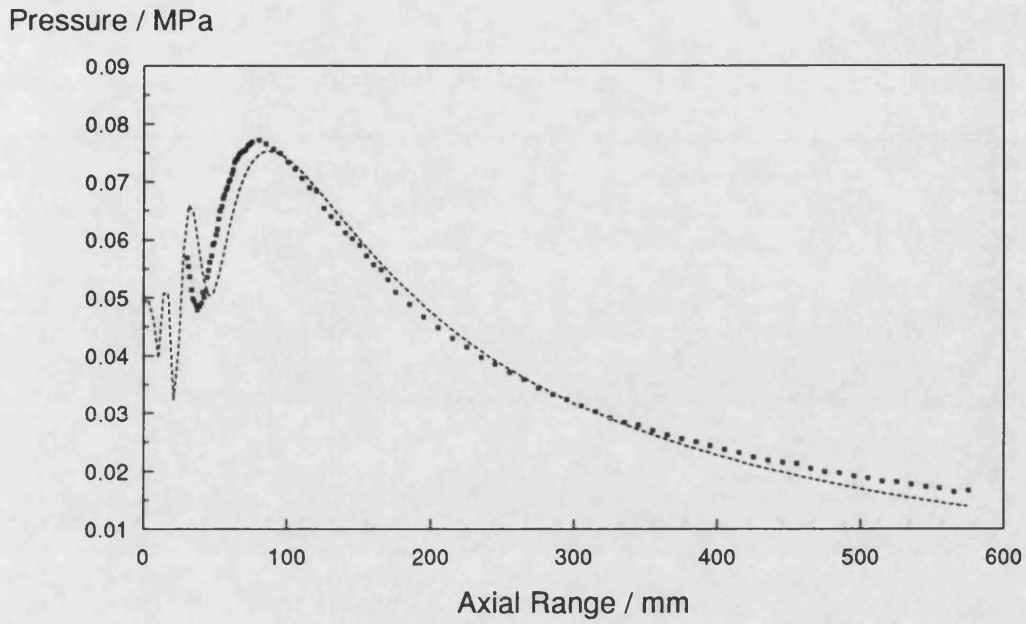

Figure 5.67 Comparison of predicted fundamental (dotted line) with measured values (markers) at DL1 for a focused rectangular aperture, a=10 mm, b=15 mm, F_y=160 mm, P_0=50 kPa.

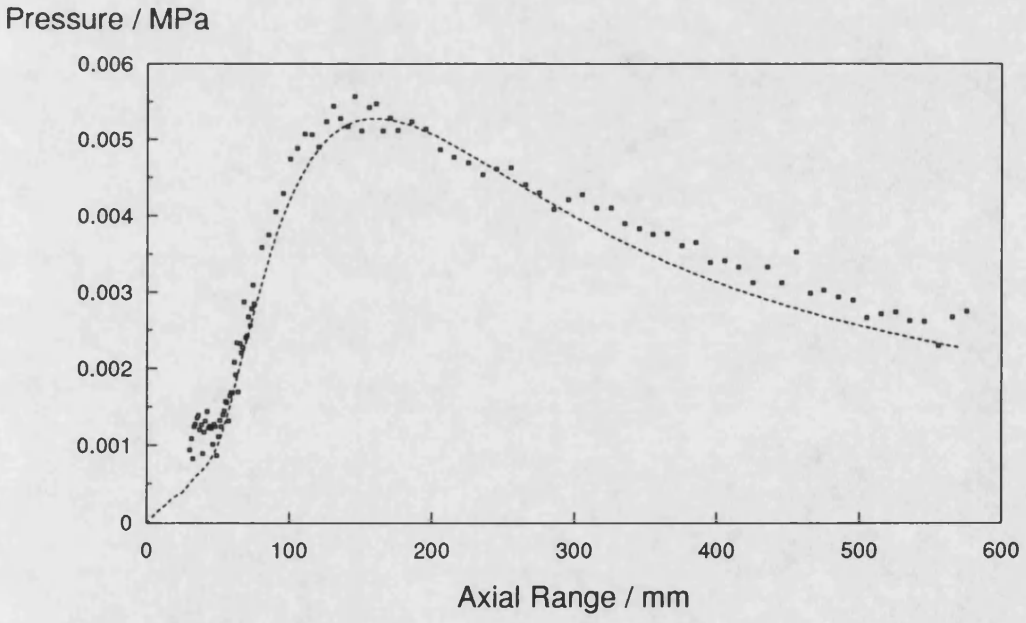

Figure 5.68 Comparison of predicted second harmonic (dotted line) with measured values (markers) at DL1 for a focused rectangular aperture, a=10 mm, b=15 mm, F_y=160 mm, P_0=50 kPa.

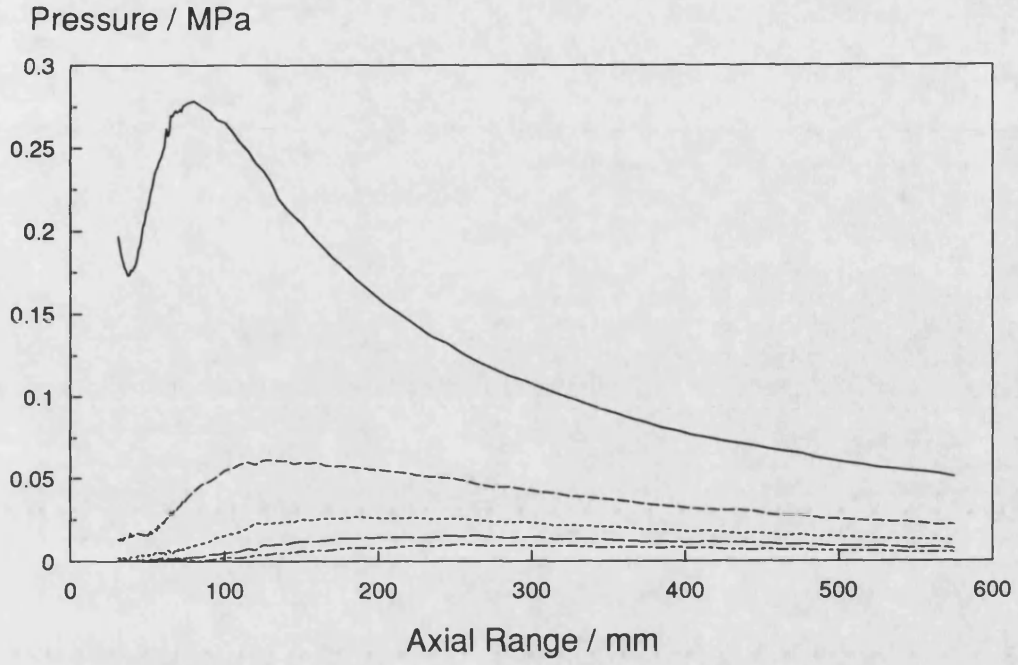

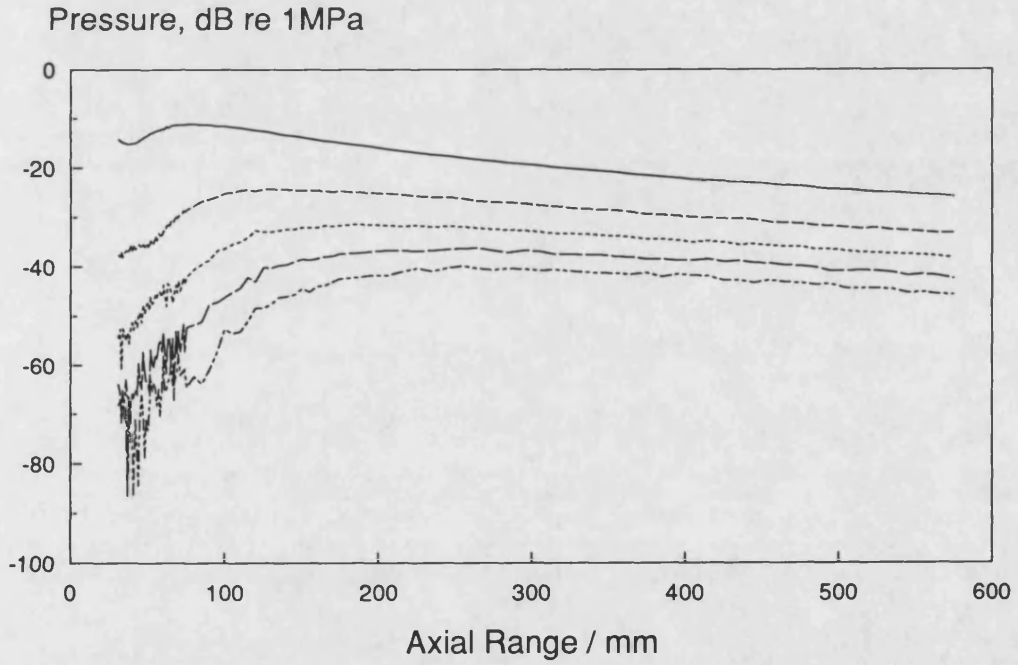

Figure 5.69 Measured axial pressure field of 10 x 15 mm focused rectangular aperture at DL3, f=2.25 MHz, F_y=160 mm, P_0=165 kPa.

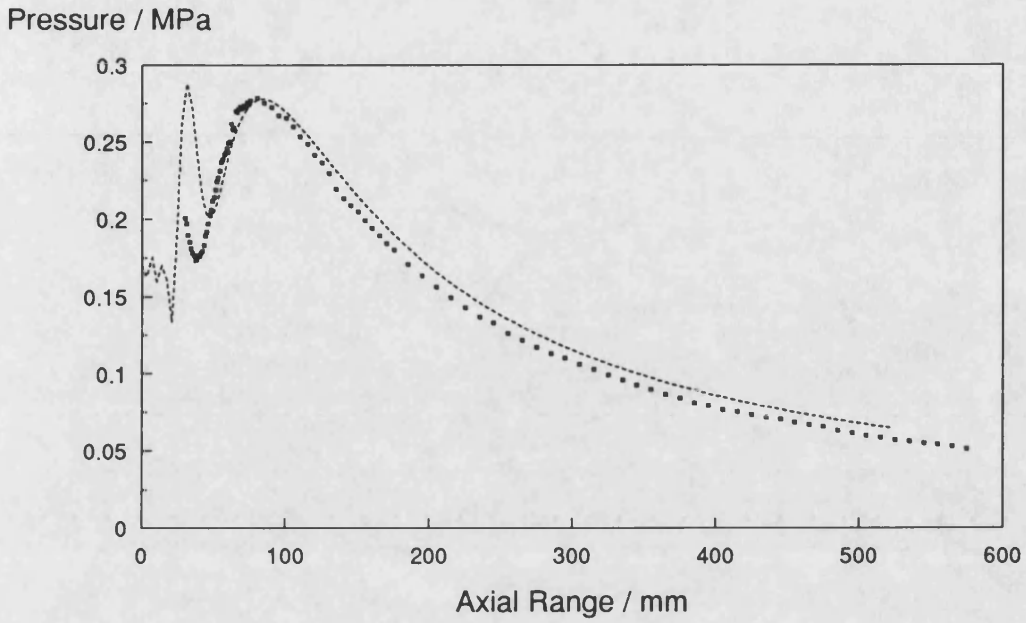

Figure 5.70 Comparison of predicted fundamental (dotted line) with measured values (markers) at DL3 for a focused rectangular aperture, a=10 mm, b=15 mm, F_y=160 mm, P_0=165 kPa.

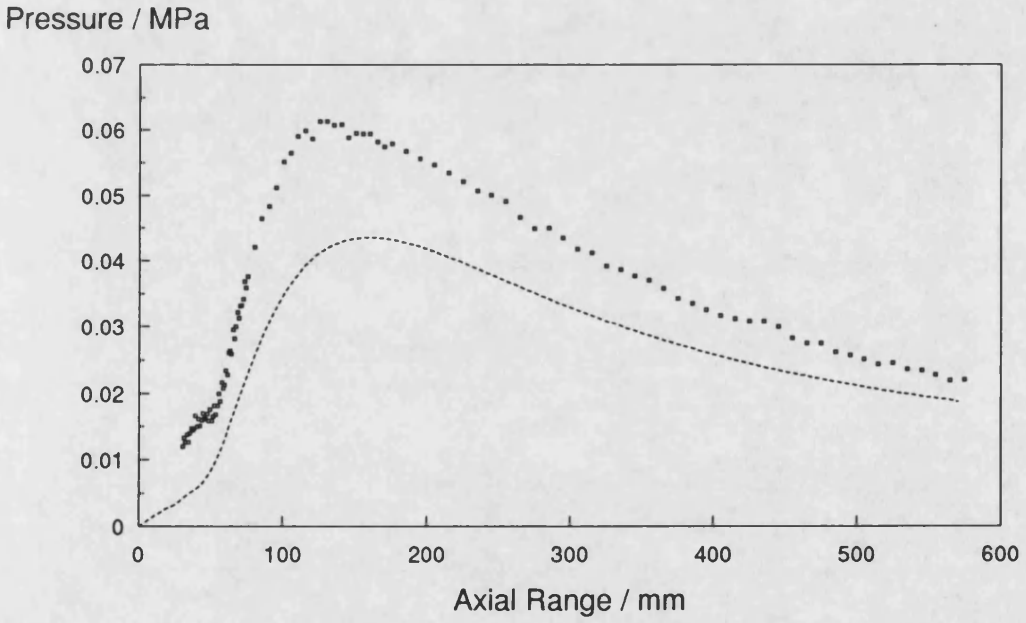

Figure 5.71 Comparison of predicted second harmonic (dotted line) with measured values (markers) at DL3 for a focused rectangular aperture, a=10 mm, b=15 mm, F_y=160 mm, P_0=165 kPa.

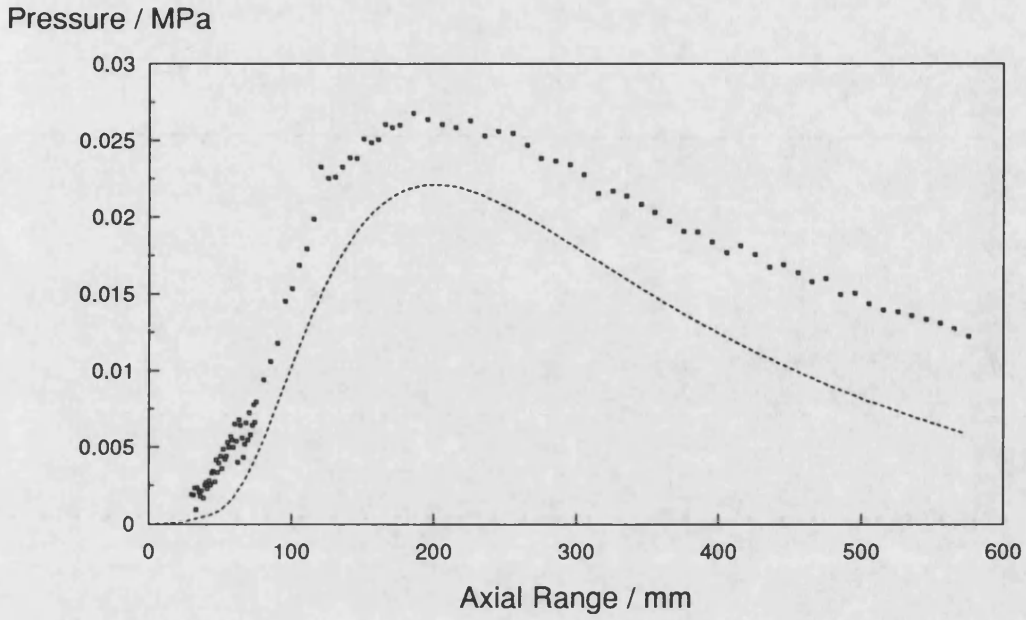

Figure 5.72 Comparison of predicted third harmonic (dotted line) with measured values (markers) at DL3 for a focused rectangular aperture, a=10 mm, b=15 mm, F_y=160 mm, P_0=165 kPa.

It was noticed that focused pressure field of rectangular apertures shares many features with rectangular plane piston field, apart from the axial pressure peak around the focal distance. Figure 5.73 and 5.74 show the on-axis pressure magnitude of the first five harmonics at DL3 for a square (25 mm) aperture focused first in the x direction then in the y direction with a lens of focal length of 160 mm. These results are not compared with theory and are presented to demonstrate that the axial pressure field structure is quite similar to each other, except a 5% peak pressure difference between the last axial maximums of the first harmonic. Since the source is square, the pressure field should be the same in the axial direction in both cases but a small discrepancy has occurred due to the errors in alignment and the focusing character of the lens. However, as expected, the first and higher harmonics show the same axial variation.

Turning to the two dimensional focusing case for the same aperture at the lowest drive level (Figure 5.75) with geometric focal lengths F_x=F_y=160 mm shows that the last axial minimum and minimum have shifted toward the aperture and the last axial maximum of the first harmonic shows a well pronounced peak compared to one dimensional focusing and plane case. The focusing gain for a rectangular aperture focused in both directions [65] is proportional to the area of the aperture divided by $F\lambda$, where F is the geometric focal length and λ is the wavelength. The measured average pressure closer to the source was 26.2 kPa and the pressure amplitude at the focal plane was 131 kPa which gives a pressure gain of 5.0 and the above definition gives 5.9. Thus, at the focal plane the discrepancy was about 15% but it was more than that between the last minimum and penultimate maximum. In this case, as the drive level is low, the second harmonic shows quite good agreement with the theory (the third harmonic is not compared at this drive level as it is very low in amplitude).

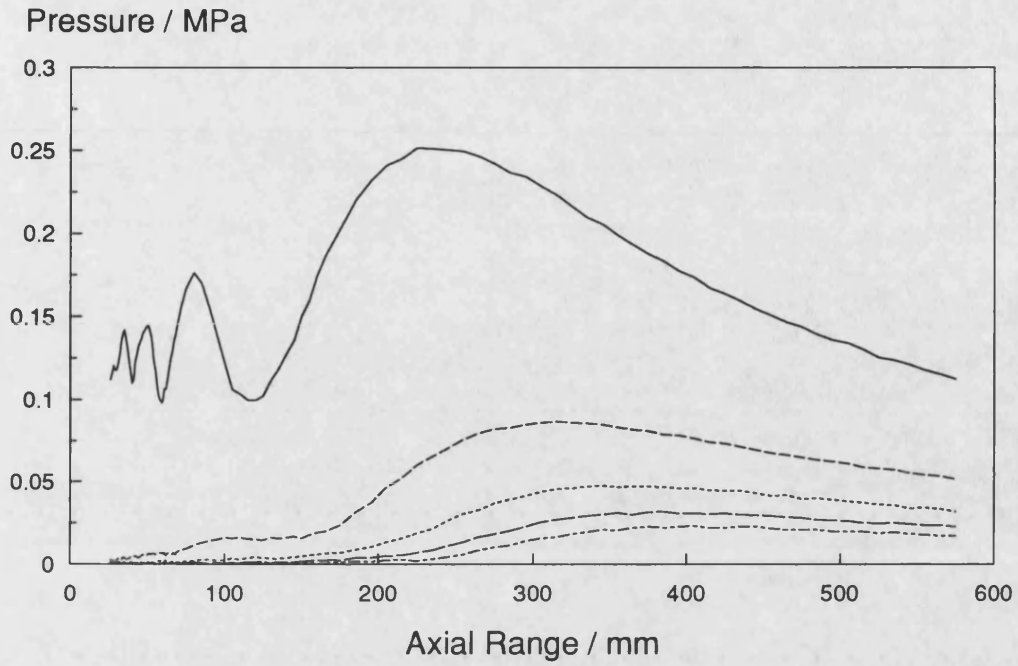

Figure 5.73 Measured axial pressure field of a focused square aperture at DL3, a=b=25 mm, f=2.25 MHz, F_x=160 mm, P_0=118 kPa.

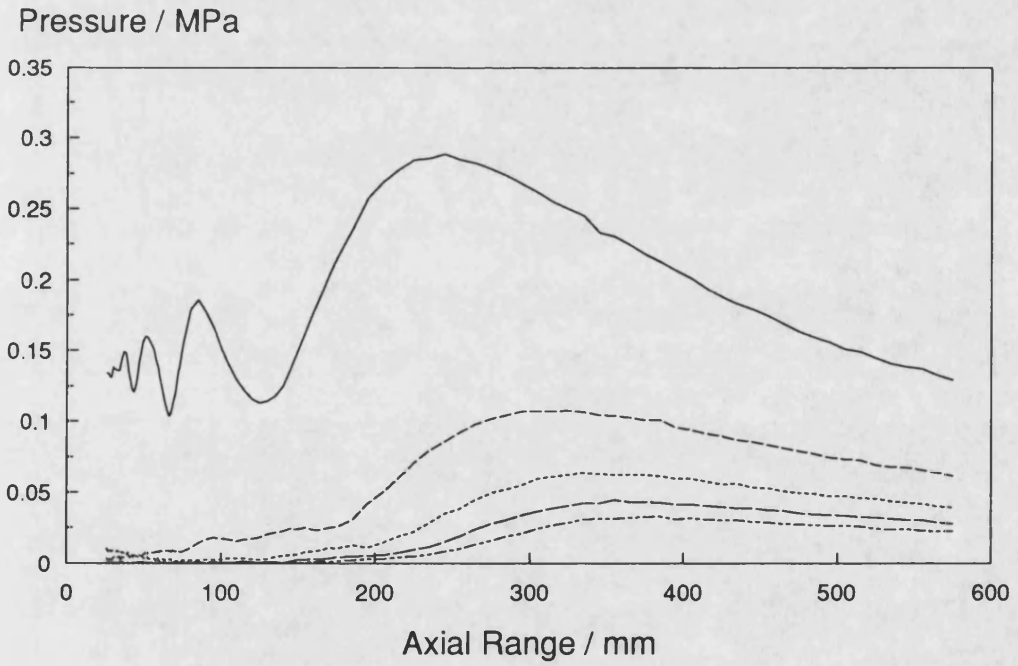

Figure 5.74 Measured axial pressure field of a focused square aperture at DL3, a=b=25 mm, f=2.25 MHz, F_y=160 mm, P_0=118 kPa.

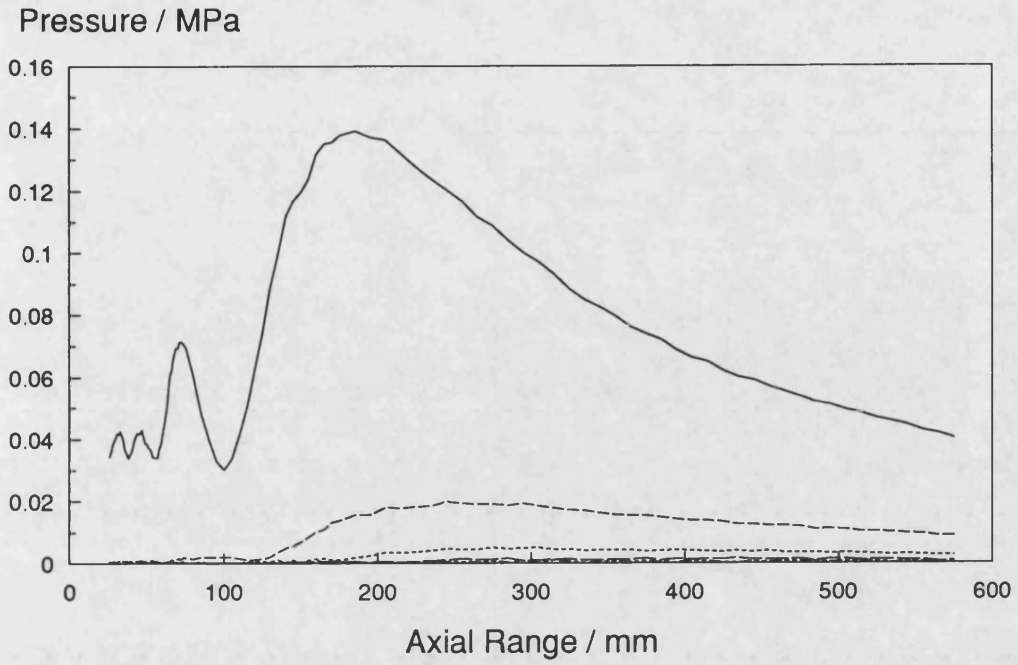

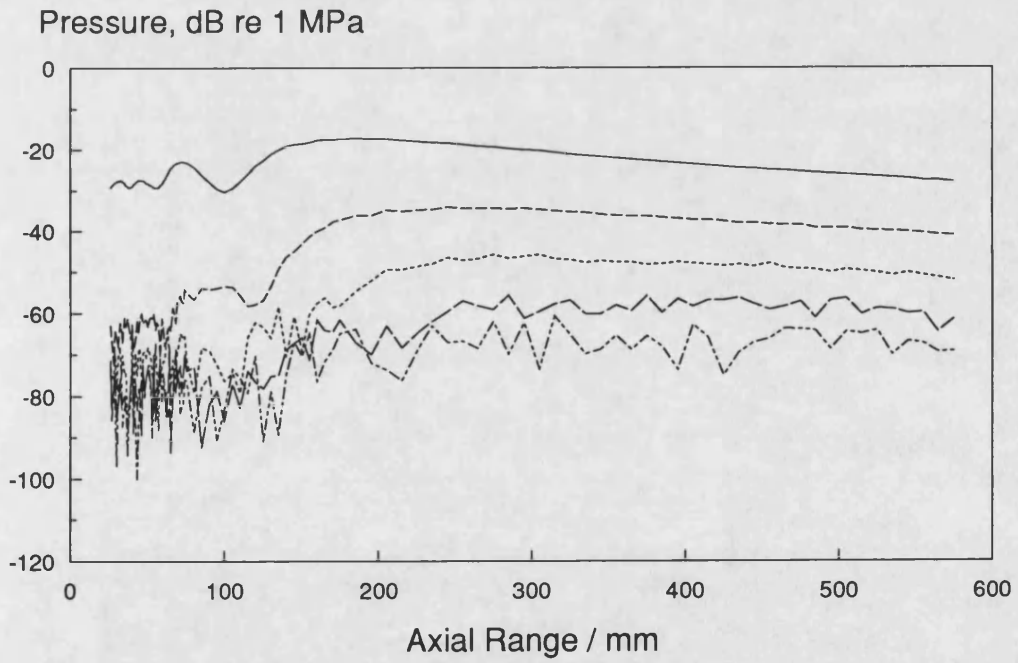

Figure 5.75 Measured axial pressure field of a focused square aperture at DL1, a=b=25 mm, f=2.25 MHz, F_x=F_y=160 mm, P_0=35 kPa.

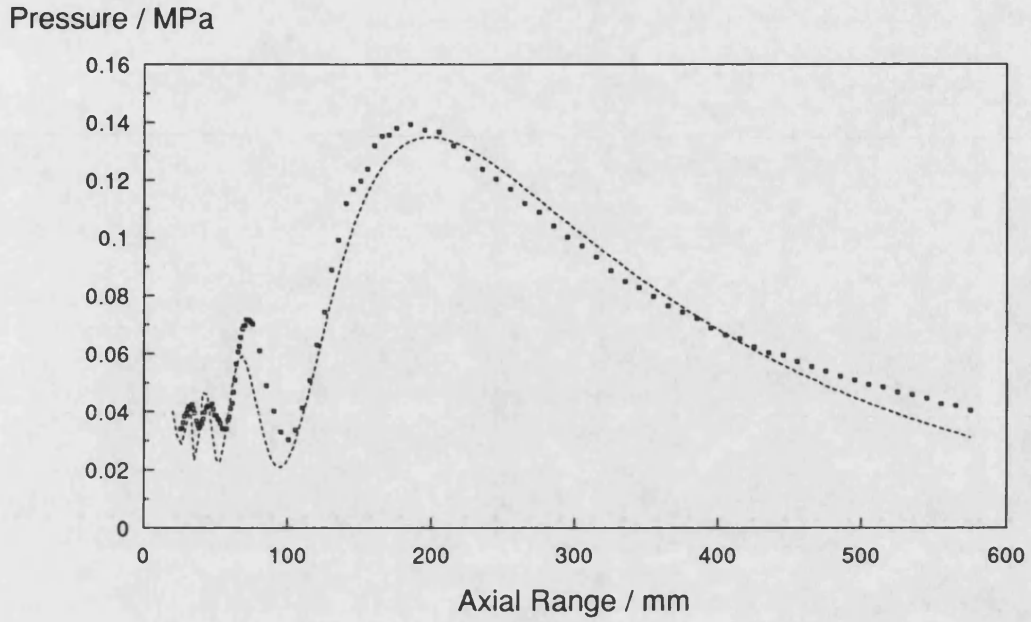

Figure 5.76 Comparison of predicted fundamental (dotted line) with measured values (markers) at DL1 for a focused square aperture, a=b=25 mm, F_x=F_y=160 mm, P_0=35 kPa.

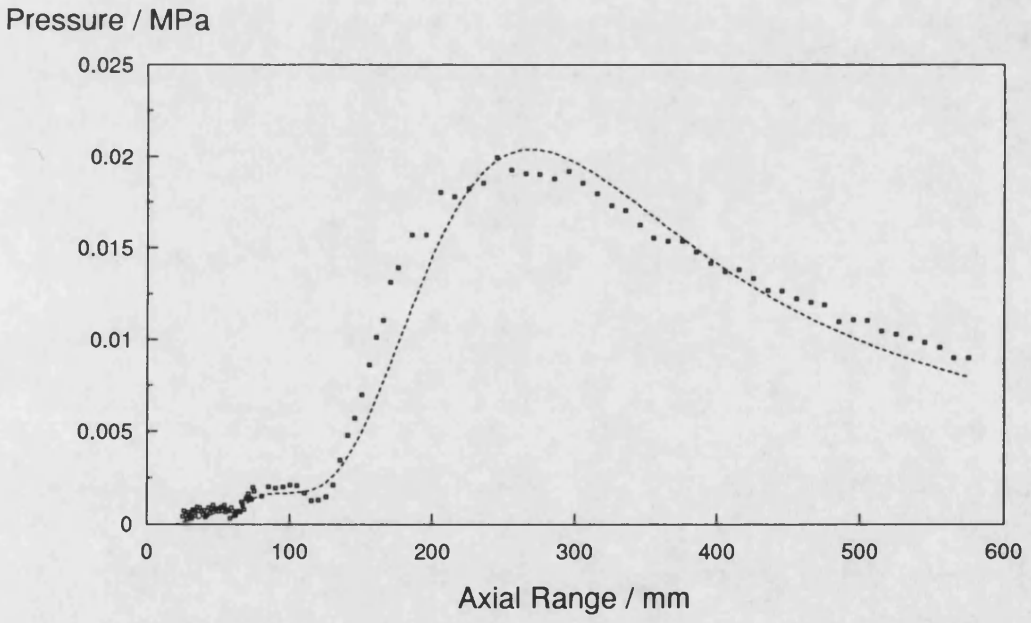

Figure 5.77 Comparison of predicted second harmonic (dotted line) with measured values (markers) at DL1 for a focused square aperture, a=b=25 mm, F_x=F_y=160 mm, P_0=35 kPa.

At the highest drive level (Figures 5.78 - 5.81), it is noticeable that the harmonic generation was quite negligible just before the focal plane but started growing with the increase in the pressure of the fundamental component and started fall off rapidly after the last axial maximum of the first harmonic. The discrepancy in the agreement at these drive levels was the same as seen at low drive level for the fundamental but more discrepancy occurred for the second and third harmonic. However, the agreement was not too bad for each drive level within the limitations of the plane wave theory and experimental configuration.

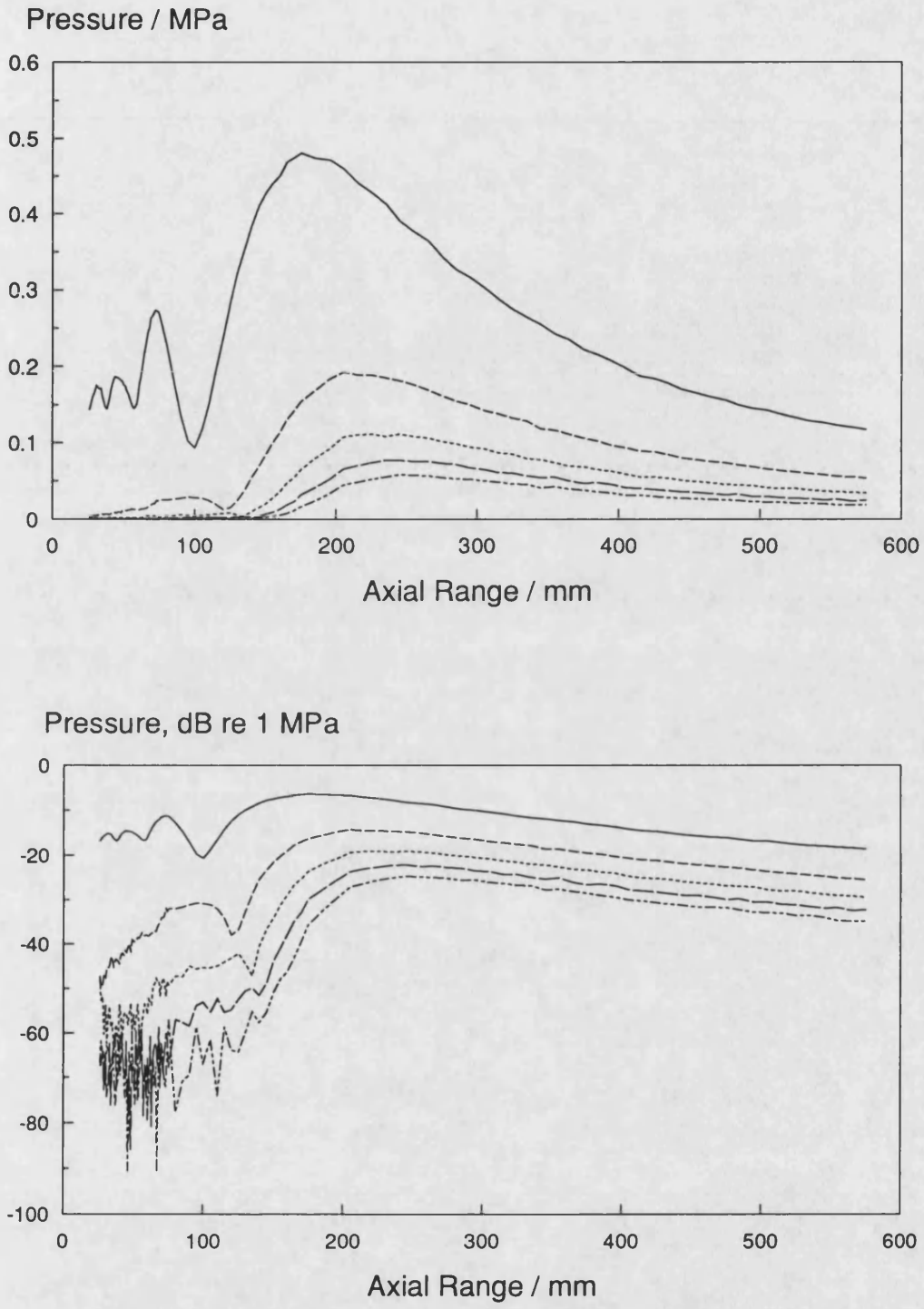

Figure 5.78 Measured axial pressure field of a focused square aperture at DL3, a=b=25 mm, f=2.25 MHz, F_x=F_y=160 mm, P_0=100 kPa.

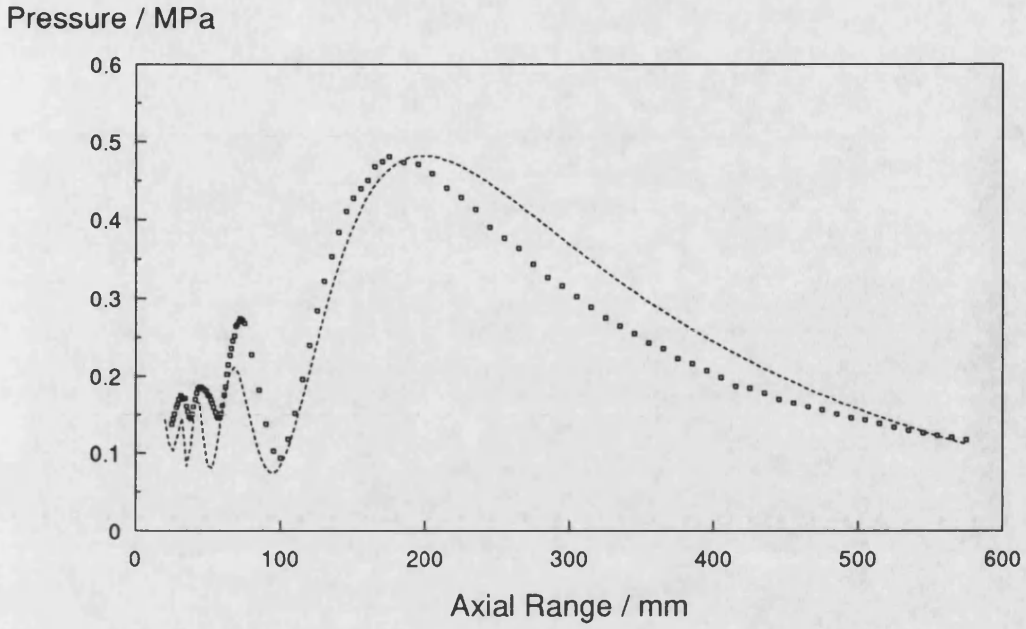

Figure 5.79 Comparison of predicted fundamental (dotted line) with measured values (markers) at DL3 for a focused square aperture, a=b=25 mm, F_x=F_y=160 mm, P_0=100 kPa.

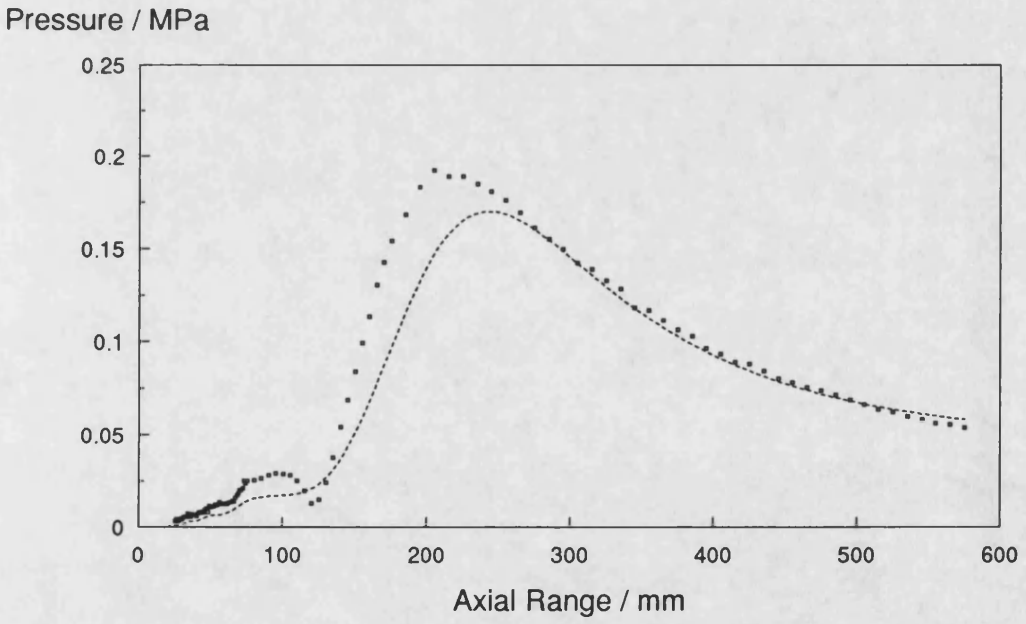

Figure 5.80 Comparison of predicted second harmonic (dotted line) with measured values (markers) at DL3 for a focused square aperture, a=b=25 mm, F_x=F_y=160 mm, P_0=100 kPa.

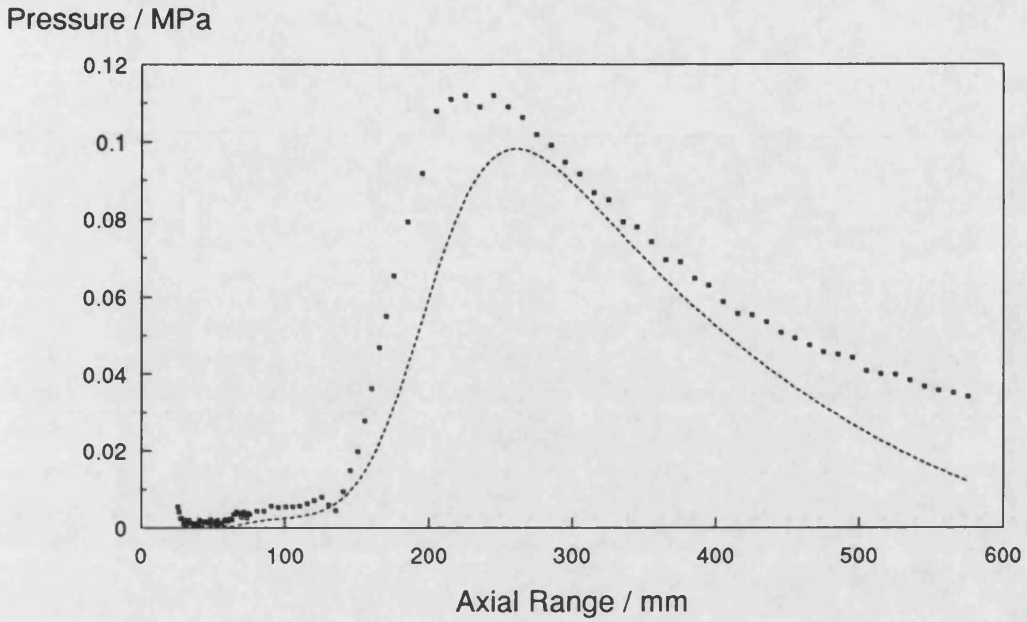

Figure 5.81 Comparison of predicted third harmonic (dotted line) with measured values (markers) at DL3 for a focused square aperture, a=b=25 mm, F_x=F_y=160 mm, P_0=100 kPa.

Since similar results to those of square apertures focused in both direction were obtained for the rectangular apertures, a limited number of results are presented only at the lowest drive level for the two dimensional focusing with equal geometric focal lengths of F_x=F_y=250 mm and different focal lengths in each direction (F_x=250 mm, F_y=160 mm). Figure 5.82 presents the measured pressure field along the acoustic axis of 18 x 10 mm rectangular aperture with two lenses in front of it with equal focal lengths F_x=F_y=250 mm. The measured pressure field results with different geometric focal lengths in x (F_x=250 mm) and y directions (F_y=160 mm) are presented in Figure 5.83 and compared with theory for the fundamental in Figure 5.84 showing good agreement after about 60 mm from the aperture. The agreement was similar for the case with equal focal length in both directions (Figure 5.85) for the fundamental after at about the same axial range.

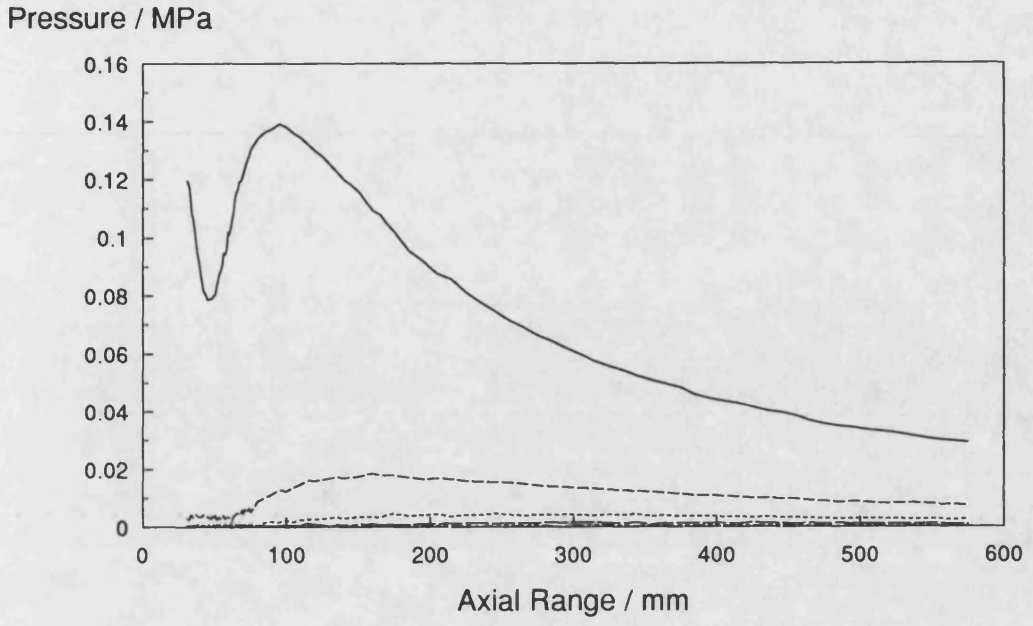

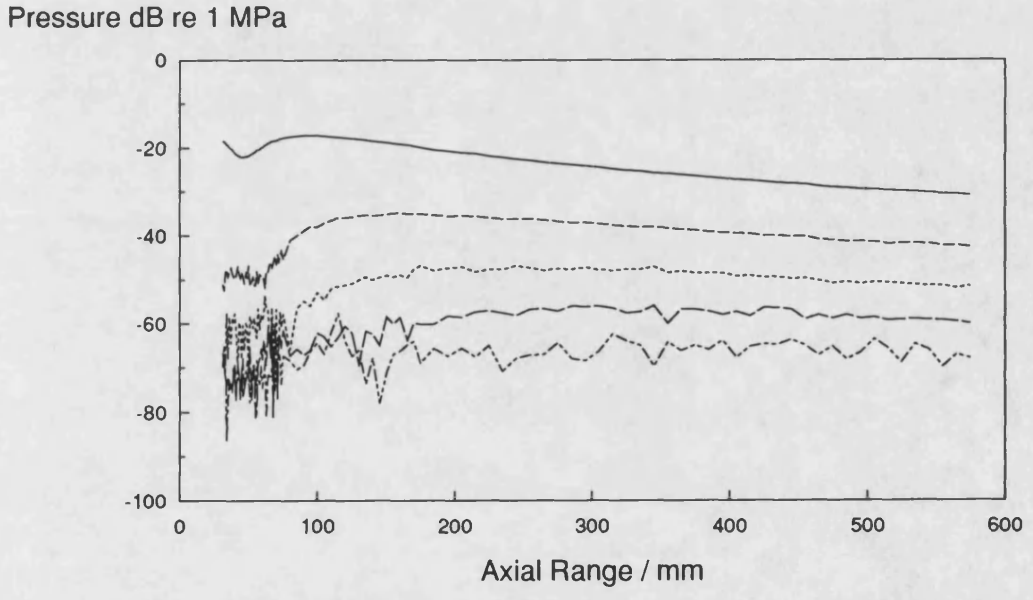

Figure 5.82 Measured axial pressure field of a focused rectangular aperture at DL1, a=18 mm, b=10 mm, f=2.25 MHz, F_x=F_y=250 mm, P_0=85 kPa.

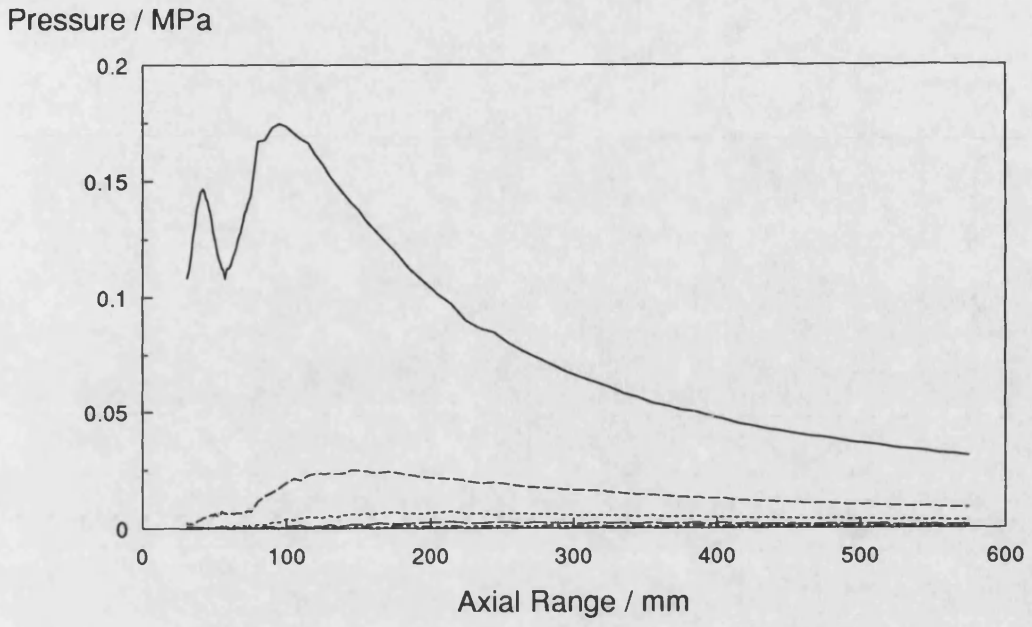

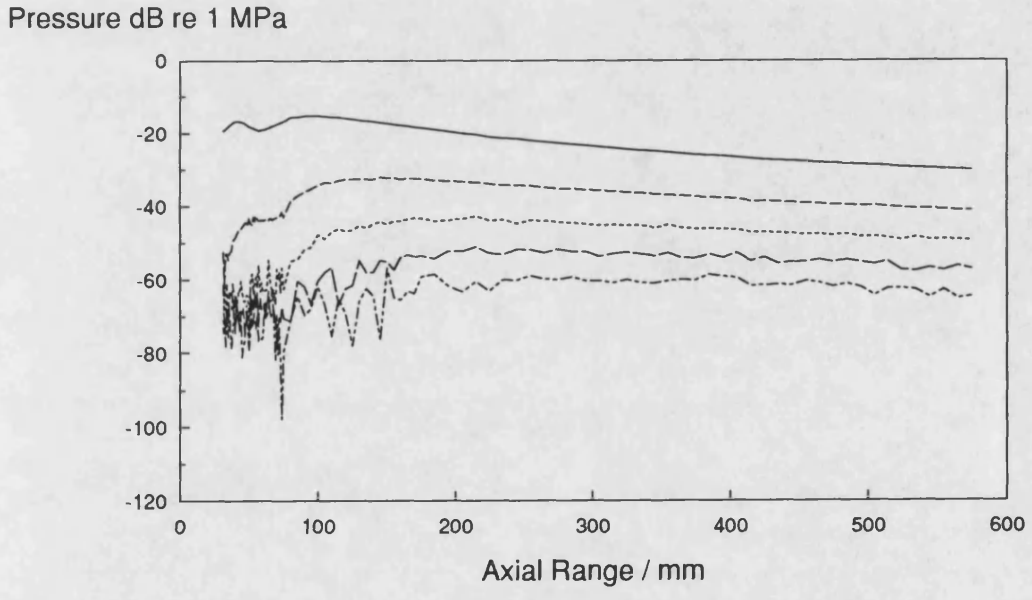

Figure 5.83 Measured axial pressure field of a focused rectangular aperture at DL1, a=18 mm, b=10 mm, f=2.25 MHz, F_x=250, F_y=160 mm, P_0=85 kPa.

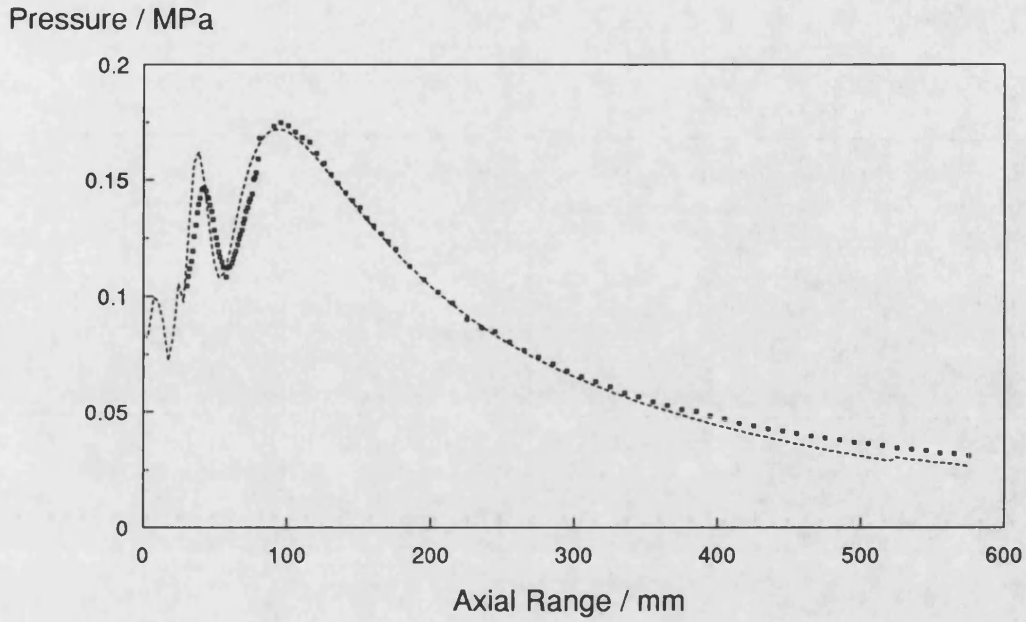

Figure 5.84 Comparison of predicted fundamental (dotted line) with measured values (markers) at DL1 for a focused rectangular aperture, a=18 mm, b=10 mm, F_x=250 mm, F_y=160 mm, P_0=85 kPa.

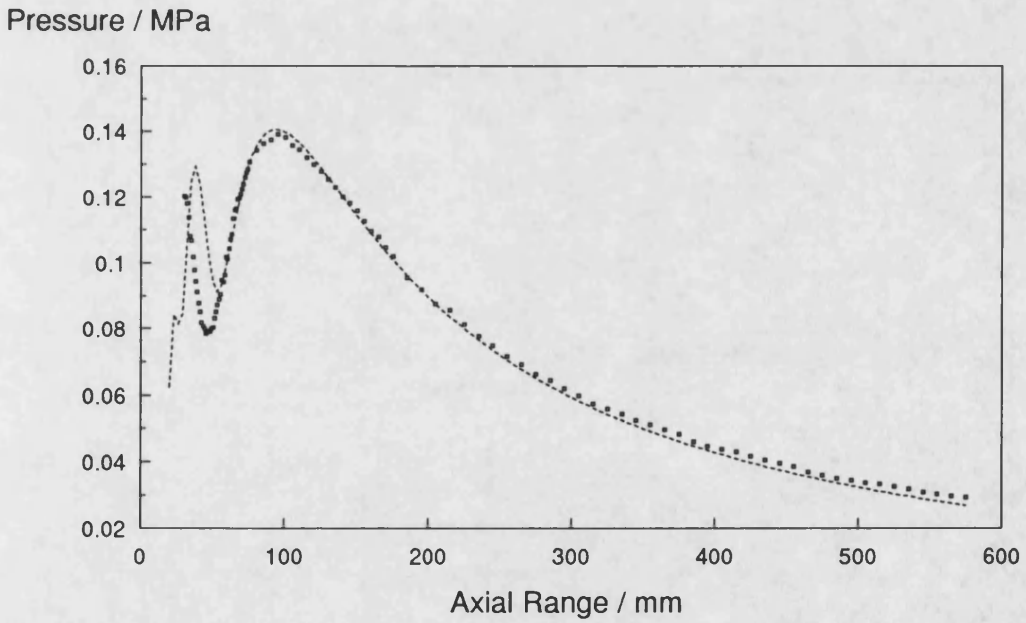

Figure 5.85 Comparison of predicted fundamental (dotted line) with measured values (markers) at DL1 for a focused rectangular aperture, a=18 mm, b=10 mm, F_x=F_y=250 mm, P_0=85 kPa.

5.4 TRANSVERSE FIELDS

The finite amplitude results for the section across the acoustic axis are presented for plane rectangular aperture of 10 x 18 mm at all drive levels and at three different distances from the aperture. Similar results were obtained for the focused rectangular (18 x 10 mm) source but results are only presented at the highest drive level. Since the theory is not able to predict the across axis pressure field, experimental results are only presented and could not be compared with theory.

5.4.1 Measured transverse fields

A typical measured transverse pressure field close to the 25 x 25 mm plane square source face (at z=20 mm) is shown in Figure 5.86 at the lowest drive level. The rapid oscillations across the acoustic axis are probably reduced due to finite hydrophone size and the interval between measurements. The second harmonic is, as expected, negligible at this range since the nonlinear distortion has not yet built up.

The measured across axis pressure field and phase variation of 10 x 18 mm plane rectangular aperture at 120 mm from the aperture face at the same drive level (DL1) is shown in Figure 5.87. It is noticeable that the fundamental component has a well pronounced main lobe and two side lobes on each side of the axis within the measured range. The second and third harmonic generation has started at this range but they have no side lobes yet. The generation of higher harmonics becomes clearer at 160 mm (Figure 5.88) and at 200 mm (Figure 5.89). The noticeable thing with increasing axial range was also that the side lobes

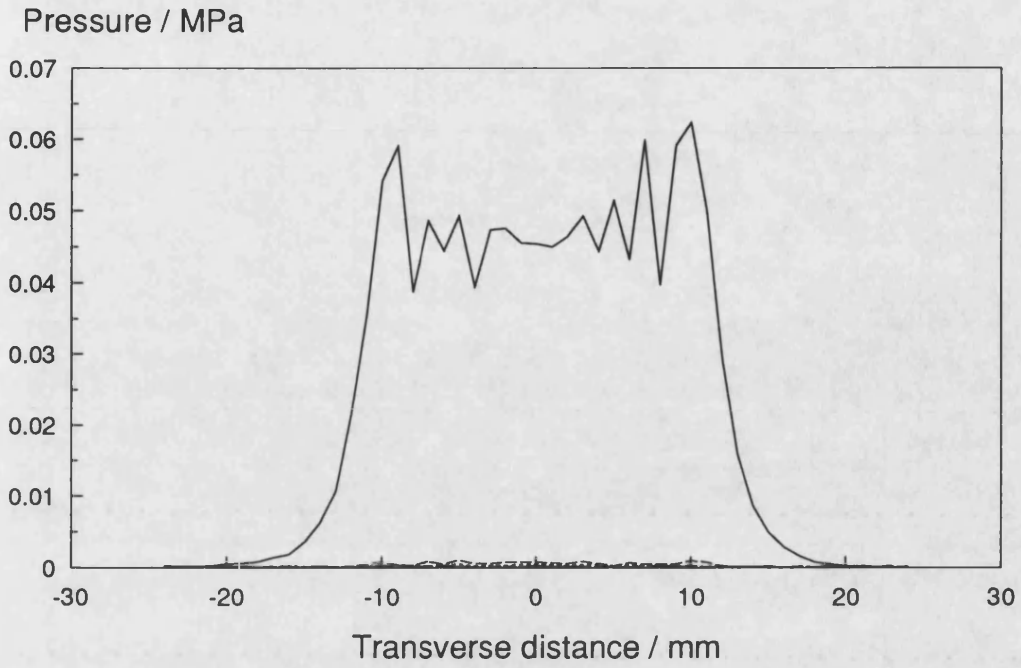

Figure 5.86 Measured transverse pressure field of 25 x 25 mm plane square aperture at DL1 and 20 mm from the aperture face.

for the fundamental were diverging. (This is also true for the higher harmonics but their pressure levels are not high enough to see the same effect.) Although the beam was narrower closer to the aperture, it started broadening at longer ranges as expected.

Figure 5.90 shows the measured transverse pressure fields for the same rectangular aperture at DL3. It could be seen that the increased drive level caused more harmonic generation. Further, we see for the fundamental that the larger the distance from the aperture, the wider the main lobes and the more pronounced the maxima and minima. The same phenomena is seen for the second and higher harmonics. This is not only true for the rectangular case but also true for the square case as well as a circular case. We also observe that the second harmonic amplitude exhibits twice as many side lobes as the fundamental.

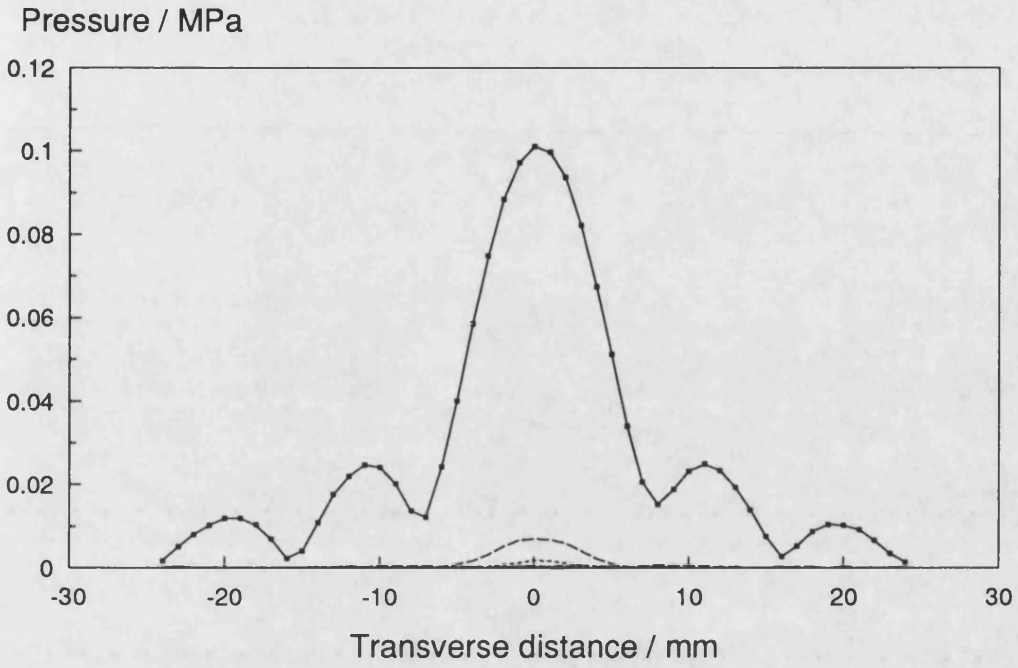

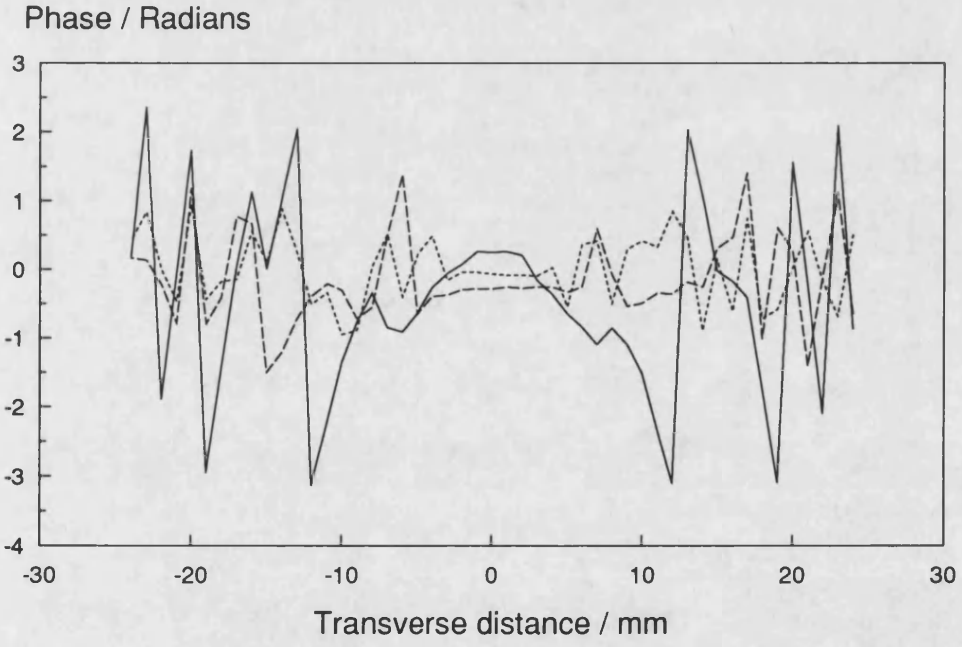

Figure 5.88 Transverse pressure field (top) and phase (bottom) of a plane rectangular source at DL1, a=10 mm, b=18 mm, z=120 mm.

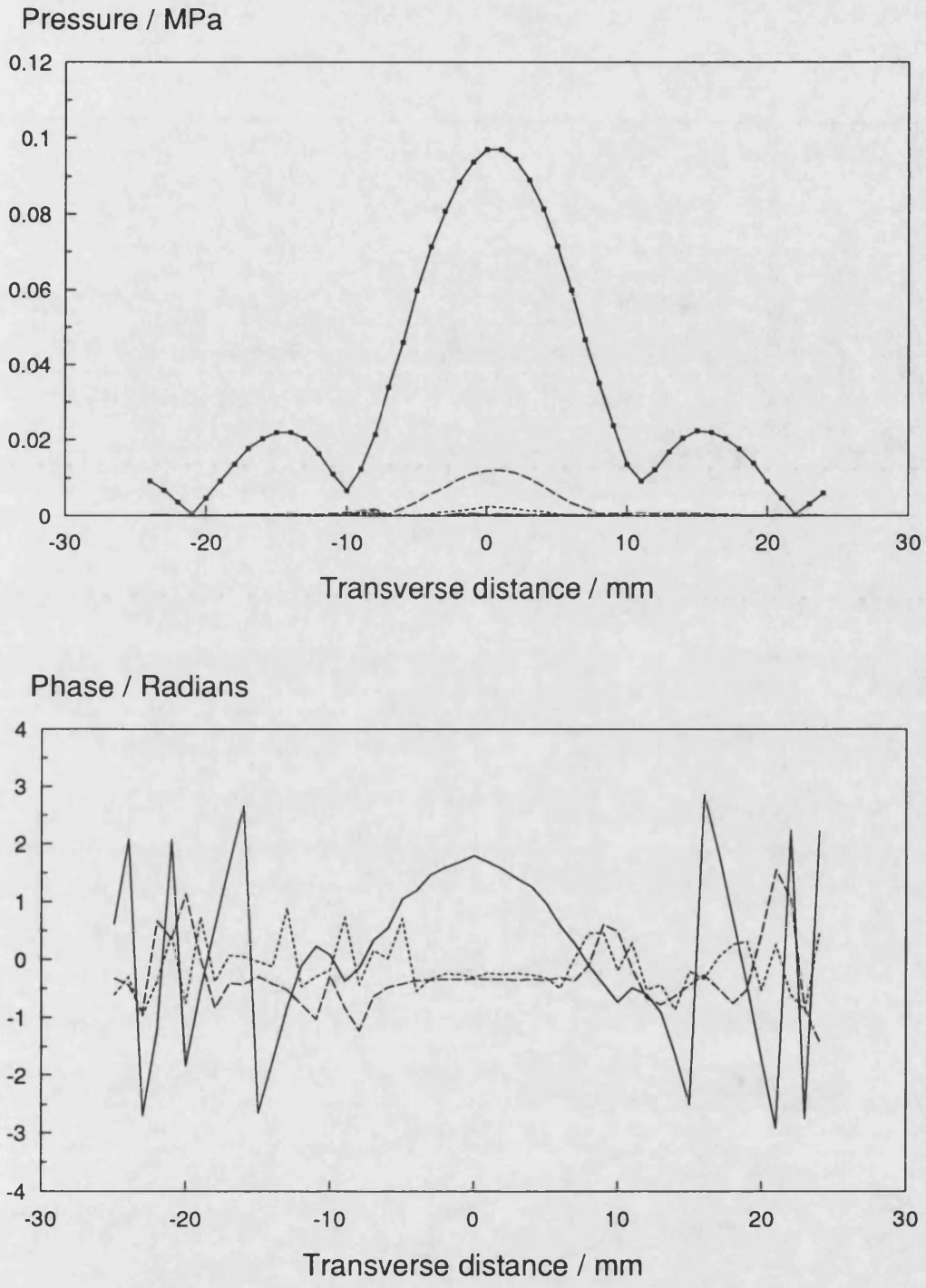

Figure 5.89 Transverse pressure field (top) and phase (bottom) of a plane rectangular source at DL1, a=10 mm, b=18 mm, z=160 mm.

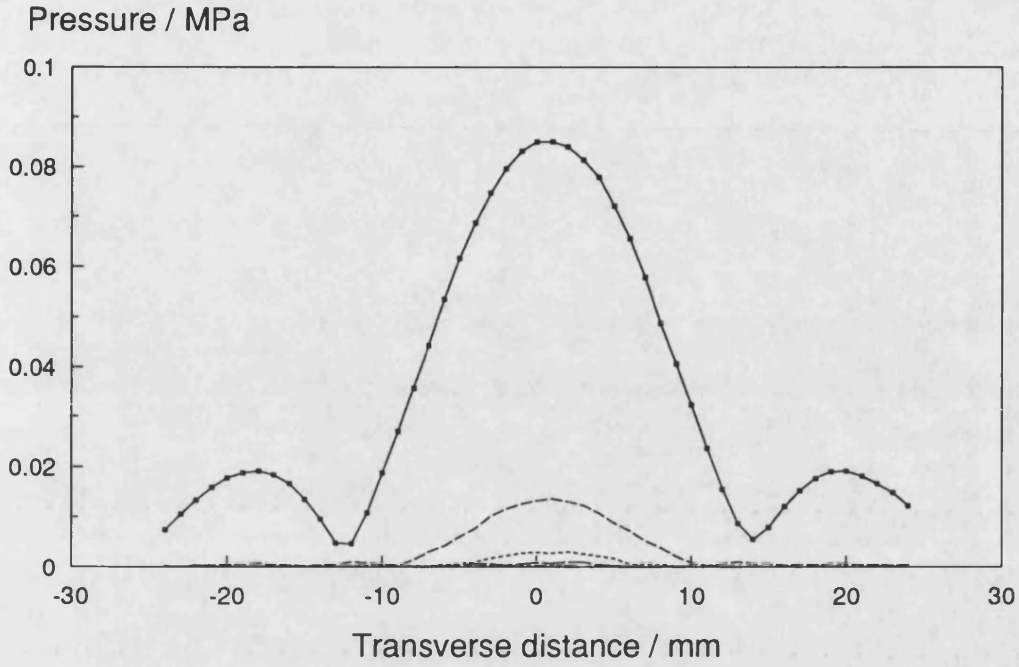

Figure 5.89 Transverse pressure field of a plane rectangular source at DL1, a=10 mm, b=18 mm, z=200 mm.

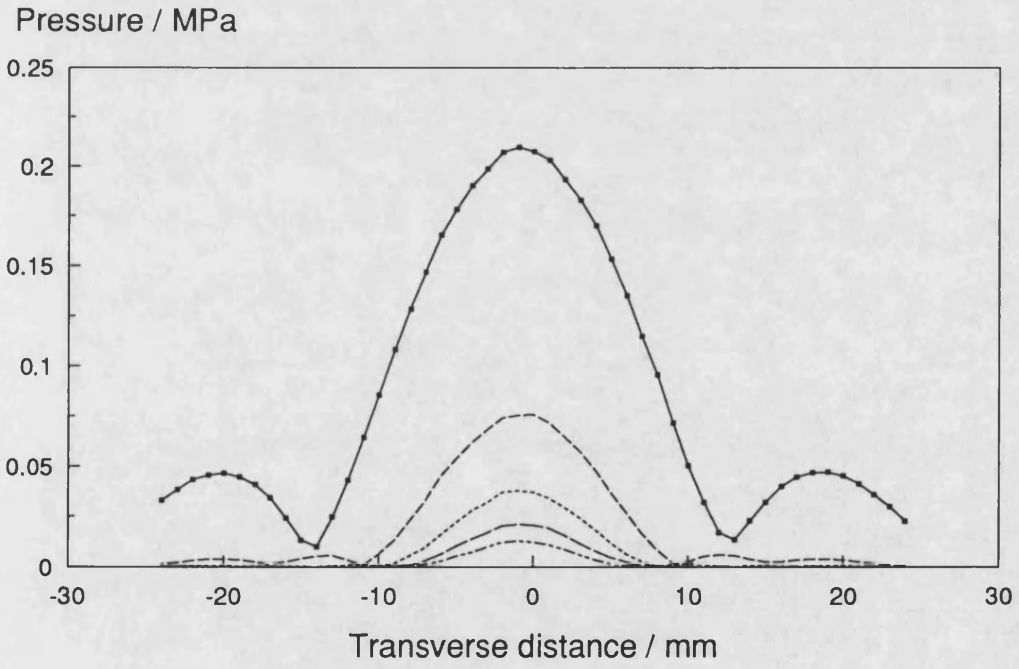

Figure 5.90 Transverse pressure field of a plane rectangular source at DL3, a=10 mm, b=18 mm, z=200 mm.

Figures 5.91 presents experimental results for 18 x 10 mm focused rectangular aperture focused in y direction with a geometric focal length F_y=160 mm. Notice that this time the aperture was turned by 90° around the acoustic axis. This generated more side lobes and narrow main lobe compared to 10 x 18 mm rectangular aperture. Focusing is also responsible for the narrow beam around the focal plane but the beam gets wider just after the focal plane with increasing axial range. This is not clear for one dimensional focusing case but is clearer for two dimensional focusing case.

Figures 5.92 is related to the focused 18 x 10 mm rectangular aperture with equal focal lengths F_x=F_y=160 mm in both directions. In this case, it was seen that the main lobe and the side lobes are not quite symmetric at the each side of the axis. This is also true for all of the harmonic components observed in this case and is probably due to errors in making the curvature of the perspex lenses and possibly the finite size of the hyrophone which reduces the rapid oscillations. The number of measurements at each side of the axis may cause the same asymmetry as well.

The same asymmetry was also seen for the two dimensional focusing with focal lengths F_x=F_y=250 mm for the same aperture, at the same drive level at 150 mm away from the aperture face. At this range, the side lobes of the fundamental and second harmonic at the left side of the axis (see Figure 5.93) have greater amplitude that the ones at the other side of the across axis. However, this almost disappeared around 250 mm from the source and the beam was quite symmetric at about 350 mm from the aperture showing a broadening character after the focal plane.

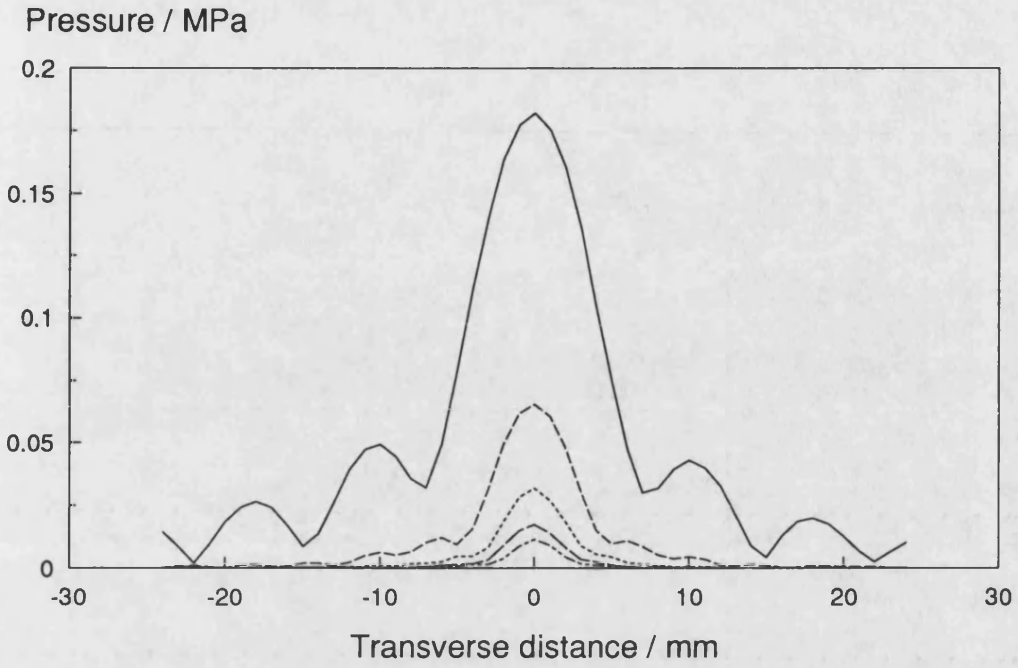

Figure 5.91 Transverse pressure field of a focused (F_y=160 mm) rectangular source at DL3, a=18 mm, b=10 mm, z=200 mm, P_0=100 kPa.

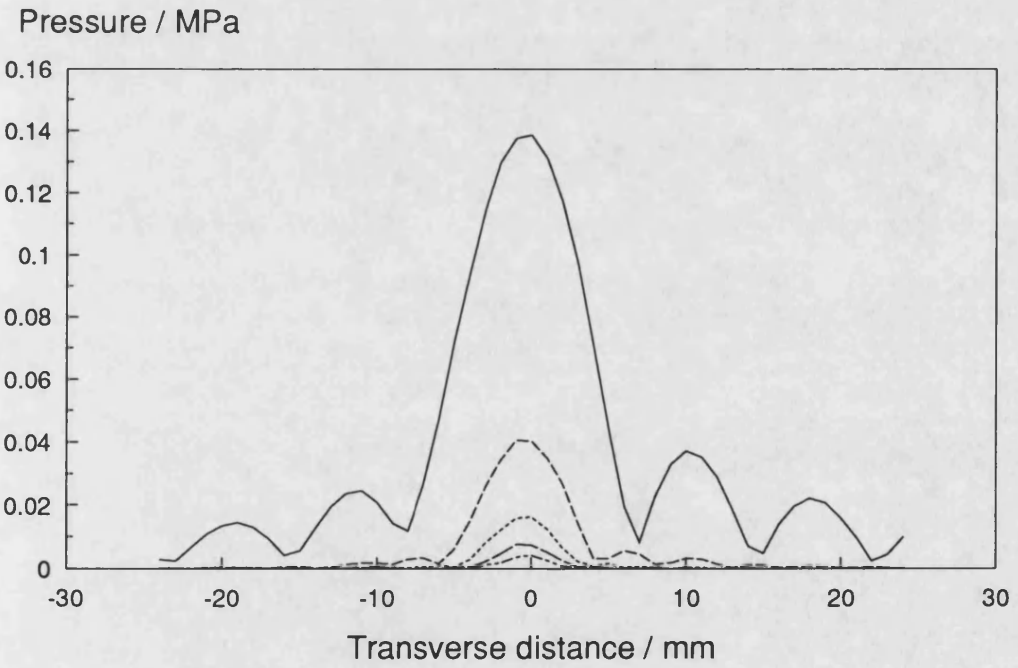

Figure 5.92 Transverse pressure field of a focused (F_x=F_y=160 mm) rectangular source at DL3, a=18 mm, b=10 mm, z=200 mm, P_0=225 kPa.

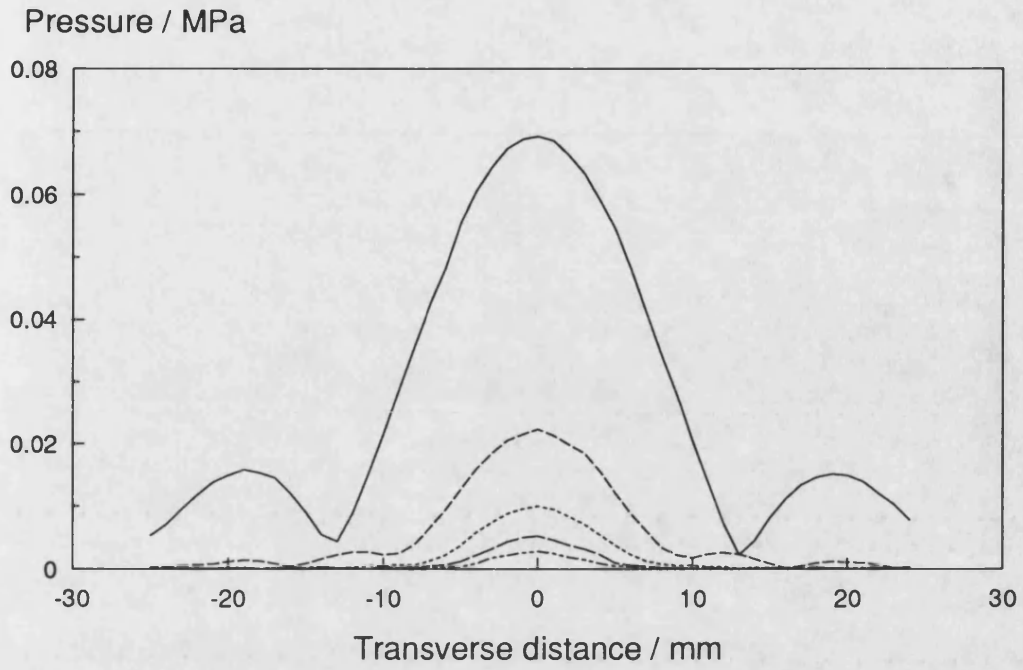

Figure 5.93 Transverse pressure field of a focused (F_x=F_y=250 mm) rectangular source at DL3, a=18 mm, b=10 mm, z=350 mm.

5.5 AGREEMENT WITH THE PERTURBATION MODEL

This section compares the measured second harmonic with the theoretical results obtained from the first order perturbation model for plane square apertures of sizes 25 mm and 27 mm. Since the agreement was similar to those presented in the earlier sections in this chapter, comparisons for the fundamental are not presented here.

Figure 5.94 compares the measured second harmonic with theoretical results from the perturbation model for 27 x 27 mm square aperture. The drive level (100 kPa) was chosen to be high enough to generate the second harmonic but not to generate the third and higher harmonics, as the perturbation model ignores the harmonics higher than the second. It also assumes that the energy loss from the fundamental will be negligible.

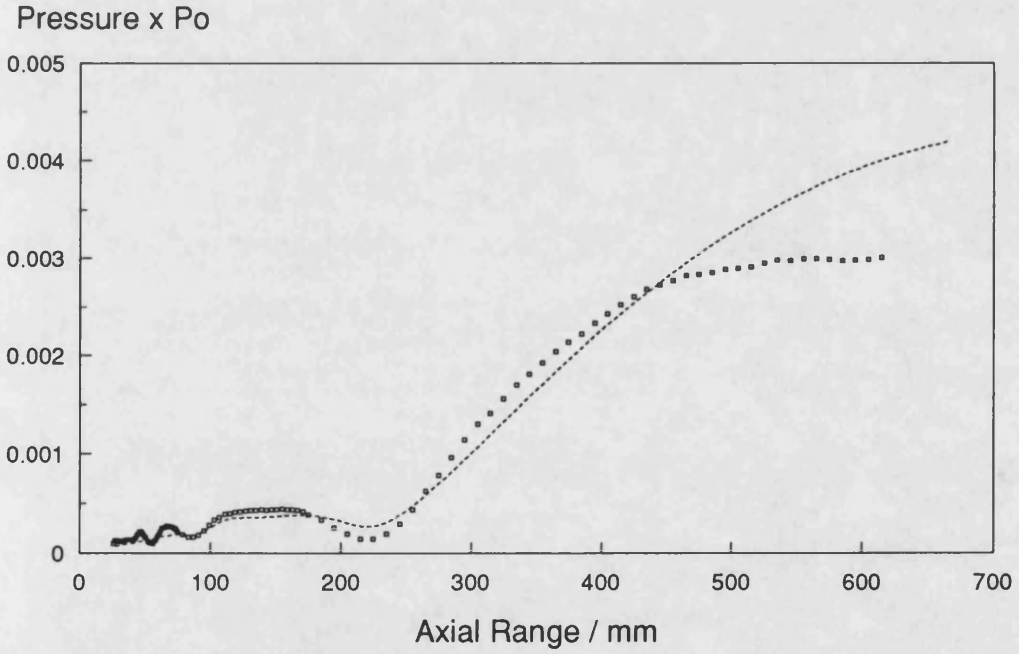

Figure 5.94 Comparison of measured second harmonic with predicted results by the perturbation model, a=b=27 mm, f=2.25 MHz, Theory (dotted line), Experiment (markers).

Figure 5.95 presents the results for 25 mm square aperture at higher drive level (225 kPa). At this drive level is was not fully possible to eliminate the third harmonic but its pressure level was negligible. For each aperture, in general, the overall agreement between experiment and theoretical predictions is quite good and is better closer to the aperture. In the near field of each aperture, experimental results closely follow the theoretical predictions but further away from the source a significant departure can be seen between experimental measurements and theoretical predictions. This can be explained by means of the energy loss process from the fundamental to the higher harmonics. Since the first order perturbation theory ignores the harmonics higher than the second, transfer energy from the fundamental stops after the second harmonic. Thus, the second harmonic amplitude starts increasing at longer ranges from the aperture.

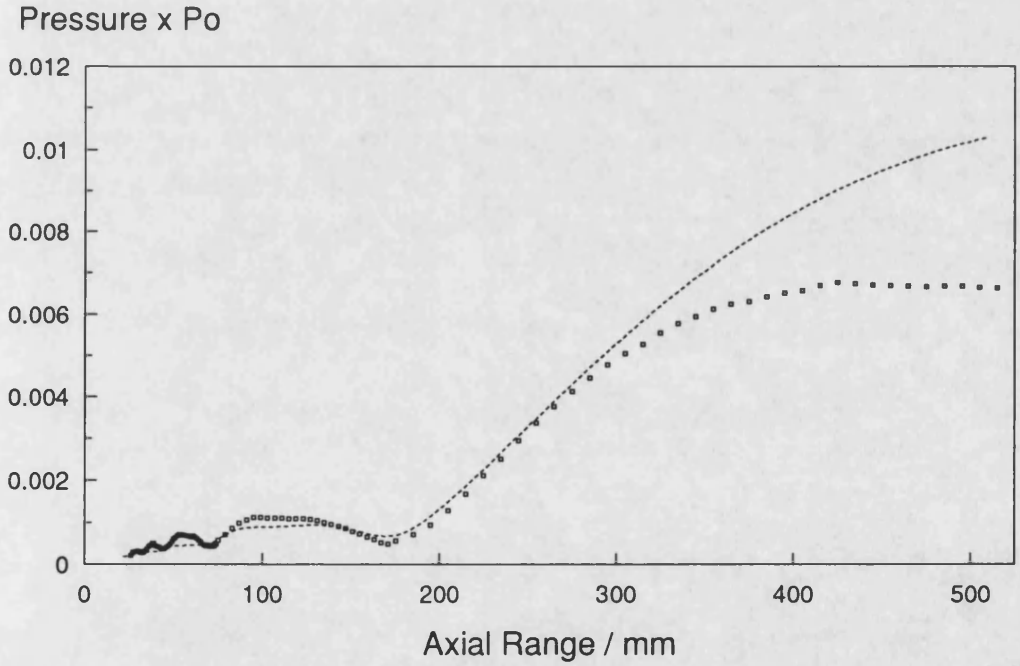

Figure 5.95 Comparison of measured second harmonic with predicted results by the perturbation model, a=b=25 mm, f=2.25 MHz, Theory (dotted line), Experiment (markers).

The second point is that the first order perturbation theory only takes account for the interaction between the first and second harmonic. However, if there is a third harmonic generated at larger ranges from the source then the perturbation theory ignores the interactions between the first and third harmonic and between the second and third harmonic. This reduces the energy transfer from the fundamental to the generated harmonics and gives rise to increase the second harmonic amplitude at larger distances from the source. However, much of the detail is accurately predicted by the perturbation theory, especially the last minima in the second harmonic compared to the plane wave model but is not able to predict higher harmonic components than the second

It is noticeable that the perturbation solution breaks down when the second harmonic amplitudes becomes comparable with fundamental. The first order perturbation model also does not work for higher values of P_0. In reality, we can not reasonably expect better success from the first order perturbation theory, presumably, the discrepancy between theoretical results from the perturbation theory and experimental measurements is due to the depletion from the second harmonic itself and possibly due to the experimental errors. However, agreement between theoretical predictions from perturbation model and experimental results is satisfactory, despite these limitations:

1. The underlying theory is not exact.

2. The first order perturbation theory neglects back scattering, absorption and depletion.

3. Several mathematical approximations; all based upon the large size of *ka* and neglect of harmonics higher than the second.

4. Mathematical difficulties in solving Equation 4.71 necessitate some further approximations, justified chiefly by the fairly large value of ka.

5. Extra attenuation is not taken into account in the computations, this would make the actual amplitude of the fundamental lower, generating less second harmonic at the larger distances. It would also produce the more rapid fall of into the far field. However, the magnitude of the this effect appears not to be too great.

The plane wave model predicts more harmonics than the perturbation solution, but a discrepancy arises because the model takes the diffraction into account in an ad hoc manner through inclusion of the on axis variation of the fundamental. Even with this limitation, the agreement between theoretical predictions from the plane wave theory and experimental results has been good enough to understand the general structure of the pressure field of rectangular apertures. But, the plane wave model has been less successful in predicting the minimas in the second harmonic, in comparison with the perturbation model. However, the plane wave model allows "quick" and "ready" predictions of nonlinear distortion in the field of a rectangular transducer for practical applications, e.g. for ultrasound systems that are in clinical use.

5.6 TIME WAVEFORMS

Although the time domain representation is useful to illustrate the waveform distortion with increasing drive level and axial range, quantative comparisons are difficult to make. However, in the frequency domain, direct comparisons can be made for the amplitude and phase of the each harmonic component. In particular, the effects of the hydrophone resonances can be removed relatively easily in the frequency domain.

In this section, the waveform distortion is presented with increasing distance from the square aperture of 25 x 25 mm size at the maximum drive level for the plane piston case. Since the increased drive level cause the same type of distortion on the time waveforms, the effect of the drive level is not presented here.

Figure 5.96 shows the time waveform closer to the plane square aperture (z=30 mm), which has almost no distortion and Figure 5.97 shows the time waveform with some distortion at 140 mm from the source where the fundamental pressure field has an axial minimum. At this range it can be seen that the compressional part of the wave is travelling further than the decompression. At 260 mm from the aperture, the rising edge of the waveform has started to resemble a step change in pressure and the waveform has taken on a sawtooth appearance (Figure 5.98). There is also a noticeable top-bottom asymmetry, caused by the phase shifts between harmonics. This leads to a higher peak positive pressure than the peak negative pressure. There was also some evidence of the hydrophone resonance at the peak positive pressure but this was more clearly visible in the time waveform measured at 575 mm (Figure 5.99) away from the aperture. The resonant frequency of the hydrophone was about 22 MHz, so it manifests as ripple at about the 10^{th} harmonic of the driving frequency (2.25 MHz).

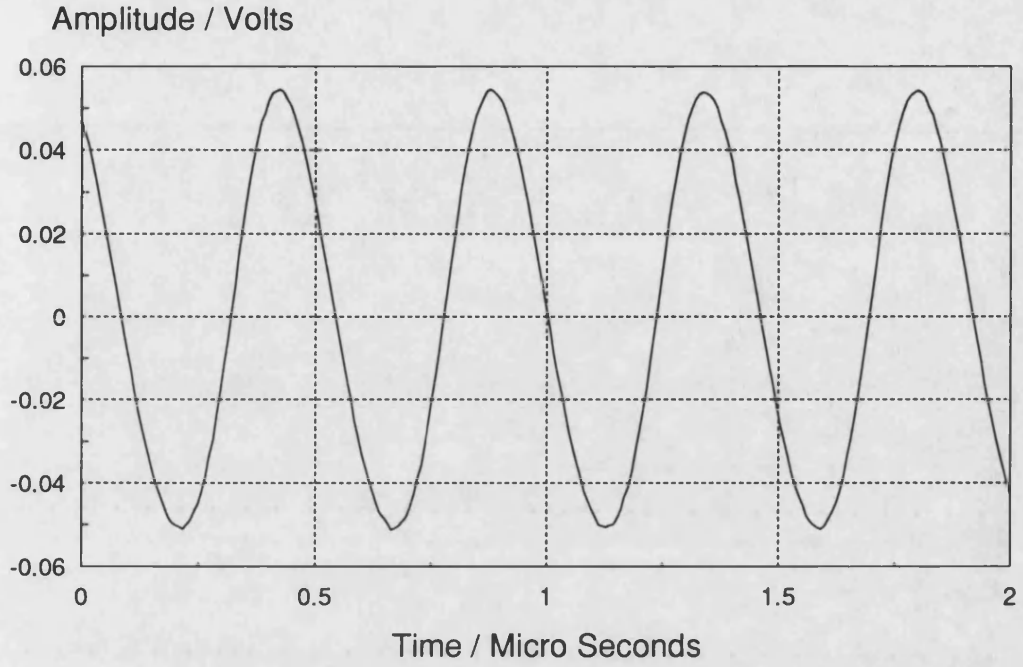

Figure 5.96 Recorded time waveform at DL3, a=b=25 mm, z=30 mm.

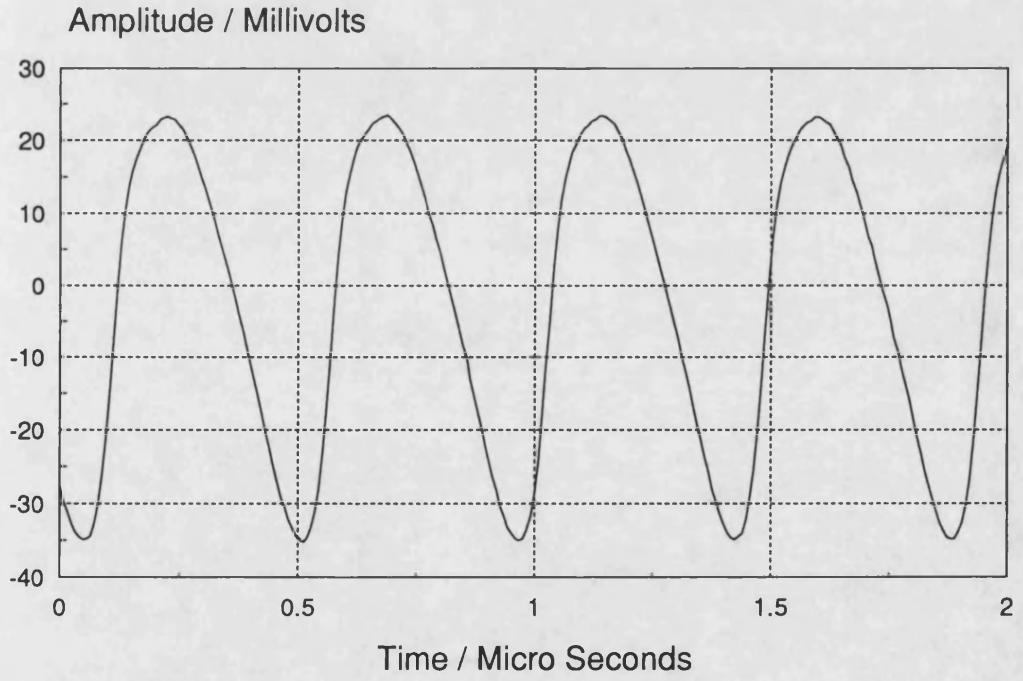

Figure 5.97 Recorded time waveform at DL3, a=b=25 mm, z=140 mm.

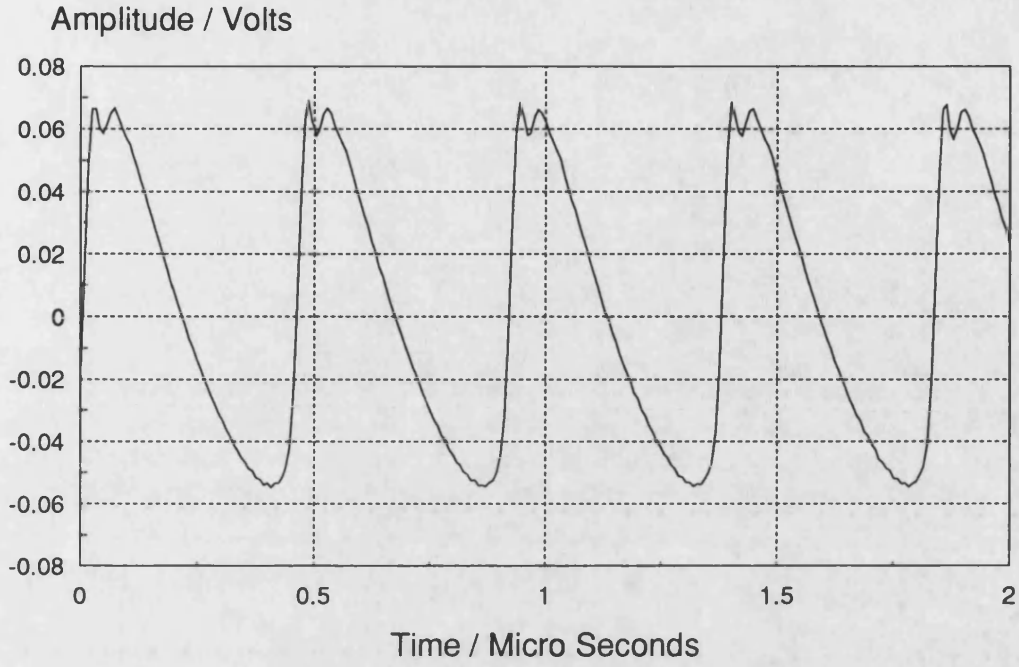

Figure 5.98 Recorded time waveform at DL3, a=b=25 mm, z=260 mm.

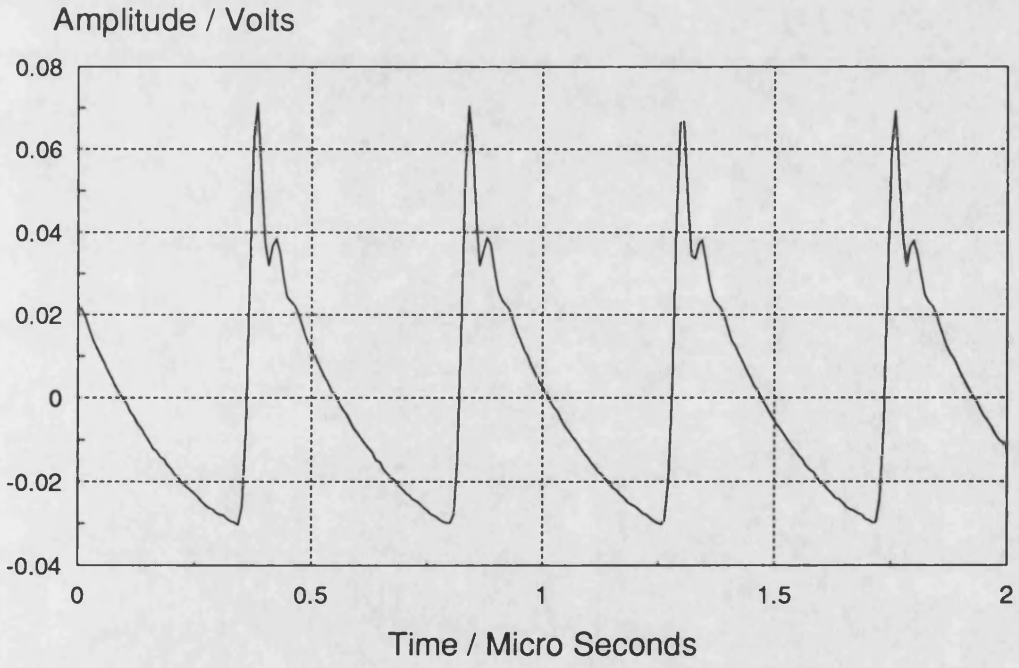

Figure 5.99 Recorded time waveform at DL3, a=b=25 mm, z=575 mm.

CHAPTER 6

CONCLUSIONS

A versatile method for producing a wide range of well characterised rectangular ultrasonic sources has been developed and tested. Experimental measurements at low drive levels show good agreement with linear theory (typically error was about 10%).

The effect of using a finite diameter circular hydrophone on field measurements of rectangular sources has been evaluated. It has been show that the importance of the diffraction losses is much reduced in comparison with those encountered with circular sources.

An extensive series of measurements has been made on a number of rectangular ultrasonic sources at finite amplitudes. The effect of focusing in one and two dimensions has also been explored.

The finite amplitude results have been compared with two theoretical models.

1. A plane wave model which can cater for any number of harmonics but diffraction effects are only included for the fundamental. This model is valid on the acoustic axis. The agreement with the plane wave model was reasonable, typically about 10% at lower drive levels. Agreement was not so good at higher drive levels and the lack of diffraction for the harmonics was identified as the main cause of discrepancy.

2. A perturbation model which evaluated the second harmonic along the acoustic axis. This produced better agreement with the measurements at short ranges but started to fail at longer ranges and higher drive levels when the second harmonic level become comparable with the fundamental.

Overall this project presents a first step towards understanding the pressure fields of diagnostic systems based on rectangular arrays. The models used could be used to provide a starting point for modelling of more complex effects such as propagation in tissue and thermal effects.

LIMITATIONS AND FUTURE WORK

1. This study uses a number of almost ideal ultrasonic sources although the range of parameters used was chosen to be comparable with "real" diagnostic ultrasound systems. The study needs extension to cover "real" systems especially the use of pulses, propagation in tissue and higher drive levels.

2. Accurate theoretical predictions rely on accurate initial conditions. The use of real diagnostic systems would require a suitable method to characterise the source, especially geometric focal lengths, aperture shading and effective aperture dimensions.

3. The plane wave, perturbation model and parabolic approximation are applicable to limited geometries. A full, exact model, similar perhaps to the Christopher and Parker model [54] is required, although there will probably always be a requirement for quicker, simpler approximate methods. A full theoretical treatment would than make a more comprehensive comparison with the measured fields of real sources feasible.

4. Extension to pulsed fields and higher drive levels will need to be coupled to an improvement in hydrophone calibration. The frequency range over which calibration is performed and the lack of phase information would pose serious limitations.

ACKNOWLEDGEMENTS

This work was performed at the School of Physics, at the University of Bath with support from the Inonu University, Malatya, TURKEY. The author would like to thank to Professor Zeki Aslan, Professor Zekeriya Aydin and Professor Orhan Ozer for their personal interest and assistance during the course of this work.

The author is pleased to extend his sincere thanks to Dr. Andy C Baker for his friendly supervision, guidance and near infinite patience he provided during the course of this study.

Thanks are also due to the Professor H. Orhan Berktay for his encouragement, interest, advice and discussions.

The author also thanks Dr. Victor F Humphrey, Dr. Francis A Duck and Tom Szabo for their interest, help and discussions.

Last and certainly not least, I would also like to thank to my wife Berrin for her support and for her patience with me during the course of this research.

REFERENCES

[1]. **Poisson, S. D.** "Memoir on the theory of sound," J. L'Ecole Polytech. 7, 364-370, 1808.

[2]. **Kumamato, Y., Tani, M. and Kamakura, T.** "Harmonic generation in the finite amplitude sound beams from a rectangular aperture," J. Acoust. Soc. Am., 91(6), 3144-3151, 1992.

[3]. **Hill, C. R.,** "Physical prenciples of medical ultrasonics," John Willey, 1st ed., 22-27, 1986.

[4]. **Kinsler, L. E., Frey, A. R.** "Fundamentals of acoustics," John Wiley, 2 ed, 117, 1962.

[5]. **Blackstock, D. T.** "Propagation of plane sound waves in nondissipative fluids," J. Acoust. Soc. Am., 34, 9-30, 1962.

[6]. **Gol'dberg, Z. A.** "On the propagation of plane waves of finite amplitude," Sov. Phys. Acoust., 2, 346-350, 1956.

[7]. **Zemanek, J.** "Beam behaviour within the near field of a vibrating piston," J. Acoust. Soc. Am., 49, 181-191, 1971.

[8]. **Oberhettinger, F.** J. Res. Nat. Bur. Stand., 65B, 1-6, 1961.

[9]. **Lockwood, J. C. and Willette, J. G.** "High speed method for computing the exact solution for the pressure variations in the near field of a baffled piston," J. Acoust. Soc. Am., 53(3), 735-741, 1973.

[10]. **Hutchins, D. A., Mair, H. D., Puhach, P.A. and Osei, A. J.** "Continuous wave pressure fields of ultrasonic transducers," J. Acoust. Soc. Am., 80, 1-12, 1986.

[11]. **Freedman, A.** "Sound field of a rectangular piston," J. Acoust. Soc. Am., 32(2), 197-209, 1960.

[12]. **Freedman, A.** "Farfield of pulsed rectangular acoustic radiator," J. Acoust. Soc. Am., 49(3), 738-748, 1971.

[13]. **Marini, J. and Rivenez, J.** "Acoustical fields from rectangular ultrasonic transducers for non-destructive testing and medical diagnosis," Ultrasonics, 251-256, November 1974.

[14]. **Szabo, T. L.** "Generalized Fourier transform diffraction theory for parabolically anisotropic media," J. Acoust. Soc. Am., 61(3), 28-34, 1978.

[15]. **Bracewell, R. M.** "The Fourier transform and its applications," McGraw Hill, New York, 1965.

[16]. **Weyns, A.** "Radiation field calculations of pulsed ultrasonic transducers Part 1: Planar circular, square and annular transducers," Ultrasonics, 183-188, July 1980.

[17]. **Orcheltree, K. B. and Frizzell, L. A.** "Sound field calculation for rectangular sources," IEEE Trans. on UFFC, 36(2), 242-248, March 1989.

[18]. **O'Neil, H. T.** "Theory of focusing radiators," J. Acoust. Soc. Am., 21, 516-526, 1949.

[19]. **Lucas, B. G. and Muir, T.G.** "The field of a finite amplitude focusing source," J. Acoust. Soc. Am., 74, 1522-1528, 1983.

[20]. **Naze Tjøtta, J. and Tjøtta, S.** "An analytical model for the near field of a baffled piston transducer," J. Acoust. Soc. Am., 68, 334-339, 1980.

[21]. **Thompson, R. B., Gray, T. A., Rose, J. H., Kogan, V. G. and Lopes, E. F.** "The radiation of elliptical and bicylindrically focused piston transducers," J. Acoust. Soc. Am., 82, 1818-1828, 1987.

[22]. **Hasegawa, T., Matsuzawa, K. and Inoue, N.** "A new expansion for the velocity potential of a circular concave piston," J. Acoust. Soc. Am., 79, 927-931, 1986.

[23]. **Hasegawa, T., Matsuzawa, K. and Inoue, N.** "A new theory for the radiation from a concave piston source," J. Acoust. Soc. Am., 82, 706-708, 1987.

[24]. **Penttinen, A. and Luukkala, M.** " The impulse response and pressure near-field of a curved ultrasonic radiator," J. Phys. D: Appl. Phys., 9, 1547-1557, 1976.

[25]. **Cobb, W. N.** "Frequency domain method for the prediction of the ultrasonic field patterns of pulsed focused radiators," J. Acoust. Soc. Am., 75, 72-75, 1984.

[26]. **Stephanishen, P. R.** "Transient radiation from pistons in an infinite baffle," J. Acoust. Soc. Am., 49, 1629-1638, 1971.

[27]. **Beaver, W. L.** "Sonic near-fields of a pulsed piston radiator," J. Acoust. Soc. Am., 56, 1043-1048, 1974.

[28]. **Naze Tjøtta, J. and Tjøtta, S.** "Near-field and far-field of pulsed acoustic radiators," J. Acoust. Soc. Am., 71, 824-834, 1982.

[29]. **Hutchins, D. A., Mair, H. D. and Taylor, R.G.** "Transient pressure fields of PVDF transducers," J. Acoust. Soc. Am., 82, 183-193, 1987.

[30]. **Bjørnø, L.** "Nonlinear ultrasound - a review," In conference proceeding Ultrasonics International, 110-115, 1975.

[31]. **Beyer, R. T.** "Nonlinear acoustics in fluids," Benchmark papers in acoustics, Volume 18, Van Nostrand Reinhold, New York, 1984.

[32]. **Hamilton, M. F.** "Fundamentals and applications of nonlinear acoustics," Nonlinear wave propagation in mechanics, AMD-Vol.77, 1-28, 1986.

[33]. **Lagrange, J.** "New researches on the nature and propagation of sound," Nisc. Taur., 2, 11-172, 1761.

[34]. **Earnshaw, S.** "On the mathematical theory of sound," Philos. Trans. R. Soc. London, 150, 133-148, 1860.

[35]. **Fay, R. D.** "Plane sound waves of finite amplitude," J. Acoust. Soc. Am., 3, 222-241, 1931.

[36]. **Fubini, G. E.** "Anomalies in the propagation of an acoustic wave of large amplitude," Sov. Phys. Acoust., 3, 340-347, 1935.

[37]. **Blackstock, D. J.** "Connection between Fay and Fubini solutions for sound waves of finite amplitude," J. Acoust. Soc. Am., 39, 1019-1026, 1966.

[38]. **Burger, J. M.** "A mathematical model illustrating the theory of turbulence," In Advances in applied mathematics, Academic Press, New York, Volume 1, 171-199, 1948.

[39]. **Fox, F. E. and Wallace, W. A.** "Absorption of finite amplitude sound waves," J. Acoust. Soc. Am., 26, 994-1006, 1954.

[40]. **Trivett, D. H. and Van Buren, A. L.** "Propagation of plane, cylindrical and spherical finite amplitude waves," J. Acoust. Soc. Am., 69, 943-949, 1981.

[41]. **Ingenito, F. and Williams, A. O.** "Calculation of second harmonic generation in a piston beam," J. Acoust. Soc. Am., 49, 319-328, 1971.

[42]. **Cobb, W. N.** "Finite amplitude method for the determination of the acoustic nonlinearity parameter B/A," J. Acoust. Soc. Am., 73, 1525-1531, 1983.

[43]. **Kunitsyn, V. E. and Rudenko, O. V.** "Second harmonic generation in the field of a piston radiator," Sov. Phys. Acoust., 24, 310-313, 1978.

[44]. **Lapidus, Y. R. and Rudenko, O. V.** "New approximations and results of the theory of nonlinear acoustic beams," Sov. Phys. Acoust., 30, 473-476, 1984.

[45]. **Ginsberg, J. H.** "Nonlinear king integral for arbitrary axisymmetric sound beams at finite amplitudes, I. Asymptotic evaluation of the velocity potential," J. Acoust. Soc. Am., 76, 1201-1207, 1984.

[46]. **Ginsberg, J. H.** "Nonlinear king integral for arbitrary axisymmetric sound beams at finite amplitudes, II. derivation of uniformly accurate expressions," J. Acoust. Soc. Am., 76, 1208-1214, 1984.

[47]. **Lockwood, J. C., Muir, T. G. and Blackstock, D. T.** "Directive harmonic generation in the field of a circular piston," J. Acoust. Soc. Am., 53, 1148-1153, 1973.

[48]. **Lancaster, M.** "The finite amplitude field of a circular piston," University of Bath, Ph.D. Thesis, 1983.

[49]. **Khokhlov, R. V. and Zabolotskaya, E. A.** "Quasi-plane waves in the nonlinear acoustics of confined beams," Sov. Phys. Acoust., 15, 35-40, 1969.

[50]. **Kuznetsov, V. P.** "Equations of nonlinear acoustics," Sov. Phys. Acoust., 16, 467-470, 1971.

[51]. **Aanonsen, S.I, Barkve, T., Naze Tjøtta J. and Tjøtta, S.** "Distortion and harmonic generation in the near-field of a finite amplitude sound beam," J. Acoust. Soc. Am., 75, 749-768, 1984.

[52]. **Hamilton, M. F., Naze Tjøtta J. and Tjøtta, S.** "Nonlinear effects in the far-field of a directive sound source," J. Acoust. Soc. Am., 78, 202-216, 1985.

[53]. **Baker, A. C., Anastasiadis, K. and Humphrey, V. F.** "The nonlinear pressure field of a plane circular piston: Theory and Experiment," J. Acoust. Soc. Am., 84, 1483-1487, 1988.

[54] **Christopher, P. T. and Parker, K. J.** "New approaches to nonlinear diffractive field propagation," J. Acoust. Soc. Am., 90(1), 488-499, 1991.

[55]. **Lahalle, D., Cervenka, P. and Guyomar, D.** "Saturation des niveaux sonores et calcul de champ rayonne en acoustique non lineaire," J. Acoustique (France) 1, 37-45, 1988.

[56]. **Berg, A.** "The weakly nonlinear field radiated from a rectangular sound source," Thesis for the Cand. Scient. Degree in Applied Mathematics, Acoustics, Department of Mathematics, University of Bergen, Norway, 1990.

[57]. **Naugol'nykh, K. A., Soluyan, S. I. and Khokhlov, R. V.** "Spherical waves of finite amplitude in a viscous thermally conducting medium," Sov. Phys. Acoust., 9, 42-46, 1963.

[58]. **Smith, C. W. and Beyer, R. T.** "Ultrasonic radiation field of a focusing spherical source at finite amplitudes," J. Acoust. Soc. Am., 46, 806-813, 1968.

[59]. **Ostrovskii, L. A. and Sutin, A. M.** "Focusing of finite amplitude acoustic waves," Sov. Phys.-Dokl. 20, 255-277, 1975.

[60]. **Lucas, B. G. and Muir, T.G.** "The field of a finite amplitude focusing source," J. Acoust. Soc. Am., 74, 1522-1528, 1983.

[61]. **Saito, S., Kim, B. C. and Muir, T. G.** "Second harmonic component of a nonlinearly distorted wave in a focused field," J. Acoust. Soc. Am., 82, 621-628, 1987.

[62]. **Hart, T. S.** "Numerical investigation of nonlinear effects in focused sound beams," Thesis, Master of Science in Electrical Engineering, University of Texas, Austin, 1987.

[63]. **Aanonsen, S. I.** "Numerical computation of the nearfield of a finite amplitude sound beam," Technical Report No:73, Department of Mathematics, University of Bergen, Norway, 1983.

[64]. **Baker, A. C.** "Finite amplitude propagation of focused ultrasonic waves in water," University of Bath, Ph.D. Thesis, 1989.

[65]. **Szabo, T. L.** Private communication.

[66]. **Preston, R. C., Bacon, D. R., Livett, A. J. and Ragendran, K.** "PVDF membrane hyrophone performance properties and their relevance to the measurement of the acoustic output of medical ultrasonic equipment," J. Phys. E: Sci. Intrum., 16, 786-796, 1983.

[67]. **Baker, A. C., Anastasiadis, K. and Humphrey, V. F.** "Nonlinear propagation in focused fields: Theory and Experiment," Proceedings of Ultrasonics International 87, Butterworths, 1987.

[68] **Baker, A. C.** Private communication.

[69]. **Bacon, D. R.** "Characteristics of a PVDF membrane hydrophone for use in the range 1 - 100 MHz," IEEE Trans. Sonics and Ultrason., SU-29, 8-25, 1982.

[70]. **Beissner, K.** "Exact integral expression for the diffraction loss of a circular piston source," Acoustica, 49, 212, 1981.

[71]. **Khimunin, A. S.** "On the ultrasound diffraction losses for circular transducers of different radii," Acoustica, 54, 13, 1983.

[72]. **Szabo, T. L.** "Anisotropic surface acoustic wave diffraction," Physical Acoustics, (Ed. Mason Thurston), Vol. 13, 79-111, Academic Press, New York, 1977.

[73]. **Waldron, R. A.** "Power transfer factors for nonuiformly irradiated interdigital piezoelectric transducers," IEEE Trans. Sonic. Ultrason., SU-19(4), 448-453, 1972.

[74]. **Digital storage oscilloscope PM3315, Operating Manual**, Philips Scientific and Industrial Equipment, 1985.

[75]. **Wilson, W. D.** "Speed of sound in distiled water as a function of temperature and pressure," J. Acoust. Soc. Am., 31, 1067-1072, 1959.

[76]. **Beyer, R. T.** "Parameter of nonlinearity in fluids," J. Acoust. Soc. Am., 32, 719-721, 1960.

[77]. **Kinsler, L. E., Frey, A. R., Coppens, A. B. and Sanders, J. V.,** "Fundamentals of Acoustics," John Wiley, 3 ed. 107 and 462, 1982.

[78]. **Baker, A. C.** "Nonlinear pressure fields due to focused rectangular apertures," J. Acoust. Soc. Am., 91(2), 713-717, 1992.

[79]. **Cohen, M. G.** "Optical study of ultrasonic diffraction and focusing in anisotropic media," J. Appl. Phys., 38, No:10, 3821-3828, 1967.

[80]. **Bracewell, R. M.** "The Fourier transform and its applications, McGraw Hill, New York, 1965.

[81]. **Papoulis, A.** "Systems and transforms with applications in optics," McGraw Hill, New York, 1968.

[82]. **Berktay, H. O.** "Postgraduate lecture notes," Bath University, School of Physics, Bath, 1990.

[83]. **Ames, W. F.** "Numerical methods for partial differential equations," Academic Press, New York, 1977.

[84]. **Smith, G. D.** "Numerical solutions of partial differential equations: Finite difference methods," Oxford University Press, Oxford, 1978.

[85]. **Heaps, H. S.** "Waveforms of finite amplitude derived from equations of hydrodynamics," J. Acoust. Soc. Am., 34, 355-356(L), 1962.

[86]. **Berktay, H. O.** Private communication.

[87]. **Szabo, T. L.** Private communication.

APPENDIX 1

In equation 4.46, in Chapter 4, we defined $F(K_x)$ as

$$F(K_x) = \int_{-\infty}^{\infty} e^{jK_x x} f(x) dx \qquad A1.1$$

where

$$f(x) = \left\{ \int_{\sqrt{\frac{k}{\pi z}(x-a)}}^{\sqrt{\frac{k}{\pi z}(x+a)}} e^{-j\frac{\pi}{2}t^2} \right\}^2 \equiv h^2(x) \qquad A1.2$$

with $h(k)$ having Fourier transform of $H(K)$, i.e,

$$h(k) = \frac{1}{2\pi} \int_{-\infty}^{\infty} H(\Omega) e^{-j\Omega x} d\Omega \qquad A1.3$$

Then, in the form of a convolution integral, $F(K_x)$ becomes

$$F(K_x) = \frac{1}{2\pi} \int_{-\infty}^{\infty} H(\Omega) H(K_x - \Omega) d\Omega \qquad A1.4$$

with,

$$H(K_x) = \int_{-\infty}^{\infty} e^{jK_x x} dx \int_{\sqrt{\frac{k}{\pi z}(x-a)}}^{\sqrt{\frac{k}{\pi z}(x+a)}} e^{-j\frac{\pi}{2}t^2} dt \qquad A1.5$$

Equation A1.5 can be evaluated by integrating by parts. Noting that the integrand vanishes for $x = \pm\infty$, thus we obtain,

$$H(K_x) = -\frac{1}{jK_x}\int_{-\infty}^{\infty} e^{jK_x x}\,dx\sqrt{\frac{k}{\pi z}}\left\{e^{-j\frac{k}{\pi z}(x+a)^2} - e^{-j\frac{k}{\pi z}(x-a)^2}\right\} \qquad A1.6$$

Evaluating the integral in Equation A1.6, we get

$$H(K_x) = \frac{1}{2\pi}\int_{-\infty}^{\infty} H(\Omega)H(K_x-\Omega)\,d\Omega$$

$$= -j\frac{4}{\pi}\int_{-\infty}^{\infty}\frac{\sin(\Omega a)\sin(K_x a-\Omega a)}{\Omega(K_x-\Omega)}e^{j\frac{z}{2k}\left[\Omega^2+(K_x-\Omega)^2\right]}d\Omega \qquad A1.7$$

$$i.e., = -j\frac{2}{\pi}\int_{-\infty}^{\infty}\frac{\cos[(2\Omega-K_x a)a-\cos(K_x a)]}{\Omega(K_x-\Omega)}e^{j\frac{k}{z}\left[\Omega^2-\Omega K_x+\frac{K_x^2}{2}\right]}d\Omega$$

with

$$\Omega^2-\Omega K_x+\frac{K_x^2}{2} = \left(\Omega-\frac{K_x^2}{2}\right)+\frac{K_x^2}{4} \qquad A1.8$$

and

$$\Omega(K_x-\Omega) = \left(\frac{K_x}{2}\right)^2-\left(\Omega-\frac{K_x}{2}\right)^2 \qquad A1.9$$

Substituting $\Omega-\frac{K_x}{2}\equiv u$, we obtain

$$F(K_x) = -j\frac{2}{\pi} e^{\frac{jzK_x^2}{4K}} \int_{-\infty}^{\infty} \frac{[\cos(2ua) - \cos(K_x a)]}{\left(\frac{K_x^2}{2}\right) - u^2} e^{j\frac{zu^2}{K}} du \qquad A1.10$$

The integral in Equation A1.10 can be evaluated by replacing $\cos(2ua)$ with $\cos(\omega u)$. Putting $\omega = 2a$ and $\omega = 0$ respectively in the result gives two integrals. Further, as the integrand is even in u, and the integration is between symmetrical limits, we can use $e^{-j\omega u}$ instead of $\cos(\omega u)$. As the Fourier transform of the exponential term in the integral in Equation A1.11 is

$$F.T \quad \left\{ e^{j\frac{zu^2}{k}} \right\} = \sqrt{\pi \frac{k}{z}} e^{i\frac{\pi}{4}} e^{\frac{-j\omega^2 k}{4z}} \qquad A1.11$$

the integrand in Equation A1.11 becomes

$$\int_{-\infty}^{\infty} \frac{e^{-j\omega u}}{\left(\frac{K_x^2}{2}\right) - u^2} e^{j\frac{zu^2}{K}} du = \frac{1}{2\pi} \sqrt{\pi \frac{k}{z}} e^{j\frac{\pi}{4}} \int_{-\infty}^{\infty} e^{-j\frac{\Omega^2 k}{4z}} d\Omega \int_{-\infty}^{\infty} \frac{e^{-j(\omega-\Omega)u}}{\left(\frac{K_x^2}{2}\right) - u^2} du \qquad A1.12$$

The last integral in u, in Equation A1.12 now can be evaluated using contour integration and gives

$$\frac{2\pi}{k_x} \sin(\omega - \Omega)\frac{K_x}{2} \qquad \textit{if} \qquad \omega - \Omega > 0,$$

$$-\frac{2\pi}{k_x} \sin(\omega - \Omega)\frac{K_x}{2} \qquad \textit{if} \qquad \omega - \Omega < 0.$$

Thus $F(K_x)$ becomes

APPENDIX 2

The symmetry of $F_0(\omega)/\omega$ is not obvious from the expressions given in Equations 4.68 and 4.69, in Chapter 4, although physical reasons can be argued for it. In Equation 4.68, we had

$$F_0(\omega) = e^{j\omega} sgn(A+B) \int_0^{A+B} e^{-j\frac{\pi}{2}t^2} dt$$

$$+e^{-j\omega} sgn(A-B) \int_0^{A-B} e^{-j\frac{\pi}{2}t^2} dt - 2\cos(\omega) sgn(A) \int_0^{A} e^{-j\frac{\pi}{2}t^2} dt \qquad A2.1$$

with

$$A = \sqrt{\frac{\eta}{2\pi M}}\omega, \qquad B = \sqrt{2\frac{M}{\pi\eta}} \qquad A2.2$$

In this case,

$$sgn(A \pm B) = sgn\left(\omega \pm 2\frac{M}{\eta}\right) \qquad A2.3$$

and

$$sgn(A) = sgn(\omega) \qquad A2.4$$

Thus, the last term in $\frac{F_0(\omega)}{\omega}$ is clearly symmetrical for ω. Let us consider the first two terms in $F_0(\omega)$

1. If $\omega > 0$:

1.a. $0 < \omega < 2\frac{M}{\eta}$:

Then $sgn(A+B) = 1$ and $sgn(A-B) = -1$. As $|A-B| = B-A$ We have

$$e^{j\omega}\int_0^{A+B} e^{-j\frac{\pi}{2}t^2}dt - e^{j\omega}\int_0^{A-B} e^{-j\frac{\pi}{2}t^2}dt \qquad A2.5$$

1.b If $\omega > 2\frac{M}{\eta}$, then $sgn(A \pm B) = 1$, $|A-B| = A-B$. We have

$$e^{j\omega}\int_0^{A+B} e^{-j\frac{\pi}{2}t^2}dt + e^{j\omega}\int_0^{B-A} e^{-j\frac{\pi}{2}t^2}dt \qquad A2.6$$

2. If $\omega < 0$:

2.a. $0 < |\omega| < 2\frac{M}{\eta}$: In this case, $sgn(A \pm B) = -1$ and

$$|A+B| = -A-B = |A| - B \qquad A2.7$$

$$|A-B| = -A+B = |A| + B \qquad A2.8$$

Thus we have,

$$e^{j\omega}\int_0^{B-|A|} e^{-j\frac{\pi}{2}t^2}dt - e^{-j\omega}\int_0^{B+|A|} e^{-j\frac{\pi}{2}t^2}dt$$

$$= e^{-j|\omega|}\int_0^{B-|A|} e^{-j\frac{\pi}{2}t^2}dt - e^{j|\omega|}\int_0^{B+|A|} e^{-j\frac{\pi}{2}t^2}dt \qquad A2.9$$

2.b. If $|\omega| > 2\frac{M}{\eta}$: Then $sgn(A \pm B) = -1$ and

$$|A+B| = -A-B = |A| - B \qquad A2.10$$

$$|A-B| = -A+B = |A| + B \qquad A2.11$$

and we get

$$-e^{j\omega}\int_0^{|A|-B} e^{-j\frac{\pi}{2}t^2}dt - e^{-j\omega}\int_0^{|A|+B} e^{-j\frac{\pi}{2}t^2}dt$$

$$= -e^{-j|\omega|}\int_0^{|A|-B} e^{-j\frac{\pi}{2}t^2}dt - e^{j|\omega|}\int_0^{|A|+B} e^{-j\frac{\pi}{2}t^2}dt \qquad A2.12$$

Comparing 1.a with 2.a, and 1.b with 2.b, we note that $F_0(-\omega) = -F_0(\omega)$: i.e, $\frac{F_0(\omega)}{\omega}$ is an even function.